

การเตรียม, การวิเคราะห์ และ การจำลองแบบโมเดล
นาโนคอมโพสิตอิเล็กทรอนิกส์แข็ง ระหว่างพอลิเอทรีนออกไซด์/
พอลิไวนิลไพโรลิโดน และมอนต์โมริลโลไนต์

นางสาวสิริรัตน์ อินทรกำแหง

วิทยานิพนธ์นี้เป็นส่วนหนึ่งของการศึกษาตามหลักสูตรปริญญาวิทยาศาสตรมหาบัณฑิต
สาขาวิชาเคมี
มหาวิทยาลัยเทคโนโลยีสุรนารี
ปีการศึกษา 2548
ISBN 974-533-520-7

**PREPARATION, CHARACTERIZATION AND
MOLECULAR MODELING OF
POLY(ETHYLENE OXIDE)/POLY(VINYL
PYRROLIDONE) MONTMORILLONITE
NANOCOMPOSITE SOLID ELECTROLYTES**

Sireerat Intarakamhang

A Thesis Submitted in Partial Fulfillment of the Requirements

for the Degree of Master of Science in Chemistry

Suranaree University of Technology

Academic Year 2005

ISBN 974-533-520-7

**PREPARATION, CHARACTERIZATION AND MOLECULAR
MODELING OF POLY(ETHYLENE OXIDE)/POLY(VINYL
PYRROLIDONE) MONTMORILLONITE NANOCOMPOSITE
SOLID ELECTROLYTES**

Suranaree University of Technology has approved this thesis submitted in partial fulfillment of the requirements for the Master's Degree.

Thesis Examining Committee

M. Tangsathitkulchai
(Assoc. Prof. Dr. Malee Tangsathitkulchai)

Chairperson

Visit Vao
(Asst. Prof. Dr. Visit Vao-Soongnern)

Member (Thesis Advisor)

Tongraar A.
(Assoc. Prof. Dr. Anan Tongraar)

Member

Jatuporn Wittayakun
(Assoc. Prof. Dr. Jatuporn Wittayakun)

Member

V. Sanghiran
(Dr. Vannajan Sanghiran Lee)

Member

S. Rattanaphani S. Thammathaworn
(Assoc. Prof. Dr. Saowanee Rattanaphani) (Assoc. Prof. Dr. Sompong Thammathaworn)

Vice Rector for Academic Affairs

Dean of Institute of Science

สิริรัตน์ อินทรกำแหง : การเตรียม, การวิเคราะห์และการจำลองแบบโมเลกุลนาโนคอมโพสิตอิเล็กโทรไลต์แข็งระบบพอลิเอทิลีนออกไซด์/พอลิไวนิลไพโรลิโดนและมอนต์โมริลโลไนต์ (PREPARATION, CHARACTERIZATION AND MOLECULAR MODELING OF POLY(ETHYLENE OXIDE)/POLY(VINYL PYRROLIDONE) MONTMORILLONITE NANOCOMPOSITE SOLID ELECTROLYTES) อาจารย์ที่ปรึกษา : ผู้ช่วยศาสตราจารย์ ดร. วิสิทธิ์ แวสูงเนิน, 205 หน้า. ISBN 974-533-520-7

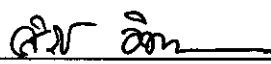

ได้ศึกษาโครงสร้าง อันตรกิริยา สมบัติทางความร้อนและการนำไฟฟ้าเชิงไอออนของสารอิเล็กโทรไลต์ระบบพอลิเมอร์นาโนคอมโพสิตและระบบพอลิเมอร์ผสม โดยระบบที่สนใจในที่นี้คือพอลิเอทิลีนออกไซด์/เกลือโซเดียมไทโอไซยานาต/มอนต์โมริลโลไนต์ ((PEO)₈NaSCN/MMT) และพอลิเอทิลีนออกไซด์/เกลือโซเดียมไทโอไซยานาต/พอลิไวนิลไพโรลิโดน ((PEO)₈NaSCN/PVP) เมื่อ PEO NaSCN MMT และ PVP ทำหน้าที่เป็นพอลิเมอร์ตัวกลาง ประจุไอออน สารเติมแต่งอนินทรีย์และสารเติมแต่งพอลิเมอร์ ตามลำดับ งานวิจัยนี้เริ่มจากการใช้เทคนิคการจำลองแบบโมเลกุลด้วยคอมพิวเตอร์เพื่อศึกษาโครงสร้างพอลิเมอร์โดยใช้ทฤษฎีไอโซเมอร์เชิงโครงสร้าง (RIS) จาก 2 วิธีที่ต่างกันสำหรับการคำนวณหาพลังงานแต่ละโครงสร้างของ PEO คือ semi-empirical (PM3) และ *ab initio* (HF-SCF และ MP2) สำหรับ PVP จะเลือกวิธีโมเลกุลาร์แมคคานิกส์เนื่องจากมีขนาดโมเลกุลใหญ่ แบบจำลอง RIS ที่ได้สามารถทำนายค่าคงที่การคลັปลิงของเอ็นเอ็มอาร์โปรตอนสเปกตรา ขนาดของโมเลกุลพอลิเมอร์ ค่าไดโพลโมเมนต์และสัมประสิทธิ์ที่ขึ้นกับอุณหภูมิได้สอดคล้องกับผลการทดลองเป็นอย่างดี

ถัดไปเป็นการศึกษาระบบอิเล็กโทรไลต์ P(EO)₈NaSCN/yMMT ซึ่งมีอัตราส่วนโมลาร์ของ PEO:NaSCN คงที่ที่ 1:8 และ y มีค่าตั้งแต่ร้อยละ 0 ถึง 20 โดยน้ำหนักและระบบ P(EO)₈NaSCN/PVP โดยมีอัตราส่วน PVP/PEO ในช่วง 0.2 ถึง 0.6 ต่อหน่วยมอนอเมอร์ จากนั้นได้ศึกษาผลของการเติมเกลือ ดินเหนียวและสารเติมแต่งพอลิเมอร์ต่อโครงสร้างและสมบัติของวัสดุพอลิเมอร์อิเล็กโทรไลต์โดยใช้เทคนิคเอกซเรย์ดิฟแฟรกชัน (XRD) ดิฟเฟอเรนเชียลสแกนนิ่งคาลอริมิเตอร์ (DSC) ฟลูอริเยร์แทรนส์ฟอร์มอินฟราเรดสเปกโทรสโกปี (FT-IR) กล้องจุลทรรศน์แสงโพลาไรซ์ (POM) และการวิเคราะห์ค่าการนำไฟฟ้า (Impedance Analyzer) จากผลของ DSC และ XRD พบว่าร้อยละความเป็นผลึกของพอลิเมอร์ลดลงเมื่อเติมดินเหนียวลงไป นอกจากนี้ได้ศึกษาจลนพลศาสตร์ของกลไกในการตกผลึกระบบ PEO/MMT โดยวิธีไอโซเทอร์มอลและนอนไอโซเทอร์มอล ส่วนการศึกษากการเกิดสารเชิงซ้อนระหว่างเกลือกับพอลิเมอร์นั้นพบว่าเกิดแถบการดูดกลืนรังสีอินฟราเรดใหม่ขึ้นซึ่งจะไม่พบใน PEO และยังพบว่าการสั่นของ

พันธะ C-O-O มีแถบที่กว้างขึ้นตามปริมาณของเกลือที่เติม ข้อมูลจาก FTIR ยังใช้ศึกษาการเกิดอันตรกิริยาแบบแข่งขันระหว่าง PEO/NaSCN และ PEO/MMT กล่าวคือเมื่อเติม MMT จะดูเหมือนทำให้มีการแตกตัวของเกลือเพิ่มขึ้นและเพิ่มจำนวนไอออนอิสระในระบบ แต่บทบาทของ PVP ที่เติมลงไปจะพบว่าแตกต่างจาก MMT เนื่องจาก PVP ไม่เข้ากันได้ดีกับ $P(EO)_8NaSCN$ ถึงแม้จะมีอันตรกิริยาระหว่าง PVP-NaSCN และ PEO-NaSCN เนื่องจากสามารถสังเกตเห็นการแยกเฟสขึ้นในสารผสม ค่าการนำไฟฟ้าของ $P(EO)_8NaSCN/MMT$ มีค่าสูงกว่า $P(EO)_8NaSCN/PVP$ ซึ่งค่าการนำไฟฟ้าของ $P(EO)_8NaSCN/PVP$ ยังพบว่ามีค่าต่ำกว่า $P(EO)_8NaSCN$ อีกด้วย

สาขาวิชาเคมี
ปีการศึกษา 2548

ลายมือชื่อนักศึกษา
ลายมือชื่ออาจารย์ที่ปรึกษา

SIREERAT INTARAKAMHANG : PREPARATION, CHARACTERIZATION
AND MOLECULAR MODELING OF POLY(ETHYLENE OXIDE)
/POLY(VINYL PYRROLIDONE) MONTMORILLONITE
NANOCOMPOSITE SOLID ELECTROLYTES. THESIS ADVISOR :
ASST. PROF. VISIT VAO-SOONGNERN, Ph.D. 205 PP. ISBN 974-533-520-7

PEO/PVP/CLAY/NaSCN/POLYMER NANOCOMPOSITE/RIS MODEL

The structure, interaction, thermal behavior and ionic conductivity of polymer nanocomposite and blend electrolytes were studied. The system of interest were P(EO)₈NaSCN/MMT and P(EO)₈NaSCN/PVP at various MMT and PVP content, where PEO (Polyethylene oxide), NaSCN (Sodium thiocyanate), MMT (Montmorillonite) and PVP (Polyvinyl pyrrolidone) act as polymer hosts, ionic charge, inorganic and polymer filler, respectively. This work started from the computational molecular modeling of polymer conformation based on Rotational Isomeric State (RIS) model using two different approaches. For PEO, conformational energies were estimated from both *semi-empirical* (PM3) and *ab initio* (HF-SCF and MP2) electronic structure calculation. In stead, due to large molecular size, force field based Molecular Mechanics (MM) method was employed for PVP. These RIS models predicted NMR coupling constants, chain dimensions, dipole moments, and temperature coefficients in reasonable agreement with experiments.

Next, the P(EO)₈NaSCN/yMMT system, where the molar ratio of PEO:NaSCN was fixed at 1:8 and y varied from 0 to 20 wt%, and P(EO)₈NaSCN/PVP, where PVP/PEO varied from 0.20 to 0.60 repeating unit were investigated. X-Ray

Diffraction (XRD), Differential Scanning Calorimeter (DSC), Fourier Transform Infrared Spectroscopy (FTIR), Polarized Optical Microscope (POM) and Impedance Analyzer were employed to investigate the effect of salt, clay and polymer filler on structures and properties of these materials. From DSC and XRD results, the percent of polymer crystallinity was decreased upon addition of clay. Isothermal and nonisothermal crystallization kinetics of PEO/MMT were also studied. Complexation of salt to polymer was substantiated by an appearance of new bands which were not presented in pure PEO and also broaden the C-O-C vibrations as the salt content increased. Competitive interaction between PEO/NaSCN and PEO/MMT can also be illustrated by FTIR data. Adding MMT was seen to enhance salt dissociation and increase the carrier concentration. The role of PVP addition is quite different from MMT in that PVP did not compatible well with P(EO)₈NaSCN. Although there was a mutual interaction between PVP···NaSCN and PEO···NaSCN, phase separation of these mixtures was observed. The magnitude of an ionic conductivity of P(EO)₈NaSCN/MMT was higher while that of P(EO)₈NaSCN/PVP was smaller compared to the undoped P(EO)₈NaSCN.

School of Chemistry

Academic Year 2005

Student's Signature

Advisor's Signature

Sireeret IntarakamhangWit Vong

ACKNOWLEDGMENTS

I am grateful to my thesis advisor, Asst. Prof. Dr. Visit Vao-Soongnern, for his valuable advices, comments for research work and for kindness and suggestions about positive thinking. I am also very thankful for thesis examining committee for reading and comments throughout the entire thesis. I wish to thank all the lecturers of the School of Chemistry, Suranaree University of Technology for their good attitude and useful advice, all of the staff at the Center for Scientific and Technological Equipment for their assistance to use instruments. Special thanks for Assoc. Prof. Dr. Sutin Kuharuangrong, Department of Ceramic Engineering for help in Impedance analyzer.

The gratitude to all the lecturers in the Department of Chemistry, KhonKaen University for advice and suggestions when I did bachelor' degree.

I am thankful to all graduate students especially, all members in Department of Chemistry for their patience, support, encouragement and made this a fun time.

I would like to thanks the Research Department at the Institute of Science Suranaree University of Technology and National Synchrotron Research for financial support.

Last, but certainly not least, I would like to thank my beloved family who support, believe and encouragement.

Sireerat Intarakamhang

CONTENTS

	Page
ABSTRACT IN THAI.....	I
ABSTRACT IN ENGLISH.....	III
ACKNOWLEDGEMENTS.....	V
CONTENTS.....	VI
LIST OF TABLES.....	XI
LIST OF FIGURES	XIV
LIST OF ABBREVIATIONS.....	XXV
CHAPTER	
I INTRODUCTION.....	1
II LITERATURE REVIEW.....	9
2.1 Solid Polymer Electrolytes (SPEs).....	9
2.2 Poly(ethylene oxide), PEO.....	11
2.3 Polymer–clay nanocomposites for solid-state Electrochemical Devices.....	18
2.4 The Rotational Isomeric State (RIS) Theory.....	24
III RESEARCH METHODOLOGY.....	30
3.1 Apparatus and Materials.....	30
3.2 Computational Part.....	31
3.2.1 Statistical Weight Matrices of PEO and PVP.....	31

CONTENTS (Continued)

	Page
3.2.2 Rotational Isomeric State (RIS) Model.....	33
3.2.2.1 RIS Parameters from Molecular Mechanics (MM) Technique.....	38
3.2.2.2 RIS parameter from Quantum Mechanics (QM) Technique.....	40
3.3 Experimental Part.....	43
3.3.1 Sample Preparation.....	44
3.3.1.1 PEO/MMT nanocomposites via solution intercalation.....	44
3.3.1.2 PEO/NaSCN/MMT nanocomposites via solution intercalation.....	45
3.3.1.3 Polymer/MMT nanocomposites via melt intercalation/exfoliation.....	45
3.3.1.4 PEO/NaSCN/PVP complexes.....	45
3.3.2 Characterization.....	46
3.3.2.1 NMR Spectroscopy.....	46
3.3.2.2 Viscometry.....	46
3.3.2.3 X-ray Power Diffraction (XRD).....	48
3.3.2.4 Differential Scanning Calorimeter (DSC).....	48

CONTENTS (Continued)

	Page
3.3.2.5 Fourier Transform Infrared Spectroscopy (FT-IR).....	49
3.4.2.6 Polarized Optical Microscopy (POM).....	50
3.4.2.7 Ionic Conductivity and Impedance Analyzer....	50
IV RESULTS AND DISCUSSION.....	54
4.1. Computational Part.....	54
4.1.1 Nuclear Magnetic Resonance (NMR) Experiment of Poly(N-vinyl-2-pyrrolidone) (PVP).....	54
4.1.2 Conformational Characteristic of Poly(N-vinyl-2- pyrrolidone) (PVP).....	62
4.1.3 Conformational Energy of PEO by <i>Semi</i> -empirical Quantum Chemistry Calculation.....	80
4.1.3.1 Statistical Weight Matrices of PEO by <i>Semi</i> - empirical Quantum Chemistry Calculation.....	81
4.1.3.2 Conformational Energy of PEO by <i>ab initio</i> Quantum Chemistry Calculation.....	90
4.1.3.2.1 Effect of Basis set and Electron Correlation Conformational Energies.	91
4.1.3.2.2 Statistical Weight Matrices of PEO by <i>ab initio</i> Electronic Calculation.....	96

CONTENTS (Continued)

	Page
4.1.3.3 Conformational Dependent Properties of PEO.	99
4.1.3.4 NMR Vicinal Coupling Constant and the RIS Model of PEO.....	105
4.2 Experimental Part	110
4.2.1 Crystallization Kinetics.....	110
4.2.1.1 Isothermal Crystallization Kinetics.....	110
4.2.1.2 Non-isothermal Crystallization Kinetics.....	115
4.2.2 X-Ray Diffraction (XRD).....	129
4.2.2.1 PEO/Montmorillonite nanocomposite.....	129
4.2.2.2 PEO/NaSCN Electrolyte Complex.....	133
4.2.2.3 PEO/NaSCN/MMT Electrolyte nanocomposite	134
4.2.3 Differential Scanning Calorimeter (DSC).....	135
4.2.3.1 PEO/Montmorillonite nanocomposite.....	136
4.2.3.2 PEO/NaSCN/MMT nanocomposite.....	138
4.2.4 Fourier Transform Infrared Spectroscopy (FT-IR).....	142
4.2.4.1 PEO/Montmorillonite nanocomposite.....	142
4.2.4.2 PEO/NaSCN Electrolyte Complex.....	150
4.2.4.3 PEO/NaSCN/MMT Electrolyte nanocomposite	157
4.2.5 Impedance Analyzer.....	161
4.2.6 PEO/NaSCN/PVP Electrolytes.....	170

CONTENTS (Continued)

	Page
4.2.6.1 X-Ray Diffraction (XRD)	170
4.2.6.1 Differential Scanning Calorimetry (DSC).....	170
4.2.6.3 Fourier Transform Infrared (FTIR)	
Spectroscopy	172
4.2.6.4 Polarized Optical Microscope.....	173
4.2.6.5 Impedance Analyzer.....	175
V CONCLUSION.....	178
REFERENCE.....	180
APPENDICES.....	188
Appendix A Statistical Weight Matrices of PEO.....	189
Appendix B Paper of Presentation.....	191
CURRICULUM VITAE.....	205

LIST OF TABLES

Table		Page
1.1	Specific properties and advantages of polymer solid electrolytes	2
2.1	Polymer hosts generally studied.....	12
2.2	Lists of salts used in polymer complex systems.....	18
2.3	Chemical formula and characteristic parameter of commonly used 2:1 phyllosilicates.....	21
4.1	The chemical shift (δ) value of protons NMR for PVP with a comparison to the reported literature.....	56
4.2	The chemical shift δ value of C^{13} NMR spectra for PVP and comparison with Ref.....	56
4.3	Intrinsic viscosities of PVP in water.....	63
4.4	Summary conformational magnitudes for <i>meso</i> and <i>racemic</i> diads of PVP as function of the dielectric constant $\epsilon=78$	73
4.5	Summary conformational magnitudes for <i>meso</i> and <i>racemic</i> diads of PVP as function of the dielectric constant $\epsilon=4$	74
4.6	Summary conformational magnitudes for <i>meso</i> and <i>racemic</i> diads of PVP as function of the dielectric constant $\epsilon=\infty$	75
4.7	Experimental values of the chain dimensions of PVP extrapolated to unperturbed dimensions from viscosity and osmotic measurements performed in several solvents at 25°C.....	78

LIST OF TABLES (Continued)

Table		Page
4.8	Conformational characteristics of PEO model compound as estimated from the semi-empirical PM3 potential energy (kcal/mol) contour map at 298K.....	89
4.9	Energies of <i>tgt</i> rotamer of 1,2-Dimethoxyethane relative to those of <i>ttt</i> rotamer, calculated by the <i>ab initio</i> method.....	94
4.10	DME conformer geometries energies.....	97
4.11	RIS model of PEO from <i>ab initio</i> calculation of DME model compound.....	100
4.12	Representative conformational energy parameter (first- and second-order) sets adopted for the comparison.....	102
4.13	Geometrical parameters used in the RIS calculation of conformation-dependent properties.....	102
4.14	Comparison of the calculation and observed values of some conformation-dependent properties of PEO.....	104
4.15	Bond conformations and NMR vicinal coupling constants of PEO	109
4.16	Results of the Avrami analysis for isothermal crystallization of PEO, PEO/NaSCN and PEO/MMT at $T_c = 50^\circ\text{C}$	114
4.17	Parameters of sample during nonisothermal crystallation process...	122
4.18	Nonisothermal crystallization kinetic parameter at difference degrees of crystallinity.....	126

LIST OF TABLES (Continued)

Table		Page
4.19	The basal spacing d_{001} (Å) of pure MMT and PEO/MMT at various MMT contents.....	131
4.20	Melting temperatures (T_m), enthalpy of melting (ΔH_m) and percentage crystallinity ($\%X_c$) of PEO and PEO+clay at various clay concentration.....	138
4.21	IR absorption bands and their assignments of PEO, dry MMT and PEO/MMT hybrid (4000-400 cm^{-1}) (mode assignments: ν (stretching); δ (bending); w (wagging); t (twisting); r (rocking)).....	149
4.22	Film thickness, Bulk Resistance (R_b) and conductivity.....	165

LIST OF ABBREVIATIONS

SPEs	Solid Polymer Electrolytes
PEO	Poly(ethylene oxide)
NaSCN	Sodium Thiocyanate
PVP	Polyvinyl pyrrolidone
MMT	Montmorillonite
XRD	X-Ray Diffraction
DSC	Differential Scanning Calorimeter
FT-IR	Fourier Transform Infrared
POM	Polarized Optical Microscope
NMR	Nuclear Magnetic Resonance
RIS	Rotational Isomeric State
MM	Molecular Mechanics
MP2	The second order Møller-Plesset perturbation theory
Φ	Hydrodynamic Factor
σ	Ionic Conductivity
S cm^{-1}	Siemen/centimeter
I	Current
V	Voltage
R	Resistance
T_g	Glass Transition Temperature

LIST OF ABBREVIATIONS (Continued)

T_m	Melting Temperature
$\langle r^2 \rangle_o$	Mean Square Unperturbed end-to-end Distance
$\langle r^2 \rangle_o / nl^2$	Characteristic Ratio
C_n	Characteristic Ratio
$\langle s^2 \rangle_o$	Mean-square Radius of Gyration
$\langle s^2 \rangle_o / nl^2$	Mean-square Unperturbed Radius of Gyration Ratio
$\langle \mu^2 \rangle_o / nm^2$	Mean-square Unperturbed Dipole Moment
t	Trans
g^+	Gauche ⁺
g^-	Gauche ⁻
Z	Conformational Partition Function
U	Statistical Weight Matrix
$E_i(\phi_i)$	Single Bond Energy
$\langle \dots \rangle$	Ensemble Average for all Possible Conformations
G	Super Generator Matrix
I	Identity Matrix
\otimes	Direct Product
ϕ	Torsion Angle

LIST OF ABBREVIATIONS (Continued)

$[\eta]$	Intrinsic Viscosity
θ	Bond Angle
η_{rel}	Relative Viscosity
η_{red}	Reduced Viscosity
η_{inh}	Inherent Viscosity
MW _j	Molecular Weight of Component j
ΔH_m	Heat of Melting
% wt	Percent Weight
K	Degree Kelvin
°C	Degree Celcius
Å	Angstrom
<i>et al.</i>	et alia (and other)

CHAPTER I

INTRODUCTION

Polymer electrolytes are new kind of ionics solid that have been widely received attention recently during the past years because these materials exhibit a potential use in electrochemical application, especially for dried cell rechargeable battery of electronic appliance and energy storage system for electric car. Since these materials have been devised for potential application, many research studies have been launched and made a lot progress in various aspects such as attempts to synthesize new polymeric materials, to search for high performance additives or salts, to study the microstructure of these materials, as well as a theoretical and computational studies for more understanding of material behavior at molecular level. All of those efforts based solely on desires to find a proper explanation of unusual diffusion and ionic conductivity mechanism of polymer solid electrolytes.

Since Wright discovered ionic conductivity in a PEO/Na⁺ complex in 1975, and Armand (1979) proposed the application of SPE to lithium batteries, the research and development effort has been made throughout the world, particularly in the United States, Japan and Europe. In these countries, such work is quite active in national projects such as UNITED STATES ADVANCED BATTERY CONSORTIUM (USABC) in the USA, (New Energy and Industrial Technology Development Organization NEDO) in Japan and JOULE in Europe. In general, polymer solid electrolyte that are suitable for battery application should contain the following properties

Table 1.1 Specific properties and advantages of polymer solid electrolytes

Specific properties	Advantages
High energy density	Small part but high energy generation
Light weight	Good for small/mobile electronic component
Long working lifetime	Low cost for application
Flexibility	Easy to process
Environmental safety	Clean technology

A major limitation for widespread application of solid polymer electrolytes is their low conductivity at ambient temperatures. A basic understanding of ionic transport mechanisms would greatly facilitate the development of new high-conductivity electrolytes. For a material to exhibit high ionic conductivity, it is necessary to optimize the number and nature of the charge carriers (free ions and clusters of ions with net charge). In order for charge carriers to exist, the cation-polymer binding energy should be comparable to the cation-anion binding energy that is, the salt must dissolve in the polymer matrix. There are three major interrelated factors that play a paramount role in ionic charge transport: cation-anion complexation, cation-polymer host and anion-polymer host complexation, and the mobility of both the charge carriers and the polymer. The conductivity is not only sensitive to the degree of crystallinity of polymer host, but also very much to salt concentration. The concentration dependence usually shows a maximum due to competing effects. As the concentration increases, the conductivity increases due to the availability of more charge carriers. At the same time, however, formation of ion pairs and larger clusters set in, which leads to a decrease in the conductivity. In addition, at higher salt concentration, the polymer becomes stiffer as can

be seen from the rise of the glass-transition temperature, which can be ascribed to an effective transient cross-linking by the salt. Lower chain mobility accounts for an additional lowering of the conductivity.

Our past works at the Laboratory of Computational and Applied Polymer Science (LCAPS) at Suranaree University of Technology involved with the preparation and characterization of solid polymer electrolyte and this research activity has been performed since 2000. (Decha, 2002; Chaodamrongsakul, 2003). Initial studies during that period showed that polymer solid electrolytes could be easily prepared and they exhibited relatively high ionic conductivity at room temperature. However, the magnitude of ionic conductivity was not constant but it varied with the amount of added salt. These findings were different from other types of electrolytes. In general, the conductivity of most electrolytes is caused by charge diffusion mechanism rather than ion diffusion. In previous works, polymer solid electrolytes were prepared for the system of polyethylene oxide/alkali salt and these materials were characterized by various instrumental techniques e.g. thermal analysis (DSC, TGA), infrared spectroscopy (FTIR), X-Ray diffraction (XRD) and electron microscopy (SEM). These studies suggested that the ionic conductivity may be related to the coupling mobility between salt ion and the coordinated segment of polymer chain. Furthermore, the conductivity is also depended on the ability of salt to dissociate and the ability of cation to form the coordinate bond with oxygen atom in polymer molecule. (Quartarone *et al.*, 1998; Song *et al.*, 1999; Dias *et al.*, 2000)

The theoretical prediction for the energy density of PEO/salt complex is up to 800 Whkg⁻¹. Even though PEO can dissolve inorganic salt well but it is later found that this polymer complex still can not give ionic conductivity higher than 10⁻⁶ Scm⁻¹ except at the

temperature above its melting temperature (60°C). In general, the ionic diffusion can best occur in the amorphous portion of these materials. Therefore, subsequent works are focused on the methodology to reduce the crystallinity of PEO/salt complex such as followings:

- Synthesis of new polymer e.g. copolymerization of macromonomer, grafting, crosslinking and networking of polymer.
- Adding small molecular plasticizer or blending with other amorphous polymer to decrease the percent of crystallinity of materials.
- Adding inorganic filler to reduce the amount of crystallinity without disturbing the mechanical properties of new materials. (If the filler is of nanosize and interact well with the polymer matrix, we will call this material as polymer nanocomposite.)

To improve the magnitude of ionic conductivity, the strategy in this thesis is to add some fillers that are either compatible with polymer matrix or interact with salt. Two type of fillers was employed in this work as: (1) nanosized inorganic fillers i.e. clay mineral which interact with polymeric matrix such that it can reduce the percent of crystallinity of these polymer complexes and (2) polymer filler with active functional groups that can interact salt and enhance salt dissociation. It has long been hypothesized that both factors (salt dissociation and percent of crystallinity) are the key to control an ability of ion to diffuse and gain higher ionic conductivity.

In the first case, adding nanosized particle to improve an ionic conductivity of polymer solid electrolytes was focused. Nanosized fillers have widely been used as reinforcement materials for polymer. Among these inorganic materials, special attention has been paid to clay mineral in field of nanocomposites because of its small particle size

and intercalation properties. Several polymer-clay mineral blends were produced by using polymer intercalation from solution into layered smectite-type clay mineral known as montmorillonite (MMT). The structure and thermal/mechanical properties of the blends were studied, and found that clay mineral has a notable structure on these blend. An interest in the present study is to investigate whether such geometry is observed in solvent-cast poly(ethylene oxide) (PEO)-clay mineral blend. Furthermore, an attempt will be made to explore the possibility to blend PEO with a second polymer component as a filler. Poly(vinyl pyrrolidone), PVP, is selected to test this idea for two reasons. First, PVP is an amorphous polymer that should permit faster ionic mobility compared to other semi-crystalline polymers. Second, due to the carbonyl groups (C=O) in the side chains and its high dielectric constant, PVP should interact well with several ions and enhance more number of free ions in the system. Another interesting point for PEO/PVP/salt mixture is to see whether if the mutual interaction for PEO...salt vs PVP...salt can overcome the entropic repulsion between these long chain polymers and how it relate to their miscibility gaps and ionic conductivity.

It is also important to understand the physico-chemical basis and atomistic mechanism for an increase in ionic conduction. Previous analytical works have been performed using some instrumental methods such as thermal analysis (DSC, TGA), infrared spectroscopy, X-Ray diffraction and electron microscope can only provide rudimentary results to explain this phenomena e.g. the enthalpy of fusion of crystalline phase, the change in vibrational frequency of chemical bonds and the change in material morphology, etc. This information can give only the qualitative explanation for the microscopic change of material structure that enhance the ionic conductivity. Therefore, a detailed model at the atomistic level is needed to construct the framework of thought

that can explain the relationship between the structure and property of these materials. In this regard, computational molecular modeling is an alternative way to correlate the structure and property of polymer molecules used in this study at the atomistic level. In this proposal, we will employ two different computational molecular modeling techniques to construct the Rotational Isomeric State (RIS) model of PEO and PVP as follows: (1) *ab initio* and *semi-empirical* quantum chemistry calculation (PEO) and (2) molecular mechanics calculation (PVP)

For more information, a study of polymeric materials by computational molecular modeling has long been developed during the past decades in Europe and U.S.A. According to the principle of Computer-Aided Material Design (CAMD), this method is to design the new materials before the real synthesis in later time. This technique will certainly reduce the cost of research and development in the experimental stage. In this proposal, we will focus mainly on in-house software initially developed by Visit Vao-soongnern (Chemistry, Suranaree University of Technology) from the past collaboration with the Department of Polymer Science, University of Akron, U.S.A during 2000-2004.

Research Objective

1. To study the effect of adding mineral clay (MMT) and amorphous polymer (PVP) on the structure and properties of semi-crystalline polymer(PEO)-salt(NaSCN) electrolyte complex.
2. To gain more understanding about the conformational dependent properties at the molecular level of the selected polymer used in the preparation of solid electrolyte nanocomposite by both theoretical and molecular modeling approach.

3. To explain the correlation between the structures of Polymer(PEO or PVP)/clay(MMT)/salt(NaSCN) nanocomposite electrolytes and the physical properties of these materials.

Scope and Limitation of the Study

Computational and Theoretical Part

The Rotational Isomeric State (RIS) model will be employed to predict the conformational dependent properties of PVP and PEO such as the unperturbed mean-square end-to-end distance, $\langle r^2 \rangle_0$, the mean square dipole moment $\langle \mu^2 \rangle_0$ and the mean-square radius of gyration, $\langle S^2 \rangle_0$ using statistical weight matrices derived from Quantum Mechanics (QM) (for PEO) and Molecular Mechanics (MM) (for PVP) calculation. The elements of the matrices will be estimated from the conformational energy of small representative segment of polymer molecules. For MM calculation, will be performed using HyperChem Release7 and QM calculation using Gaussian 98 revision A.3.

Experimental Part

In this research work, structures and properties of the intercalation nanocomposite for the system of Polymer (PEO,PVP)/Clay(MMT)/Salt(NaSCN) at various stoichiometric ratio will be investigated. The experimental techniques employed in this section are as follows:

Polymer Characterization

Viscometer: to determine the intrinsic viscosity and to estimate the molecular weight and size of polymeric molecule.

Nuclear Magnetic Resonance (NMR) Spectroscopy: to determine the microstructure of PVP chain.

Polymer-clay Nanocomposite Characterization

X-Ray Diffraction (XRD): to verify the structure formation of nanocomposite (intercalation or exfoliation) and microstructure of solid polymer electrolyte.

Fourier Transform Infrared Spectroscopy (FT-IR): to monitor an ionic association and to study the interaction between polymer-clay, polymer-polymer and polymer-salt complexes.

Differential Scanning Calorimeter (DSC): to obtain the percent crystallinity, temperature and enthalpy of transition of polymer electrolyte and polymer nanocomposite, and kinetic study of PEO, PEO/salt, PEO/MMT and PEO/salt/MMT system.

Impedance Analyzer: to determine the ionic conductivity and impedance response of the sample as a function of input frequency.

CHAPTER II

LITERATURE REVIEW

2.1 Solid Polymer Electrolyte

Polymer electrolyte may generally be defined as a membrane that possesses transport properties comparable with that of common liquid ionic solutions. The development of polymer electrolytes has drawn the attention of many researchers in the last three decades as they find applications not only in lithium batteries but also, in other electrochemical devices such as super capacitors and electrochromic devices, etc.

In principle, a Solid Polymer Electrolyte (SPEs) battery can be formed by sandwiching the electrolyte between a solid metal (or a composite carbon) anode and a composite cathode as depicted in Figure 2.1. The pre-requisites for a SPEs are (i) high ionic conductivity at ambient and sub-ambient temperatures, (ii) good mechanical strength, (iii) appreciable transference number, (iv) thermal and electrochemical stabilities, and (v) better compatibility with electrodes. The polymer electrolyte should allow good cycle lives at low temperatures and must withstand with the internal pressure build up during the battery operations. Although, the polymer electrolyte was launched in 1973 by Fenton *et al.*, its technological importance was appreciated in early 1980.

SPEs consist of salts dissolved in high molecular weight polymer. Polymer, which can dissolve salt must be comprised of O, N or S atom because these atoms can

interact with cation, and make decompositive salt to have better ionic conductivity. A considerable scientific effort has been dedicated to exploring and understanding the characteristics of these electrolyte systems. Many investigations have focused on developing SPEs with high ionic conductivities (10^{-3} S/cm or higher) at ambient temperature (Chintapalli, 1996). In majority of reported system, an alkaline metal salt is solubilized in a polymer, generally through complex formation with ion-chelating monomer unit or with pendant moieties of the macromolecule.

The important criteria for a polymer to act as a host for complex formation include: (Mendolia *et al.*, 1995)

- (i) Having atom or groups of atom with sufficient donor ability to coordinate cation.
- (ii) Low bond rotation energy barriers to facilitate polymers segmental motion.
- (iii) A suitable distance between coordinating heteroatoms allowing interaction with the ions.

To date, several polymer hosts have been developed and characterized that shown in Table 2.1.

Poly(ethylene oxide) (PEO) is the most interesting base material for SPEs because of its high chemical and thermal stability. The chemical structure of PEO consists of the series of polyethers ($[-(\text{OCH}_2\text{CH}_2)-]$). PEO is a semicrystalline polymer, possessing both an amorphous and a crystalline phase at room temperature. PEO is a linear polymer and the regularity of the structure unit allows a high degree of crystallinity of about 70 to 80% usually with a density 1.2 g/cm^3 and a heat of fusion value of 188.2 J/g . PEO readily crystallizes in 7_2 helical structure as shown in

Figure 2.2 which contains seven ethylene oxide repeat units with two turns in a fiber period of 19.3 Å.

2.2 Poly(ethylene oxide), PEO

The crystalline structure of PEO is monoclinic unit cell as displayed in Figure 2.3. by Takahashi and coworkers (1973). From XRD analysis confirmed that PEO molecules are well packed and that the molecules are neither unreasonably close nor too far apart. The internal rotation angles are considerably distorted from the uniform helix, as a result of intermolecular forces. This distortion and the ability of the PEO to orient when stressed show the high degree of flexibility of the PEO chains.

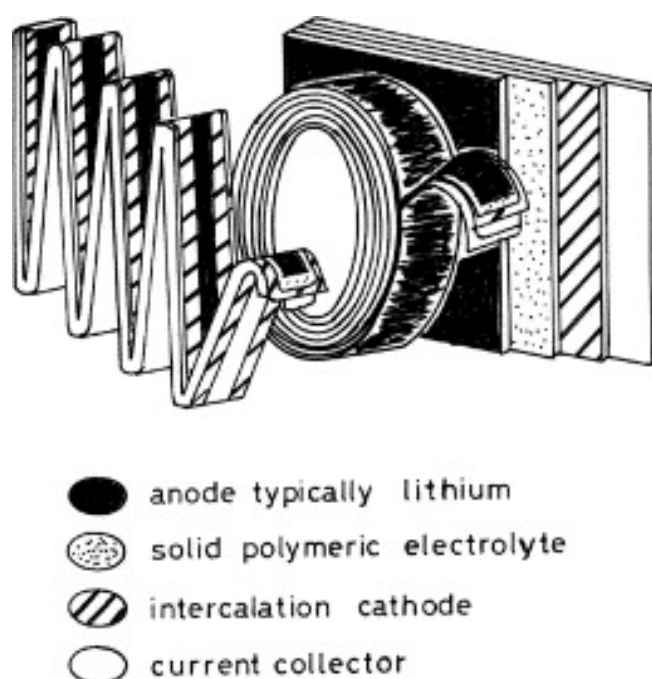


Figure 2.1 Diagram of basic construction of polymer-based batteries. The thin membrane composites are flexible and can be arranged into several desired geometries (Mendolia *et al.*, 1995)

Table 2.1 Polymer hosts generally studied (Stephan, 2006)

Polymer host	Repeat unit	Glass transition temperature, T_g ($^{\circ}\text{C}$)	Melting point, T_m ($^{\circ}\text{C}$)
Poly(ethylene oxide)	$-(\text{CH}_2\text{CH}_2\text{O})_n-$	-64	65
Poly(propylene oxide)	$-(\text{CH}(-\text{CH}_3)\text{CH}_2\text{O})_n-$	-60	- ^a
Poly(acrylonitrile)	$-(\text{CH}_2-\text{CH}(-\text{CN}))_n-$	125	317
Poly(methyl methacrylate)	- $(\text{CH}_2\text{C}(\text{CH}_3)(\text{COOCH}_3))_n$	105	-
Poly(vinyl chloride)	$-(\text{CH}_2-\text{CHCl})_n-$	85	-
Poly(vinylidene fluoride)	$-(\text{CH}_2-\text{CF}_2)_n-$	-40	171
Poly(vinylidene fluoride-hexafluoropropylene)	$-(\text{CH}_2-\text{CH})$	-90	135

^aAmorphous.

PEO can also solvate a wide variety of salts, even at very high salt concentration (Wright *et al.*, 1975; Armand, 1979; Chintapalli, 1996; Quartarone *et al.*, 1998). The solvation of salt occurs through the association of the metallic cation with the oxygen atom in the backbone. Because pure PEO is a semicrystalline polymer, significant ionic transport occurs only within the amorphous phase. This feature explains the dramatic decrease in ionic conductivity seen in many PEO-based

systems for temperature below the melting point of pure crystalline PEO ($T_m \sim 66^\circ\text{C}$); the crystalline PEO regions are non-conductive and serve to hinder bulk ionic transport. Clearly, the inherent crystallinity of PEO is not very attractive for applications in solid electrolytes.

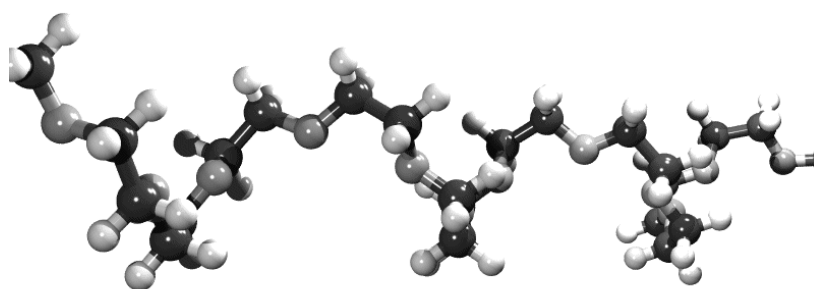


Figure 2.2 PEO viewed perpendicular to the crystalline helix

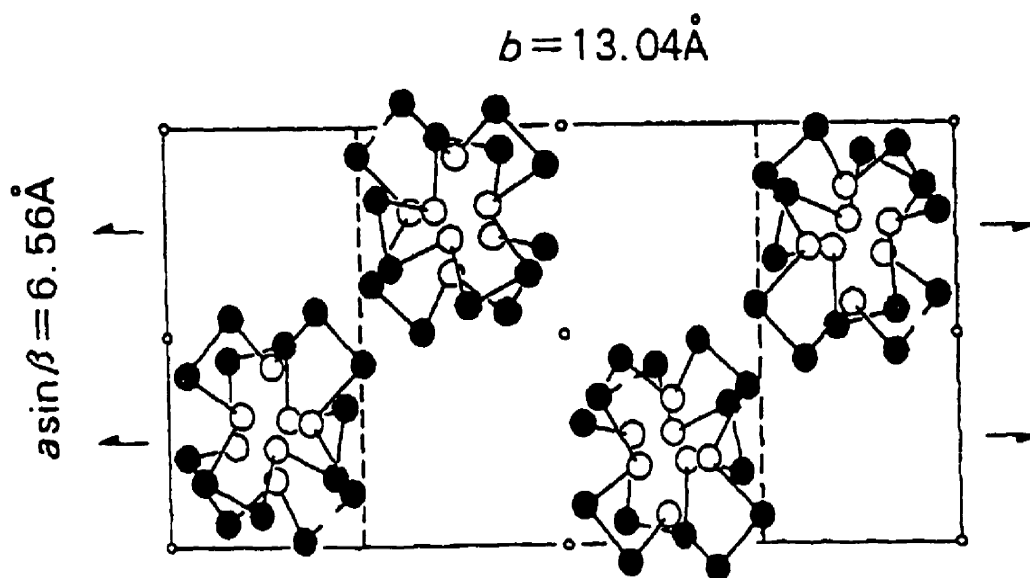


Figure 2.3 Crystal structure of PEO

PEO-Salt Electrolytes

Large research efforts have been devoted on PEO-based electrolyte systems in the last two decades. As mentioned earlier, after Wright's discovery of ionic conductivity in alkali metal salt complexes of PEO in 1973. These electrolytes combine the advantages of solid-state with the ease of casting as thin films. However, PEO-based electrolytes offer very low ionic conductivity that ranges from 10^{-8} to 10^{-4} Scm^{-1} at temperatures between 40 and 100°C , which excludes ambient temperature applications (Hooper, A. and North, J. M., 1983; Fontenella *et al.*, 1983). The mechanism of ionic motion of a lithium ion in a PEO-host is proposed and displayed in Figure 2.4.

In 1981, Papke and coworkers support a single strand helical arrangement with a 2.6 \AA inside diameter of PEO chains with Na and K salt complexes on the basis of infrared and Raman studies as illustrated in Figure 2.5. Their molecular model indicates that this tunnel comprises *trans* (*t*) C-O bonds and alternating *gauche* (*g*) C-C bonds, and four oxygen atoms of polymer coordinate with cation placed inside the helix. On the contrary, Wright *et al.* proposed a double strand helical arrangement of the PEO chains based on their investigations on the interpretation from crystallographic data from X-ray fiber photograph on KSCN and NaSCN complexes.

It is clear that PEO is able to solvate a wide range of metal salts, including alkali metals, alkaline earth metals and transition metals. The different of salt influence the electrolyte properties. The hard-soft acid-base principle, proposed by (Pearson, 1963), is likely to give a good prediction for stability of acids-bases complexes. The hard acids and bases have high electronegativity (electron held tightly), but low polarizability and to oxidize. The soft acids and bases are opposite.

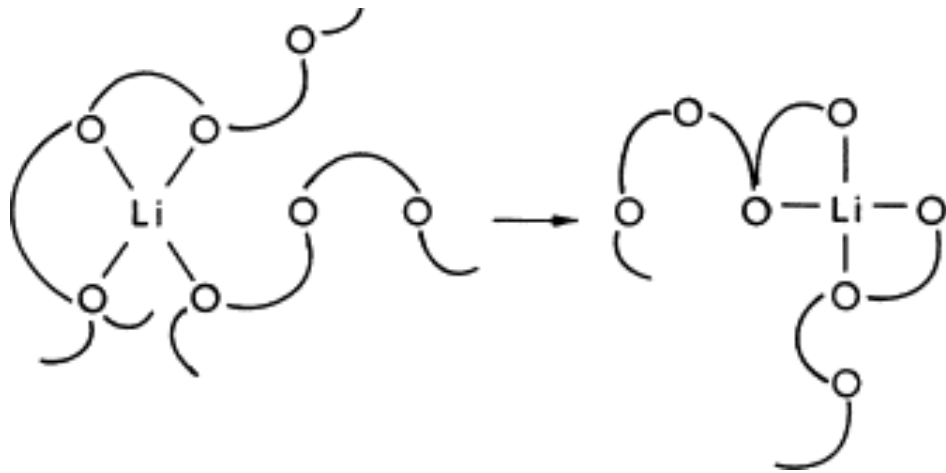


Figure 2.4 Cartoon of ion motion in a polymer host (Stephan, 2006)

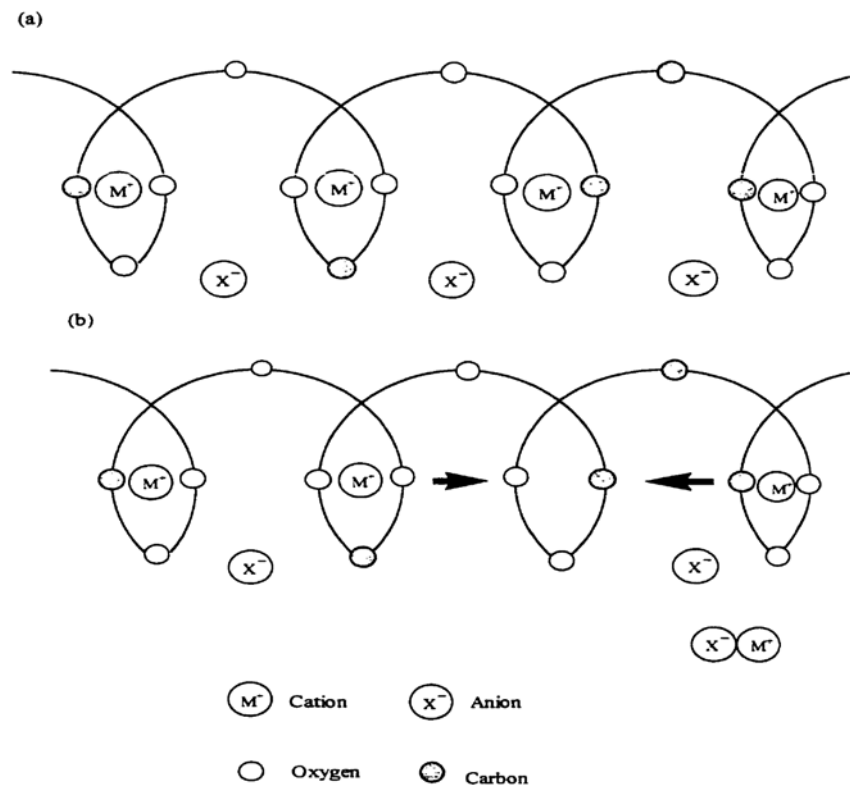
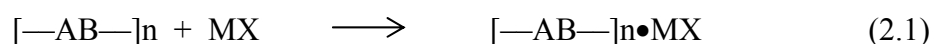


Figure 2.5 A regular helix model of the crystalline PEO complex (a) below the melting transition temperature (b) above the melting transition temperature. (Puatrakul, 2000)

Generally, the strongest interactions occur by matching between hard acids and bases or soft acids and bases. Thus, ether oxygen in PEO may be regarded as hard bases having oxygen as donor atoms with electronegativity and low polarizability. Consequently, Armand (1987) suggested that the strongest solvation in PEO would be with a hard cation, *e.g.* Li^+ , Na^+ , Mg^{2+} and Ca^{2+} . This is reasonable that these cations have been widely used as a lightweight, high energy density polymer electrolyte battery. MacCallum and Vincent (1987) explained that in water or hydrogen bonded solvent such as alcohols, hydrogen bonding is crucial for specific anion solvation. On the other hand in less polar solvents such as acetonitrile or polymer solvent charge dispersion is main factor for the stability of the anion solvation. Due to the fact that large anion with delocalized charge, ether “soft” (*e.g.* I^-) or “hard” bases (*e.g.* CF_3SO_3^-), requires little solvation, the most appropriate anions for polyether-type polymer electrolyte formation would be expected to follow the order (Gray, 1991):



In general, salts of singly charged polyatomic anions such as LiCF_3SO_3 or LiClO_4 will dissolve in polyethers. Ratner *et al.* (1987) discusses the formation of a complex as the result of the competition between solvation energy of salt, according to equation (2.1).



where $[\text{---AB---}]$ represents the polymer repeating unit, M is generally an alkali metal and X is an anion. In the case of PEO and PPO, the repeating unit consists of lone

pair oxygen as hard base. The solvation of the ions must be strong enough to overcome the lattice energy of the salt in order to form complex (Puatrakul, 2000).

PEO has been found to form complexes with lithium salts such as LiI, LiCl, LiSCN, LiClO₄, LiCF₃SO₃, LiBF₄, and LiAsF₆ (Kovac *et al.*, 1998; Smith *et al.*, 1996). Crystal structure of polymer-salt determination from powder x-ray diffraction data have been shown to provide valuable information on ion-polymer and ion-ion interactions since the local environment in the melt is likely to be very similar to that in the crystal from which it was obtained. Preechatiwong and Schultz (1996) studied the conductivity of PEO-salt systems, the effect of mixed salts and mixed molecular weight. They found that mixed salt and mixed anion can increase the ionic conductivity of these SPEs systems. Up to date, many types of salts have been used in polymer complex, as shown in Table 2.2

Considerable efforts have been devoted to the development of solid polymer electrolytes with high ionic conductivity and dimensional stability. Various efforts have been made to design new polymeric matrices by synthetic processes or modifying existing polyether-salt complexes, and improve ionic conductivity. There are two means to increase the ionic conductivity of the dry SPE: (I) suppression of crystallization of polymer chains to improve polymer chain mobility; (II) increase in the carrier concentration (Ruiz *et al.*, 2000; Chen *et al.*, 2002; Shen *et al.*, 2002, 2003). The suppression of crystallization of polymer chains to improve polymer chain mobility can be realized by (i) cross-linking; (ii) co-polymerization; (iii) comb formation (side chains and dendritic polymers); (iv) polymer alloy (including IPN: Inter Penetrating Network), and (v) inorganic filler blend (Shen *et al.*, 2002,2003). In this research, the method of nanocomposite preparation will be used because of its

low cost and convenient preparation. One promising way to synthesize polymer nanocomposites is by intercalating polymers in layered inorganic host.

2.3 Polymer–clay nanocomposites for solid-state Electrochemical Devices

Various methods have been applied to reduce the crystallinity of PEO based electrolytes while maintaining their high flexibility and mechanical stability, which extends over a wide temperature range. One of the most successful approaches relies on the preparation of polymer electrolyte nanocomposite (Chen *et al.*, 2002). Clay mineral is an inorganic filler with intercalation property.

Table 2.2 Lists of salts used in polymer complex systems.

Host Polymer	Salt	Conductivity about 10^{-5} (S/cm)at T (°C)	Ref.
PEO	NaI	70	(Wright, 1975)
	NaSCN	70	
	KSCN	90	
	NH ₄ SCN	90	
PEO	LiSCN	70	(Armand, 1987)
	KSCN	60	
	CsSCN	50	
PEO	MgCl ₂	80	(Yangetal, 1986)
Crosslinked PEO	LiClO ₄	30	(Watanabe <i>et al.</i> , 1986)
PEO/PPO	Cu(AA) ₂	10^{-7} at room temperature	(Tandel, 1994)

Intercalating polymer in layered clay host can produce polymer electrolyte nanocomposite, with huge interfacial area. The higher interfacial area not only reduces the crystallinity of PEO chains resulting in higher ionic conductivity, but also sustains the mechanical property of this semi-crystalline PEO based electrolyte.

The commonly used layered silicates for the preparation of polymer-clay nanocomposites belong to the same general family of 2:1 layered or phyllosilicates. Their crystal structure consists of layers made up of two tetrahedrally coordinated silicon atoms fused to an edge-shared octahedral sheet of either aluminum or magnesium hydroxide. The layer thickness is around 1 nm, and the lateral dimensions of these layers may vary from 30 nm to several microns or larger, depending on the particular layered silicate. Stacking of the layers leads to a regular van der Waals gap between the layers called the *interlayer* or *gallery*. Isomorphic substitution within the layers (for example, Al^{3+} replaced by Mg^{2+} or Fe^{2+} , or Mg^{2+} replaced by Li^{1+}) generates negative charges that are counterbalanced by alkali and alkaline earth cations situated inside the galleries. This type of layered silicate is characterized by a moderate surface charge known as the cation exchange capacity (CEC), and generally expressed as mequiv/100 gm. This charge is not locally constant, but varies from layer to layer, and must be considered as an average value over the whole crystal.

MMT, hectorite, and saponite are the most commonly used layered silicates. Layered silicates have two types of structure: tetrahedral-substituted and octahedral substituted. In the case of tetrahedrally substituted layered silicates the negative charge is located on the surface of silicate layers, and hence, the polymer matrices can react interact more readily with these than with octahedrally-substituted material.

Details regarding the structure and chemistry for these layered silicates are provided in Figure 2.6 and Table 2.3, respectively.

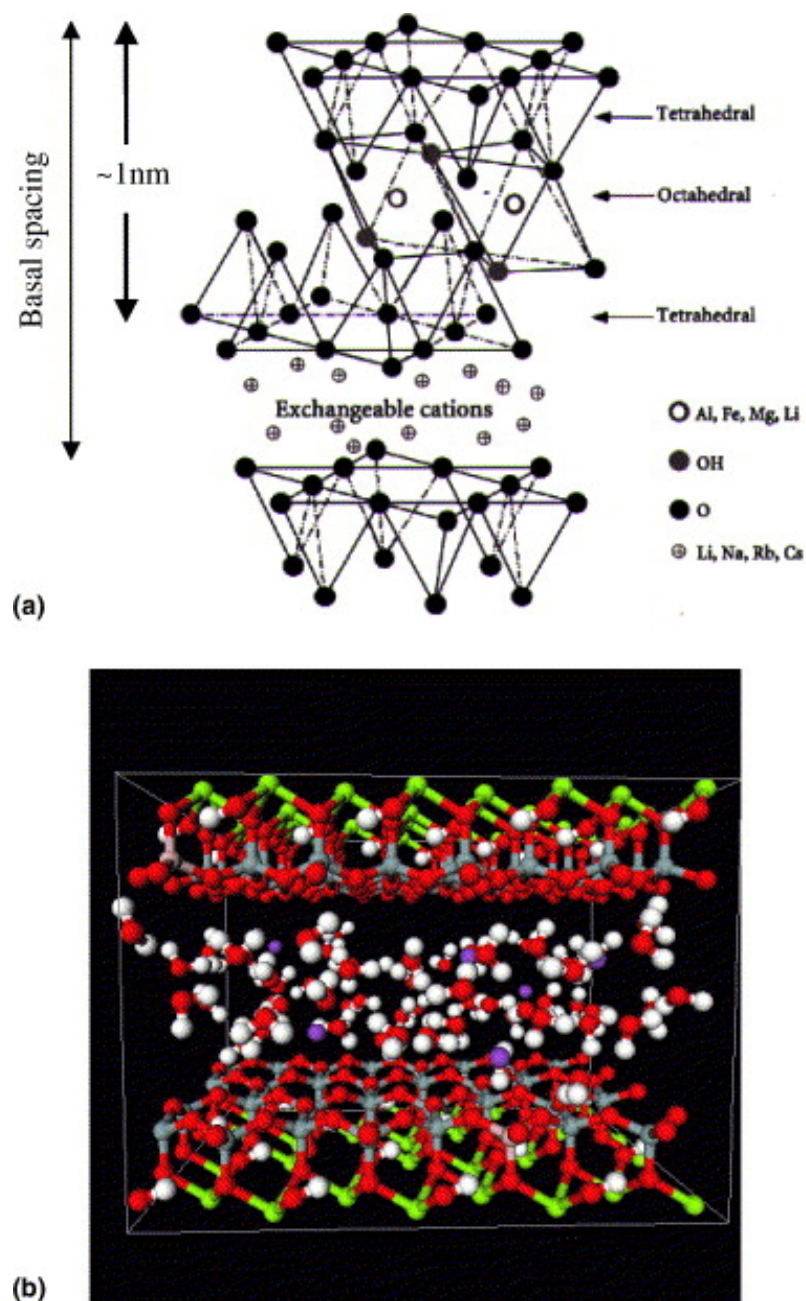


Figure 2.6 (a) Structure of 2:1 phyllosilicates. (b) 3D crystal image of MMT. (Ray, 2005)

Table 2.3 Chemical formula and characteristic parameter of commonly used 2:1 phyllosilicates

2:1 phyllosilicates	Chemical formula^a	CEC, mequiv/100 g	Particle length/nm
Montmorillonite	$M_x(Al_{4-x}Mg_x)Si_8O_{20}(OH)_4$	110	100-150
Hectorite	$M_x(Mg_{6-x}Li_x)Si_8O_{20}(OH)_4$	120	200-300
Saponite	$M_xMg_6(Si_{8-x}Al_x)Si_8O_{20}(OH)_4$	86.6	50-60

^a M = monovalent cation; x = degree of isomorphous substitution (between 0.5 and 1.3). (Ray, 2005)

The structure and properties of the resulting nanostructure can be conveniently mediated by controlling subtle guest-host interactions. Beyond the conventional phase separated polymer/silicate composites, for which the polymer and the inorganic host remain immiscible, two types of hybrids are possible (Figure 2.7) intercalated in which a single, extended polymer chain is intercalated between the host layers resulting in a well ordered multilayer with alternating polymer/inorganic layers and a repeat distance of a few nanometers, and exfoliated or delaminated, in which the silicate layer (1 nm thick) are exfoliated and dispersed in a continuous polymer matrix. (Giannelis *et al.*, 1999)

Intercalation of polymers in layered hosts, such as layered silicates, has proven to be a successful approach to synthesize polymer-clay nanocomposites. The preparative methods are divided into four main groups according to the starting materials and processing techniques:

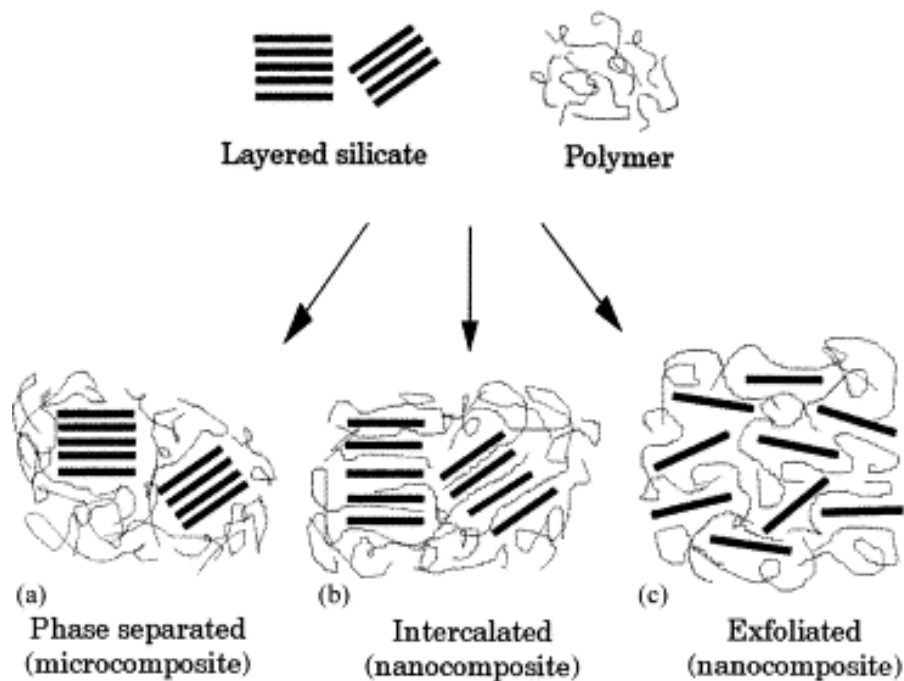


Figure 2.7 The different polymer/silicate hybrid structures. (Giannelis *et al.*, 1999)

- *Exfoliation–adsorption*: The layered silicate is exfoliated into single layers using a solvent in which the polymer (or a prepolymer in case of insoluble polymers) is soluble. Layered silicates, owing to the weak forces that stack the layers together can be easily dispersed in an adequate solvent. The polymer then adsorbs onto the delaminated sheets and when the solvent is evaporated (or the mixture precipitated), the sheets reassemble, sandwiching the polymer to form, in the best case, an ordered multilayer structure.

Intercalation of polymer or pre-polymer from solution. This is based on a solvent system in which the polymer or pre-polymer is soluble and the silicate layers are swellable. The layered silicate is first swollen in a solvent, such as water, chloroform, or toluene. When the polymer and layered silicate solutions are mixed, the polymer chains intercalate and displace the solvent within the interlayer of the

silicate. Upon solvent removal, the intercalated structure remains, resulting in PLS nanocomposite.

In situ intercalative polymerization method. In this method, the layered silicate is swollen within the liquid monomer or a monomer solution so the polymer formation can occur between the intercalated sheets. Polymerization can be initiated either by heat or radiation, by the diffusion of a suitable initiator, or by an organic initiator or catalyst fixed through cation exchange inside the interlayer before the swelling step.

Melt intercalation method. This method involves annealing, statically or under shear, a mixture of the polymer and clay above the softening point of the polymer. This method has great advantages over either *in situ* intercalative polymerization or polymer solution intercalation. First, this method is environmentally benign due to the absence of organic solvents. Second, it is compatible with current industrial process, such as extrusion and injection molding. The melt intercalation method allows the use of polymers which were previously not suitable for *in situ* polymerization or solution intercalation.

Ruiz (2000) immersed powder of self supporting film of homoionic (Li^+ , Na^+ , NH_4^+ , Ba^{2+} , etc) MMT into PEO ($M_w \sim 10^5$) solution in anhydrous acetonitrile. The intercalation is clearly detected from X-ray diffraction (XRD), the interlayer distance was determined via the d_{001} spacing. They deduced that the thickness layer of Li^+ -MMT and Na^+ -MMT are expanded from 9.5 Å to 17.5 Å. The ionic conductivity determined by a.c. impedance plot were reported ranging from 10^{-7} to 10^{-4} Scm^{-1} (400-500K) for PEO/ Na^+ MMT nanocomposite.

Additionally, They stated that the charge carriers in intercalated polymer-clay nanocomposite are limited to cations, since the counter anions are the negatively charged immobile silicated layer. In comparison to the conventional polymer complexes described earlier, both anions and cations are mobile and contribute to ionic conduction mechanism. Similar results from XRD data are obtained by Wu and Lerner. They prepared nanocomposites from Na-MMT and PEO in CH₃CN or water.

Giannelis and coworker (1999) introduced the direct polymer melt intercalation. They mixed PEO into Na⁺ or Li⁺ MMT in an agate mortar and form into pallet under applied pressure. From XRD result, after heating to 80°C, the intensity of the peaks belonging to the unintercalated silicated (d=11.4 Å) and crystalline PEO (d=4.6, 3.8 and 3.2 Å) was gradually reduced, whereas a set of new peak of PEO-intercalated silicates was observed. After six hours of heating, only the primary peak of PEO intercalated silicates at 17.7 Å was observed. This indicates the complete intercalation. XRD and FTIR data were in agreement with previously result from solution intercalation. They therefore concluded that both melt and solution intercalation yield the same intercalated phase. Comparatively, they studied the ionic conductivity, determined by a.c. impedance method, between conventional PEO/Li⁺-MMT nanocomposite. The former system exhibits the decreases of conductivity below the melting temperature. This probably due to the formation of crystallinity impeded ionic mobility. The reported ionic conductivity value was 1.6×10^{-6} S/cm at 30°C.

2.4 The Rotational Isomeric State (RIS) Theory

In addition to the experimental work mentioned above, it is commonly accepted that the knowledge about the polymer conformation should contribute to

more understanding of the ion-polymer interaction which plays an important role to ion conduction mechanism in SPEs. Theoretical studies based on statistical thermodynamics have been extensively performed for macromolecules in order to interpret and to understand their physical properties which strongly depend on the spatial arrangement of chain molecules. The Rotational Isomeric State (RIS) theory is an excellent calculation technique to predict the conformation-dependent physical properties of polymeric chains (Flory, 1965). The theory assumes that each skeletal bond has a small number of discrete rotational states and considers interactions between atoms on a chain separated by only a small number of bonds (short-range interactions). Interaction appearing upon a rotation around a single bond and two consecutive bonds is called *the first-order interaction* and *the second-order interaction*, respectively. These interactions are then parameterized and grouped into the matrix called *the statistical weight matrix*. Then the conformation-dependent physical properties can be computed from these statistical weight matrices. The most frequently calculated properties are the unperturbed mean-square end-to-end distance $\langle r^2 \rangle_0$, the mean square dipole moment $\langle \mu^2 \rangle_0$ and the mean-square radius of gyration $\langle S^2 \rangle_0$.

The first RIS model for PEO was introduced by Flory in 1965. However, various RIS models of PEO have been subsequently proposed. The statistical parameters used for polymer have been calculated with semiempirical expressions for energy. In general, the energy has been considered to consist of three parts: (i) intrinsic torsional potentials, (ii) van der Waals repulsion between nonbonded atoms and groups, and (iii) dispersion attractions between nonbonded atoms. The RIS theory

assumes that the total conformational energy for a chain molecule can be revolved into a finite number of conformational energy states which depend chiefly upon consecutive pairs of bond rotations. The energy of the minimum energy state is usually assigned a value of zero and the remaining energy states are calculated relative to this value. The statistical weight element is obtained from the well-known expression $\exp(-E/RT)$ (Darsey, 1981).

RIS review of PEO by QM method

In past several decades, the RIS method has become a popular tool to analyze the physical properties of polymers. However, it is important to obtain the statistical weight parameters in RIS theory. The conformational energies are used to determine the rotational interaction energies, by means of which statistical weight parameters can be obtained. This method of determining the statistical weight parameters requests the accuracy of conformational energies. It is popular to calculate conformational energies and geometry properties by MM method. But the MM calculations do not explicitly treat the electrons in a molecular system. Instead, the calculation is based upon the interactions among nuclei. Therefore, the MM method can not accurately describe the molecule systems where the electronic effects are predominant. Moreover, the force field achieved good results only for a limited class of molecules. No force field can be generally used for all molecular systems.

In recent years, electronic structure theory has been developed quickly. In order to better quantify the conformational energies, several groups have successfully employed *ab initio* electronic structure (quantum chemistry) calculations on the model segments of polymers. Quantum chemistry calculation bases upon the interactions among electrons rather than nuclei. So it can describe molecular systems

where the electronic effects are predominant and be applicable for all kinds of molecules.

The conformations of small ether molecules have been the subject of extensive experimental and computational studies in recent years. These molecules serve as models for larger, technologically important molecules such as polyethers and crown ethers, where an improved understanding of conformational properties would greatly facilitate development of new materials. In many of these studies, the ability of quantum chemistry calculations to yield conformational energies and populations consistent with results of diffraction, spectroscopy, and NMR vicinal coupling studies was thoroughly investigated. When an adequate level of theory is employed, excellent agreement between *ab initio* predictions and experimental results has been found. The accuracy of the *ab initio* calculations has been further validated by the ability of quantum chemistry based rotational isomeric state (RIS) models and molecular mechanics models to reproduce the conformational properties of polyethers.

This research has been encouraged to recalculate the energies of PEO in various conformations in this manner (Darsey, 1981). These energies and RIS theory will be employed to calculate various statistical parameters, the characteristic ratio, and temperature coefficient of an infinitely long PEO chain. The calculated results will also be compared with experimental values and also with numbers of available calculations performed with energies obtained with the more traditional semi-empirical methods already described. (Abe *et al.*, 1998)

Poly(N-vinyl-2-pyrrolidone)(PVP) is a non-ionic water-soluble polymer having a hydrocarbon chain with strong polar side groups. This polymer has been the subject of numerous reviews and general surveys. This water-soluble polymer shows

a number of interesting properties such as a high capability to interact with different kinds of molecules like iodine, detergents, drugs, dyes, aromatic compounds, carboxylic acids and many other compounds. Moreover, the biological behavior of PVP, or more specifically its physiological and pharmaceutical performance, is responsible of a variety of applications including its use as blood-plasma substitute or in hair sprays and other aerosol products.

For PVP chain as reported by Tonelli (1982) and Saiz (1993), dimensions and dipole moments were calculated using the RIS model developed from the conventional semi-empirical force field. The effects of stereosequence, temperature and varying dielectric constant for charge interaction were also considered in those works. It is expected that previous RIS models for PVP using semi-empirical force fields may not be so accurate for detailed calculation.

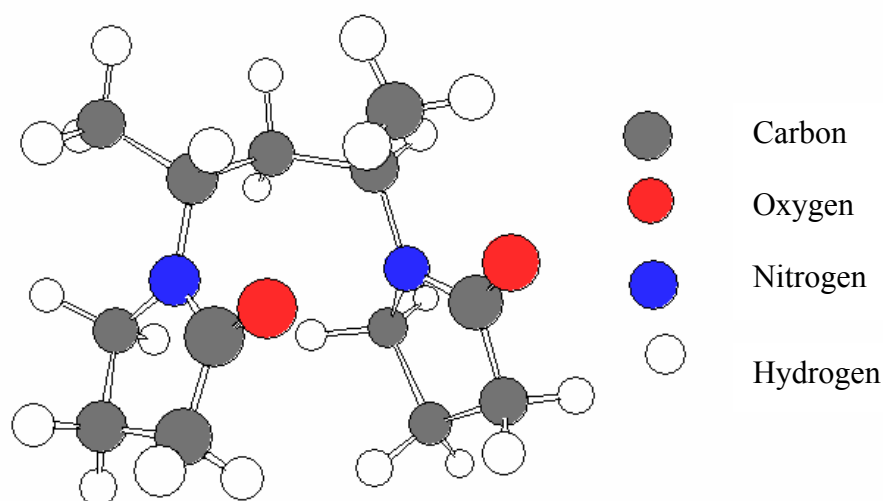


Figure 2.8 A meso dyad in the tt conformation along PVP chain

In Tonelli's model (1982), the side groups of PVP were assumed to be rigid so that the final structure may not be fully optimized. Saiz *et al.*, also performed similar calculation as Tonelli except that all side groups were allowed to be relaxed. The solvent effect was included by vary the dielectric constant. However, statistical weight matrices of PVP were not reported in that paper and further application of this RIS model was therefore limited. The conformation energy map of PVP will be recalculated in this work by Molecular Mechanic (MM) using the more up-to-state force field (e.g. MM⁺ and Amber). In addition, the effect of solvent on PVP conformation will also be investigated to gain more understanding and to clarify the unusual findings from the viscosity experiment of PVP solution.

CHAPTER III

RESEARCH METHODOLOGY

3.1 Apparatus and Materials

- Magnetic stirrers and magnetic bars
- Microwave Oven (Daewoo)
- Hot air oven
- Cannon-Ubbelohde Viscometer No. 150.
- Digital temperature controller, capable of maintaining $10-100^{\circ}\text{C} \pm 0.1^{\circ}\text{C}$
- Water bath shaker
- Na-Montmorillonite (Na-MMT), SWy-1, Source Clay Minerals (USA)
- Poly(ethylene oxide) (PEO MW 600, 20 000, 200 000 g/mol), Aldrich.
- Poly(vinyl pyrrolidone) (PVP MW 55 000, 1 300 000 g/mol), Aldrich.
- Sodium Thiocyanate (NaSCN), APS Finechem.
- Methanol (CH_3OH), Analytical Reagent, Merck
- Benzene (C_6H_6), Analytical Reagent, Merck.
- Acetonitrile (CH_3CN), Analytical Reagent, Merck.
- Tetrahydrofuran (THF), Analytical Reagent, Merck.
- Acetone (CH_3COH), Analytical Reagent, Merck.

3.2 Computational Part

3.2.1 Statistical Weight Matrices of PEO and PVP

Statistical weight matrices were estimated from the conformational energy map of representative small segments of the polymer chain by Quantum Mechanics (QM) and Molecular Mechanics (MM) techniques. In this proposal, the statistical weight matrices for PVP were estimated by MM method (rather than QM) due to the limit of computational resource. QM and MM will be carried out using HyperChem Release7 which was installed on a PC computer. The descriptive procedures of this calculation are as following

- The portions of PEO and PVP chain of which conformations depend on one or both of two neighboring backbone bond rotation angles was selected. For an energy and geometry optimization, QM technique were employed for PEO chain whereas MM was selected for PVP chain.
- Before performing the calculation, the atom coordinates were adjusted to minimize the energy while torsional angles were kept constant.
- The conformational energies for each of these fragments was calculated as a function of the rotation angles $E(\phi_1, \phi_2)$, ϕ_1 and ϕ_2 torsion were rotated from 0° to 360° (10° for each step of torsional rotation).
- The conformational energy maps were constructed with respect to ϕ_1 and ϕ_2 torsions for each segment.
- For PVP chain, the statistical weight $SW_{\alpha\beta}$ was evaluated for each of the nine pair-wise dependent rotational states ($\alpha\beta = tt, tg^\pm, g^\pm t, g^\pm g^\pm, g^\pm g^\mp$).

As an example, $SW_{g^+g^+}$ was obtained by

$$SW_{g^+g^+} = \frac{\sum_{\phi_1=10^\circ}^{120^\circ} \sum_{\phi_2=10^\circ}^{120^\circ} \exp[-E(\phi_1, \phi_2)/RT]}{\sum_{\phi_1=0^\circ}^{360^\circ} \sum_{\phi_2=0^\circ}^{360^\circ} \exp[-E(\phi_1, \phi_2)/RT]} \quad (3.1)$$

where $E(\phi_1, \phi_2)$ is the conformational energy (kcal/mole) at torsional angles ϕ_1 and ϕ_2 , R is the gas constant, and T is the absolute temperature. The RIS approximation for chain molecules are usually based on the first- and second-order interactions for three rotational isomeric states i.e. *trans* (*t*), *gauche*⁺ (*g*⁺), and *gauche*⁻ (*g*⁻). Then, all the statistical weight matrices assigned to the skeletal bonds are 3 x 3 dimension [20].

$$U_{C-C} = \begin{bmatrix} SW_{tt} & SW_{tg^+} & SW_{tg^-} \\ SW_{g^+t} & SW_{g^+g^+} & SW_{g^+g^-} \\ SW_{g^-t} & SW_{g^-g^+} & SW_{g^-g^-} \end{bmatrix} \quad (3.2)$$

For PEO chain, two different QM methods were employed i.e. Semi-empirical (PM3) and *ab initio* QM calculation. The statistical weight matrices of PEO using Eqs. (3.1) and (3.2) for the case Semi-empirical method.

On the other hand, *ab initio* QM (HF-SCF, DFT) method was employed to calculate different conformer of representative molecule of PEO i.e. DME (Dimethoxyethane). These energetic parameters (E_ρ , E_σ and E_ω) were obtain from different level of calculation and basis sets.

The statistical weight matrices of PEO can be evaluated as follow:

$$U_{C-C} = \begin{bmatrix} 1 & \sigma & \sigma \\ 1 & \sigma & \sigma\omega \\ 1 & \sigma\omega & \sigma \end{bmatrix}$$

$$U_{C-O} = \begin{bmatrix} 1 & \sigma & \sigma \\ 1 & \sigma & 0 \\ 1 & 0 & \sigma \end{bmatrix} \quad (3.3)$$

$$U_{o-c} = \begin{bmatrix} 1 & \rho & \rho \\ 1 & \rho & \rho\omega \\ 1 & \rho\omega & \rho \end{bmatrix}$$

where,

$$\begin{aligned} \sigma &= \sigma_o \exp(-E_\sigma/RT) \\ \rho &= \rho_o \exp(-E_\rho/RT) \\ \omega &= \omega_o \exp(-E_\omega/RT) \end{aligned} \quad (3.4)$$

3.2.2 Rotational Isomeric State (RIS) Model

RIS analysis is useful in gaining greater insight into conformational-dependent interaction of polymer molecules. The conformational properties, \mathbf{A} , are assumed to be a function only of dihedral angles in the chain backbone. According to statistical mechanics, the average value, $\langle A \rangle$, is approximated as a sum over the discrete rotational states by

$$\langle A \rangle = Z^{-1} \int \dots \int \exp[-E(\phi_1 \dots \phi_n)/RT] A(\phi_1 \dots \phi_n) d\phi_1 \dots d\phi_n \quad (3.5)$$

The statistical weights can then be used to calculate conformational properties in the matrix multiplication form as:

$$\langle A_0 \rangle = Z^{-1} \prod_i \mathbf{G}_i \quad (3.6)$$

where \mathbf{G}_i are “super” generator matrices defined by

$$\mathbf{G}_i = (\mathbf{U}_i \otimes \mathbf{E}_s) \|\mathbf{F}_i\| \quad (3.7)$$

Here \otimes indicates a direct matrix product, $\|\mathbf{F}_i\|$ is the diagonal array of generator matrices \mathbf{F}_i , and \mathbf{E}_s is the identity matrix of the same order as \mathbf{F}_i . The other conformational dependent properties such as $(\langle S^2 \rangle_0, \langle \mu^2 \rangle_0)$ can be calculated in the

same manner by changing only the super generator matrix for each of these properties. As an illustration, the calculation of the means-square end-to-end as presented.

Let each bond be characterized by a vector \mathbf{b}_i (Figure 3.1). By convention, bond i connects backbone atoms $i-1$ and i . For a specific conformation, the squared end-to-end distance of the chain is

$$\begin{aligned} r^2 &= (\mathbf{b}_1 + \mathbf{b}_2 + \dots + \mathbf{b}_n)^2 \\ &= \sum_{i,j=1}^n \mathbf{b}_i \cdot \mathbf{b}_j = \sum_{i=1}^n \mathbf{b}_i^2 + 2 \sum_{i < j} \mathbf{b}_i \cdot \mathbf{b}_j \end{aligned} \quad (3.8)$$

Next, let a coordinate system be associated with each backbone bond (excluding the first) as illustrated in Figure 3.1. For bond i , the x_i axis is collinear with the bond, with the origin at backbone atom $i-1$. The y_i axis is in the plane defined by bond i and $i+1$ with its positive direction chosen such that its projection on the x_{i-1} axis is positive. The direction of the z_i axis is chosen so that it completes a right-handed coordinate system. A bond vector \mathbf{b}_i is expressed in its own coordinate frame as the column vector

$$\mathbf{b}_i = \begin{bmatrix} \mathbf{b} \\ 0 \\ 0 \end{bmatrix} \quad (3.9)$$

A vector in the coordinate frame of bond $i+1$ can be expressed in the coordinate frame of bond i by making use of the transformation matrix \mathbf{T}_i .

$$\mathbf{v}^{(i)} = \mathbf{T}_i \mathbf{v}^{(i+1)} \quad (3.10)$$

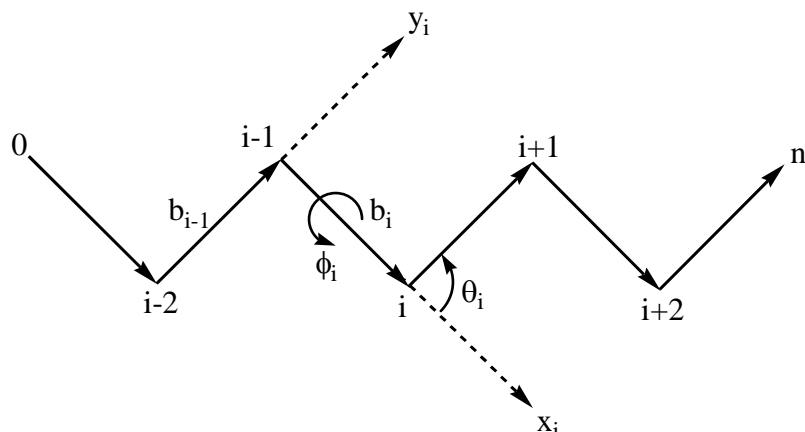


Figure 3.1 Chain representation and coordinates used in the RIS calculation

where, using the dihedral (ϕ) and valence angles (θ) as defined in Figure 3.1, the transformation matrix is given by

$$T_i = \begin{bmatrix} \cos \theta & \sin \theta & 0 \\ \sin \theta \cos \phi & -\cos \theta \cos \phi & \sin \phi \\ \sin \theta \sin \phi & -\cos \theta \sin \phi & -\cos \phi \end{bmatrix} \quad (3.11)$$

By convention, ϕ_i is 180° when the bond is in the planar *trans* conformation, and deviations from 180° are measured in right-handed sense. RIS theory normally assumes that the value of θ_i is conformation independent. A bond vector \mathbf{b}_j , as expressed in its own coordinate frame, can be transformed into coordinate frame i as follows (for $j > i$):

$$T_i T_{i+1} \dots T_{j-1} \mathbf{b}_j \quad (3.12)$$

Using Eqs. (3.9) and (3.12), the expression for \mathbf{r}^2 becomes

$$\mathbf{r}^2 = \sum_{i=1}^n \mathbf{b}_i^2 + 2 \sum_{i < j} \mathbf{b}_i^T T_i T_{i+1} \dots T_{j-1} \mathbf{b}_j \quad (3.13)$$

This can be expressed in the matrix form as

$$\mathbf{r}^2 = \mathbf{F}_1 \mathbf{F}_2 \dots \mathbf{F}_n \quad (3.14)$$

where the *generator matrix* F for a given bond is

$$F_i \equiv \begin{bmatrix} 1 & 2\mathbf{b}^T \mathbf{T} & \mathbf{b}^2 \\ 0 & \mathbf{T} & \mathbf{b} \\ 0 & 0 & 1 \end{bmatrix}_i \quad (3.15)$$

except for the first and last bonds of the chain. For terminal bonds, the F matrices take on a special form. Form the first bond, the matrix is

$$F_1 \equiv \begin{bmatrix} 1 & 2\mathbf{b}^T \mathbf{T} & \mathbf{b}^2 \end{bmatrix}_1 \quad (3.16)$$

and for the last bond,

$$F_n \equiv \begin{bmatrix} \mathbf{b}^2 \\ \mathbf{b} \\ 1 \end{bmatrix}_n \quad (3.17)$$

Equation (3.14) gives the squared end-to-end distance for a specific conformation, but many different conformations are possible. We require a suitably weighted average of this quantity over all conformations. It is at this point that the statistical weights are introduced.

Let the statistical weight matrix for an interior bond of the chain be written as

$$U_i = \begin{bmatrix} \mathbf{u}_{\alpha'\alpha} & \mathbf{u}_{\alpha'\beta} & \cdots \\ \mathbf{u}_{\beta'\alpha} & \mathbf{u}_{\beta'\beta} & \cdots \\ \vdots & \vdots & \ddots \end{bmatrix}_i \quad (3.18)$$

where α', β', \dots represent states of bond $i-1$, and α, β, \dots represent states of bond i .

Then let a new generator matrix G_i be defined as

$$G_i \equiv \begin{bmatrix} \mathbf{u}_{\alpha'\alpha} F(\alpha) & \mathbf{u}_{\alpha'\beta} F(\beta) & \cdots \\ \mathbf{u}_{\beta'\alpha} F(\alpha) & \mathbf{u}_{\beta'\beta} F(\beta) & \cdots \\ \vdots & \vdots & \ddots \end{bmatrix}_i \quad (3.19)$$

As was the case for the F matrices, the G matrices at the chain ends take on special forms:

$$\mathbf{G}_1 \equiv [\mathbf{F}_1 \ 0 \ 0 \ \dots \ 0] \quad (3.20)$$

and

$$\mathbf{G}_n \equiv \begin{bmatrix} \mathbf{F}_n \\ \mathbf{F}_n \\ \vdots \\ \mathbf{F}_n \end{bmatrix} \quad (3.21)$$

With the above definitions, the matrix product

$$\mathbf{G}_1 \mathbf{G}_2 \dots \mathbf{G}_n \quad (3.22)$$

generates all possible serial products, $\mathbf{F}_1 \mathbf{F}_2 \dots \mathbf{F}_n$, corresponding to all possible chain conformations. Each of these products is multiplied by its overall statistical weight. It only remains to normalize Eq. (3.23) in order to obtain the mean-squared end-to-end distance.

The normalization factor is simply the serial product of the statistical weight matrices, otherwise known as the configurational partition function:

$$\mathbf{Z} = \mathbf{U}_1 \mathbf{U}_2 \dots \mathbf{U}_n \quad (3.23)$$

where, as usual, terminal matrices have a special form:

$$\mathbf{U}_1 \equiv [1 \ 0 \ \dots \ 0] \quad (3.24)$$

and

$$\mathbf{U}_n \equiv \begin{bmatrix} 1 \\ 1 \\ \vdots \\ 1 \end{bmatrix} \quad (3.25)$$

Thus, the final expression for the mean-squared end-to-end distance of the chain is

$$\langle \mathbf{r}^2 \rangle_0 = \mathbf{Z}^{-1} \mathbf{G}_1 \mathbf{G}_2 \dots \mathbf{G}_n \quad (3.26)$$

This is quite a remarkable result. In this expression, an average over an enormously large number of conformations has been reduced to a simple serial product of matrices, while still accounting for the specific geometry and chemical makeup of the chain.

3.2.2.1 RIS Parameters from Molecular Mechanics (MM) Technique

There are various methods on obtaining the RIS parameters. The classical techniques are usually based on an assumption of unknown variables denoted as statistical weights for each conformation. These parameters are then parameterized with some selected conformational dependent properties deriving from experiments. This classical method has been done in the past and works reasonably well. Unfortunately, there are some limitations on employing this technique due mainly to a difficulty on assigning the conformational states as well as lack of experimental data to verify the model.

On the other hand the RIS model derived from the computational method provides an alternative and a convenient way to solve a forementioned problems. Molecular Mechanics is the calculation technique based on the approximated potential model, which can be summarized as:

$$\mathbf{V}(\mathbf{r}) = V_{bond} + V_{non-bond} \quad (3.27)$$

$$\textit{where} \quad V_{bond} = V(\mathbf{r})_{stretch} + V(\theta)_{bend} + V(\chi)_{torsion} \quad (3.28)$$

$$V_{non-bond} = V(\mathbf{r})_{van-der-Waals} + V(\mathbf{r})_{electrostatic} \quad (3.29)$$

The collective set of the parameters called “force field” can be obtained basically by spectroscopies such as IR, Raman, NMR, and X-ray and by higher level *ab initio* quantum simulations. Molecular optimization is then performed to find the

minimum energy state of a molecule for each conformer. The structure obtained by the energy minimization exists at the deep well of the potential function satisfying following conditions.

$$\frac{\partial V(\mathbf{r})}{\partial \mathbf{r}} = 0 \quad \text{and} \quad \frac{\partial^2 V(\mathbf{r})}{\partial \mathbf{r}^2} > 0 \quad (3.30)$$

To find the minimized structure, many efficient search algorithms have been developed, such as Newton-Raphson and Conjugate Gradient method. The conformational energies are obtained by rotating the dihedral angles and should correspond to the minimized structure at each pair of dihedral angle (ϕ_i, ϕ_j) . The increment in dihedral angle for ϕ_i and ϕ_j (at **C-C**, **C-O** or **O-C** bond) is set to 10° (rotation from 0° to 360°). Three short segments of PEO chain used in the computation are presented in Figure 3.2.

The model assumes three states (trans, gauche⁺ and gauche⁻, abbreviated as *t*, *g*⁺ and *g*⁻, for each rotatable bond). The statistical weight (U_{ϕ_i, ϕ_j}) can be defined as:

$$U_{\phi_i, \phi_j} = \frac{\sum_{\phi_i} \sum_{\phi_j} \exp[-V(\phi_i, \phi_j)/RT]}{\sum_{10^\circ}^{360^\circ} \sum_{10^\circ}^{360^\circ} \exp[-V(\phi_i, \phi_j)/RT]} \quad (3.31)$$

Where $V(\phi_i, \phi_j)$ is a conformational energy (kcal mol⁻¹) at ϕ_i and ϕ_j , **R** is the gas constant and **T** is the absolute temperature (K). Then, the statistical weight matrix for each bond pair is of the form:

$$\begin{bmatrix} U_{tt} & U_{tg^+} & U_{tg^-} \\ U_{g^+t} & U_{g^+g^+} & U_{g^+g^-} \\ U_{g^-t} & U_{g^-g^+} & U_{g^-g^-} \end{bmatrix} \quad (3.32)$$

To test the quality of parameters obtained from MM method, some conformational dependent properties and fraction of bond conformation can be calculated using the RIS scheme and then compared with results obtained from experiments.

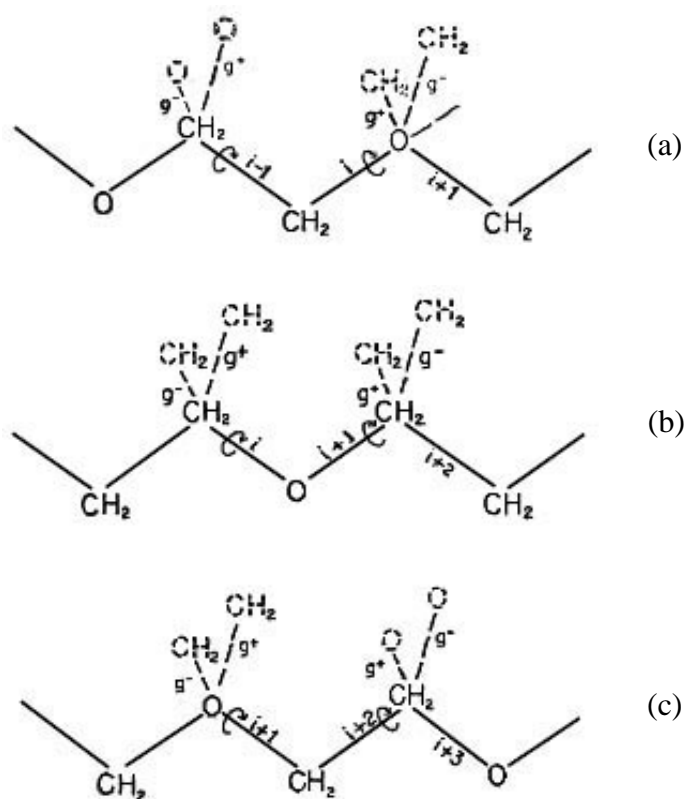


Figure 3.2 Schematic representation of three short segments of PEO chain (a) C-C, C-O bond pair (b) C-O, O-C bond pair (c) O-C, C-C bond pair.

3.2.2.2 RIS parameter from Quantum Mechanics (QM) Technique

For a molecule in any particular conformation one writes down the electronic Hamiltonian after the Born-Oppenheimer approximation as

$$H = \frac{-\hbar^2}{8\pi^2 m} \sum_p \nabla_p^2 - \sum_A \sum_p e^2 Z_A r_{Ap}^{-1} + \sum_{p < q} \sum e^2 r_{pq}^{-1} \quad (3.33)$$

The total energy of the system is obtained as a sum of electronic energy and the nuclear repulsion energy. The electronic energy is the expectation value $\langle \psi | H | \psi \rangle$

where ψ is the wave function for the system obtained from the solution of the time-independent Schrodinger equation. For a closed shell system with $2n$ electrons, one can write ψ in the form

$$\psi = N \sum_p (-1)^p P \{ \psi_1(1) \alpha(1) \psi_1(2) \dots \psi_n(2n) \beta(2n) \} \quad (3.34)$$

where ψ_i are molecular orbitals and P is a permutation of the electron numbers. α and β represent the spin of the electron involved.

Now the Hamiltonian can be separated into one- and two-electron parts. In terms of atomic units we have

$$H = H_1 + H_2 \quad (3.35)$$

where $H_1 = \sum_p H^{core}(p)$ with $H^{core}(p) = -\frac{1}{2} \nabla_p^2 - \sum_A Z_A r_{pA}^{-1}$ is the one-electron

Hamiltonian corresponding to the motion of an electron in the field of the bare nuclei and $H_2 = \sum_{p < q} \sum r_{pq}^{-1}$. Then we get the total electronic energy as

$$E = 2 \sum_i^n H_{ii} + \sum_i^n \sum_j^n (2J_{ij} - K_{ij}) \quad (3.36)$$

where

$$H_{ii} = \int \psi_i^*(1) H^{core} \psi_i(1) d\tau_1$$

$$J_{ij} = \iint \psi_i^*(1) \psi_j^*(2) \frac{1}{r_{12}} \psi_i(1) \psi_j(2) d\tau_1 d\tau_2 \quad \text{(Coulomb integral)}$$

$$K_{ij} = \iint \psi_i^*(1) \psi_j^*(2) \frac{1}{r_{12}} \psi_j(1) \psi_i(2) d\tau_1 d\tau_2 \quad \text{(Exchange integral)}$$

The best value of ψ is the one that gives the lowest energy for that particular configuration of the molecule. Therefore, one can use the variational principle and can adjust the molecular orbital till the energy is minimized. In actual practice, one represents a molecular orbital as a linear combination of atomic orbitals (LCAO) as

$$\psi_i = \sum_{\mu} C_{\mu i} \phi_{\mu}$$

Furthermore, the properties of orthonormality imply that

$$\sum_{\mu\nu} C_{\mu i}^* C_{\nu j} S_{\mu\nu} = \delta_{ij}$$

and the density matrix is defined as

$$P_{\mu\nu} = 2 \sum_i^{occ} C_{\mu i}^* C_{\nu i}$$

Finally, the total energy of the molecule can be represented as

$$E = \sum_{\mu\nu} P_{\mu\nu} H_{\mu\nu} + \frac{1}{2} \sum_{\mu\nu\lambda\sigma} P_{\mu\nu} P_{\lambda\sigma} [(\mu\nu | \lambda\sigma) - \frac{1}{2}(\mu\lambda | \nu\sigma)] \quad (3.37)$$

where

$$H_{\mu\nu} = \int \phi_{\mu}^*(1) H^{core} \phi_{\nu}(1) d\tau_1$$

$$(\mu\nu | \lambda\sigma) = \iint \phi_{\mu}^*(1) \phi_{\nu}^*(1) \frac{1}{r_{12}} \phi_{\lambda}(1) \phi_{\sigma}(2) d\tau_1 d\tau_2$$

Now the variational principle can be used to minimize the energy; than one ends up with the equations

$$\sum_{\nu} (F_{\mu\nu} - \varepsilon_i S_{\mu\nu}) C_{\nu i} = 0 \quad (3.38)$$

where

$$F_{\mu\nu} = H_{\mu\nu} + \sum_{\lambda\sigma} P_{\lambda\sigma} [(\mu\nu | \lambda\sigma) - \frac{1}{2}(\mu\lambda | \nu\sigma)]$$

where

$$F_{\mu\nu} = H_{\mu\nu} + \sum_{\lambda\sigma} P_{\lambda\sigma} [(\mu\nu | \lambda\sigma) - \frac{1}{2}(\mu\lambda | \nu\sigma)]$$

This equation was first set forth by Roothaan and is known as Roothaan equation. The set of coefficients are to be solved consistently to get the final eigenfunctions and the energy. The SCF procedure involves a choice of atomic orbitals from which the density matrices are calculated by using some arbitrary value of $C_{\nu i}$. Then one solve

the above equation to get new values of C_{vi} which in turn are used in the above equation again. This is repeated until the value of C_{vi} is self-consistent. This is known as Roothaan-Hartree-Fock procedure.

Because the *ab initio* method has some drawbacks in term of its computational cost, other modified versions of these methods, which are called semi-empirical quantum methods, have been devised. Even though there are many versions of the modification from *ab initio* method, basically they are simplified models that reduce the integral evaluation and use some empirical information, which makes the dimension of the corresponding matrix smaller. By neglecting the integral evaluation and using empirical data, semiempirical quantum methods can gain computational speed. Furthermore, in some molecular systems, the semiempirical method can give a better agreement with experiment compared to the *ab initio* method.

In this work, HyperChem7 and Gaussian98w software, which go through the above mentioned procedure self-consistently, were employed for semi-empirical and *ab initio* calculation, respectively. Both use a combination of Gaussian functions as the input atomic functions. The only other input is the geometry of the molecule in particular configuration. The program can then finds the best energy for that situation. Semiempirical quantum methods was used to calculate the conformational energies as a function of dihedral angles. These energies were subsequently employed to generate the conformational energy map and the statistical weights of PEO conformers in a similar manner of the Molecular Mechanics method. For *ab initio* calculation, some conformers of the representative molecule of PEO i.e. DME (dimethoxyethane) was selected to determine the interacting energies and the RIS parameters of PEO i.e. σ , ρ and ω .

3.3 Experimental Part

3.3.1 Sample preparation

3.3.1.1 PEO/MMT nanocomposites via solution intercalation.

PEO (MW $4 \times 10^6 \text{ g mol}^{-1}$) was used as received. The salts were dried in the vacuum oven at $\sim 100\text{-}140^\circ\text{C}$ for 48 hours and then stored a dessicator. Stoichiometric amount of PEO and MMT (different percent MMT) were dissolved in methanol and stirred continuously for 24 hours at room temperature. A set up of tools was shown in Figure 3.3. After continuous stirring, the solution was allowed to stand at room temperature for 24 hs to facilitate degassing. To obtain thin film of the sample, the gelatinous polymer solution was cast on the glass plate. The films were dried in vacuum oven at 50°C for 24 hours to remove solvent. The amount of MMT was expressed as a weight percent (% wt) of the PEO present, followed by

$$y\% = [Wt(MMT)/Wt(PEO)] \times 100 \quad (3.39)$$



Figure 3.3 Preparation of SPEs films with sets up of tool for mix sample

3.3.1.2 PEO/NaSCN/MMT nanocomposites via solution intercalation.

The concentration of salt in polymer-salt complexes was expressed in terms of molar ratios of the ether oxygen in the polymer to metal cation of salt (O:M). The O:M ratios could be converted to molal concentrations (moles of salt per kg of polymer) or to weight ratios (w) of salt to polymer using Eqs. (3.40) and (3.41) respectively. The mixture was prepared in a similar method for polymer/MMT system as described in 3.3.1.1

$$Molal = (M : O) \times (1000 / MW_{per\ oxygen}) \quad (3.40)$$

$$w = W_{salt} / W_{polymer} = (M : O) \times (MW_{salt} / MW_{per\ oxygen}) \quad (3.41)$$

where

$$MW_{per\ oxygen} = MW_{polymer} / (n + 1).$$

3.3.1.3 Polymer/MMT nanocomposites via melt intercalation/exfoliation

The powder of PEO and MMT with designated weight ratio of polymer-to-silicate as express in Eq. (3.39) was mechanically mixed using mortar and pestle and formed into pellets using a hydraulic press at a pressure of 10 tons. Polymer melt intercalation was accomplished by annealing the pressed pellets in an hot air oven at a temperature higher than the melting point (T_m) of PEO. In addition, an attempt will be made using microwave oven as a heat supplier for polymer nanocomposite preparation.

3.3.1.4 PEO/NaSCN/PVP complexes

A mixture of PVP, PEO and salt were prepared in a similar method for polymer/MMT system as described in 3.3.1.1. The calculation is the ratio of PVP repeat units to PEO repeat unit as follow:

Polymer1: Polymer2 = X:Y or Z (per repeat unit)

$$\frac{\frac{X}{MW_1} x U_1 x N_A}{\frac{Y}{MW_2} x U_2 x N_A} \quad (3.42)$$

Where; X = The amount of polymer number 1 (g)

Y = The amount of polymer number 2 (g)

U_1 = The amount of repeat unit of polymer chain number1 (PEO)

U_2 = The amount of repeat unit of polymer chain number 2 (PVP)

N_a = Avogadro Number

3.3.2 Characterization

3.3.2.1 Nuclear Magnetic Resonance (NMR) Spectroscopy

The ^1H and ^{13}C -NMR experiments were performed on a Varian Unity INOVA NMR spectrometer operating at 300 MHz. The spectra were collected on 5% wt of PVP in D_2O solution. The spectra were collected on 5% wt of PVP in D_2O solution. 1D-NMR experiments including DEPT-45 were performed to distinguish carbon signals such as methine (-CH-), methylene (-CH₂-) and methyl (-CH₃-) in the polymer structure. 2D-NMR techniques [Heteronuclear Chemical Shift Correlation (HETCOR) and Correlated spectroscopy (COSY)] were used. HETCOR experiment provides a relationship between ^1H -NMR and ^{13}C -NMR spectra. The correlating of ^1H - ^1H connectivity can be monitored by a COSY experiment.

3.3.2.2 Viscometry

The intrinsic viscosities, $[\eta]$, of PVP was measured using a Cannon-Ubbelohde capillary viscometer No 100. Polymer solution was prepared directly by dissolving a known weight of PVP in water/acetone. Viscosities of

water/acetone and PVP solution were measured at 30, 40, 50, 60 and 70°C. Concentrations were expressed in g dl⁻¹ of solution. A constant temperature bath was used to maintain the temperature of the solutions. The bath was thermostatted to $\pm 0.1^\circ\text{C}$ in order to measure the intrinsic viscosity. The capillary viscometers used for dilute solution measurements are made of glass. They were operated by filling with a suitable volume of liquid, drawing the liquid level to a point above the upper mark on the bulb, and measuring the time required for the liquid meniscus to fall from the upper mark to the lower mark. The flow time is related to the viscosity of the liquid.

If the viscometer has an outflow time greater than 100 sec for the pure solvent, the kinetic energy correction B/At^2 are negligible compared to unity, then the relative viscosity can be calculated according to:

$$\eta_{rel} = \frac{t}{t_0} \quad (3.43)$$

The relative viscosity is used to calculate the reduced viscosity, (η_{red}), and the inherent viscosity, (η_{inh}). For given polymer solution, the reduced viscosity and inherent viscosity calculated according to the following equations.

$$\eta \equiv \frac{\eta_{sp}}{c} = \frac{\eta_{rel} - 1}{c} \quad (3.44)$$

$$\eta \equiv \frac{\ln \eta_{rel}}{c} \quad (3.45)$$

where η_{sp} is $\eta_{rel} - 1$ and c is the polymer concentration (g/dl).

After that, $[\eta]$ can be determined by using the Huggins and Kraemer Equation, which is the viscosity number (the reduced viscosity) or the logarithmic viscosity number (the inherent viscosity), extrapolated to $c = 0$. It is shown as follows:

The Huggins Equation is

$$\frac{\eta_{sp}}{c} = [\eta] + k'[\eta]^2 c \quad (3.46)$$

and the Kraemer Equation is

$$\frac{\ln \eta_{rel}}{c} = [\eta] + k''[\eta]^2 c \quad (3.47)$$

where both k' and k'' are constants.

Where

$$[\eta] \equiv \lim_{c \rightarrow 0} \left(\frac{\eta_{sp}}{c} \right) = \lim_{c \rightarrow 0} \left(\frac{\ln \eta_{rel}}{c} \right)$$

Furthermore, the intrinsic viscosity is related to $\langle r^2 \rangle_0$, which can be predicted by RIS theory. The relation is equated as follows:

$$[\eta] = \Phi \left[\frac{\langle r^2 \rangle_0}{M} \right]^{3/2} \quad (3.48)$$

where Φ is the hydrodynamic factor (2.6×10^{21}) and M is the average molecule weight.

3.3.2.3 X-ray Power Diffraction (XRD)

In this thesis, XRD technique was employed to study the effect of adding MMT into PEO with a focus on two aspects i.e. the reduction of crystalline portion in PEO and the formation of intercalated PEO/MMT nanocomposites. A Bruker D5005 X-ray generator was used to give Cu K_α radiation. The diffraction patterns were recorded at room temperature between 2θ values 2° to 30° .

3.4.2.4 Differential Scanning Calorimeter (DSC)

The melting temperature, T_m and the percentage crystallinity of PEO and SPEs films were investigated using PerkinElmer PYRIS (Diamond) Differential

Scanning Calorimeters (DSC). Indium sample was employed to calibrate the instrument. The amount of sample used in the study was about 10 mg, loaded using aluminum pans, the range of testing temperature was from 10°C to 100°C with the heating ramp 10°C min⁻¹ under Nitrogen atmosphere. In this work, isothermal and non-isothermal crystallization kinetic of PEO, PEO/MMT and PEO/NaSCN/MMT were studied.

For non-isothermal crystallization experiment, samples were cooled at various cooling rates 5, 10, 20 and 40°C/min. Then, the crystallinity of samples can be determined from the heat of crystallization. Next, the raw DSC thermograms were analyzed quantitatively to see the effect of adding MMT and salt on the non-isothermal crystallization kinetic of polymer complexes. The DSC temperature program in this experiment is shown in Figure 3.4.

Isothermal crystallization was performed at 50°C. The samples were initially melted at 100°C for 5 min in order to erase all previous thermal history. The temperature selected to begin the thermal treatment was quite higher than the measured melting point of all samples (around 60°), although not very high in order to avoid any possible thermal degradation of the polymer chains. Subsequently, the specimens were cooled at a rate of 40°C/min to a temperature about 10°C below the melting temperature (T_m) and this temperature ($T_m - 10^\circ\text{C}$) was set as a crystallization temperature (T_c) in isothermal crystallization study. The samples were held at T_c until no change in the heat flow was recorded.

3.4.2.5 FT-IR Spectroscopy

The interactions between polymer/MMT, polymer/polymer and polymer/salt complexes, and salt association were investigated by FTIR. The study

was carried out with FT-IR spectrometer Perkin-Elmer model: spectrum GX. The numbers of scans were 4 at the resolution of 4 cm^{-1} . The range of measurement was between 4000 cm^{-1} and 400 cm^{-1} . The technique analyzed samples are ATR (thin film) and KBr (powder sample).

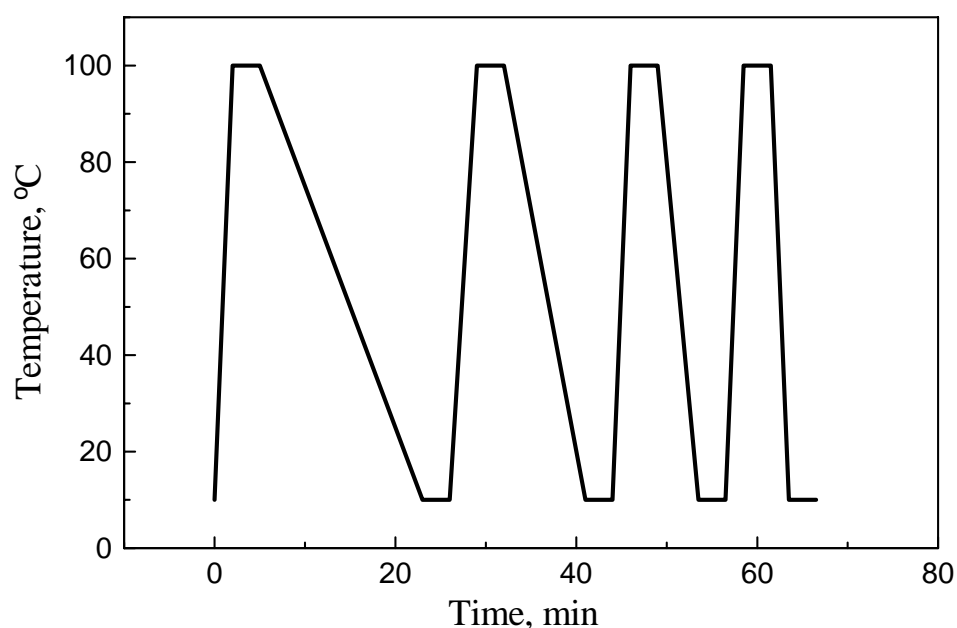


Figure 3.4 The DSC temperature program for an experiment of non-isothermal crystallization kinetics.

3.4.2.6 Polarized Optical Microscopy

Polarized optical microscopy was performed using a Nikon model ECLIPSEE600WPOL instrument equipped to study the PEO spherulites and phase separation.

3.4.2.7 Ionic Conductivity and Impedance Analyzer

Ionic conductivity and impedance response were obtained using Solartron 2610 Impedance Analyzer. The composite film sample was sandwiched between two stainless steel blocking electrodes provided by Prof. Muhammad

Careem (Department of Physics, University of Peradeniya, Sri Lanka). The specimen thickness was varied from 0.03 to 0.08 mm. The impedance response was gauged at room temperature (30°C). These films were contacted with polished steel disc electrodes in an O-ring sealed sample holder, and the room temperature conductivity determined from a.c. impedance measurements in the frequency interval of 10 MHz to 1 Hz. The experimental impedances were analyzed in terms of a model or equivalent circuit, using the computerized fitting software (Zview version 2.8d, Scribner Associates, Inc.).

Impedance analysis for the system of polymer solid electrolytes is usually based on the measurement of alternating current (a. c.) response as a function of input frequency. The a. c. data contain information about the long-range migration of ion and polarization phenomena occurring within the cell such as the relaxation of trapped ions. For the a. c. response for an ideal polymer electrolyte, a sinusoidal passing through the cell, as a function of an applied sinusoidal voltage was determined. In electrochemical cell, the ration of the voltage and current maxima yields the magnitude of impedance ($|Z|=V_{\max}/I_{\max}$). The phase angle of the impedance (θ) is the phase difference between the voltage and current. $|Z|$ and θ are normally the functions of applied frequency. Since impedance is a vector quantity, it can be expressed as a point the vector diagram shown in Figure 3.5.

The length of vector represents the magnitude of impedance and the angle form with the x-axis refer to the phase difference (θ). The expression of the impedance on a vector diagram is similar to the complex number expression in the complex plane. It is therefore often called as the complex impedance which is defined as Eq. (3.49).

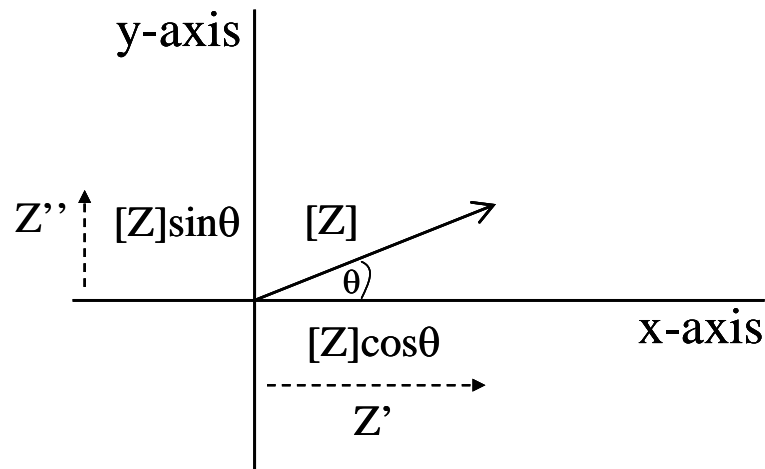


Figure 3.5 The complex impedance plot of Z

$$Z^* = |Z|\cos\theta + |Z|i\sin\theta = Z' + iZ'' \quad (3.49)$$

For polymer-salt complex, in which only one ionic species is mobile, one can employ an equivalent circuit to represent the impedance response of a sample as a function of frequency. An equivalent circuit, mainly consists of resistances and capacitors, which individually represent charge migration and polarization occurring within the sample can represent the response of a polymer complex cell to an a. c. signal. An equivalent circuit and corresponding complex impedance plot are explained in the followings. The electrodes are alternatively made positive and negative and the alternative field across the sample induced migration of metal ion back and forth in phase with the voltage. The resistance R_b refers to this ion migration in the circuit. Immobile polymers become polarized at the same time, in the alternative field. Capacitor, C_b , refer to this dielectric polarization. While mobile ions move in an alternative field, they are alternatively accumulated and depleted at each electrode. Each electrode is similar to the parallel plate capacitor and can be expressed by such a capacitance, C_e . Ionic migration and bulk polarization are physically in parallel, hence their equivalent components are R_b and C_b combination. Total impedance response from this

equivalent circuit can be represented by a plot between Z' vs Z'' . This model gives a high frequency bulk semicircle and low frequency electrode spike at R_b . The ionic conductivity can be obtained from $1/R_b = \sigma_{cation} + \sigma_{anion}$ which is consistent with the equation derived from a response from an equivalent circuit, as following

$$Z^* = R_b \left[\frac{1}{(1 + \omega R_b C_b)^2} \right] - i \left[R_b \left(\frac{\omega R_b C_b}{1 + (\omega R_b C_b)^2} \right) + \frac{1}{\omega C_e} \right] \quad (3.50)$$

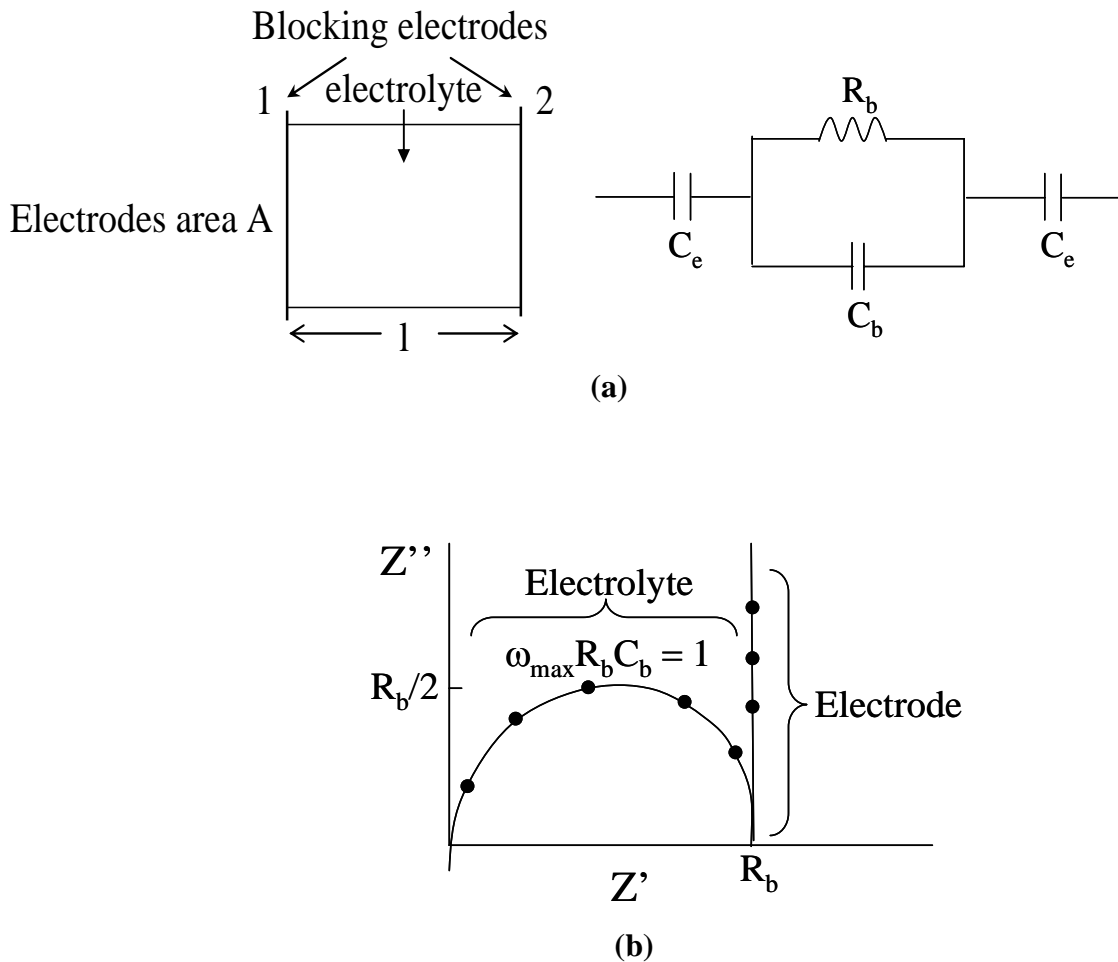


Figure 3.6 Schematic representation of polymer-salt complex (a) with blocking electrode and (b) simulated complex impedance plot for the circuit in (a)

CHAPTER IV

RESULTS AND DISCUSSIONS

4.1 Computational Part

4.1.1 Nuclear Magnetic Resonance (NMR) of Poly(N-vinyl-2-pyrrolidone) (PVP)

A. One-Dimensional NMR Spectroscopy (1D-NMR)

PVP (MW 55,000 g/mol) was first studied using 1D-NMR technique. The ^1H -NMR experiment was performed to give all protons signal. The ^1H -NMR spectrum of PVP, as shown in Figure 4.1, represent the peak position and integration numbers of CH_2 , and CH groups of PVP unit. However, ^1H -NMR technique was not completely successful in establishing the microstructure presented in PVP.

To consider protons at C_α and C_β , the two protons at C_β are up point and down point thus the protons down point were effected by oxygen and nitrogen of pyrrolidone ring. It indicated that deshield or chemical shift values were higher than up point proton. As a comparison between protons in pyrrolidone and protons in backbone, the shielding from pyrrolidone ring should affect to proton in the backbone, thus the chemical shifts of proton in backbone were higher than protons in pyrrolidone. The chemical shift values of protons are listed in Table 4.1.

^{13}C -NMR generally offers the potential for greater spectroscopic resolution than ^1H -NMR and is expected to be better suit for the analysis for PVP microstructure. The ^{13}C -NMR spectrum, in Figure 4.2, gives all carbon signals in

chemical structures. The positions of chemical shift and carbon types of PVP are characterized in Table 4.2. The considerable at C_α and C_β in the position of polymer backbone have many splitting peaks, indicating that polymer was various conformations of atactic polymer. The triad tacticity of the polymer was determined base on the peak height of the methine carbon of the backbone (C_α). Using the equation $r = rr + mr/2$. From Figure 4.2, the recemo percentage of this atactic PVP is $r = 35.9\%$.

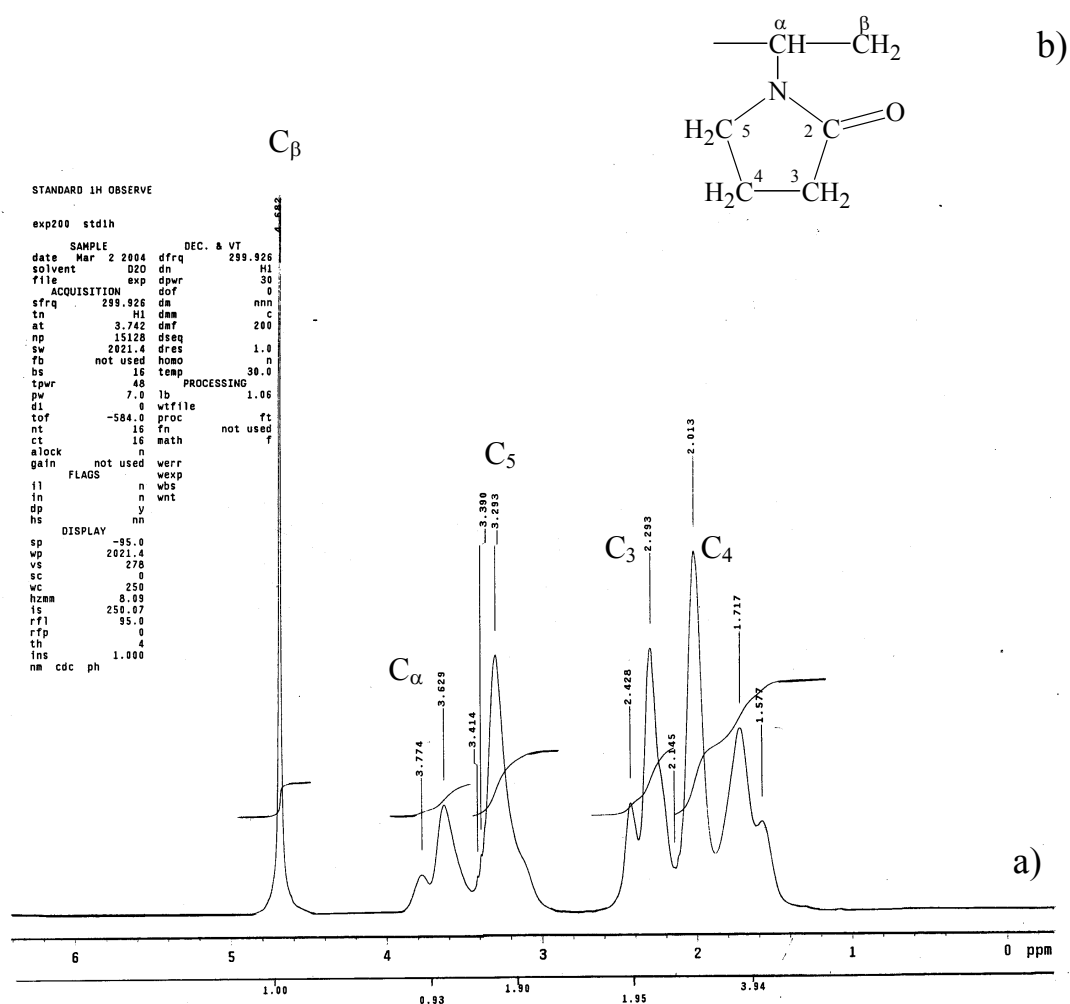


Figure 4.1 a) ¹H-NMR spectrum of PVP measured from 300 MHz of Unity Inova NMR spectrometer. b) The repeating unit and assign the position of carbon in PVP

Table 4.1 The chemical shift (δ) value of protons NMR for PVP with a comparison to the reported literature.

Proton at C position	Chemical shift δ , ppm	
	Ref (Szaraz, 2000)	Experimental
C3	2.46	2.43
	2.41	2.29
	2.33	
C4	2.04	2.01
C5	3.34	3.29
	3.16	
C α	3.82	3.77
	3.68	3.63
C β	1.77	1.72
	4.42	4.63

Table 4.2 The chemical shift (δ value) of C¹³ NMR spectra for PVP and comparison with Ref.

Proton at carbon position	Carbon types	Chemical shift δ , ppm	
		Ref (Szaraz, 2000)	Experimental
C2	C tetra	180.2	180.3
C3	Methylene	34.0	33.9
C4	Methylene	20.2	20.2
C5	Methylene	45.6, 45.4, 47.2	45.1
C α	Methine	48.5, 47.6, 47.2	47.3, 48.4
C β	Methylene	38.0, 37.4,	37.9, 37.3
		36.5, 35.6	36.3

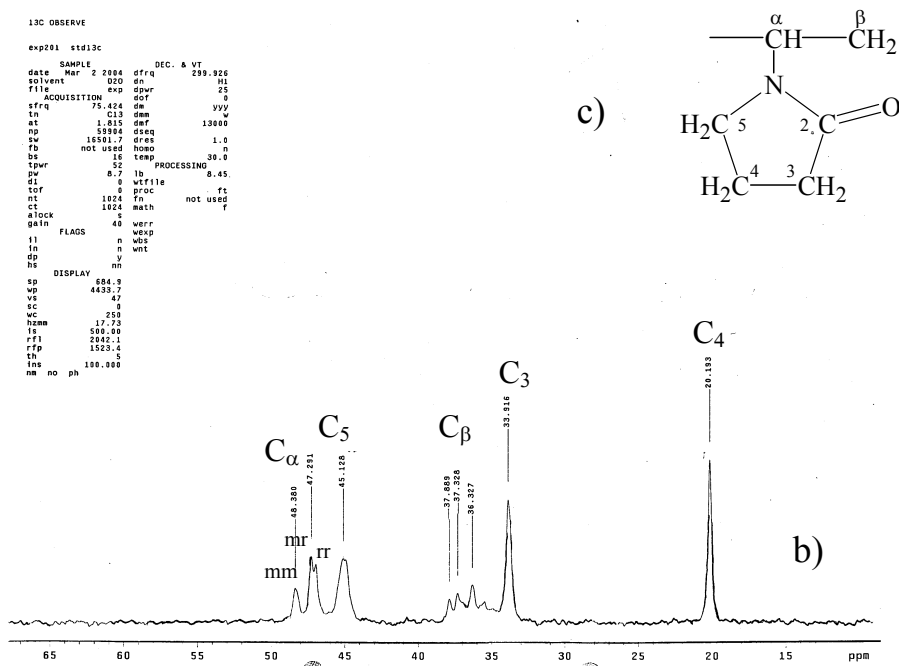
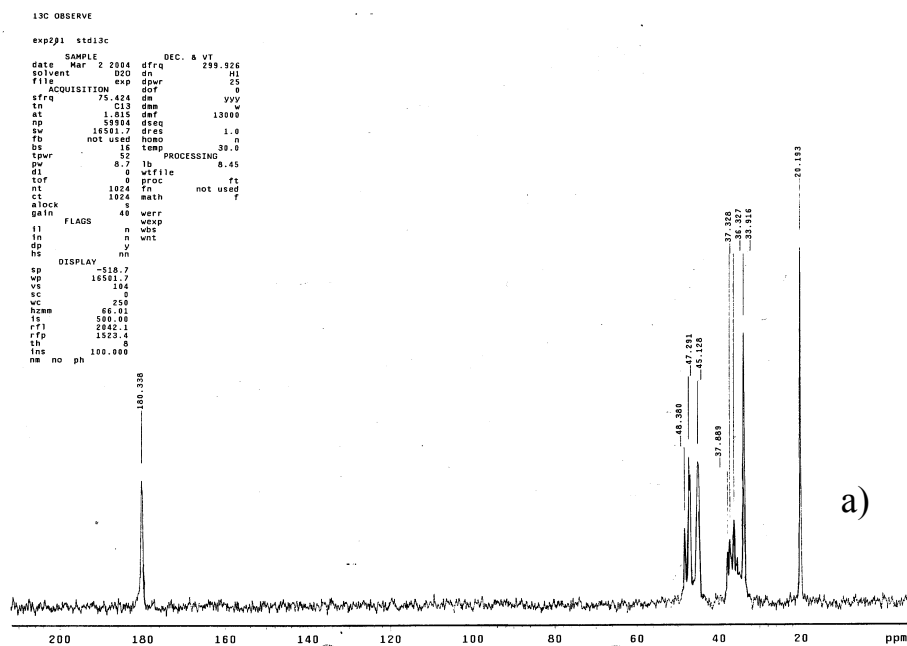


Figure 4.2 ^{13}C -NMR spectrum of PVP measured from 300 MHz of Unity Inova NMR spectrometer a) 20-200 ppm and b) 15-65 ppm. c) The repeating unit and assign the position of carbon in PVP

Different carbon characteristics were distinguished by DEPT experiment. DEPT was performed to characterize carbon signals in the polymer structure. The DEPT-45 spectrum, shown in Figure 4.3, was conducted to provide information for methine carbon, CH, which represented for carbon peak at ~47 ppm, (methylene carbon, CH₂), and at ~45, 37, 34 and 20 ppm (methyl carbon, CH₃), which disappear in this spectra because CH₃ can exist only a very small amount as it represent the repeating unit of the end of PVP chain. The different environment of C_β proton were 3 type i.e. syndiotactic, isotactic and heterotactic resulting in 3 peaks (36-37 ppm).

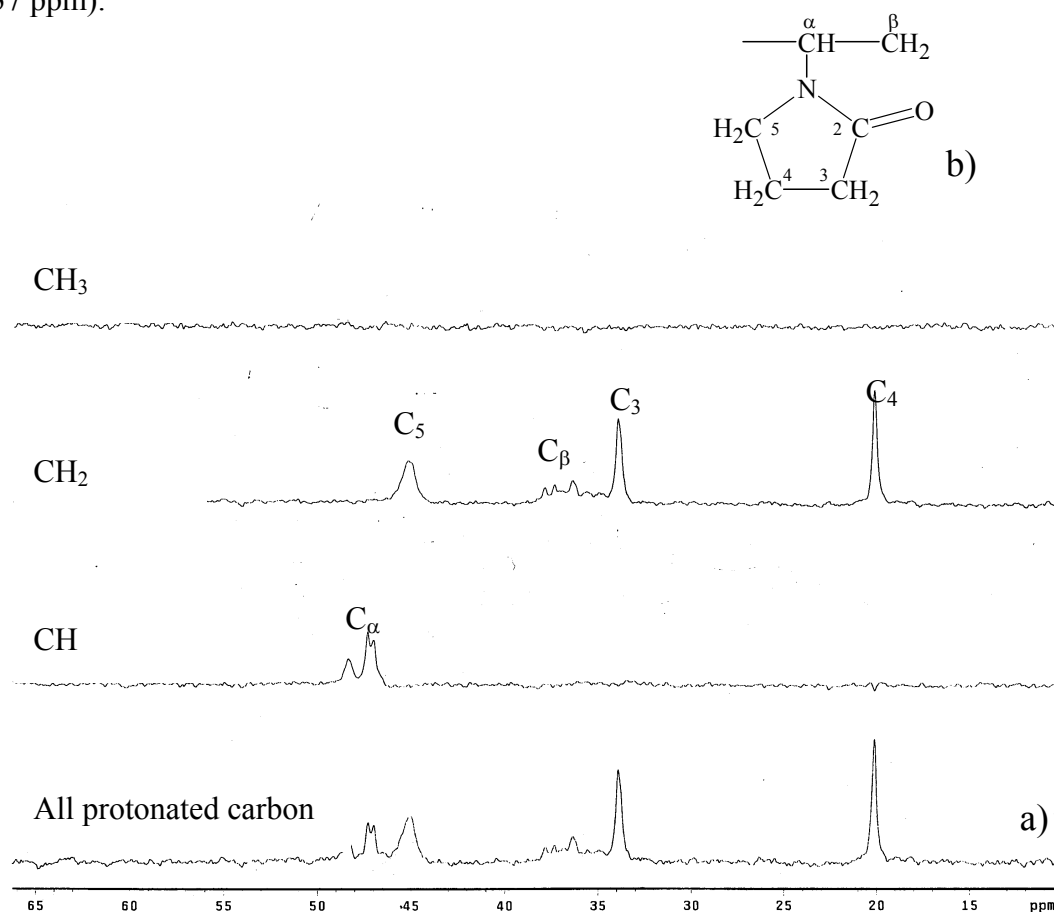


Figure 4.3 a) DEPT-45 spectrum of PVP measured from 300 MHz Unity Inova NMR spectrometer. b) The repeating unit and assign the position of carbon in PVP.

B. Two-Dimensional NMR Spectroscopy (2D-NMR)

To assign all carbon peaks in PVP, 2D-NMR technique, namely Heteronuclear Chemical Shift Correlation (HETCOR) and COrelated Spectroscopy (COSY) were used. The HETCOR experiment provides a relationship between ^1H -NMR and ^{13}C -NMR spectra by elucidating the specific protons attached to each carbon atoms. ^1H - ^1H COSY technique also leads to greater separation of the overlapping proton resonances. Although, even the application of this spectroscopic technique, it was not completely successful in establishing the microstructures presented in PVP.

COSY Experiment

Figure 4.4 shows the COSY spectra of PVP. The ^1H -NMR spectrum is presented on the vertical axis and the horizontal axis. The ^1H - ^1H correlation is shown by a cross peak contour at the intersection of a horizontal line drawn and a vertical line drawn from proton peak. The signals of cross peak are appeared at 4 positions (shown alphabet in figure 4.8), as following;

- | | | | |
|-----|------------------------|---------------|-----------------------|
| (a) | H of C_5 | coupling with | H of C_4 |
| (b) | H of C_4 | ,, | H of C_3 |
| | H of C_α | ,, | H of C_β |

(not observed in this Figure)

Thus this technique confirms the correlation between proton/proton in the vicinity carbon.

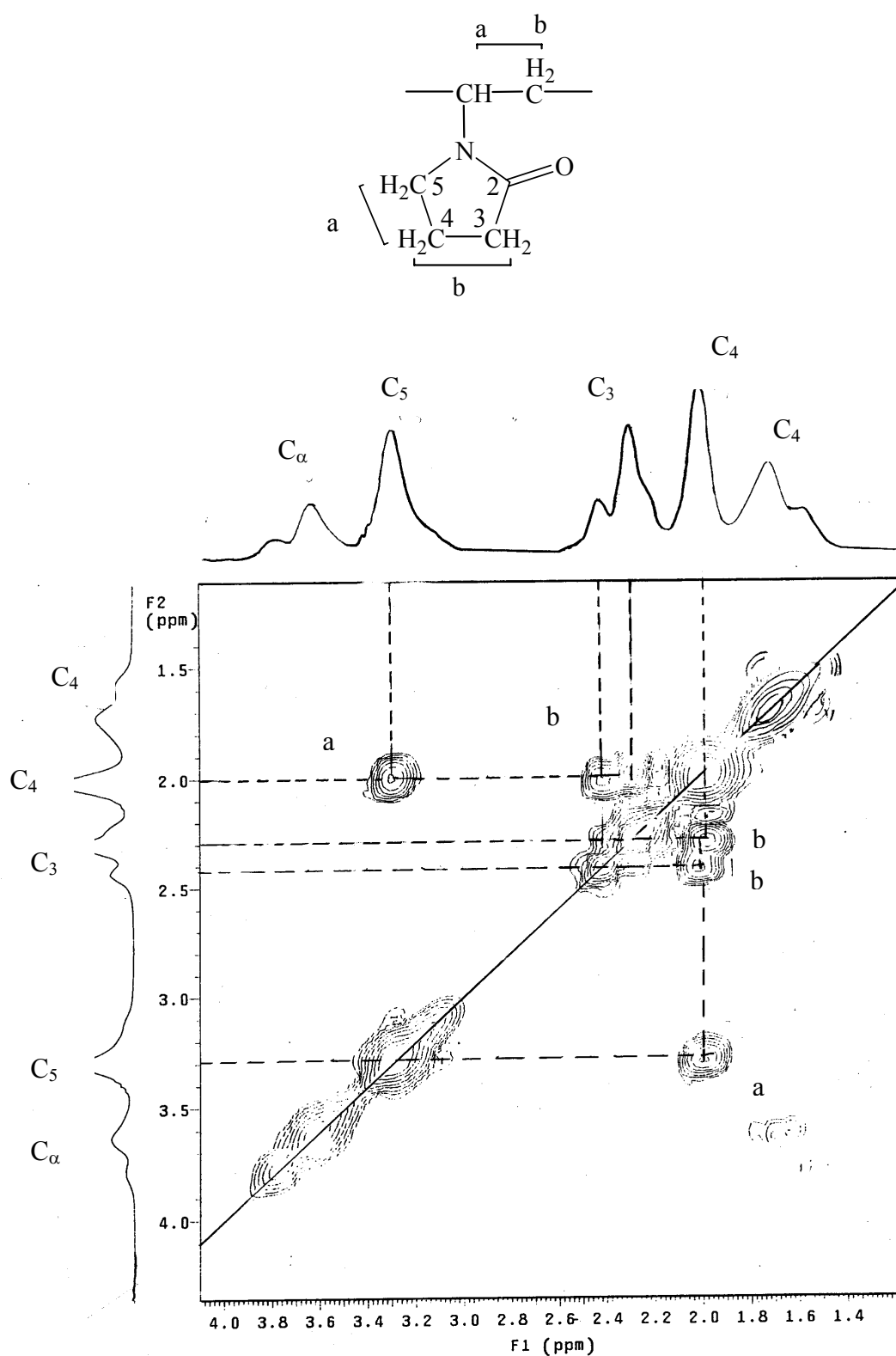


Figure 4.4 COSY spectrum of PVP measured from 300 MHz Unity Inova NMR spectrometer

HETCOR Experiment

Figure 4.5 shows the HETCOR spectra of PVP. The ^{13}C -NMR spectrum is presented on the vertical axis and the ^1H -NMR spectrum is presented on the horizontal axis. The ^1H - ^{13}C correlation is shown by a cross peak contour at the intersection of a horizontal line drawn from a ^{13}C peak and a vertical line drawn from a proton peak. The signals of carbon (methylene groups) appearing at ~ 20 , 34 and 45 ppm are matched to proton signals C4, C3 and C5, respectively. The methine carbons at ~ 47 -50 ppm, representing C_α have 3 cross peaks with C_β proton. The many cross peaks of carbon at polymer backbone indicate that PVP is an atactic polymer.

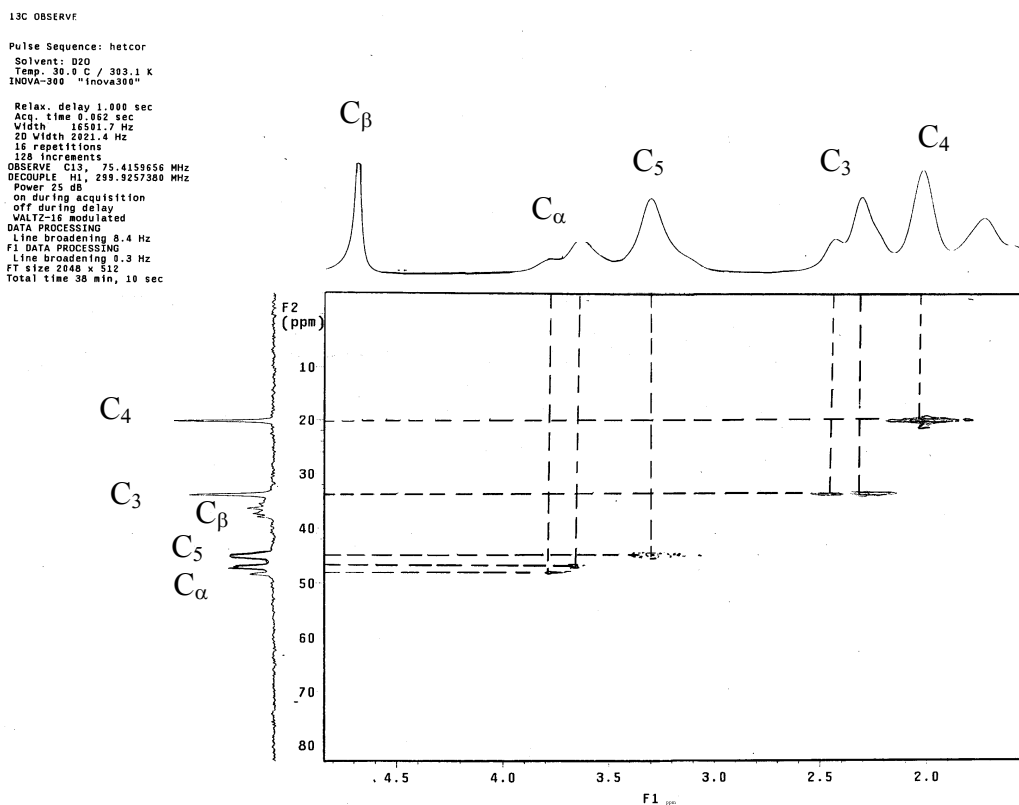


Figure 4.5 HETCOR spectrum of PVP measured from 300 MHz Unity Inova NMR spectrometer

4.1.2 Conformational characteristic of Poly(N-vinyl-2-pyrrolidone) (PVP)

The unperturbed dimensions of PVP were determined several years ago by Meza and Gargallo [7]. These authors measured the viscosity and osmotic pressure of dilute solution of PVP in various solvents at 25°C. Extrapolated each set of results to unperturbed conditions using the Stockmayer-Fixman equation showed a remarkable dependence of the unperturbed dimensions on the nature of the solvent. Although the authors presented a qualitative explanation of these results, only a few works on quantitative analysis have been performed.

In this thesis, the commercial molecular modeling package, HyperChem version7 was employed to compute the conformational energies of both *meso* and *racemic* diads of PVP as a function of the rotational angles over consecutive backbone bonds. The results of these energy calculations were employed to formulate a statistical model of the PVP chain, thus allowing the calculation of its unperturbed dimensions which were then compared with the results of the experimental determinations.

The outline of this section is as follows. Firstly, the characteristic of chain configuration and molecular size were determined using viscosity measurement. Secondly, the conformational energy maps for each representation segment of PVP were calculated. Finally, a simple RIS model of PVP was formulated and some comparisons between experimental results and predicted values were discussed.

Intrinsic Viscosity Measurement

Intrinsic viscosities of PVP in water were measured at 30°, 40°, 50°, 60° and 70°C. At least four concentrations were investigated for each polymer

solution. Intrinsic viscosities, $[\eta]$, were obtained in the usual manner by extrapolation of η_{sp}/c to infinite dilution, according to Eq. (3.48). Results are showed in table 4.3.

The intrinsic viscosity of PVP in water:acetone = 66.8:33.2 (theta condition) at 30°C was 0.1216. These results gave molecular weights equal to 43955 g mol⁻¹ according to the relationship.

$$[\eta] = 58 \times 10^{-5} M_v^{0.5} \quad (4.2)$$

where M_v is a viscosity average molecular weight. Our finding seems to be reasonable as it is close to the molecular weight provided by the manufacture (55,000 g mol⁻¹). The dependence of $\ln [\eta]$ on temperature for these samples is shown in Figure 4.6. The results are well represented by the linear correlation as straight lines with covariance equal 0.978. The slopes of the lines give $10^3 d \ln \langle \eta \rangle_o / dT = -0.020$. These values are comparable in magnitude to range of values -1.2 to $-2.0 \times 10^{-3} \text{ K}^{-1}$ obtained by de Candia and coworker on four PVP fractions having viscosity-average molecular weights M_v in the interval 400-4,000 g mol⁻¹ in the thermodynamically good solvents (Candia *et al.*, 1972).

Table 4.3 Intrinsic viscosities of PVP in water.

Temperature (°C)	Intrinsic viscosities $[\eta]$ (g dl ⁻¹)
30	0.167
40	0.155
50	0.111
60	0.089
70	0.083

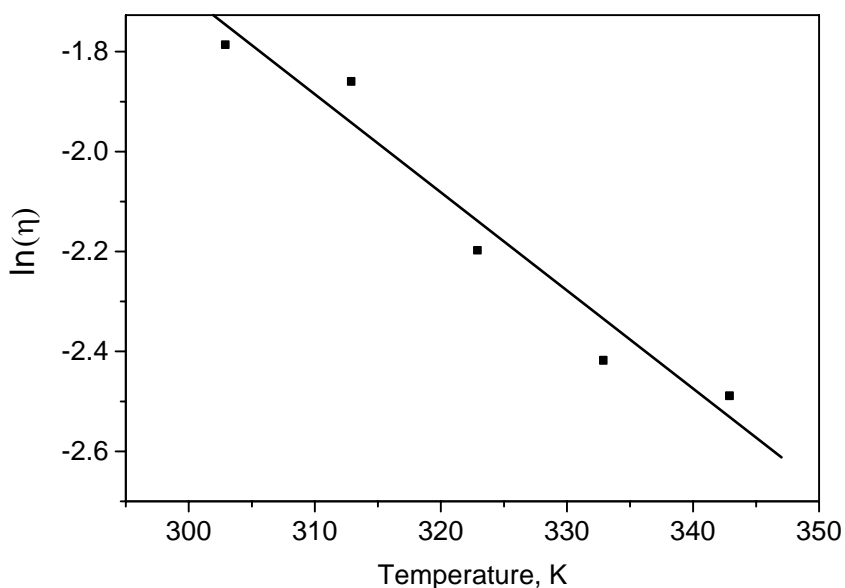


Figure 4.6 Intrinsic viscosity vs. temperature for PVP in water; the molecular weights of the samples is $55,000 \text{ g mol}^{-1}$

From these results, we are confident on using these data to further calculate the size of PVP molecule. From a well-known the intrinsic viscosity under the theta (θ) condition, $([\eta]_{\theta})$ is related to $\langle r^2 \rangle_0$ that can be calculated from :

$$[\eta] = \Phi \left[\frac{\langle r^2 \rangle_0}{M} \right]^{3/2} \quad (4.2)$$

where Φ is the hydrodynamic factor (2.6×10^{21}) and M is the average molecule weight.

From this relation, $\langle r^2 \rangle_0$ and $\langle r^2 \rangle_0/nl^2$ were estimated from the viscosity experiment equal to 3380 \AA^2 and 7.94, respectively.

Conformational energies

Figure 4.7 shows the structure of *N*-methyl-2-pyrrolidone that was taken as a model compound for the repeating unit of PVP. The geometry of this

molecule was fully optimized overall bond lengths and angles using the semi-empirical (PM3) method. The obtained geometry and charge as shown in Figure 4.7 was used in all the sub-sequent calculations. The dipole moment of this molecule, in its optimized geometry, was $\mu = 3.52\text{D}$ or in the vector form of $[-3.39, -0.45, 0.83]$. This value was in good agreement with the experimental results of $\mu = 3.52\text{D}$ and 3.75D measured in benzene and cyclohexane solution, respectively, at 30°C . The charge distribution indicated in Figure 4.7 was then employed to compute coulombic interaction between atoms of PVP diads.

A sketch of the *meso* diad of PVP is represented in Figure 4.8. Rotational angles over the backbone bond ϕ_i were taken as 180° for *trans* conformations. Rotations over the side groups are represented by ρ_i and taken as 180° when C^* is located in the plane defined by NC^αH . Conformational energies of both *meso* and *racemic* diads were computed by evaluating the interactions between each pair of atoms employing AMBER force field. For each conformation of backbone, (ϕ_1, ϕ_2) full rotations of the side groups were performed seeking for the orientation of lowest energies. The energy of this orientation was then optimized using Polak-Ribiere Conjugate Gradient algorithm. The $\text{CH}_2\text{-C}^\alpha\text{-CH}_2$ bond angle was varied accordingly and the range of θ is $110\text{-}114^\circ$. Full conformational space was performed moving ϕ_1 and ϕ_2 from 0 to 350° with increments of 10° in order to locate the areas of minimum local energy that should correspond to rotational isomers of the chain. The averages of energy $\langle E \rangle$ and rotational angles $\langle \phi_1 \rangle, \langle \phi_2 \rangle$ were computed for each rotational isomer.

The results of these calculations were then used to formulate a conformational model similar to those previously employed for other vinyl polymer. Thus, statistical-weight matrices U' and U'' were defined as

$$U' = \begin{bmatrix} 1 & p_{tg} & p_{tg^-} \\ p_{gt} & p_{gg} & p_{gg^-} \\ p_{g^-t} & p_{g^-g} & p_{g^-g^-} \end{bmatrix} \quad (4.3)$$

for a pair of bonds flanking a substituted carbon,

$$U''_m = \begin{bmatrix} 1 & m_{tg} & m_{tg^-} \\ m_{gt} & m_{gg} & m_{gg^-} \\ m_{g^-t} & m_{g^-g} & m_{g^-g^-} \end{bmatrix} \quad U''_r = \begin{bmatrix} 1 & r_{tg} & r_{tg^-} \\ r_{gt} & r_{gg} & r_{gg^-} \\ r_{g^-t} & r_{g^-g} & r_{g^-g^-} \end{bmatrix} \quad (4.4)$$

for the bond pairs within a *meso* and *racemic* diad, respectively. In this equation $m_{\zeta\xi}$ and $r_{\zeta\xi}$ represent Boltzmann factors ($e^{-\Delta E/kT}$) of the averaged energies of *meso* and *racemic* diads having the first bond in rotational state $m_{\zeta\xi}$ and second one in $r_{\zeta\xi}$ (with subscripts ζ and ξ representing *trans* (*t*) and, *gauche* (*g*) or negative *gauche* (*g*⁻) states).

These matrices, together with the averaged geometrical parameters $\langle\phi_1\rangle$ and $\langle\phi_2\rangle$ for each conformational state, were used to compute mean-squared values of the end-to end distance $\langle r^2 \rangle_0$ for chains according to standard procedures of the matrix multiplication scheme. The values of $\langle r^2 \rangle_0$ were then transformed into the characteristic ratio $C_n = \langle r^2 \rangle_0 / (nl^2)$, where l indicated the length of each skeletal bond ($l=1.53 \text{ \AA}$ in the present work), and extrapolated to $n \rightarrow \infty$.

Figures 4.9, 4.10 and 4.11 represent, respectively, the conformational energies of *meso* and *racemic* diads of PVP as function of rotational angles of the backbone.

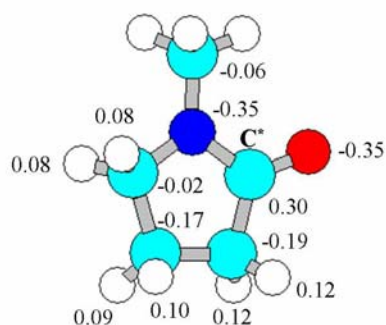


Figure 4.7 Sketch of *N*-methyl-2-pyrrolidone molecule that was used as model compound for the repeating unit of PVP. Full optimization of the geometry was performed with HyperChem7 (PM3), and the resulting geometry was used in all the calculations. Partial charges, were assigned as to reproduce both module ($\mu = 3.52\text{D}$) and direction of the dipole moment.

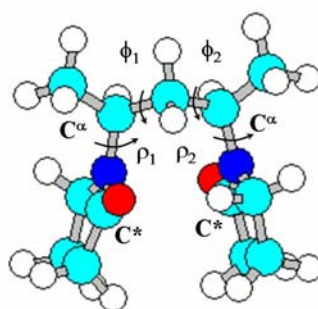


Figure 4.8 Sketch of the *meso* diad of PVP, backbone rotational angles: $\phi_1 = \phi_2 = 180^\circ$ defined for the *trans-trans* conformation. Side group rotations: $\rho = 180^\circ$ when C^* is located in the plane defined by $NC^\alpha H$

These energies were computed with a dielectric of $\epsilon=4$, 78 and ∞ (no charge/coulombic interaction), and optimized with respect to the rotations ρ_1 and ρ_2 of the side groups and the backbone angle θ' . The conformation of lowest energy was represented by blackest color (it corresponds to *tt* in both cases) and renormalized by taking this lowest value as zero.

It is interesting to notice that the energy becomes quite high in rather large areas of both *meso* and *racemic* diads. Thus, for instance, the white area in Figures 4.9, 4.10 and 4.11 enclose the conformations in which the energy is higher than 10 kcal/mol above the minimum. This kind of results is typical of polymeric chains having bulky side groups that produce strong interactions for many orientations of the main chain, and although these interactions could be relieved in part by adjustments of the rotations over the side groups or by opening the backbone angles, the resulting energy is still rather high.

A more quantitative description of the conformational energies is given in Tables 4.4, 4.5 and 4.6 for $\epsilon=4$, 78 and ∞ , respectively, that summarizes all the pertinent results of this calculation. The first column of this table lists the rotational isomer for both *meso* and *racemic* diads. Isomer *gt*, *g't* and *g'g* are mirror images of *tg*, *tg'* and *gg'*, respectively, and therefore they are not included in the table. The second and third column give the values of the averaged energies and backbone rotational angles for each isomer. These conformations are drawn in Figures 4.12 and 4.13, respectively, for *meso* (*dd*) and *racemic* (*dl*) diads. The last column of the table summarizes the averaged values of the relative energies computed with respect to the minimum value. These parameters were employed in the Rotational Isomeric State (RIS) model, namely the averages of rotational angles, the average of the backbone

angle θ' and the average energies normalized with respect to the tt state for both *meso* and *racemic* diads. Boltzmann factors of these energies were the elements of the U'' matrices given by Eqs. (3.3 and 3.4). Numerical values for the statistical weight matrices derived from these conformational energies are listed in Appendix A.

As the last column of Tables 4.5, 4.6 and 4.7 indicates, the extended tt conformation is the preferred state for both *meso* and *racemic* diads. Generally, the difference in energy to the other conformations in the case of *meso* are larger than those of *racemo* ($g'g'$ conformation). Therefore, the sequence of preferred $tttt\dots$ states should be disrupted by gg or gg' more frequently in the case of *racemic* than in *meso* and, consequently, isotactic chains should have higher molecular dimensions than their syndiotactic counterparts (Tonelli 1981). Characteristic ratios of the unperturbed dimensions computed with this set of conformational parameters are represented in Figure 4.14 when the tacticity of the sample changes from 0.1 to 0.9.

Line a, b and c in Figure 4.14 can be compared with the experimental results reported by Meza and Gargallo which are summarized in Table 4.7. This polymer is usually obtained by radical polymerization which produces almost perfectly atactic chains with fractions of meso diads $w_m \approx 0.5-0.6$. The calculated C_∞ for $\epsilon=4, 78, \infty$ are 3.20, 3.95 and 11.47, respectively, based on this calculation method. Among the solvent collected in Table 4.7, chloroform is less polar ($\epsilon=4.8$) and the dimension obtained in this solvent $C_\infty = 6.4$. Replacing chloroform by 2-propanol ($\epsilon=18.3$) to increase the polarity of the solvent, and the characteristic ratio is raised to ca. 10. For water solution, C_∞ decreases to 5.5 even though the polarity of solvent increase. The change in molecular size from experimental results found not only sensitive to the polarity of solvent.

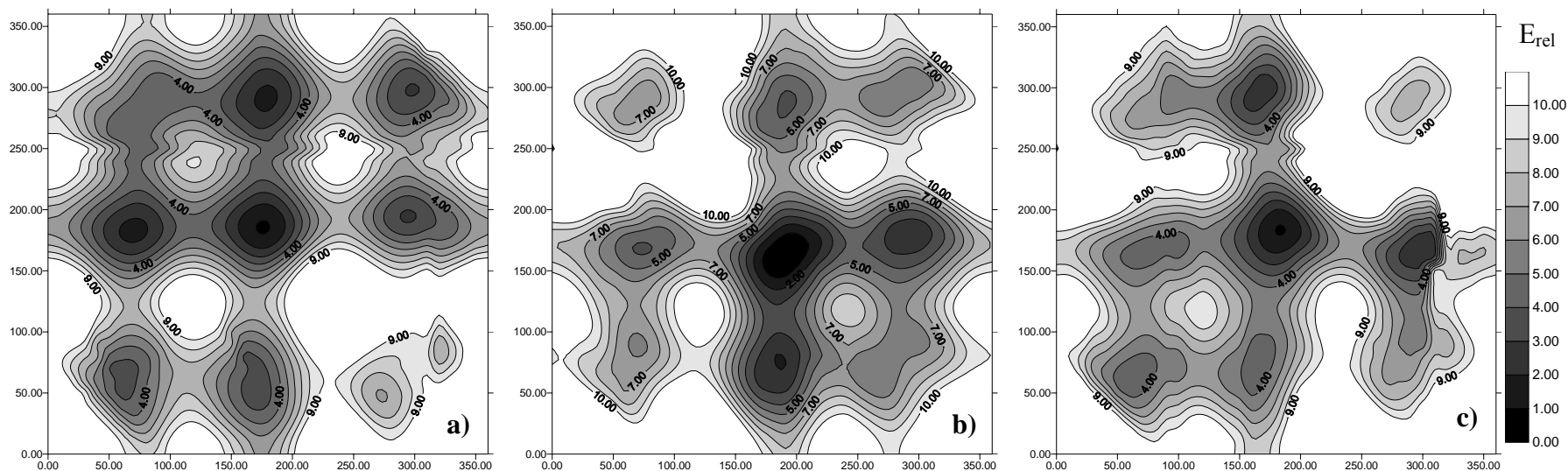


Figure 4.9 a), b) and c) Conformational energies of *d*, *dd* and *dl* fragment of PVP respectively, computed with $\epsilon = 78$ as a function of rotational angles ϕ_1 and ϕ_2 of the backbone. The energies for each set of (ϕ_1, ϕ_2) were optimized with respect to side group rotations (ρ_1, ρ_2) and backbone angle θ' . Energy contour are drawn at 1 kcal/mol intervals.

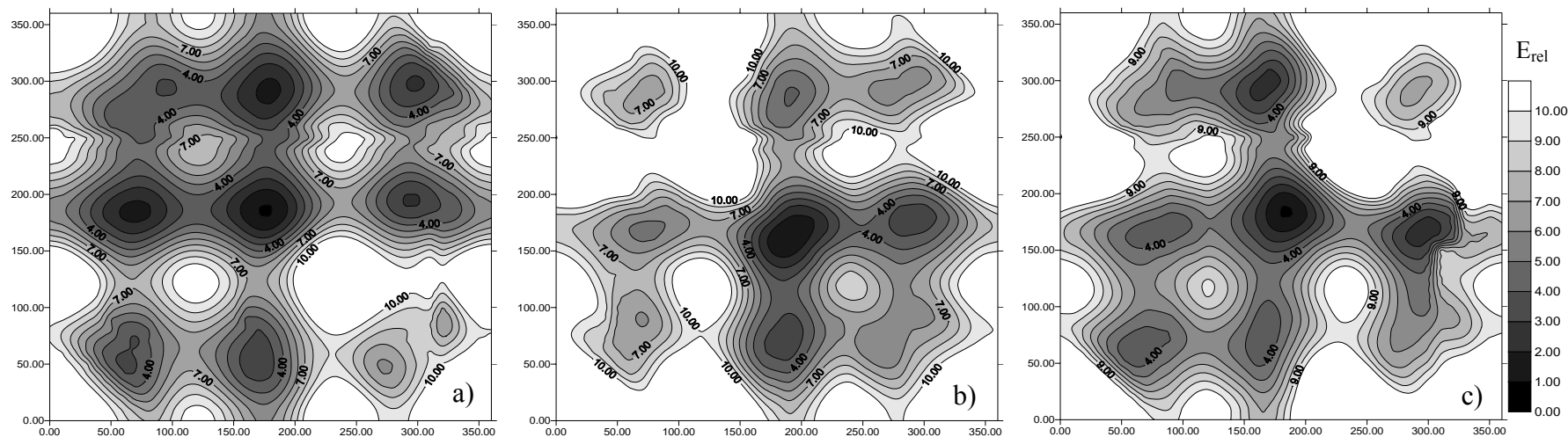


Figure 4.10 a), b) and c) Conformational energies of d , dd and dl fragment of PVP respectively, computed with $\epsilon = 4$ as a function of rotational angles ϕ_1 and ϕ_2 of the backbone. The energies for each set of (ϕ_1, ϕ_2) were optimized with respect to side group rotations (ρ_1, ρ_2) and backbone angle θ' . Energy contour are drawn at 1 kcal/mol intervals.

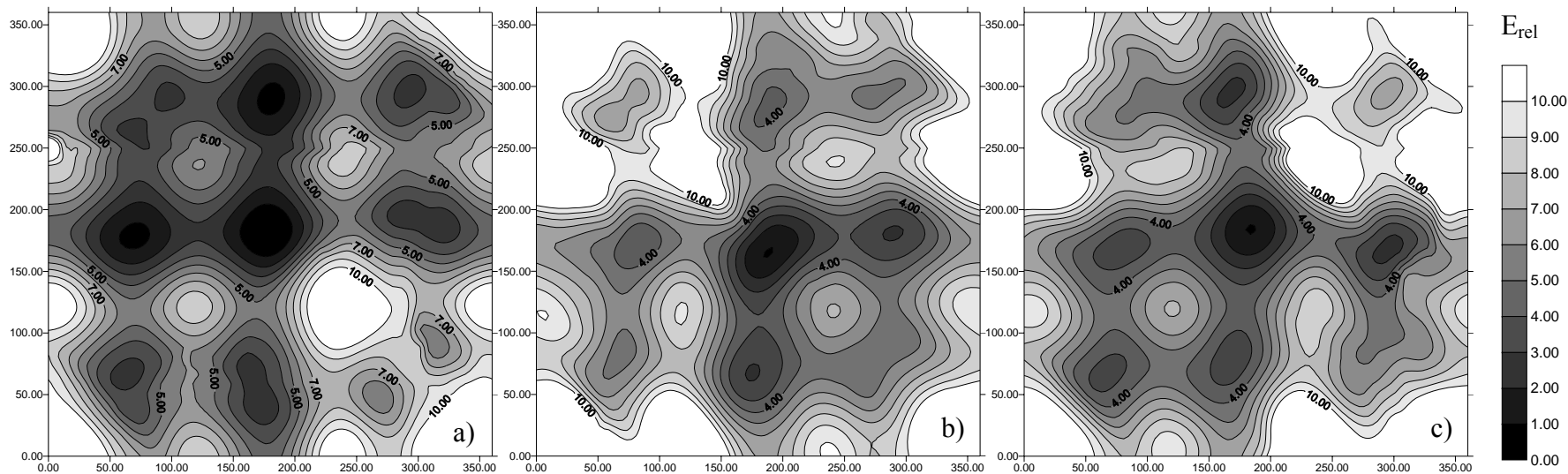


Figure 4.11 a), b) and c) Conformational energies of d , dd and dl fragment of PVP respectively, computed with $\epsilon = \infty$ as a function of rotational angles ϕ_1 and ϕ_2 of the backbone. The energies for each set of (ϕ_1, ϕ_2) were optimized with respect to side group rotations (ρ_1, ρ_2) and backbone angle θ' . Energy contour are drawn at 1 kcal/mol intervals.

Table 4.4 Summary conformational magnitudes for *meso* and *racemic* diads of PVP as function of the dielectric constant $\epsilon=78$ (angle are given in degree and energies in kcal/mol)

Conformation	$\langle E \rangle$	$\langle \phi_1 \rangle$	$\langle \phi_2 \rangle$	E_{rel}
<i>tt u</i>	0.52	173.91	188.45	0.00
<i>tg u</i>	2.16	173.91	71.59	1.64
<i>tg' u</i>	1.96	173.91	288.93	1.44
<i>gg u</i>	3.08	71.59	58.99	2.56
<i>gg' u</i>	5.12	71.59	288.93	4.60
<i>g'g' u</i>	2.52	292.29	288.93	2.00
<i>tt dd</i>	0.58	188.79	169.45	0.00
<i>tg dd</i>	3.52	188.79	80.79	2.94
<i>tg' dd</i>	3.65	188.79	289.63	3.07
<i>gg dd</i>	6.41	70.86	80.79	5.83
<i>gg' dd</i>	6.28	70.86	289.63	5.70
<i>g'g' dd</i>	5.72	282.21	289.63	5.14
<i>tt dl</i>	1.02	170.80	171.50	0.00
<i>tg dl</i>	4.45	170.80	80.22	3.42
<i>tg' dl</i>	2.40	170.80	292.30	1.38
<i>gg dl</i>	4.47	82.35	80.22	3.44
<i>gg' dl</i>	5.36	82.35	171.50	4.34
<i>g'g' dl</i>	7.53	291.70	292.30	6.50

Table 4.5 Summary conformational magnitudes for *meso* and *racemic* diads of PVP as function of the dielectric constant $\epsilon=4$ (angle are given in degree and energies in kcal/mol)

Conformation	$\langle E \rangle$	$\langle \phi_1 \rangle$	$\langle \phi_2 \rangle$	E_{rel}
<i>tt u</i>	0.52	173.58	188.96	0.00
<i>tg u</i>	2.11	173.58	57.60	1.59
<i>tg' u</i>	1.92	173.58	290.22	1.40
<i>gg u</i>	3.28	72.99	57.60	2.75
<i>gg' u</i>	4.96	72.99	290.22	4.44
<i>g'g' u</i>	2.44	292.75	290.22	1.92
<i>tt dd</i>	0.59	189.73	169.31	0.00
<i>tg dd</i>	4.08	189.73	81.07	3.49
<i>tg' dd</i>	3.72	189.73	289.87	3.13
<i>gg dd</i>	6.53	70.63	81.07	5.94
<i>gg' dd</i>	6.34	70.63	289.87	5.75
<i>g'g' dd</i>	6.02	281.05	289.87	5.43
<i>tt dl</i>	0.52	171.56	171.74	0.00
<i>tg dl</i>	3.86	171.56	81.94	3.34
<i>tg' dl</i>	2.08	171.56	292.91	1.56
<i>gg dl</i>	3.98	82.98	81.94	3.46
<i>gg' dl</i>	5.01	82.98	292.91	4.49
<i>g'g' dl</i>	7.23	291.82	292.91	6.71

Table 4.6 Summary conformational magnitudes for *meso* and *racemic* diads of PVP as function of the dielectric constant $\epsilon=\infty$ (angle are given in degree and energies in kcal/mol)

Conformation	$\langle E \rangle$	$\langle \phi_1 \rangle$	$\langle \phi_2 \rangle$	E_{rel}
<i>tt u</i>	0.91	174.89	185.35	0.00
<i>tg u</i>	2.47	174.89	62.55	1.56
<i>tg' u</i>	2.43	174.89	287.07	1.52
<i>gg u</i>	3.52	73.74	62.55	2.61
<i>gg' u</i>	4.81	73.74	287.07	3.90
<i>g'g' u</i>	3.52	297.89	287.07	2.61
<i>tt dd</i>	0.55	181.02	171.60	0.00
<i>tg dd</i>	3.19	181.02	80.83	2.64
<i>tg' dd</i>	3.43	181.02	288.23	2.87
<i>gg dd</i>	5.18	72.62	80.83	4.63
<i>gg' dd</i>	5.82	72.62	288.23	5.27
<i>g'g' dd</i>	5.22	280.43	288.23	4.66
<i>tt dl</i>	0.59	172.28	172.29	0.00
<i>tg dl</i>	3.01	172.28	82.76	2.42
<i>tg' dl</i>	2.29	172.28	291.92	1.70
<i>gg dl</i>	3.28	85.57	82.76	2.69
<i>gg' dl</i>	5.00	85.57	291.92	4.41
<i>g'g' dl</i>	7.25	292.21	291.92	6.66

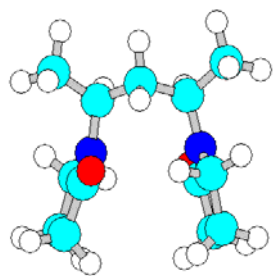
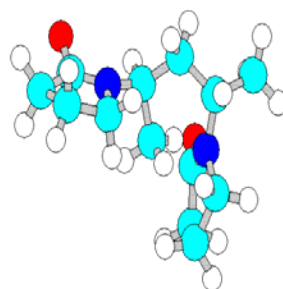
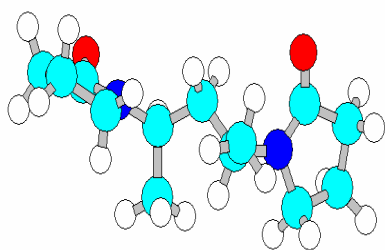
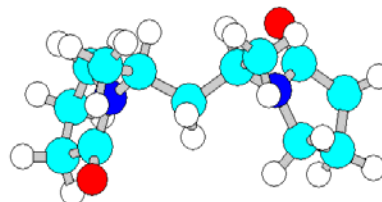
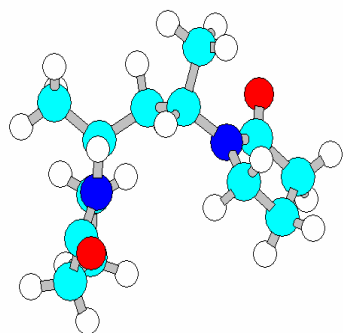
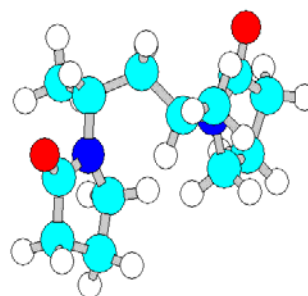
**dd *tt*****dd *tg*****dd *tg'*****dd *gg*****dd *gg'*****dd *g-g'***

Figure 4.12 Sketches of the conformation whose energies represent local minima in the conformational space of *dd* diads of PVP. Conformations *gt*, *g't* and *g'* are mirror images of *tg*, *tg'* and *gg'*, respectively, and not presented here.

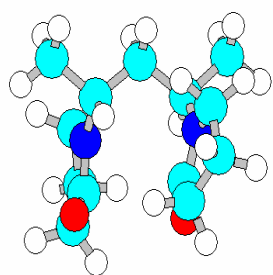
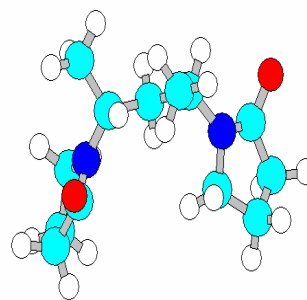
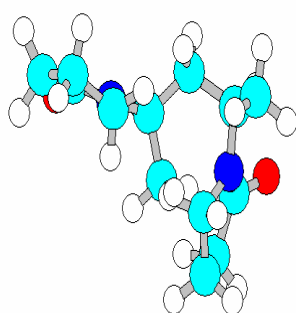
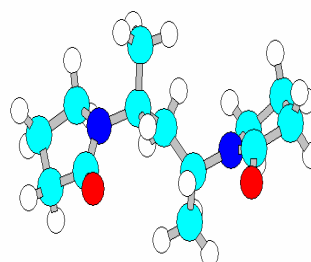
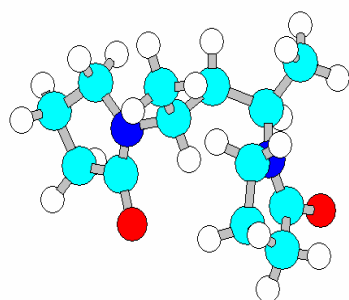
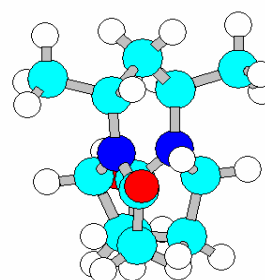
**dl *tt*****dl *tg*****dl *tg*⁻****dl *gg*****dl *gg*⁻****dl *g*⁻*g*⁻**

Figure 4.13 Sketches of the conformation whose energies represent local minima in the conformational space of *dl* diads of PVP. Conformations *gt*, *g⁻t* and *g⁻* *g* are mirror images of *tg*, *tg⁻* and *gg⁻*, respectively, and not presented here.

This was opposite to the calculated C_∞ value from this work in that C_∞ was decreased with the dielectric constant used in the conformational energy calculation. This discrepancy may arise from the fact the calculation technique does not take into account the effect of solvent size. It is expected that smaller solvent should interact with polymer easier than the larger ones. This induces polymer chain to coil up and results in smaller molecular dimension. The size effect describes reasonably well why PVP dissolved in water shows smallest dimension even though it has the highest dielectric constant. To elucidate this effect more clearly, explicit solvent simulation is needed e.g. molecular dynamic simulation. It is, however, beyond the scope of this thesis.

Therefore, it was concluded that the change in the conformational characteristics produced by interactions that sensitive to the dielectric constant may be responsible, at least in part, for the differences in the dimensions of the PVP chains obtained by evaluation of viscosity measurement in different solvents.

Table 4.7 Experimental values of the chain dimensions of PVP extrapolated to unperturbed dimensions from viscosity and osmotic measurements performed in several solvents at 25°C. (Saiz, 1993)

Solvent	$C_n = \langle r^2 \rangle_0 / nl^2$
2-Propanol ($\epsilon=18.3$)	10.0
Chloroform ($\epsilon=4.8$)	6.4
Water ($\epsilon=78.5$)	5.5

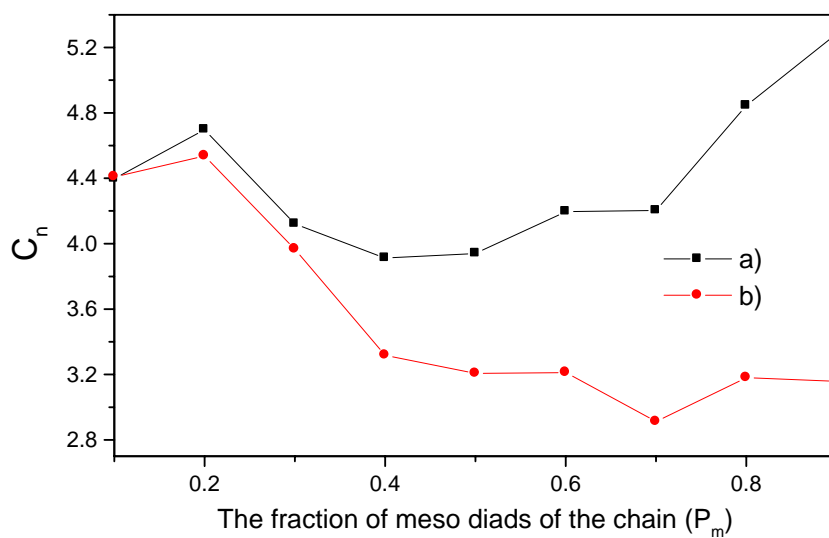
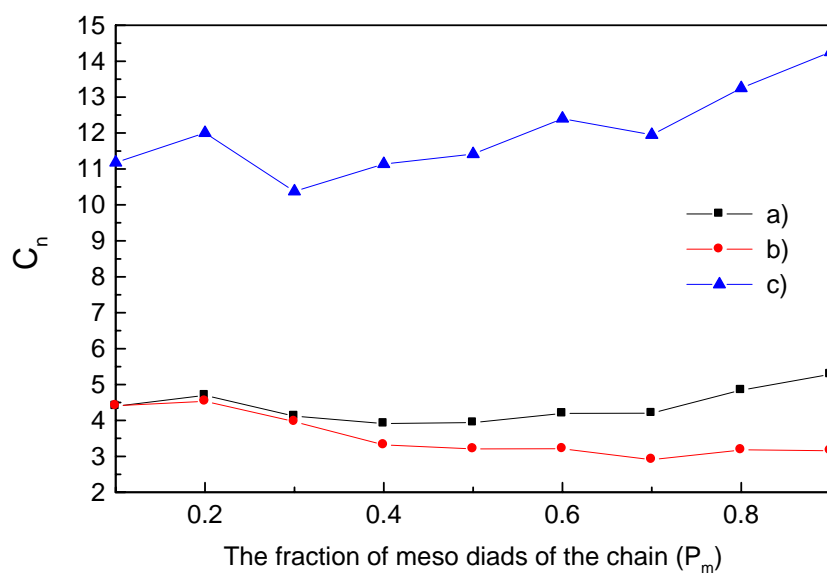


Figure 4.14 Limiting value of the characteristic ratio of the fraction of *meso* diads of the chain. Calculation was performed at 25°C using the conformational parameters computed with three different values of the dielectric constant of solvent, $\epsilon = 78, 4$ and ∞ in line a, b and c, respectively.

4.1.3 Conformational Energy of PEO by *Semi-empirical Quantum Chemistry Calculation*

RIS model was employed to predict the conformational dependent properties of PEO using statistical weight matrices as the input. The elements of these matrices were estimated from the conformational energy map for small representative segment of polymer molecules using PM3 technique. Model of PEO chain was represented by four skeletal bonds or pairs of dihedral angles (ϕ_i, ϕ_j) (Abe, 1998). To find the minimized structure, the PM3 method was adopted with the search algorithm provided by HyperChem version7 software. The conformational energies were obtained by rotating the dihedral angles and the optimized structure should be corresponded to the energy minimum structure for each pair of dihedral angles. An increment of dihedral angles (ϕ_i, ϕ_j) was set to 20° (rotation from 0° to 360°). Model of PEO used in the computation was defined by three short segments according to each skeleton bond as : C-C (Figure 4.15), C-O (Figure 4.16) and O-C (Figure 4.17) bond, respectively.

Calculation was carried out for energies $E(\phi_{OC}, \phi_{CC})$, $E(\phi_{CC}, \phi_{CO})$ and $E(\phi_{CO}, \phi_{OC})$ taken at 20° intervals. All regions for which $E \leq 5$ kcal/mol (12.6 kJ/mol) relative to the *tt* minimum were included. The model assumes three discrete states: *trans*, *gauche*⁺ and *gauche*⁻, abbreviated as *t*, *g*⁺ and *g*⁻. The nine pair-wise (*tt*, *tg*⁺, *tg*⁻, *g*⁺*t*, *g*⁻*t*, *g*⁺*g*⁺, *g*⁻*g*⁺, *g*⁺*g*⁻, *g*⁻*g*⁻) dependent rotational isomeric states and conformational energy contour maps for each bond pair of PEO model are plotted in Figures 4.18a/4.18b, 4.19a/4.19b and 4.20a/4.20b, respectively. The positions and magnitudes of the energy minima on the resulting energy-contour maps yield the values of the preferred rotational angles and their associated statistical-weights for

each two-bond sequence. The conformational properties for the whole polymer chain can then be calculated from the properties of individual two-bond sequences using matrix multiplication technique.

4.1.3.1 Statistical Weight Matrices of PEO by *Semi-empirical*

Quantum Chemistry Calculation

The conformational partition function z , average energies $\langle E \rangle$, and average rotation angles $\langle \phi \rangle$ were estimated for the nine nonequivalent states. The results are summarized in Table 4.8. The RIS model for poly(A-A-B) chains, in which all bonds are subject to a symmetric 3-fold torsion potential with the nearest neighbor interdependent, is given by the following three statistical weight matrices for three successive bond of type A-A, A-B and B-A. For example, statistical weight parameters of CC bond are given in the form of following equations (3.1) and (3.2)

The statistical weights of PEO are calculated for the conformational energies from PM3 calculation and grouped into the matrix. The statistical weight matrices at $T = 298$ K of C-O-C-C-O (O-C, C-C), O-C-C-O-C (C-C, C-O) and C-C-O-C-C (C-O, O-C) bond pairs are as Eq.4.5. Some calculated values from these RIS parameters such as $\langle \mu^2 \rangle_o / nm^2$, C_n , f_t^{CC} and f_t^{CO} 2.08, 0.19 and 0.63, respectively. In general, these predicted values are seen to differ from experimental ones. For example, value from intrinsic viscosity experiment is 5.2 which gives large difference from RIS prediction based on PM3 method. Thus, we employ more accurate method using *ab initio* calculation in order to get better RIS parameters so that the predicted values of conformational dependent properties possibly be closer to the experimental results.

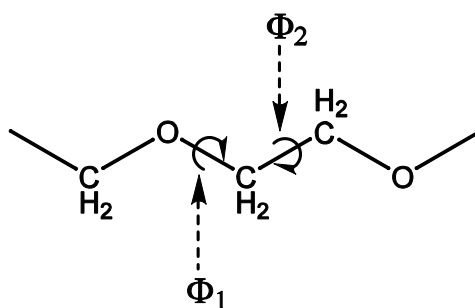


Figure 4.15 Schematic representation of PEO model with O-C and C-C (ϕ_1 , ϕ_2) bond pair

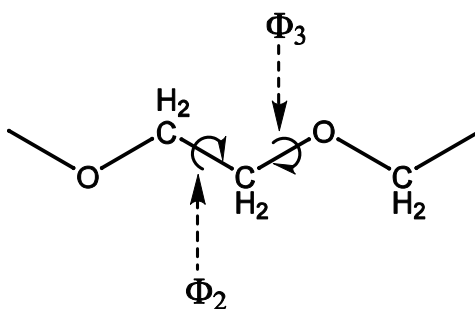


Figure 4.16 Schematic representation of PEO model with C-C and C-O (ϕ_2 , ϕ_3) bond pair

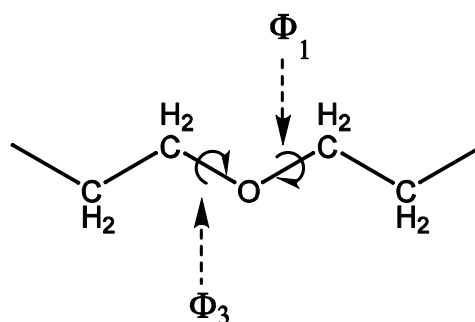


Figure 4.17 Schematic representation of PEO model with C-O and O-C (ϕ_3 , ϕ_1) bond pair

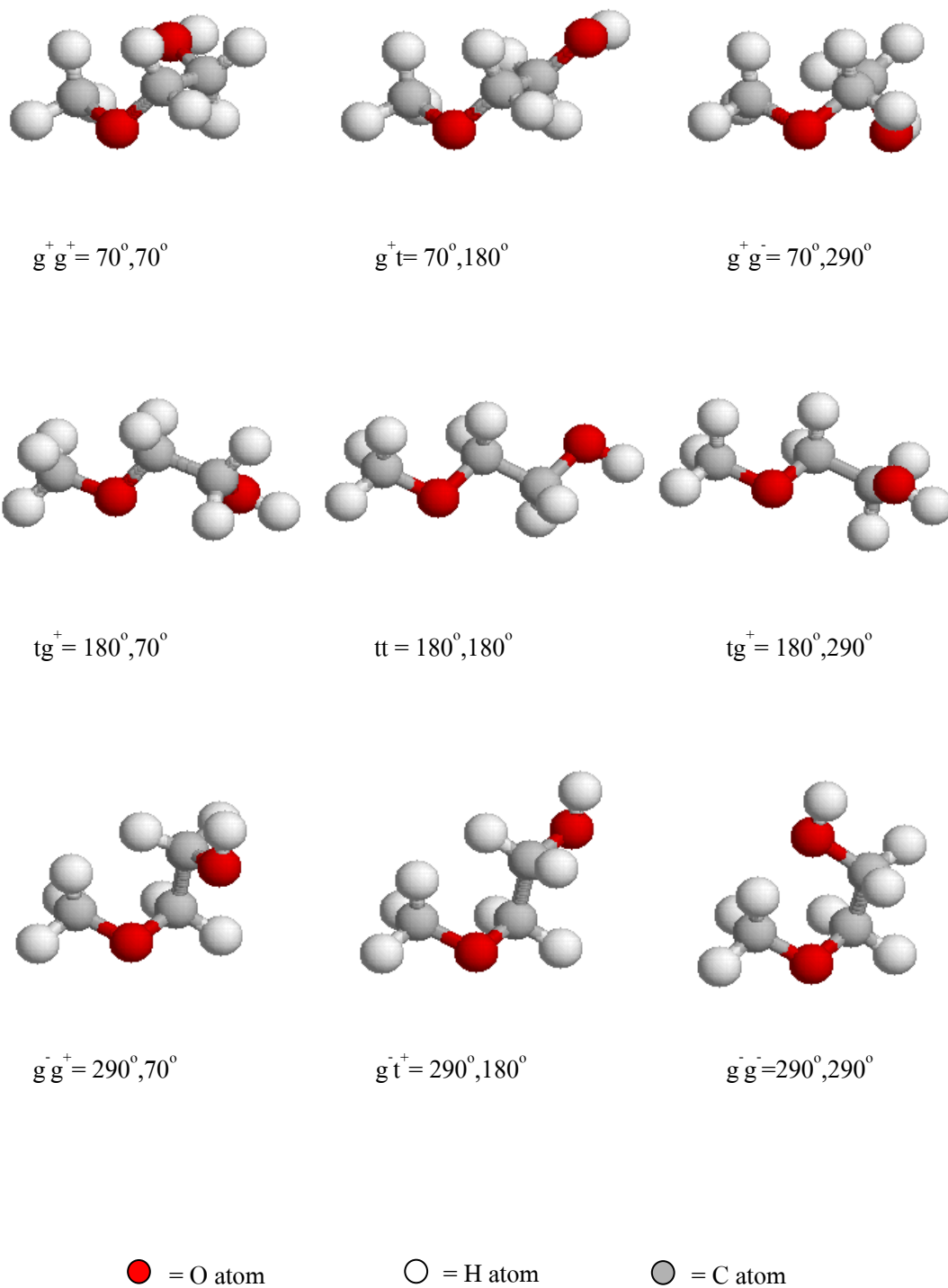


Figure 4.18a The nine pair-wise dependent rotational isomeric states of the optimized PEO model with O-C and C-C (ϕ_1, ϕ_2) bond pair

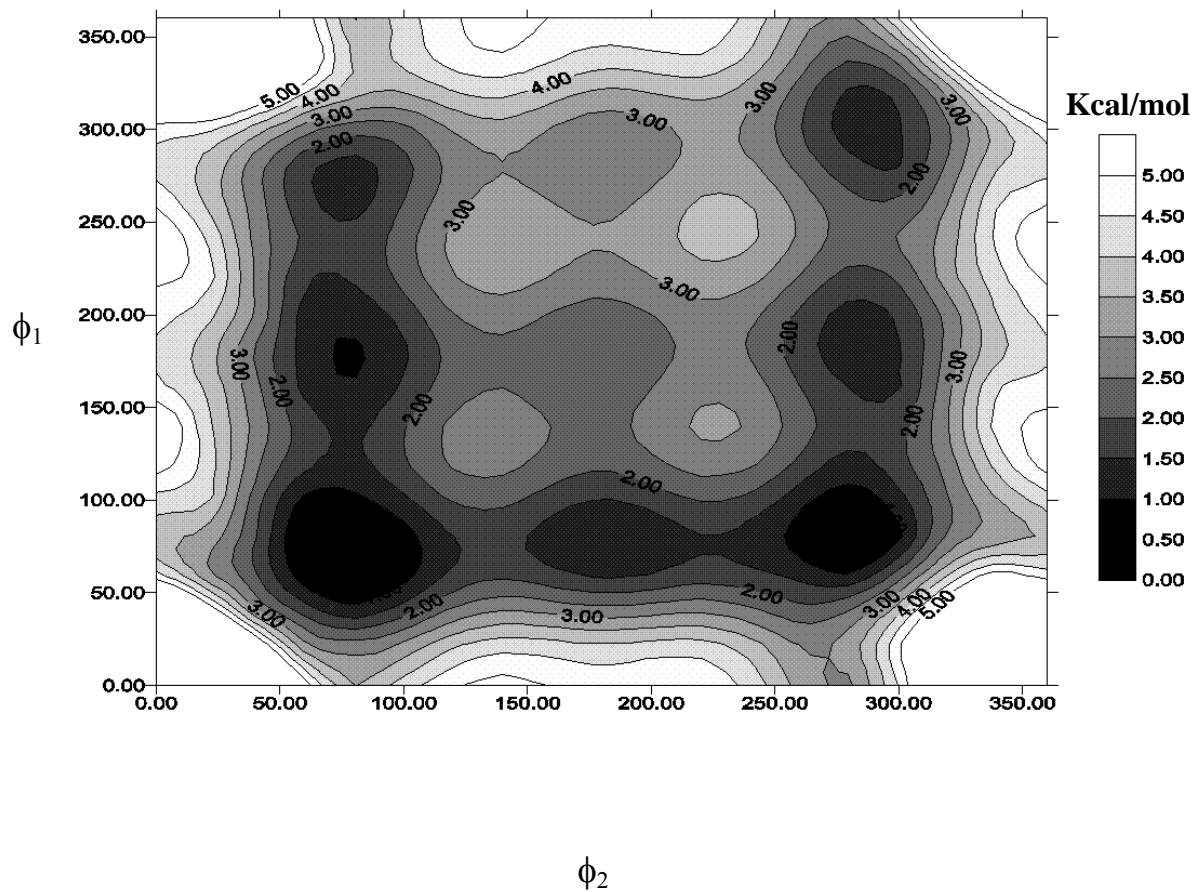


Figure 4.18b The conformational energy contour map (kcal/mol) for the optimized

PEO (C-O-C-C-O) model with O-C and C-C (ϕ_1, ϕ_2) bond pair

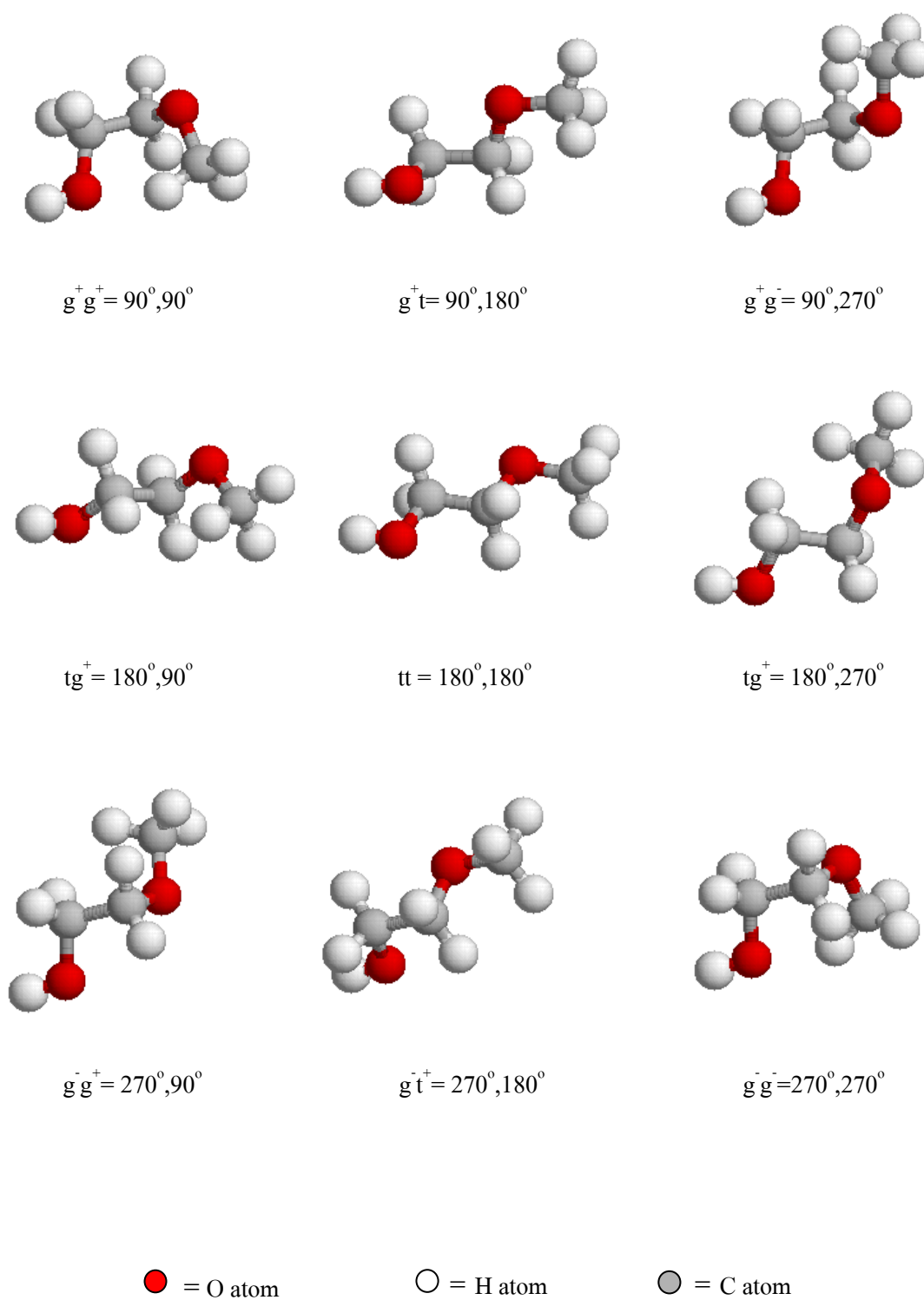


Figure 4.19a The nine pair-wise dependent rotational isomeric states of the optimized PEO (O-C-C-O-C) model with C-C and C-O (ϕ_2, ϕ_3) bond pair.

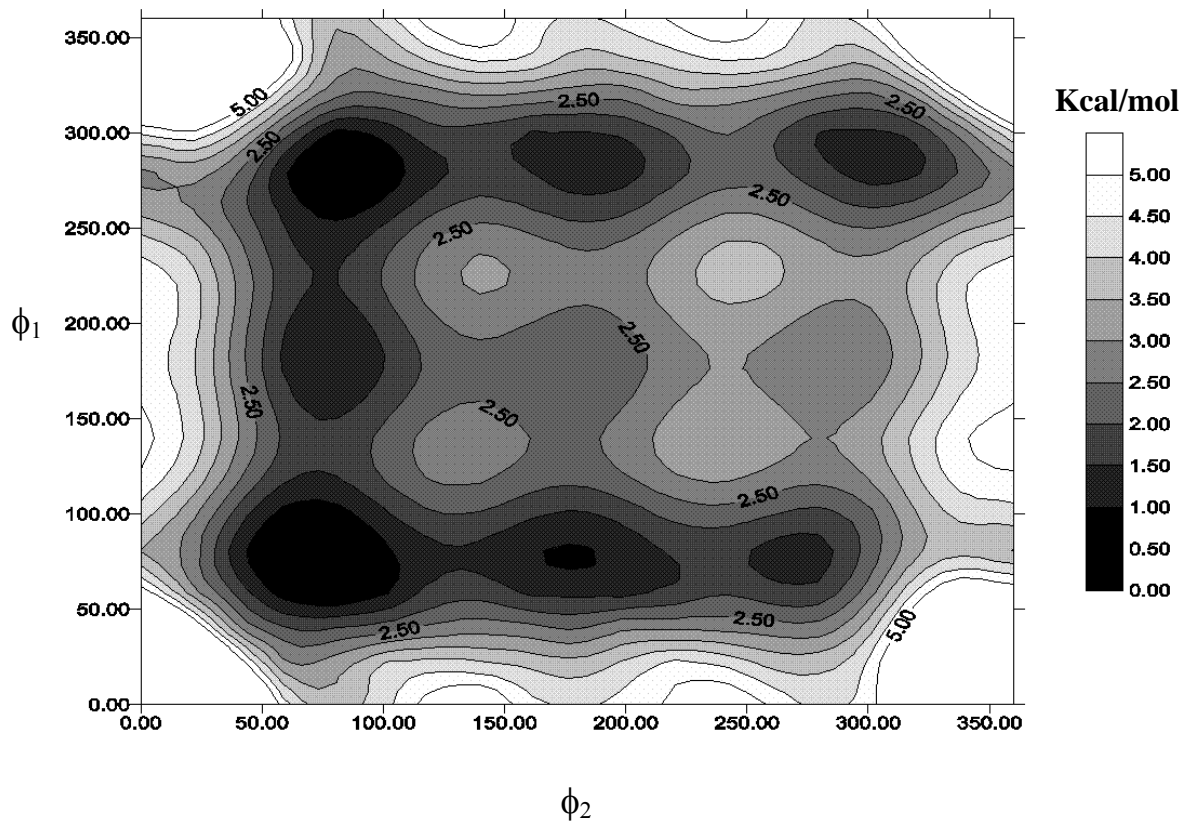


Figure 19b The conformational energy contour map (kcal/mol) for the optimized PEO (O-C-C-O-C) model with C-C and C-O (ϕ_2, ϕ_3) bond pair

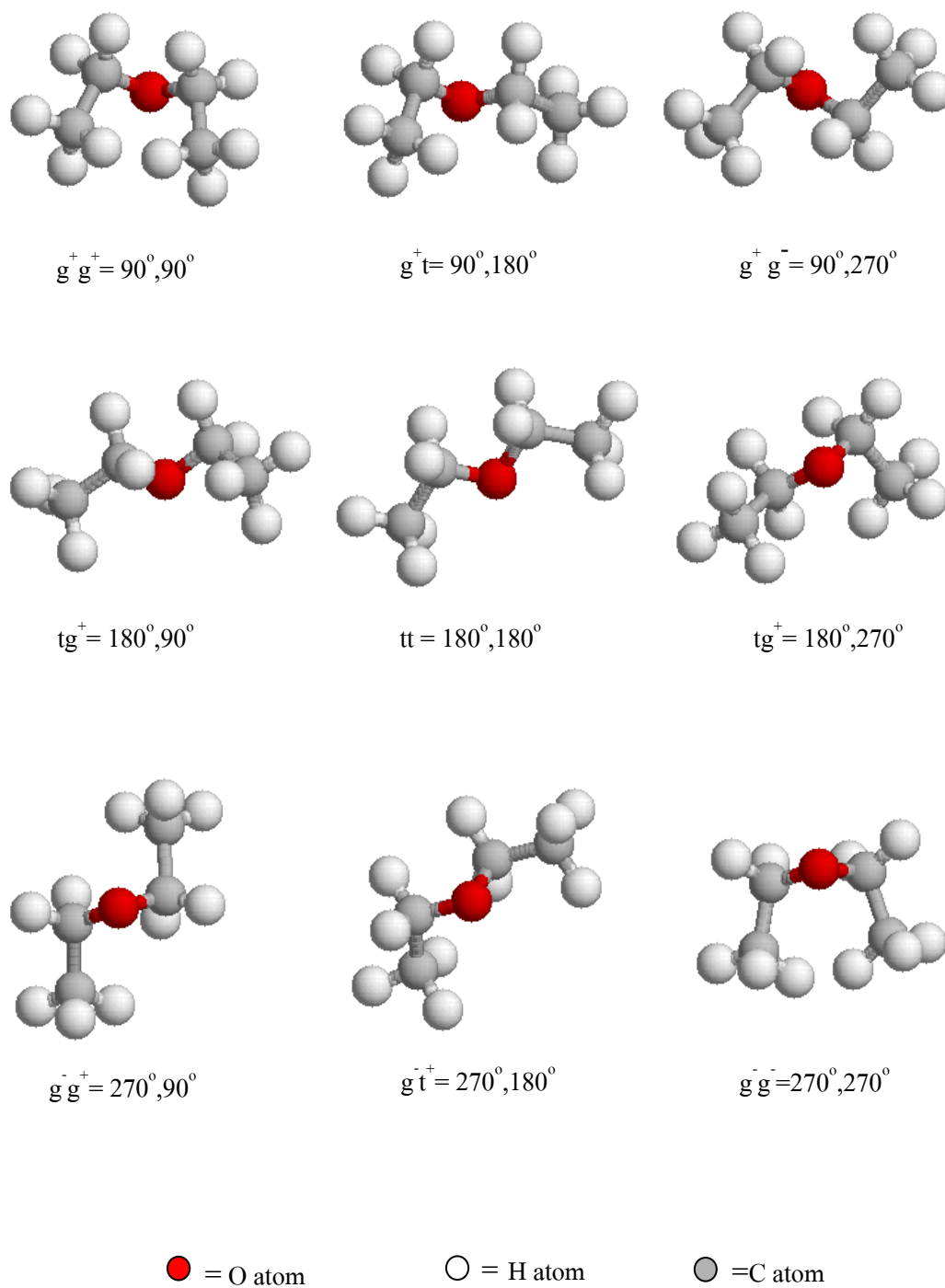


Figure 4.20a The nine pair-wise dependent rotational isomeric states of the optimized PEO (C-C-O-C-C) model with C-O and O-C (ϕ_3, ϕ_1) bond pair

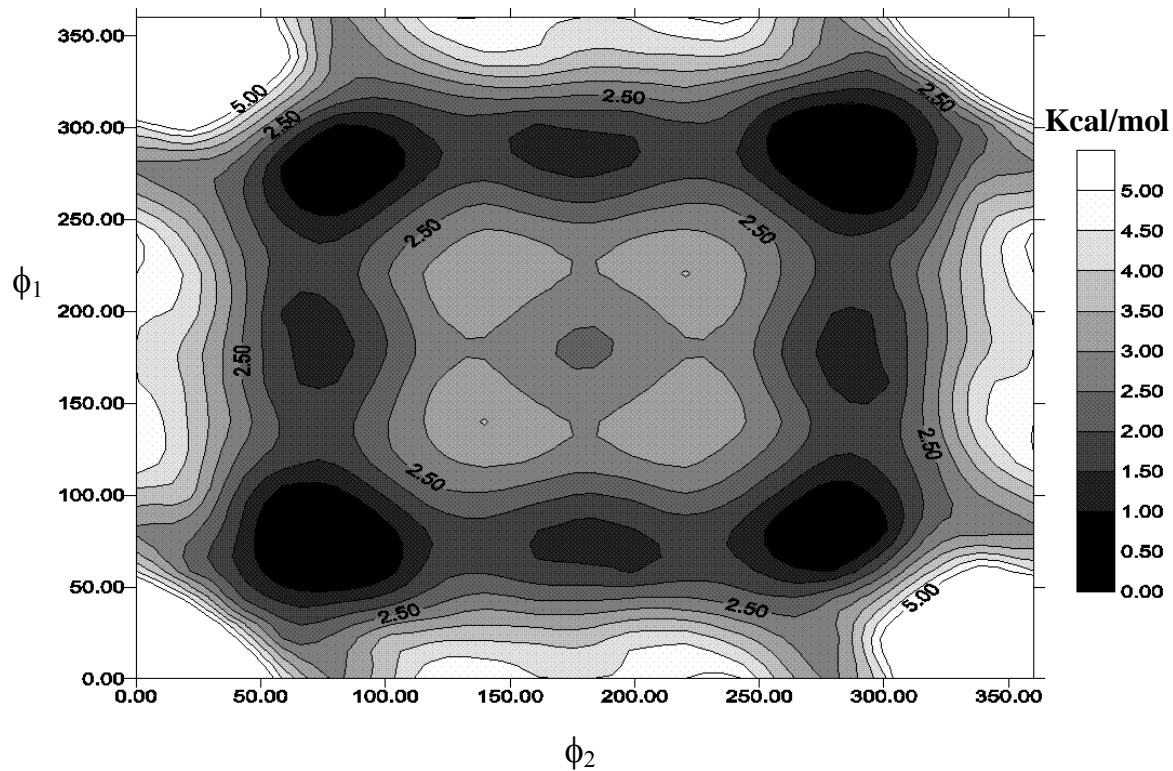


Figure 4.20b The conformational energy contour map (kcal/mol) for the optimized PEO (C-C-O-C-C) model with C-O and O-C (ϕ_3, ϕ_1) bond pair

Table 4.8 Conformational characteristics of PEO model compound as estimated from the semi-empirical PM3 potential energy (kcal/mol) contour map at 298K

Rotational State	C-O-C-C-O				O-C-C-O-C				C-C-O-C-C			
	Z	<E>	< ϕ_1 >	< ϕ_2 >	Z	<E>	< ϕ_2 >	< ϕ_3 >	Z	<E>	< ϕ_3 >	< ϕ_1 >
<i>tt</i>	0.43	2.51	184.3	179.8	0.43	2.51	179.8	184.3	0.25	2.89	189.2	189.2
<i>tg⁺</i>	1.58	1.54	190.7	79.5	1.72	1.46	183.8	78.1	1.11	1.75	191.8	74.6
<i>tg⁻</i>	0.14	3.03	188.9	288.8	1.02	1.68	181.9	285.5	1.05	1.72	187.2	287.6
<i>g⁺t</i>	1.72	1.46	78.1	183.8	1.58	1.54	79.5	190.7	1.11	1.75	74.5	191.8
<i>g⁻t</i>	1.02	1.67	285.3	181.9	1.34	3.00	287.9	188.7	1.04	1.72	287.4	187.2
<i>g⁺g⁻</i>	0.55	1.77	78.6	275.7	2.75	0.70	84.5	280.1	2.89	0.69	83.3	279.9
<i>g⁺g⁺</i>	4.06	0.74	78.4	75.7	4.06	0.74	75.7	78.4	4.58	0.64	75.4	75.4
<i>g⁻g⁺</i>	2.71	0.69	279.7	84.3	0.55	1.76	275.2	78.6	2.83	0.68	279.4	83.2
<i>g⁻g⁻</i>	0.76	1.74	287.4	299.8	0.75	1.72	298.8	287.8	4.30	0.55	286.1	286.4

$$\begin{aligned}
 U_{oc-cc} &= \begin{matrix} & g^+ & t & g^- \\ \begin{matrix} g^+ \\ t \\ g^- \end{matrix} & \begin{pmatrix} 0.74 & 1.46 & 1.77 \\ 1.54 & 2.51 & 3.03 \\ 0.69 & 1.67 & 1.74 \end{pmatrix} \end{matrix} \\
 & \hspace{25em} (4.5) \\
 U_{co-oc} &= \begin{matrix} & g^+ & t & g^- \\ \begin{matrix} g^+ \\ t \\ g^- \end{matrix} & \begin{pmatrix} 0.74 & 1.54 & 0.70 \\ 1.46 & 2.51 & 1.68 \\ 1.76 & 3.00 & 1.72 \end{pmatrix} \end{matrix}
 \end{aligned}$$

$$U_{cc-co} = \begin{matrix} & g^+ & t & g^- \\ \begin{matrix} g^+ \\ t \\ g^- \end{matrix} & \begin{pmatrix} 0.64 & 1.75 & 0.69 \\ 1.75 & 2.89 & 1.72 \\ 0.68 & 1.72 & 0.55 \end{pmatrix} & & \end{matrix} \quad (4.5)$$

4.1.3.2 Conformational Energy of PEO by *ab initio* Quantum Chemistry Calculation

For many molecules, *ab initio* electronic structure calculations have been shown to accurately predict conformational energies provided adequate atomic orbital basis sets are used. Furthermore, the errors occurred by using smaller basis sets and by neglecting of electron correlation effects are well understood. In this present study complete optimization of conformational geometries at the SCF level of theory was performed using the *ab initio* electronic structure calculation and additional single-point energy were calculated using GAUSSIAN98w. For the study of energy difference between the *tgt* and *ttt* conformers, geometry optimization was carried out at the MP2 level. Most of the HF-SCF calculations were carried out on a PC (Pentium IV, CPU 3.2 GHz, RAM 1GB).

Calculations were carried out using atomic orbital basis sets comprised of linear combinations of GAUSSIAN-type functions. The basis sets in this study (6-311G and D95) are split valence (with three functions for the valence orbitals) and *double- ζ* , respectively. The basis sets can be further augmented by including a set of diffuse *sp* functions, denoted by “+”. An additional set of diffuse *sp* functions yields a “+(+)” basis sets. Diffuse functions are important for polar molecules and for systems in which a large portion of the valence-electron density is allocated to lone-

pair orbitals. For basis sets with polarization function, the notation “**” indicates a set of d functions for the heavy atom and p functions for the hydrogen atoms. A single “*” denotes carbon and oxygen d functions without the hydrogen p function. Standard GAUSSIAN98 exponents were used for the polarization functions. Note that different polarization function exponents are used for the D95 and 6-311G basis sets. Generally, Hartree-Fock or self-consistent-field (SCF) calculations do not include contribution from electron correlation. For conformational energy studies, the most important contributor to electron correlation effects is the dispersion energy which can be accounted for adequately through use of second-order Møller-Plesset perturbation theory (MP2). (Tsuzuki *et al.*, 1993; Jaffe *et al.*, 1993)

In this section, 1,2-dimethoxyethane (DME) was selected as a model molecule for understanding the conformations of Poly(ethyleneoxide) (PEO). (Tsuzuki *et al.*, 1993; Jaffe *et al.*, 1993) It has long been established that PEO chains have a large fraction of bond in *gauche* effect. In ethers and polyether, this is usually referred to as the oxygen *gauche* effect. We use DME to represent PEO because it is a small molecule and can mimic most of the interaction that influences on PEO conformation. Also, these considerations warrant reduction of the general expressions the statistical weights of DME molecule in equivalent to PEO as follows: (Flory, 1953)

$$U_a = \begin{bmatrix} 1 & \sigma & \sigma \\ 1 & \sigma & \sigma\omega \\ 1 & \sigma\omega & \sigma \end{bmatrix} \quad U_b = \begin{bmatrix} 1 & \sigma & \sigma \\ 1 & \sigma & 0 \\ 1 & 0 & \sigma \end{bmatrix} \quad U_c = \begin{bmatrix} 1 & \rho & \rho \\ 1 & \rho & \rho\omega \\ 1 & \rho\omega & \rho \end{bmatrix} \quad (4.5)$$

where,

$$\begin{aligned}\sigma &= 0.99\exp(-E_{\sigma}/RT) \\ \rho &= 0.61\exp(-E_{\rho}/RT) \\ \omega &= 0.88\exp(-E_{\omega}/RT)\end{aligned}\tag{4.6}$$

Where the numerical values of the pre-exponential factors are those estimated by the energy calculation in previous section (PM3 method).

Means-square chain dimensions and dipole moments can be calculated according to this scheme using the geometrical parameters given in Table 4.13 and a value of 0.99D for C-O bond dipole moment. Initial calculation suggests that the dimensions turn out to be sensitive to the values of ρ but comparatively insensitive to σ . The dipole moment is nearly 20 time more sensitive than $\langle r^2 \rangle_0$ to σ . Simultaneous agreement with the temperature coefficient of $\langle r^2 \rangle_0$ of and with its characteristic ratio requires $\omega > 0$. Values of the parameters derived from *ab initio* QM calculation should obey this trend in order to meet result from experiment.

4.1.3.2.1 Effect of Basis set and Electron Correlation

Conformational Energies.

The effect of basis set and electron correlation on the energy of *tgt* conformer of DME relative to *ttt* conformer were investigated as follows. First, molecular geometries of the *tgt* and *ttt* conformers of DME were optimized at the HF level for various basis sets. Then, these optimized geometries were used in single-point energy calculations at both HF and MP2 for various basis sets considered. These basis sets, along with calculated HF and MP2 energies, are given in Table 4.9.

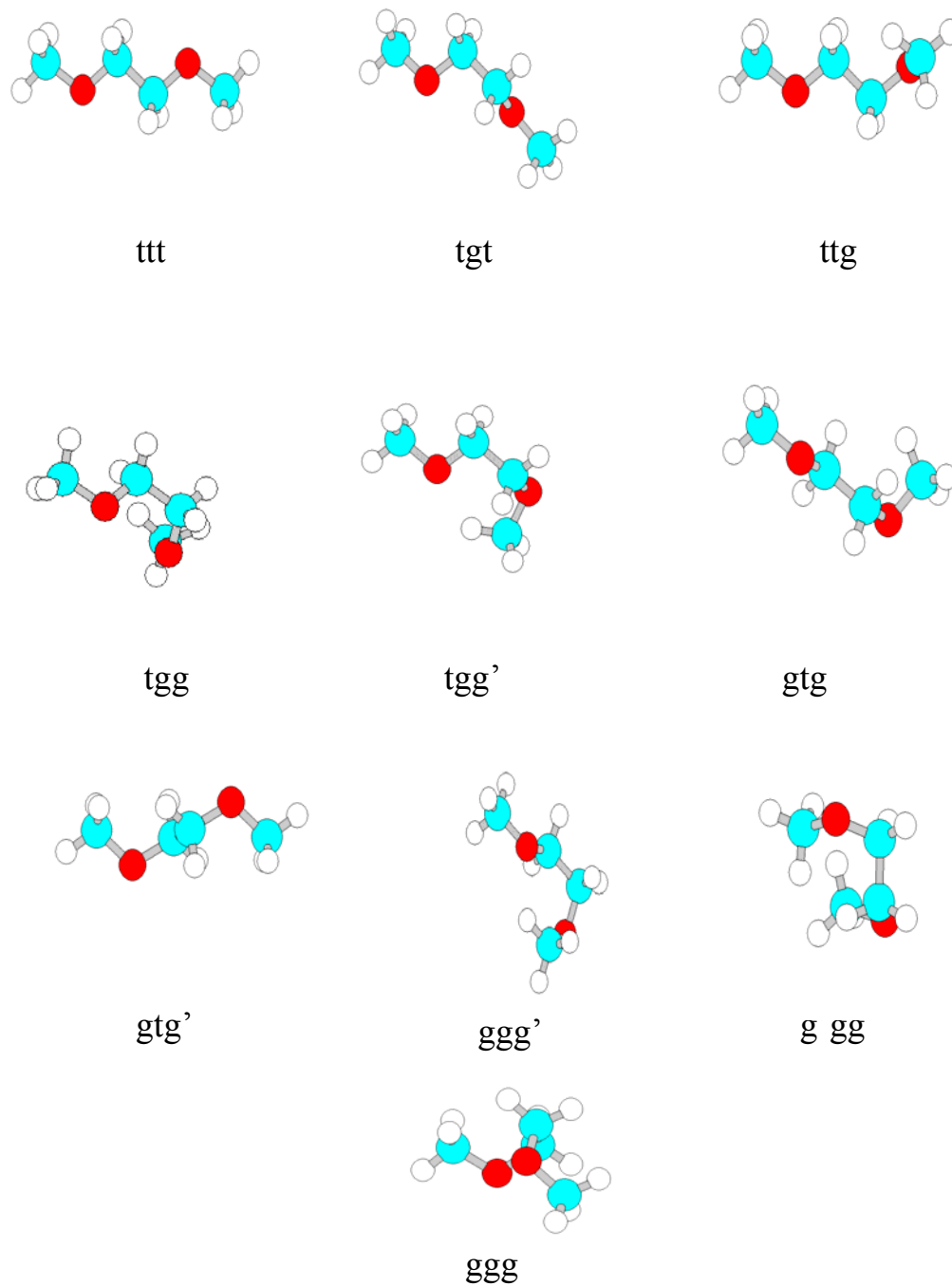


Figure 4.21 Representative conformations of DME. Torsional states are denoted by t for *trans*, g for *gauche* (of either sign), g^+ for a *gauche* of positive right-hand rotation with respect to *trans*, and g^- for a state with the opposite rotation

Table 4.9 Energies of *tgt* rotamer of 1,2-Dimethoxyethane relative to those of *ttt* rotamer, calculated by the ab initio method^a

Basis set	ΔHF	ΔMP2	ΔB3LYP
6-31G*	1.40	0.60	0.52
6-31+G*	1.40	0.41	0.64
6-311+G*	1.26	0.28	0.71
6-311++G*	1.24	0.23	0.54
D95**	1.30	0.83	NA
D95+(2df,p)	0.96	NA	NA

^a Energies in kcal/mol.

NA = not available

The *tgt* rotamer was calculated to be 1.24-1.40 kcal/mol less stable than the *ttt* rotamer at HF levels. The MP2 levels electron correlation energy correction (MP2) decreased the energy difference to 0.23-0.83 kcal/mol. The MP2 relative energies was generally smaller than the corresponding B3LYP relative energies. The calculated energy differences with electron correlation correction were decreased by using a larger basis set. The effect of including *sp* diffuse function in the atomic orbital representation of the carbon and oxygen atoms were explored by comparing energies from the 6-31G* basis set with those from 6-311+G* basis set. Examination of Table 4.9 revealed that the *gauche* energy was reduced to a greater or lesser degree by inclusion of these additional polarization functions, depending upon the particular basis set.

The effect of basis set size on *gauche* energy may indicate a possible origin of the *gauche* conformation in DME. If the *gauche* energy was considered to be due to

an intrinsic torsional energy difference plus differences in non-bonded interactions between atoms in the *gauche* and *trans* conformations of the O-C-C-O bond, it was expected the *gauche* conformation to be high in energy due to stronger electrostatic repulsion between the negatively charged oxygen atoms. However, the withdrawal of charge from carbon atoms, which is facilitated by the use of larger basis sets, may counteract this increase in coulombic repulsion by changing the intrinsic torsional energy difference between the two conformations. The difference in intrinsic torsional energy may be due to differential stabilization of the O-C-C-H conformations, where bond-antibond orbital interactions favor the *trans* arrangement and hence a O-C-C-O *gauche* arrangement. The uncertainty in the conformational energies, arising from sources such as basis set superposition (which is conformation dependent), basis set incompleteness, use of conformational geometries is obtained at the SCF level with a smaller basis set. Given this uncertainty, the smallest of the three basis sets listed above, D95**, appears adequate and is used exclusively in further analysis of DME conformer energies described below.

Conformer Populations

The ten unique low-energy conformers of DME are listed in Table 4.10. Optimized geometries for the conformations were determined at the SCF level employing the D95** basis set. The optimized torsional angles for the three torsions defining each conformation are shown in Table 4.10. Also given are the SCF and MP2 single-point energies (using the SCF optimized geometries) for each conformer relative to the *ttt* conformer. The conformational energies were calculated using both 6-311+G* and D95** basis sets with the 6-311+G* HF optimized geometries. Comparing HF and MP2 results, it is apparent that inclusion of electron correlation

significantly reduces the energy of all conformations relative to the *ttt* conformer for both basis sets.

The *ggg* and *ggg'* conformers exhibit the largest differential correlation energy effect, and the *ttg* conformer has the smallest. In going from the smaller to the larger basis set, the relative energy of the *tgt* conformer is most significantly affected. The energies of conformers from Table 4.10 (at MP2/D95**) are significantly different from those predicted by simply adding the appropriate C-C and C-O *gauche* energies. The *ggg* and *ggg'* conformers are lower in energy than expected from this additive approach. On the other hand, the energy of the *tgg'* conformer is only 0.24 kcal/mol higher than *ttt* conformer. It appears that the lower energies of these four conformers are due to a favorable electrostatic interaction between one of the oxygen atoms and opposite terminal CH₃ group. This is illustrated in Figure 4.23 for the *tgg'* conformer, where the O...C (methyl) and O...H (methyl) separation are 3.15 and 2.57 Å, respectively. These are greater distances than found in typical intramolecular hydrogen bonds but are considerably shorter than seen for other conformers (e.g., 4.70 and 4.90 Å for the *ttt* conformer and 4.14 and 4.25 Å for the *tgt* conformer for the O...C(methyl) and O...H(methyl) separations, respectively).

4.1.3.2.2 Statistical Weight Matrices of PEO by *ab initio*

Electronic Calculation

Statistical weights (Boltzmann populations) of each conformer are readily calculated based on the relative electronic energy and degeneracy of each conformation. To elucidate conformational energies from statistical weight matrix, the same prescriptions are adopted for the statistical weight parameters. Our *ab initio* calculation yield energetics relative to the *ttt* conformer and the *tgg* and *tgg'* energies

are relative to the *tgt* energies. The *tgg'* state is much more favorable and is indicated by the RIS model and thereby accounting for our prediction of a relatively high population of *tgg* + *tgg'* states. A similar effect was seen in the molecular mechanics investigation of 1,2-diethoxyethane by Jaffe *et al.*, 1993. The *tgg'* conformer appears to be the results of strong attractive interactions between an O atom and a hydrogen on the opposite methyl groups, as illustrated in Figure 4.23.

Table 4.10 DME conformer geometries energies.

Conformation (degeneracy)	ϕ_1^a	ϕ_2^a	ϕ_3^a	$\Delta 6-311+G^*$		$\Delta D95^{**}$	
				HF	MP2	HF	MP2
<i>ttt</i>	179.9	-179.9	-180.0	0.00	0.00	0.00	0.00
<i>tgt</i>	-174.8	-174.7	73.4	1.26	0.29	1.30	0.75
<i>ttg</i>	-178.2	89.7	179.5	2.08	1.67	1.89	1.24
<i>tgg</i>	-178.3	80.0	66.0	3.34	1.96	3.13	1.77
<i>tgg'</i>	-177.9	-91.1	71.5	1.78	0.28	1.63	0.24
<i>gtg</i>	90.1	90.1	178.2	4.30	3.48	3.52	2.90
<i>gtg'</i>	88.9	-89.0	178.0	4.09	3.37	3.10	2.61
<i>ggg'</i>	85.2	-82.4	72.7	4.13	2.10	3.52	1.68
<i>g'gg'</i>	-90.2	-178.2	-90.1	4.31	3.48	3.84	2.53
<i>ggg</i>	63.8	63.8	48.2	4.26	1.68	3.85	1.69

^aTorsional angles for the C-O, C-C and O-C bonds, in deg, with *trans* defined as 180°

^b Δ indicated energy relative to the *ttt* state, in kcal/mol

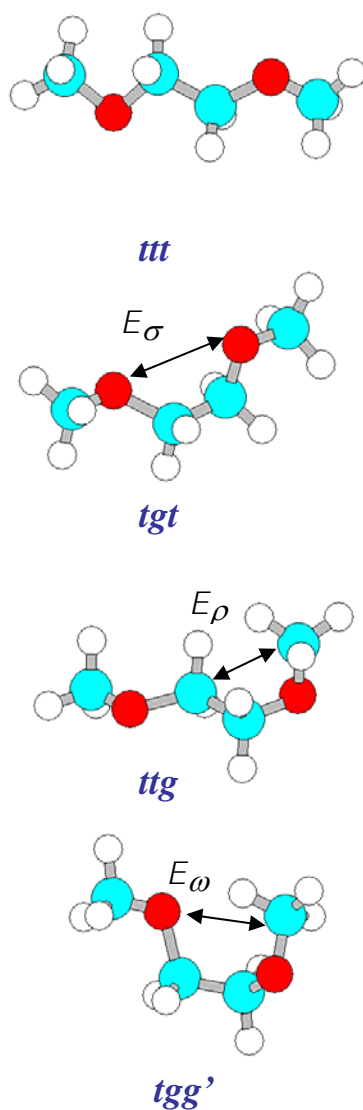


Figure 4.22 The conformation dependent first-order and second-order interaction between atoms and groups in DME (Jaffe *et al.*, 1993)

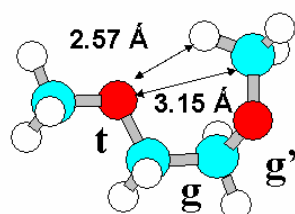


Figure 4.23 The *tgg'* conformation of DME. The close approach between an oxygen and a methyl hydrogen is indicated (Jaffe *et al.*, 1993)

One may introduce the effect of the O...H attractions in the second-order RIS model by changing the second-order interaction parameter E_ω . The second-order model takes into account interactions between atoms or groups separated by a maximum of four bonds and hence two consecutive torsions. Using values of $E_\sigma = -200$, $E_\rho = 1400$ and $E_\omega = -825$ cal/mol and $E_\sigma = 230$, $E_\rho = 1750$ and $E_\omega = -1680$ cal/mol, for example, one can represent the energies of eight of the ten DME conformers, including *tg*g' reasonably well as indicated in Table 4.11. The *ggg* conformer cannot be successfully described by the present second-order RIS model as indicated in Table 4.11, due probably to attractive interactions between the oxygen lone pair electrons and methyl hydrogen atoms and alleviation of repulsive lone pair interactions. These considerations point to the necessity of including the interactions between atom and groups separated by five bonds and hence three consecutive torsions into the RIS model. Such a third-order RIS model is beyond the scope of this thesis and will not be presented here.

4.1.3.3 Conformational Dependent Properties of PEO

The RIS model is excellent for the rapid analysis of conformation-dependent properties of chain molecules in their 'unperturbed' state. The most frequently calculated property is the mean square unperturbed end-to-end distance, $\langle r^2 \rangle / nl^2$ (subscript zero designates the unperturbed state or θ point). The other property susceptible to rapid computation include the mean-square dipole moment, $\langle \mu^2 \rangle / nm^2$. The viscosity of dilute polymer solution in θ condition can be estimated from $\langle r^2 \rangle / nl^2$ via the equivalent sphere model for hydrodynamic properties.

Table 4.11 RIS model of PEO from *ab initio* calculation of DME model compound

Conformer	RIS	MP2	MP2	RIS	RIS
	Representation	6-311+G*	D95**	Energy ^a	Energy ^b
<i>ttt</i>	0	0.00	0.00	0.00	0.00
<i>tgt</i>	E_{σ}	0.29	0.75	-0.20	0.23
<i>ttg</i>	E_{ρ}	1.67	1.24	1.40	1.75
<i>tgg</i>	$E_{\sigma} + E_{\rho}$	1.96	1.77	1.20	1.98
<i>tgg'</i>	$E_{\sigma} + E_{\rho} + E_{\omega}$	0.28	0.24	0.38	0.30
<i>gtg</i>	$2E_{\rho}$	3.48	2.90	2.80	3.50
<i>gtg'</i>	$2E_r$	3.37	2.61	2.80	3.50
<i>ggg'</i>	$E_{\sigma} + 2E_{\rho} + E_{\omega}$	2.10	1.68	1.78	2.05
<i>g'gg'</i>	$E_{\sigma} + 2E_{\rho} + 2E_{\omega}$	3.48	2.53	0.95	0.37
<i>ggg</i>	$E_{\sigma} + 2E_{\rho}$	1.68	1.69	2.60	3.73

^aParameter set 3 are $E_{\sigma} = -200$, $E_{\rho} = 1400$ and $E_{\omega} = -825$ cal/mol.

^bParameter set 4 are $E_{\sigma} = 230$, $E_{\rho} = 1750$ and $E_{\omega} = -1680$ cal/mol.

The analysis in this thesis was mainly focus on the conformation-dependent properties of the polymer chain such as the $\langle r^2 \rangle / nl^2$, $\langle \mu^2 \rangle / nm^2$ and their temperature coefficients. Calculation was carried out according to a conventional method. Also examined in detail is the conformation of DME, for which the conformer fractions

have been estimated in solution as well as in the gas phase by the NMR technique. Reliable experimental data are available for all of these properties in the literature.

As indicated in Table 4.12, the magnitude of E_ρ adopted by various investigators mostly falls in a range 1.2 ± 0.4 kcal mol⁻¹. Values of the other two conformational energy parameters, i.e. E_σ and E_ω were treated as variables. We first tried to find combinations of these parameters which reproduce experimental values of characteristic ratio $\langle r^2 \rangle_o / nl^2 = 5.2$ were tried to find. The results are illustrated in Figure 4.22, where the value of E_ω varies from -1.7 to 1.0 and E_σ from -0.5 to 0.8 kcal mol⁻¹. It is interesting to note here that these two parameters can be mutually adjusted over a wide range to reproduce the aforementioned experimental data. These results immediately suggest the reason why so many different RIS parameter sets have been proposed for the PEO chain. The E_ω and E_σ values used by various investigators can be accommodated in the figure, although not shown here for simplicity.

Next, we present an application of the RIS model is presented to estimate some conformational dependent properties and to compare with experimental results. Values of $\langle r^2 \rangle_o / nl^2$ and $\langle \mu^2 \rangle_o / nm^2$, were computed for PEO chain using the RIS model with geometrical parameters. The geometrical data adopted in this analysis are listed in Table 4.13. The statistical weight matrices used in this calculation are from Table 4.12. The calculated results are summarized in Table 4.14.

Table 4.12 Representative conformational energy parameter (first- and second-order) sets adopted for the comparison.

Parameter set	RIS energy parameters (kcal/mol)		
	E_ρ	E_σ	E_ω
1 ^a	0.80	-0.20	-0.50
2 ^a	1.10	-0.20	-0.66
3 ^a	1.40	-0.20	-0.82
4 ^b	1.75	2.30	-1.68
5 ^b	1.34	0.58	-1.65
6 ^c	0.9	-0.5	0.5
7 ^c	1.7	0.5	-1.7
8 ^c	1.2	-0.1	-0.2

^a Multiple linear regression from ten conformers of DME

^b Combination of E_σ and E_ω compatible with the experimental values of the unperturbed dimension ($\langle r^2 \rangle_0 / nl^2 = 5.2 \pm 0.2$).

^c Abe *et al.* (1998)

Table 4.13 Geometrical parameters used in the RIS calculation of conformation-dependent properties (Abe *et al.*, 1998)

l_{CC} (Å)	l_{CO} (Å)	CCO (degree)	COC (degree)	ϕ_{CC}^g (degree)	ϕ_{CO}^g (degree)
1.53	1.43	111.5	111.5	± 98.0	± 112.0

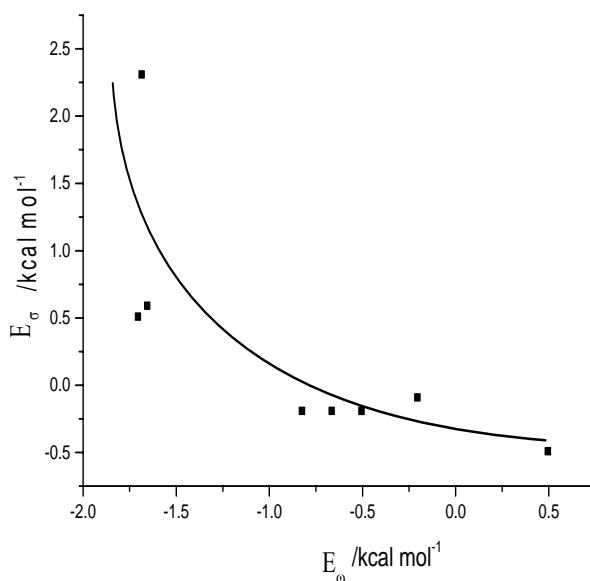


Figure 4.24 Pairs of E_σ and E_ω adjusted so as to reproduce the observed values of $\langle r^2 \rangle_o / nl^2 = 5.2$, E_ρ being set equal to $1.2 \text{ kcal mol}^{-1}$. Calculation were performed for temperature of 25°C

Comparison of conformational energy parameter sets proposed by various groups

Direct comparisons of conformation-dependent properties calculated using the energy parameters from different laboratories are presented in Figure 4.25-4.27. The values of E_ρ , E_σ and E_ω adopted in these calculation are reported in Table 4.14 and 4.15.

Figure 4.25 indicates variation of $\langle r^2 \rangle_o / nl^2$ as a function of temperature. Predicted values from parameter sets 1, 2 and 3 are closed to the experimental results. Similar plots for the dipole moment ratio $\langle \mu^2 \rangle_o / nm^2$ are shown in Figure 4.26. Although the temperature coefficients are all positive within a ranges of

$d \ln \langle \mu^2 \rangle_0 / nm^2 = 0.27-3.45 \times 10^{-3} \text{ K}^{-1}$, the values of $\langle \mu^2 \rangle_0 / nm^2$ are somewhat smaller than those observed except in the case of parameter set 6 (PM3 method).

In Figure 4.27, the fraction of *trans* conformation (f_t) around the central C-C bond of DME is plotted against temperature. For this compound, the f_t values have been estimated from the observed NMR vicinal coupling constant in solution as well as the gas phase. Experimental values determined in a nonpolar solvent (c-C₆H₁₂)_q and the gaseous state are also presented.

Table 4.14 Comparison of the calculation and observed values of some conformation-dependent properties of PEO

	$\langle r \rangle_0^2 / nl^2$	$\langle \mu \rangle_0^2 / nl^2$	$[d \ln \langle r \rangle_0^2 / dT]$	$[d \ln \langle \mu \rangle_0^2 / dT]$
	(273 K)	(273 K)	(10^{-3} K^{-1})	(10^{-3} K^{-1})
Observed*	5.2	0.53	0.23	2.6
PM3	2.08	0.54	0.17	0.27
Ab initio				
Parameter sets 1	5.2	0.27	0.26	1.46
Parameter sets 2	5.2	0.24	0.26	1.80
Parameter sets 3	5.2	0.24	0.26	1.98
Parameter sets 4	3.75	0.15	0.95	3.34
Parameter sets 5	3.57	0.51	1.27	3.45

Note : Observed*, D. R. Beech and C. Booth, *J. Polym. Sci., Part A-2*, 1969, **7**, 575. **Parameter set 1** are $E_\sigma = -200$, $E_\rho = 800$ and $E_\omega = -497$ cal/mol. **Parameter set 2** are $E_\sigma = -200$, $E_\rho = 1100$ and $E_\omega = -660$ cal/mol. **Parameter set 3** are $E_\sigma = -200$, $E_\rho = 1400$ and $E_\omega = -825$ cal/mol. **Parameter set 4** are $E_\sigma = 230$, $E_\rho = 1750$ and $E_\omega = -1680$ cal/mol. **Parameter set 5** are $E_\sigma = 580$, $E_\rho = 1340$ and $E_\omega = -1650$ cal/mol.

Parameter sets 4 and 5 predict f_t somewhat higher than experimental values while parameter 6 shows lower. The parameter sets 1, 2 and 3 predict f_t values within range covering experimental values from DME in solution to the gas phase.

4.1.3.4 NMR vicinal coupling constant and the RIS model of PEO

Experimental NMR vicinal coupling constants have been analyzed by utilizing a three-state (t, g, g') RIS model that takes into account the interactions between atoms or groups separated by up to four bonds and which depend upon the torsional states of the two intervening bonds. This RIS model was established by utilizing an *ab initio* QM method to calculate the energies of the low-energy conformations of DME. The first- and second-order RIS energy parameters E_σ , E_ρ and E_ω , illustrated in Figure 4.22, were initially determined so as to give best representation of the conformational energies.

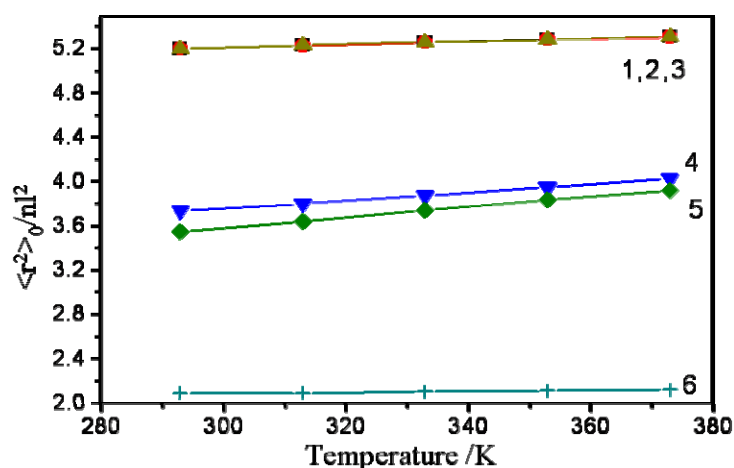


Figure 4.25 $\langle r^2 \rangle_0 / nl^2$ versus temperature for DME with $n=524288$ and $l^2 = 6.4307$

\AA^2 , Calculated using energy parameter sets assembled in Table 4.12.

The range of experimental value = 5.2 ± 0.2

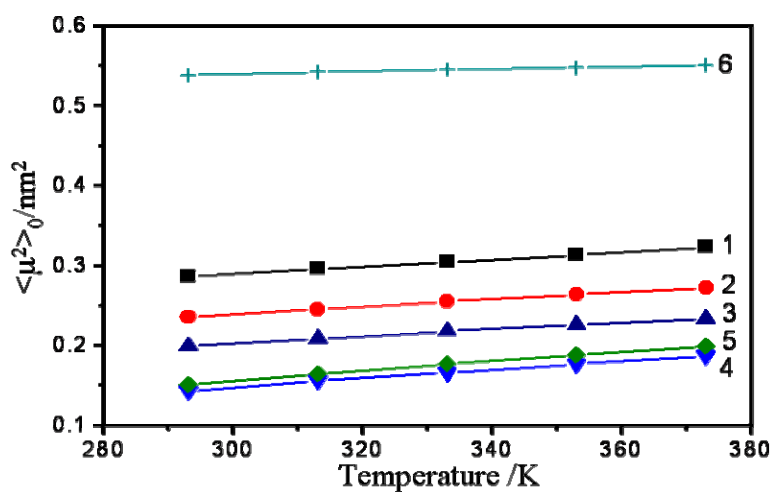


Figure 4.26 $\langle \mu^2 \rangle_0 / \text{nm}^2$ versus temperature for DME with $n=524288$ and $m^2 = 6.4307 \text{ D}^2$. Bond dipole moments $m_{\text{CO}} = 1.07 \text{ D}$ and $m_{\text{CC}} = 0$ were commonly used in this analysis. The range of experimental value = 0.5 ± 0.1

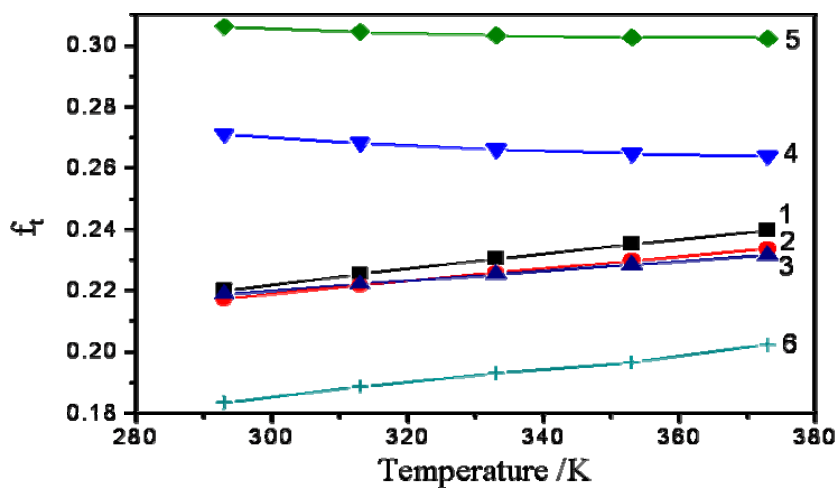


Figure 4.27 The *trans* fraction around center C-C bond of DME calculated as a function of temperature. The range of experiment in the $c\text{-C}_6\text{D}_{12}$ = 0.22 ± 0.01 and in the gas phase = 0.25 ± 0.01

Note: 1,2,3,4,5 are parameter set in Table 4.12 except 6 is from PM3 values

With the statistical weight parameters thus evaluated, the fractions of conformers may be calculated for given bonds of the chain. For DME, analytical expressions, as shown below, can be obtained by simple manipulation.

$$f_g = 1 - f_t^{CC} = p\sigma / (1 + p\sigma) \quad (4.7)$$

where

$$p = 2[(1 + \rho + \rho\omega)/(1 + 2\rho)]^2 \quad (4.8)$$

and

$$f_g^{CO} = 1 - f_t^{CO} = q\sigma / (1 + q\sigma) \quad (4.9)$$

where

$$q = 2[1 + \sigma(1 + \omega) + \rho(2 + \sigma + 2\sigma\omega + \sigma\omega^2)]/[1 + 2\sigma(1 + \rho\omega) + 2\rho(1 + \sigma)] \quad (4.10)$$

Fractions were calculated and shown in Table 4.15. The values of f_g^{CC} and f_g^{CO} thus obtained from *ab initio* method were found to be nearly identical with those of the monomer model, suggesting that the bond conformations are predominantly determined by the local structure in this polymer system.

In NMR spectra of DME, the ^{13}C H satellite side bands provide the information for the $\text{CH}_2\text{-CH}_2$ bond, and similarly for the rotation about the adjoining C-O bond, the vicinal $^{13}\text{C}\text{-}^1\text{H}$ coupling constant associated with the terminal methyl group is useful to determine bond conformation.

The definition of coupling constants are given in Figure 4.28. The parameters E_ρ and E_ω along with the couplings J_G and J_T , for *gauche* and *trans* H-C-C-H arrangements, respectively, were then adjusted to give the best fit to experimental NMR coupling constants according to the relationships for $^1\text{H}\text{-}^1\text{H}$ coupling about the C-C bond.

$${}^3J_{HH} = J_G f_t^{CC} + \frac{1}{2}(J_T + J_G)(1 - f_t^{CC}) \quad (4.11)$$

$${}^3J^1_{HH} = J_T f_t^{CC} + J_G(1 - f_t^{CC}) \quad (4.12)$$

For ${}^{13}\text{C}$ - ${}^1\text{H}$ coupling about the C-O bond, the relationship

$${}^3J_{CH} = J_G f_t^{CO} + \frac{1}{2}(J_T + J'_G)(1 - f_t^{CO}) \quad (4.13)$$

was utilized with conventional methoxy alkane values of $J_G = 2.0$ Hz and $J_T + J'_G = 16.0$. In these expressions, f_t^{CC} and f_t^{CO} are average fractions of C-C and C-O bonds in the *trans* conformation and are a function of the conformer populations and hence the RIS energy parameters. After adjustment of the RIS energy parameters to optimize agreement between calculated and experimental gas-phase NMR coupling constants, values of E_σ , E_ρ and E_ω are shown in Table 4.15. Coupling for *trans* and *gauche* H-C-C-H arrangements were determined to be $J_T = 11.7$ and $J_G = 2.4$ Hz, respectively.

Calculated values of f_t^{CC} and f_t^{CO} from RIS model at 298 K are compared with estimates from analysis of electron diffraction data are shown in Table 4.15. Good agreement for f_t^{CC} is seen for parameter sets 1, 2, 3 and PM3. Our calculated value for f_t^{CO} lies between the electron diffraction and the previous RIS data. Values of $J_G = 3.2$, $J_T = 10.1$ Hz for ${}^1\text{H}$ - ${}^1\text{H}$ coupling and $J_G = 1.6$ Hz, $J_T + J'_G = 16.8$ Hz for ${}^{13}\text{C}$ - ${}^1\text{H}$ coupling, which agree reasonably well with the values used above in the RIS analysis, were found to give optimal agreement between calculated and experimental coupling constant. The resulting NMR coupling constants at 25°C are also compared with experimental gas-phase NMR coupling at 125 and 170°C in Table 4.15.

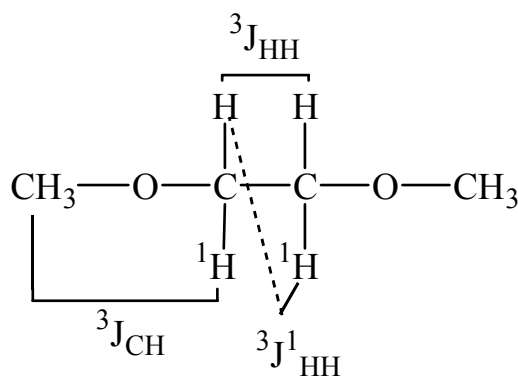
Table 4.15 Bond conformations and NMR vicinal coupling constants of PEO

Case	f_t^{CC}	f_t^{CO}	298 K		
			J_{HH} (Hz)	J_{HH}^1 (Hz)	J_{CH}^1 (Hz)
PM3	0.19	0.63	6.17	4.51	4.41
Ab initio					
Parameter sets 1	0.22	0.68	6.17	4.51	4.41
Parameter sets 2	0.22	0.75	6.03	4.71	3.47
Parameter sets 3	0.22	0.81	6.03	4.72	3.03
Parameter sets 4	0.27	0.74	5.79	5.07	3.61
Parameter sets 5	0.31	0.62	5.63	5.31	4.49
Electron diffraction^a	0.21	0.64	-	-	-
RIS^a	0.21	0.79	-	-	-
Exptl^{a,b}	-	-	5.85 5.81	4.69 4.78	4.09 4.23

^a Jaffe *et al.* (1993)

^b At 125°C and 170°C, respectively

Parameter set 1,2,3,4 and 5 from Table 4.12

**Figure 4.28** Vicinal coupling in DME

It is apparent that the calculated coupling constants agree well with experiment and that the temperature dependence of J_{HH} and J_{HH}^1 is somewhat underestimated. Certainly the agreement could be improved further with additional minor changes in the conformer energies. It should also be pointed out that Eqs. (4.11)-(4.13) are simplifications by treating all *trans* conformations and all *gauche* conformations as equivalent and does not account for geometry differences between conformers. Anyway, an agreement of calculated coupling constant with experimental values is sufficiently good to indicate that this RIS model yields NMR coupling constants which are consistent with the experimental data.

4.2 Experimental Parts

4.2.1 Crystallization Kinetics

4.2.1.1 Isothermal Crystallization Kinetics

The crystallization kinetics of PEO, PEO/MMT, PEO/NaSCN and PEO/NaSCN/MMT system were studied under both isothermal and non-isothermal condition. Thermal and mechanical properties of the polymer complex can be significantly improved using fillers that will act as artificial nucleating agents. However, different and some times contradictory results have been mentioned about the effect of salt and MMT on crystallization rate of semicrystalline polymers. In the heat flow versus time plot, from the enthalpy evolved during crystallization, the kinetics of crystallization was evaluated. Based on the assumption that the evolution of crystallinity is linearly proportional to the evolution of heat released during the crystallization, the relative degree of crystallinity, X_t , can be obtained according to the following equation:

$$X_t = \frac{\int_{T_0}^{T_t} (dH_c / d_t)}{\int_{T_0}^{T_\infty} (dH_c / d_t)} = \frac{A_o}{A_\infty} \quad (4.13)$$

where dH_c denotes the measured enthalpy of crystallization during an infinitesimal time interval d_t . The limits t_0 and t_∞ are used to denote the elapsed time during the course of crystallization and at the end of the crystallization process, respectively.

Isothermal crystallization of PEO, PEO/NaSCN, PEO/MMT and PEO/NaSCN/MMT samples were investigated at 50°C. Figure 4.29 shows the DSC traces for isothermal crystallization of the PEO/NaSCN, PEO/MMT and PEO/NaSCN/MMT nanocomposite. This result implies that small PEO crystallites are formed in the presence of the salt and MMT mineral. Figure 4.30 shows a typical example of the relationship between X_t and time. The crystallization rate was found to increase with adding NaSCN and MMT. Thus MMT and NaSCN seem to act as a good nucleating agent but MMT should be a better nucleating agent than NaSCN because the crystallization time of PEO is shorter for the PEO/MMT system.

For the analysis of the isothermal crystallization, the most common approach is the so-called Avrami method (Karayannidis *et al.*, 2005). Accordingly, the relative degree of crystallinity, X_t , is related to the crystallization time, t , according to:

$$X_t = 1 - \exp(-kt^n) \quad (4.14)$$

where n is the Avrami exponent which is a function of the nucleation process and k is the growth function, which is dependent on nucleation and crystal growth. The Avrami equation in its simple form represents unimpeded spherical crystal growth. However, the sample does not reach complete crystallization as required for the model. To

continue the analysis one assumes that complete crystallization is reached. The values of n , k and K , can be calculated from the fitting to experimental data using the double logarithmic form of Eq. (4.14)

$$\log - \ln[1-X_t] = \log k + n \log t \quad (4.15)$$

Eq. (4.15) is thus used to fit the experimental data and compare crystallization behaviors of pure PEO and its complex with MMT and NaSCN. Plots of $\log - \ln[1-X_t]$ versus $\log t$ were constructed for the isothermal crystallization of PEO, PEO/NaSCN and PEO/MMT as shown in Figure 4.31. The crystallization half time, $t_{1/2}$ can be find from the time when $X_t = 50\%$ in Figure 4.30.

In these these plots, an initial linear part is observed, which is used for the estimation of the parameters n and k . The deviation, which is observed after this first linear part in the Avrami plots, is often attributed to secondary crystallization. From the slope and the intersection of the Avrami plots, values of n and k , respectively, were calculated and the results are summarized in Table 4.16. It is known that the value of n strongly depends on both the mechanism of nucleation and the morphology of crystal growth, and that ideally n would be an integer (Qui *et al.*, 2003; Karayannidis *et al.*, 2005). The n values found in the case of PEO and PEO complexes are in the vicinity of 2.0, for the crystallization temperatures 50°C and they should possibly be related with three-dimensional growth.

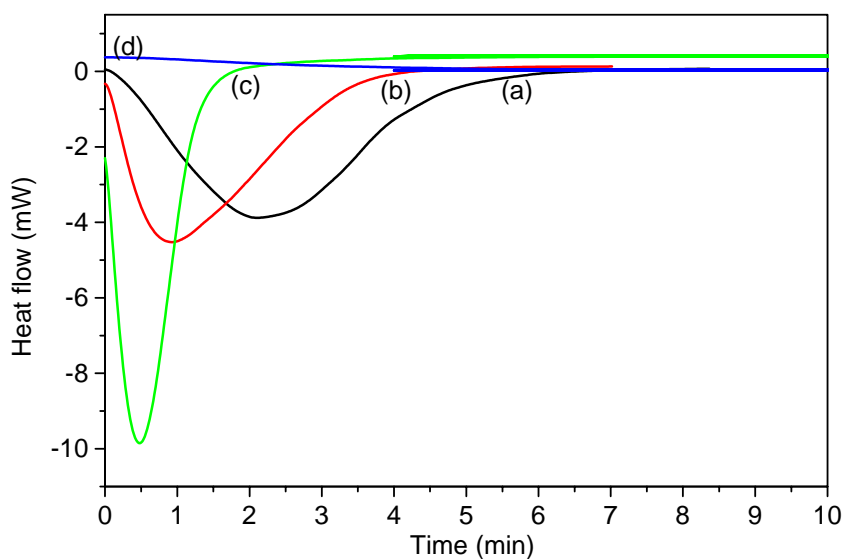


Figure 4.29 DSC thermograms of isothermal crystallization for a) PEO b) PEO/NaSCN, c) PEO/MMT and d) PEO/NaSCN/MMT at $T_c = 50^\circ\text{C}$

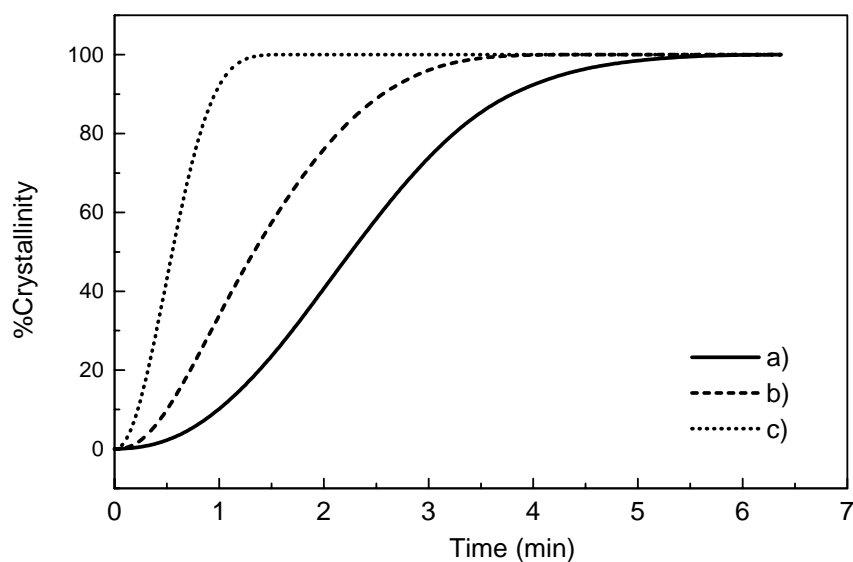


Figure 4.30 The plots of relative crystallinity X_t versus crystallinity time of the crystallization of a) PEO b) PEO/NaSCN and c) PEO/MMT at $T_c = 50^\circ\text{C}$

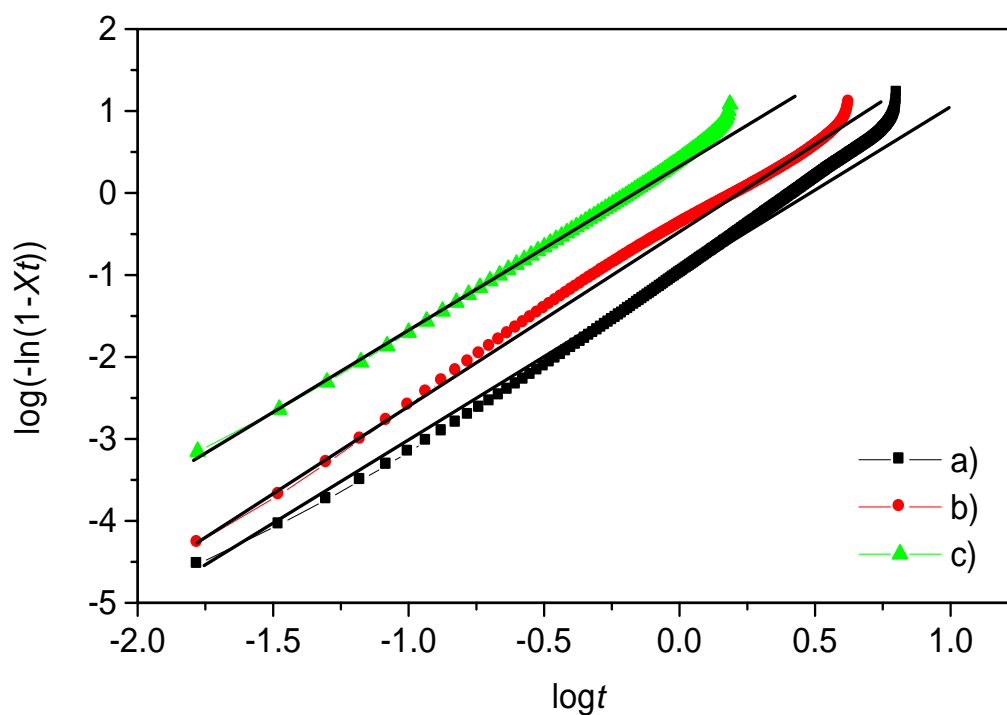


Figure 4.31 Avrami plots of $\log[-\ln(1-X_t)]$ vs. $\log t$ for the isothermal crystallization of the a) PEO, b) PEO/NaSCN and c) PEO/MMT

Table 4.16 Results of the Avrami analysis for the isothermal crystallization of PEO, PEO/NaSCN and PEO/MMT at $T_c = 50^\circ\text{C}$.

Sample	n	k	$t_{1/2}(\text{min})$
PEO	2.2460	0.1101	2.23
PEO/NaSCN	2.0434	0.0090	1.33
PEO/MMT	2.0941	0.3943	0.55

For a given specimen, the crystallization half time, $t_{1/2}$, decreased following the adding mixture into PEO, while the inverse effect was observed for the growth function, k and $t_{1/2}$ for PEO/MMT and PEO/NaSCN were reduced while k were increased. This verifies that the crystallization rates increase when MMT and NaSCN

were added. It seems that MMT can improve the crystallization rates of PEO than that of NaSCN.

4.2.1.2 Non-isothermal Crystallization Kinetics

In this section, the role of the layered silicate existing in the intercalated polymer the crystallization procedure in further investigated. For the polymer crystallization, generally, studies of crystallization process are limited to isothermal conditions, the theoretical analysis is easy to handle, and problems associated with cooling rates and thermal gradients within the specimens are avoided. In practice, however, the crystallization in a continuously changing thermal environment is of greater interest, given that industrial processes generally proceed under non-isothermal conditions. (Xu *et al.*, 2001; Kim *et al.*, 2003; Manias *et al.*, 2003). From the DSC curves of melting crystallization, the values of relative degree crystallinity at different cooling rates as a function of temperature, X_t , can be calculated according to the following Eq. (4.13)

Figure 4.33 presents the results for the change in sample crystallinity with temperature. As expected, all curves are sigmoidal. Apparently, the changes in the percent of crystallinity for all polymer system depend on the cooling rate. The relationship between crystallization temperature T and time t is given by Eq. (4.16) during the non-isothermal crystallization process, as follows:

$$t = \frac{|T_0 - T|}{a} \quad (4.16)$$

where t is the crystallization time, T_0 is the temperature at which crystallization begins ($t=0$), T is the crystallization temperature, and a is the cooling rate.

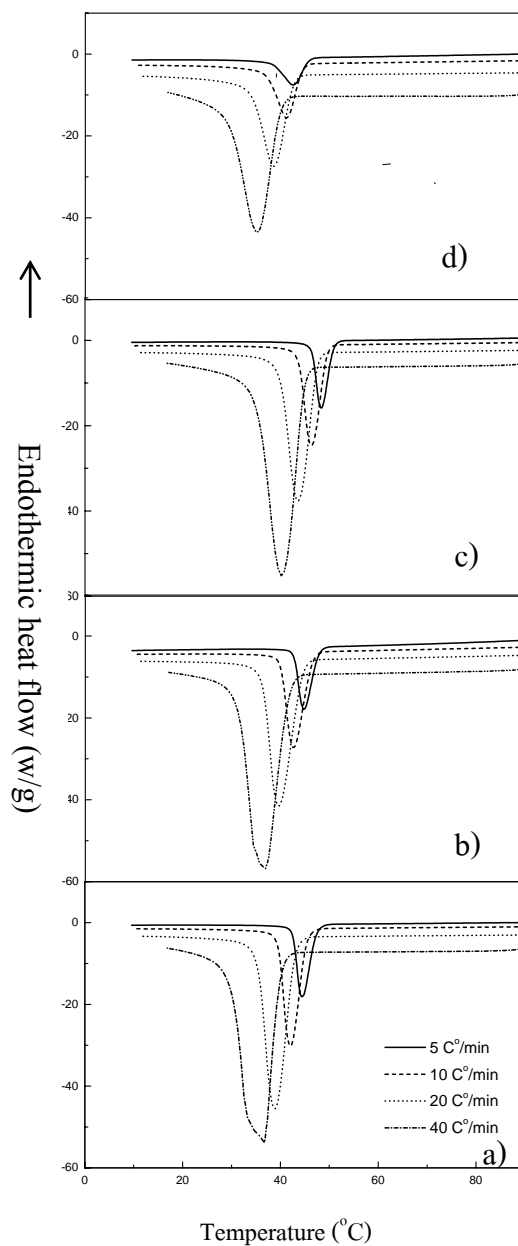


Figure 4.32 DSC thermograms of a) PEO, b) P(EO)₈NaSCN, c) PEO/10%MMT and d) P(EO)₈NaSCN/10%MMT at various cooling rates : 5 °C/min, 10 °C/min, 20 °C/min and 40 °C/min.

According to Eq. (4.16), the value of T on the X -axis in Figure 4.33 can be transformed into the crystallization time t as shown in Figure. 4.34. All of these curves have the same sigmoidal shape. It can be seen that the higher the cooling rate,

the shorter the time for completing crystallization. The half-time ($t_{1/2}$) of non-isothermal crystallization of PEO, PEO/MMT, P(EO)₈NaSCN and P(EO)₈NaSCN/MMT could be obtained from Figure 4.34, and the results are listed in Table 4.17. As expected, $t_{1/2}$ decrease with the increasing cooling rates. However, at a given cooling rate, the $t_{1/2}$ value of PEO/MMT system is lower than that of the P(EO)₈NaSCN system, signifying the difference of accelerating the overall crystallization process with MMT and NaSCN addition. A reasonable explanation is that a strong interaction exists between PEO molecule and silicate layer, leading to a greater nucleation effect of PEO/MMT system than others.

Next, Avrami theory (Xu *et al.*, 2001; Kim *et al.*, 2003; Manias *et al.*, 2003) is used to interpret of the non-isothermal crystallization process. Avrami equation can be illustrated in the form as:

$$1-X_c(t) = \exp(-Z_t t^n) \quad (4.17)$$

Taking double logarithm at both sides, one can get

$$\log[-\ln(1-X_c(t))] = n \log t + \log Z_t \quad (4.18)$$

where $X_c(t)$ is the relative degree of crystallinity at time t ; the exponent n is a mechanism constant with a value depending on the type of nucleation and the growth dimension, and Z_t is a growth rate constant involving both nucleation and growth rate parameters. Although, the physical meanings of Z_t and n cannot be related to the non-isothermal case in a simple way, their use provides further insight into the kinetics of non-isothermal crystallization. By using Eq. (4.18), a plot of $\log [-\ln(1-X_c(t))]$ versus $\log t$ is shown in Figure 4.35. The values of the Avrami exponent n and the rate parameter Z_t could be determined from the slope and intercept. An accurate analysis of the non-isothermal crystallization data could not be performed because of the

curvature in the plots. The non-isothermal crystallization of PEO, P(EO)₈NaSCN and PEO/MMT nanocomposites do not follow the Avrami equation, probably because of the disregarded assumptions in Avrami's theory.

Considering the non-isothermal characteristics of the process investigated, the parameter for the crystallization rate, Z_t , should be corrected, because the temperature is constantly changing during the process. The parameter characterizing the kinetics of non-isothermal crystallization was given as follows:

$$\log Z_c = -\frac{\log Z_t}{a} \quad (4.19)$$

Where a is the cooling rate. The results, obtained from Avrami plots and Eq.(4.19) are listed in Table 4.17. The exponent n varied from 0.65 to 0.67 for PEO, from 0.58 to 0.81 for P(EO)₈NaSCN, from 0.76 to 0.92 for PEO/10%MMT and from 0.62 to 0.64 for P(EO)₈NaSCN/10%MMT. Although the exponent n obtained from non-isothermal crystallization shows a wide range of values and data are more scattered than these obtained from isothermal crystallization, it is interesting that the values of n for PEO/MMT are larger than that of PEO at the same cooling rate, indicating that MMT can act as a nucleating agent for the PEO matrix. Z_c values of P(EO)₈NaSCN and PEO/MMT are, as expected, higher than that of PEO at the same cooling rate.

Ozawa explained the effect of cooling rate on the non-isothermal crystallization by modifying the Avrami equation, assuming that the crystallization occurs at a constant cooling rate a and may be composed of infinitesimally small isothermal crystallization steps. According to Ozawa's theory, the relative degree of crystallization at temperature t , $X_c(T)$, can be calculated from the following equations:

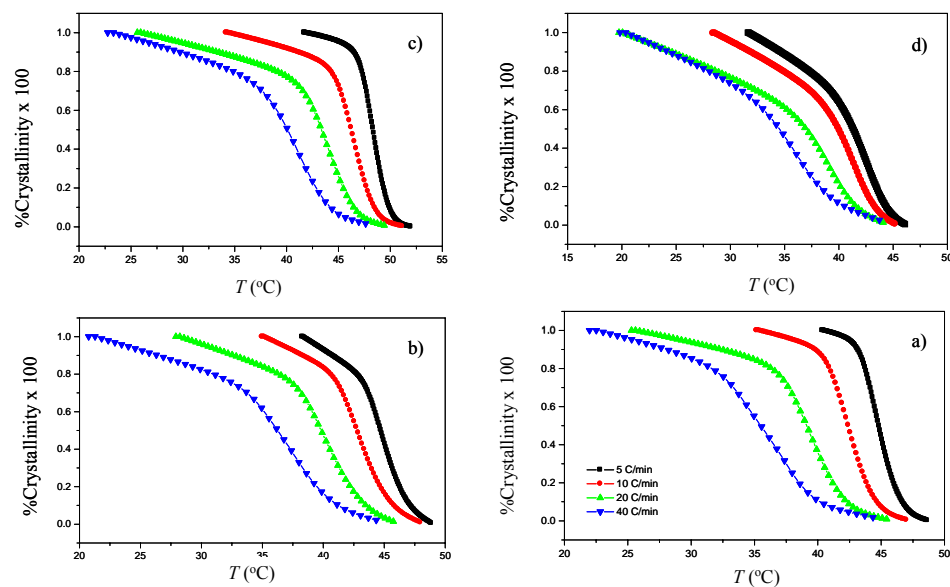


Figure 4.33 Plots of Relative crystallinity versus T for crystallization of a) PEO, b) $P(\text{EO})_8\text{NaSCN}$, c) PEO/10%MMT and d) $P(\text{EO})_8\text{NaSCN}/10\%\text{MMT}$ at various cooling

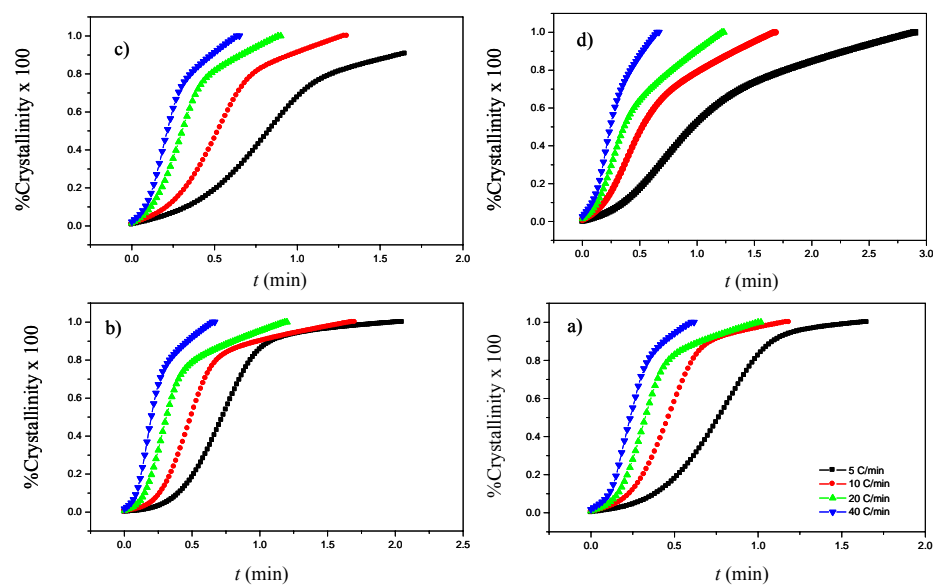


Figure 4.34 Plots of X_t versus time for crystallization of a) PEO, b) $P(\text{EO})_8\text{NaSCN}$, c) PEO/10%MMT and d) $P(\text{EO})_8\text{NaSCN}/10\%\text{MMT}$ at various cooling rates

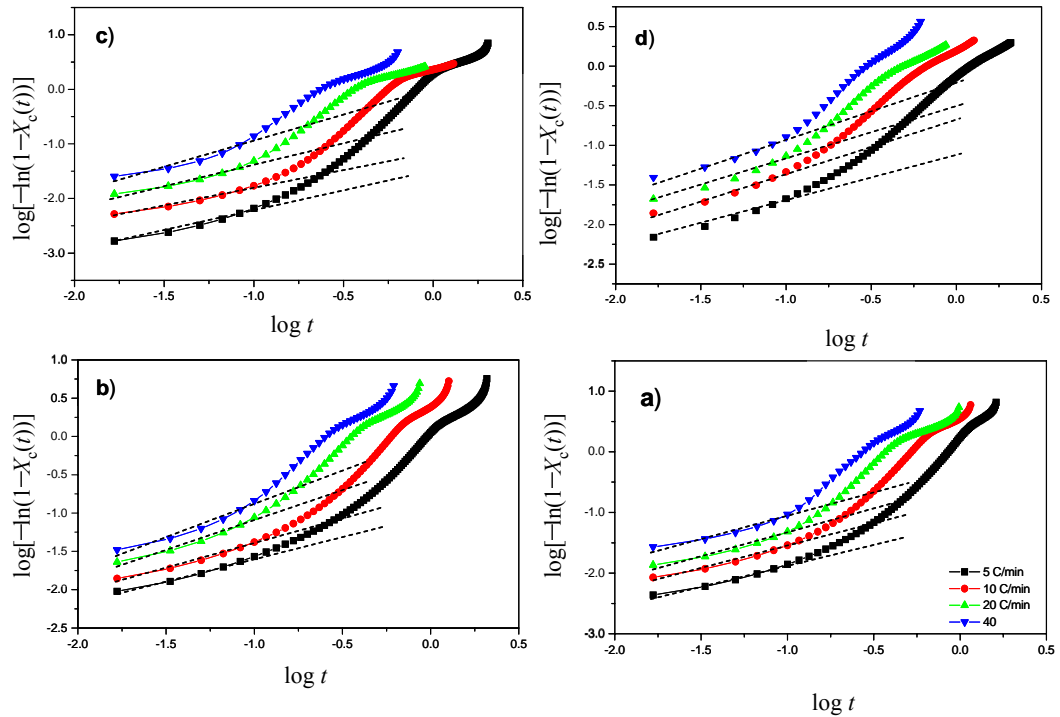


Figure.4.35 Avrami plots of $\log[-\ln(1-X_c(t))]$ versus $\log t$ for crystallization of a) PEO, b) $P(\text{EO})_8\text{NaSCN}$, c) PEO/10%MMT and d) $P(\text{EO})_8\text{NaSCN}/10\%\text{MMT}$ at various cooling rates

$$1 - X_c(T) = \exp\left[-\frac{K(T)}{|a|^m}\right] \quad (4.20)$$

where $K(T)$ is a function related to the overall crystallization rate that indicates how fast crystallization proceeds, and m is the Ozawa exponent that depends on the dimension of crystal growth. The following equation was derived by

$$\log[-\ln(1-X_c(T))] = \log K(T) - m \log a \quad (4.21)$$

By plotting $\log[-\ln(1-X_c(T))]$ against $\log a$ at a given temperature, a straight line should be obtained if the Ozawa analysis is valid. The kinetic parameters m and $K(T)$ can be derived from the slope and the intercept, respectively. The results of the Ozawa analysis for PEO, $P(\text{EO})_8\text{NaSCN}$ and PEO/10%MMT nanocomposites are

shown in Figure 4.36. The curvature in Figure 4.36 presents an inaccurate analysis of the non-isothermal crystallization data. This can be explained that, at a given temperature, the crystallization process at different cooling rates are at different stages, The lower cooling rate process is toward the end of the crystallization process, whereas at the higher cooling rate, the crystallization process is at an early stage. The change in the slope with temperature means that the parameter m is not a constant during crystallization, indicating that Ozawa's approach is not a good method to describe the non-isothermal crystallization of PEO/MMT and P(EO)₈NaSCN.

Mo and coworkers proposed a different kinetic equation by combining the Ozawa and Avrami equations. (Xu *et al.*, 2001; Kim *et al.*, 2003; Manias *et al.*, 2003) As the degree of crystallinity is related to the cooling rate a and the crystallization time t (or temperature T), the relation between a and t could be defined for a given degree of crystallinity. Consequently, a new kinetic equation for non-isothermal crystallization is derived by combining Eqs. (4.21) and (4.18):

$$\log Z_t + n \log t = \log K(T) - m \log a \quad (4.22)$$

$$\log a = \log F(T) - b \log t \quad (4.23)$$

where the parameter $F(T)=[K(T)/Z_t]^{1/m}$, the Avrami exponent n is calculated using Ozawa's method, and b is the ratio between the Avrami and Ozawa exponents, i.e. $b=n/m$. $F(T)$ refers to the value of the cooling rate chosen at unit crystallization time, when the system has a defined degree of crystallinity. It can be seen that $F(T)$ has a definite physical and practical meaning. According to Eq. (4.23), at a given degree of crystallinity, the plot of $\log a$ against $\log t$ should give a straight line with an intercept of $\log F(T)$ and a slope of $-b$.

Table 4.17 Parameters of sample during nonisothermal crystallation process

Sample	a	T_p	T_c	$t_{1/2}$	Z_c	n
	$^{\circ}\text{C}/\text{min}$	$^{\circ}\text{C}$	$^{\circ}\text{C}$	min		
PEO-Pure	5	44.52	49.54	0.77	0.06	0.65
	10	42.00	48.17	0.47	0.81	0.68
	20	39.04	45.89	0.33	0.22	0.70
	40	36.54	43.37	0.24	0.38	0.67
P(EO) ₈ NaSCN	5	44.70	49.38	0.83	0.10	0.58
	10	42.57	48.24	0.52	0.16	0.61
	20	39.29	46.64	0.31	0.43	0.74
	40	36.75	43.90	0.22	0.80	0.81
PEO/10%MMT	5	48.28	52.23	0.73	0.03	0.76
	10	46.17	50.86	0.49	0.07	0.66
	20	43.55	49.72	0.30	0.24	0.76
	40	40.26	46.98	0.20	0.91	0.92
P(EO) ₈ NaSCN/10%MMT	5	42.55	46.59	0.96	0.08	0.62
	10	41.09	45.90	0.53	0.20	0.66
	20	38.68	44.31	0.36	0.33	0.69
	40	35.19	41.79	0.25	0.51	0.64

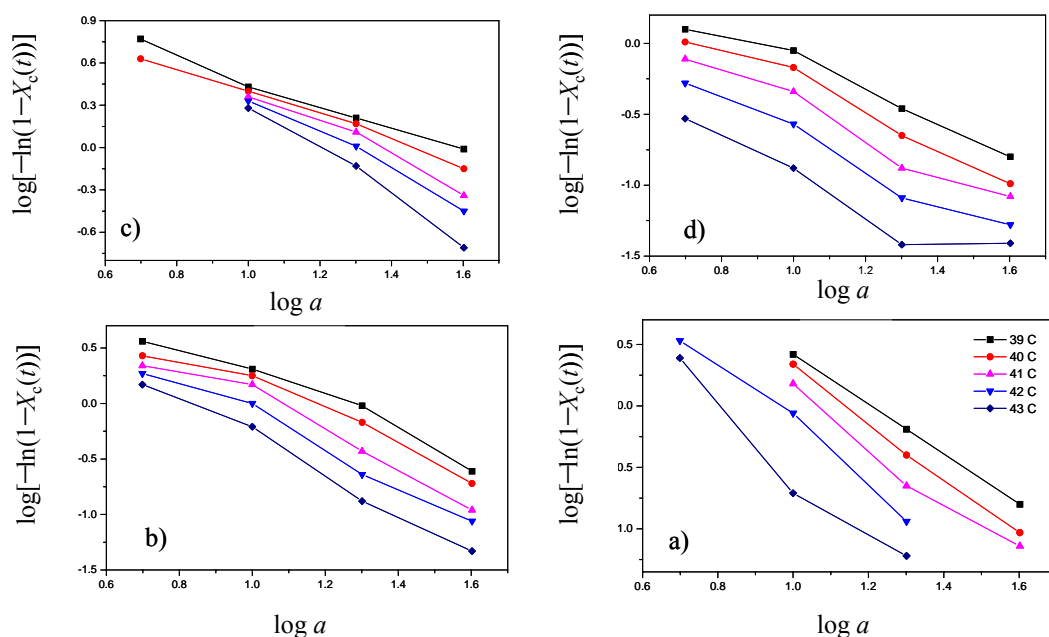


Figure 4.36 Ozawa plots of $\log[-\ln(1-X_c(t))]$ versus $\log(a)$ for crystallization of a) PEO, b) $P(\text{EO})_8\text{NaSCN}$, c) PEO/10%MMT and d) $P(\text{EO})_8\text{NaSCN}/10\%\text{MMT}$ at various T

As shown in Figure. 4.37, plotting $\log a$ against $\log t$ gave a linear relationship at a given degree of crystallinity, and the values of $F(T)$ and b are listed in Table 4.18. The $F(T)$ values increase with the relative degree of crystallinity for all investigated systems. The value of b varies from 1.65 to 1.91 for PEO, from 0.51 to 0.61 for PEONaSCN, from 1.38 to 1.91 for MMT/PEO and from 1.45 to 1.68 for 10%MMT/PEONaSCN. It is clear that this approach is successful in describing the non-isothermal crystallization process of PEO, PEONaSCN and MMT/PEO nanocomposites as they have done for polypropylene/Montmorillonite nanocomposites, Nylon-11, and polyoxymethylene/Montmorillonite nanocomposites. (Xu *et al.*, 2001).

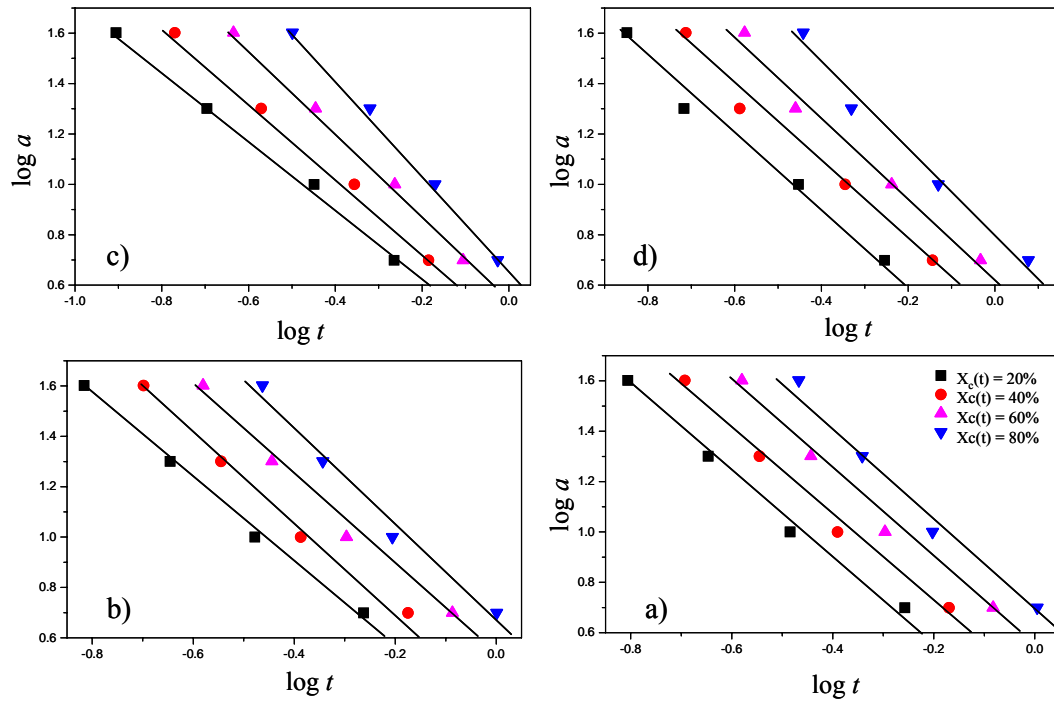


Figure 4.37 $\log a$ versus $\log t$ from the combined Avrami and Ozawa equation for a) PEO, b) $\text{P}(\text{EO})_8\text{NaSCN}$, c) PEO/10%MMT and d) $\text{P}(\text{EO})_8\text{NaSCN}/10\%\text{MMT}$ at various $X_c(t)$

Considering the influence of the cooling rates on the non-isothermal crystallization process, Kissinger proposed that the activation energy could be determined by calculating the variation of the crystallization peak with cooling rate (Xu *et al.*, 2001):

$$\frac{[\ln(a/T_p^2)]}{d(1/T_p)} = \frac{-\Delta E}{R} \quad (4.23)$$

where R is the gas constant and T_p is the crystallization peak temperature. The crystallization activation energy (ΔE) was calculated from the slope of $[\ln(a/T_p^2)]$ versus $1/T_p$. As shown in Figure 4.38, activation energies of non-isothermal melt

crystallization of PEO, $P(\text{EO})_8\text{NaSCN}$, PEO/10%MMT and $P(\text{EO})_8\text{NaSCN}/10\%\text{MMT}$ were determined to be 212.92, 215.90, 197.2 and 223.98 kJ/mol, respectively. It can be seen that the activation energy of non-isothermal crystallization of PEO/MMT is lower than that of pure PEO. Accordingly, the addition of MMT may accelerate the overall non-isothermal crystallization process of PEO.

From Manias *et al.*, (2003), similar experimental observations was also found and explained as follows: (1) The introduction of MMT fillers hindered PEO crystallization. (2) The overall PEO crystallinity was not affected by the filler introduction for small filler loadings, but the crystal morphology was strongly altered by the MMT presence, resulting in more, smaller, and nonisotropic crystallites. (3) The overall crystallization kinetics become faster with the addition of MMT (from $t_{1/2}$ data).

At first glance, the first observation seems at odds with the last. Although crystallization was hindered by an introduction of MMT fillers, the overall crystallization kinetics becomes faster. This is a consequence of the much larger number of crystallites created in the presence of MMT compared to the neat PEO system. Because the overall crystallization rate (as measured by $t_{1/2}$) is the product of the nucleation rate and the crystal growth rate, it is actually possible for the overall kinetics to increase despite a slowing down of the crystal growth rate, when more crystals are nucleated, as is the case here. The most interesting finding of that work is probably the fact that the introduction of MMT inorganic fillers slows down the polymer crystal growth in the vicinity of the filler.

Table 4.18 Nonisothermal crystallization kinetic parameter at difference degrees of crystallinity.

Sample	$X_c(t)$ (%)	b	$F(T)$	ΔE (kJ/mol)
PEO-Pure	20	1.65	1.76	
	40	1.73	2.36	
	60	1.81	3.27	212.92
	80	1.91	4.68	
P(EO) ₈ NaSCN	20	0.51	1.41	
	40	0.54	1.62	
	60	0.57	1.86	215.9
	80	0.61	2.14	
PEO/10%MMT	20	1.38	2.24	
	40	1.52	2.71	
	60	1.70	3.43	197.26
	80	1.91	4.62	
P(EO) ₈ NaSCN/10%MMT	20	1.45	2.12	
	40	1.52	2.95	
	60	1.60	4.19	223.98
	80	1.68	6.35	

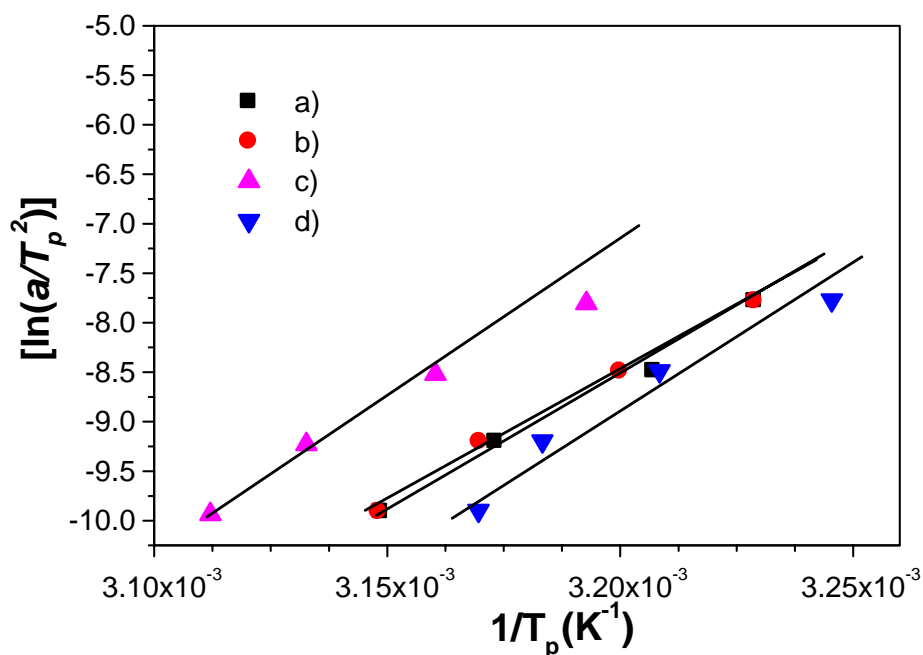


Figure 4.38 Kissinger plot for evaluating non-isothermal crystallization activation energies of a) PEO, b) P(EO)₈NaSCN, c) PEO/10%MMT and d) P(EO)₈NaSCN/10%MMT

This contrasts the usual behavior of semicrystalline polymers, where fillers normally result in heterogeneous nucleation, promoting crystals in their vicinity. Such crystal nucleating effects are in fact observed also for MMT when incorporated in other semicrystalline polymers, such as poly(vinyl alcohol), polypropylene, and nylon-6. (Manias *et al.*, 2003) The unusual behavior observed herein for PEO originates from the specific manner that MMT interacts with poly(ethylene oxide). Addition of small cations, in the form of salts, has been shown to reduce or completely destroy the crystallinity of PEO. This behavior is attributed to the strong coordination of PEO to small cations, such as Na⁺ and Li⁺, which promote "crown ether" type of backbone conformations coordinated to the cations. Such crown-ether conformations deviate from the helical PEO conformations, typically found in bulk PEO crystals-and therefore amorphize the PEO. Because the MMT surfaces bear

large numbers of cations, PEO chains in their vicinity are highly coordinated to the Na^+ , adopting conformations with many crown-ether arrangements, which are highly amorphous. A similar behavior-with cations promoting an amorphous PEO structure-has also been seen in the interlayer gallery between the MMT layers in PEO/MMT composites by computer simulations, and this is also an important effect on the external surfaces of the MMT.

It is believed that the slowing of the crystal growth rate is due to this amorphization of the polymer in the vicinity of the silicate, which forces the spherulite to grow around the dispersed tactoids, resulting in "broken" lamellar pathways and geometrically anisotropic shapes. This T_c reduction (Table 4.17) is additional evidence that crystallization is inhibited with the addition of silicate fillers, as larger under cooling rate. If this is the case, reducing the surface density of Na^+ cations on the MMT surfaces should result in enhanced PEO crystallization. Finally, putting all these pieces together, we can trace the crystallization behavior of PEO in the presence of MMT fillers can be traced: the primary nucleation takes place in the bulk-away from the MMT surfaces-and initially spherulites grow normally until they encounter a filler. At this point, because amorphous PEO structures are promoted in the vicinity of the MMT, there is a retardation of the spherulite growth front, resulting in jagged edges and nonspherulitic morphologies. This delay in covering space allows for the nucleation of other spherulites that grow in the same manner until all volume is filled. These additional nuclei cause the PEO to crystallize faster overall, despite the slower crystal growth rate, and allows for the total volume to crystallize more quickly, but with much smaller crystallite sizes than in bulk PEO.

4.2.2 X-ray diffraction (XRD)

4.2.2.1 PEO/Montmorillonite nanocomposite

Depending on the method of preparation, different interlayer spacing may be obtained when layered clay is associated with polymer. In such nanocomposites, the repetitive multilayer structure is well preserved, allowing the interlayer spacing to be determined. X-ray diffraction technique is often applied to identify intercalated structures through the Bragg's relation: (Brown, 1961)

$$\lambda = 2d \sin \theta \quad (4.24)$$

where λ corresponds to the wave length of the X-ray radiation ($\lambda = 1.5405 \text{ \AA}$ for CuK_α) used in the diffraction experiment, d corresponds to the spacing between diffractive lattice planes and θ is the measured angle.

In this thesis, XRD technique was employed to study the effect of adding MMT into PEO with a focus on two aspects i.e. the reduction of crystalline portion in PEO and the formation of intercalated PEO/MMT nanocomposites. It was found that PEO could be intercalated in the clay layer and form nanocomposite which was confirmed by the diffraction peak at 2θ lower than 10° . Next the intensity of the crystalline PEO peaks (19.5 and 23.7°) decreased when MMT was added to the mixture indicating the reduction of crystallinity compared to that of pure PEO.

The ionic conductivity (σ) of polymer electrolyte is related to the product of the concentration of ionic charged carriers and its mobility according to the following equation; (Puatrakul, 2000)

$$\sigma = \sum_i \eta_i z_i \mu_i \quad (4.25)$$

where η_i , z_i and μ_i refer to number of charge carriers, ionic charges, and ionic mobility, respectively. According to the aforementioned equation, the ionic conductivity depends on the number of charged carrier (η_i) in the system and the mobility (μ_i) of various species. When the inorganic filler are mixed in, the number of charged carriers (η_i) increase because MMT interact with salt and cause it to dissociate more. Hence, the fraction of free ions and the ability of mobility (μ_i) are increased accordingly. In addition, MMT can causes a reduction of polymer crystallinity resulting in an increase of the amorphous portion that can enhance the ionic mobility. On the other hand, if the concentration of MMT in solid polymer electrolyte is too high, the viscosity of the complex will increase and affect to the mobility of ion species.

The phenomenon of intercalation

Figure 4.39 shows X-ray diffraction patterns of PEO, MMT and PEO/MMT nanocomposites. The XRD pattern of MMT exhibits a silicate peak at low angle ($2\theta = 6.0^\circ$, $d_{001} = 14.7 \text{ \AA}$). The XRD pattern of PEO/MMT at various weight percent of MMT 5-20% appears a set of new peaks corresponding to the intercalated structure in polymer/layer-silicate nanocomposites. The repeated distance in these polymer/layer-silicate nanocomposites increases from 14.7 to 17.6 \AA . The results are summarized in Table 4.19 which shows that the change in 2θ and d_{001} of MMT/PEO mixture at various MMT are not significant. These findings suggest that all intercalated structures of PEO/MMT with different MMT doping are similar.

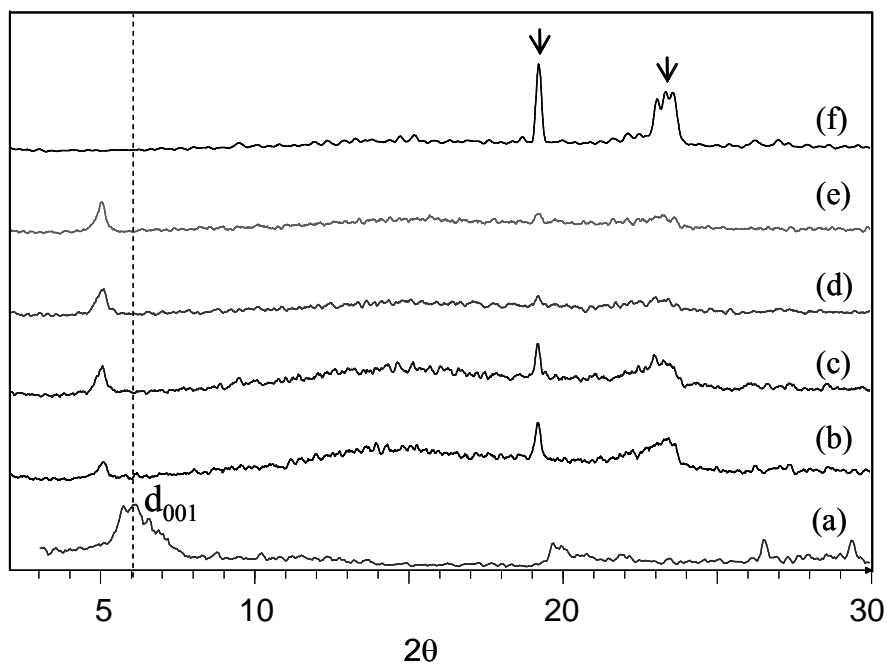


Figure 4.39 XRD pattern of: (a) pure MMT, (b) PEO/5%MMT, (c) PEO/10%MMT, (d) PEO/15%MMT, (e) PEO/20%MMT and (f) pure PEO

Table 4.19 The basal spacing d_{001} (Å) of pure MMT and PEO/MMT at various MMT contents.

Sample	2θ	d_{001} (Å)
Pure MMT	6.00	14.7
PEO/5%MMT	5.03	17.5
PEO/10%MMT	5.00	17.7
PEO/15%MMT	5.03	17.6
PEO/20%MMT	4.99	17.7

The PEO crystallinity

Figure 4.39(f) shows the XRD pattern of pure PEO. The crystalline peaks of PEO show two intense peaks at $2\theta = 19.5^\circ$ and 23.7° , respectively. With the addition of MMT into PEO, the intensity of these two sharp peaks decrease with an increase in MMT contents as shown in Figure 4.39 (b) to (e), indicating an increase of amorphous phase volume fraction. However, the relative intensities of both peaks are different from those of pure PEO and indicate that the PEO crystal induced by MMT is different from that formed in the pure polymer. This is consistent with the fact that the surface of inorganic fillers, in some cases, can promote polymers to grow a different crystal phase. The percent crystallinity and crystallization kinetics of PEO and PEO/MMT nanocomposites will later be studied by DSC technique and the results/discussion will be presented next in Section 4.2.1.

The intercalation of PEO into silicate layer of MMT can be proposed by a computational molecular model. A snapshot of the hydrated Li-montmorillonite system is shown in Figure 4.40. (Hackett *et al.*, 2000) Although this is a snapshot of a particular water-containing system, it illustrates many of the features, that are apparent in both dry and hydrated system. These features include the preferred locations of ions and the disorderd bilayer structure of polymer. The bilayer structure of polymer in this system is even more pronounced, and the disordered nature of chain configurations can be seen clearly from the snapshot. Again, the liquid-like structure contrasts with previous suggestions of helical or all *trans* extended polymer structures within the gallery. The observed configurations are also in very good agreement with Small-Angle Neutron Scattering (SANS) experiments. SANS profiles from 15 K to room temperature can only be simulated by assuming a disordered polymer configuration.

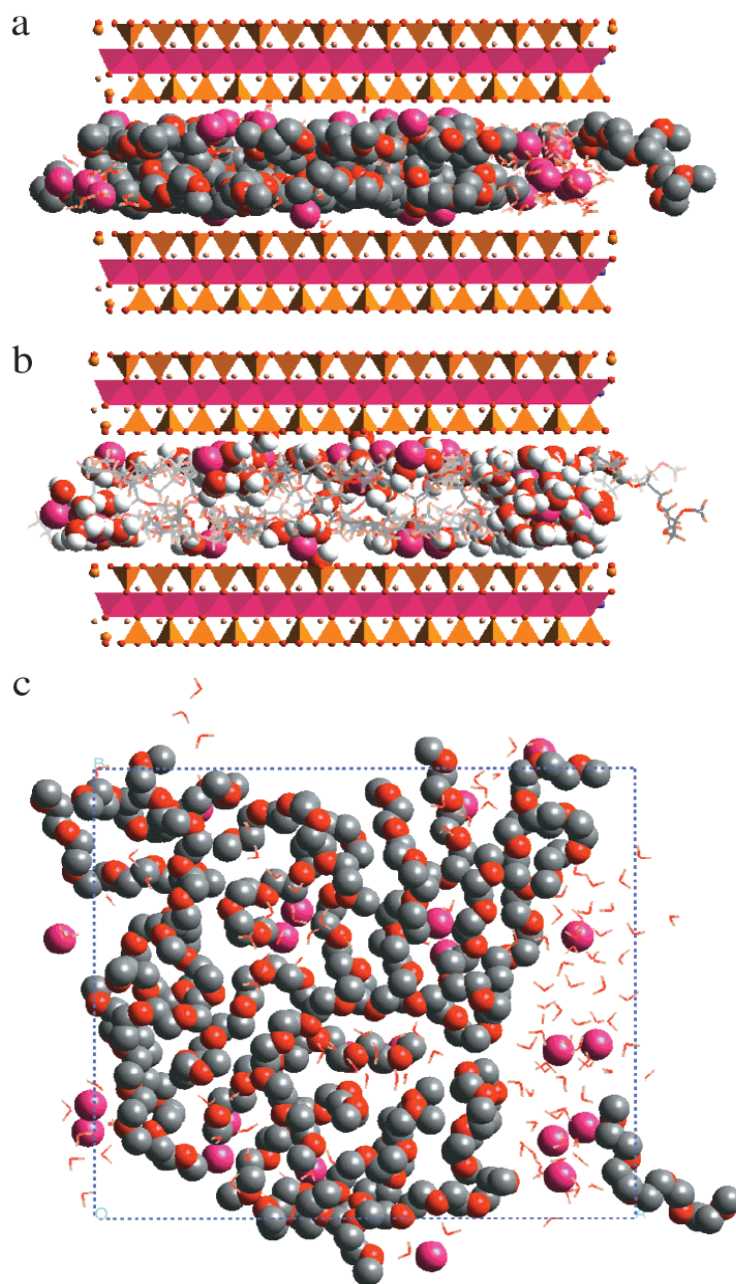


Figure 4.40 Snapshot of PEO-silicate nanocomposite: (a) showing the silicate crystal as polyhedral, Li^+ as spheres, and highlighting PEO as spheres; (b) showing the silicate crystal as polyhedra, Li^+ as spheres, and highlighting water as spheres, (c) top view with silicate removed, showing PEO and Li^+ as spheres and water as sticks

4.2.2.2. PEO/NaSCN Electrolyte Complex

Figure 4.41 shows X-ray diffractograms in the region $2\theta = 0-40^\circ$ for the systems with O:M ratios of 60:1, 20:1 and 8:1. In addition, XRD data for pure PEO and NaSCN are also given for comparison. It can be seen that the 8:1 system consists of a few new peaks (lower arrow) in addition to those corresponding to pure PEO. These new peaks do not coincide with those of pure NaSCN either (Figure 4.41 (a)). The intensities of PEO crystallinity peaks decrease with adding salt concentrations from Figure 4.41 (b) to (d) and completely disappear in the EO:Na⁺ = 8:1 system. The XRD data are also consistent with the spectroscopic data and confirm the formation of a crystalline compound with an O:M ratio of 8:1.

4.2.2.3. PEO/NaSCN/MMT Electrolyte nanocomposite

Figure 4.42 shows the X-ray diffractogram of P(EO)₈NaSCN/MMT. As NaSCN merges into PEO and causes the changes of crystalline PEO, the two intense crystallinity peaks of pure PEO disappear in P(EO)₈NaSCN. When the content of MMT in the mixtures increase, the identification of the two intense peaks of PEO becomes difficult as seen from Figure 4.42 (c) – (e), indicating that the long-range crystalline order of PEO is reduced significantly and PEO emerges in an amorphous profile. However, the peak at $2\theta = 20.5^\circ$ is associated PEO with NaSCN crystalline complex, and can be observed clearly only if the content of MMT is less than 5%, suggesting that the intrinsic semi-crystalline nature of PEO is still slight in the mixtures. In addition, we also observe the intensity peak at $2\theta = 6.0^\circ$. This peak is a d_{001} of the silicate layer which its intensity increases with MMT contents.

Since no diffraction peak occurs at $2\theta < 6^\circ$, it indicates that no intercalated PEO/MMT structures exist. These results imply that PEO interacts stronger with salt

ions than that of MMT. The molecular model to explain these finding is also proposed in Section 4.2.2.2.

4.2.3 Differential Scanning Calorimeter (DSC)

Thermal behavior of PEO-salt complexes can be better understood based on characterization of the crystalline and amorphous phase present in the complexes using Differential Scanning Calorimeter (DSC). The DSC thermograms of the PEO-salt complex give information on melting temperature (T_m), enthalpy of melting (ΔH_m) and the percentage of crystallinity ($\%X_c$). The percentage of crystallinity can be calculated by integrating the area under the melting peak to obtain the endothermic energy change and comparing to a theoretical volume of 100% crystalline PEO.

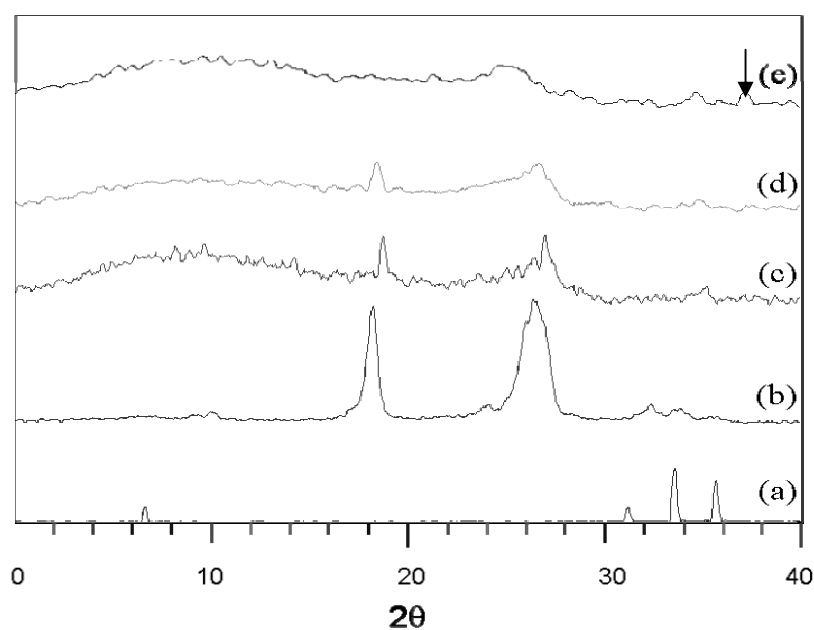


Figure 4.41 XRD pattern of: (a) NaSCN salt, (b) pure PEO, (c) P(EO)₆₀NaSCN, (d) P(EO)₂₀NaSCN, (e) P(EO)₈NaSCN

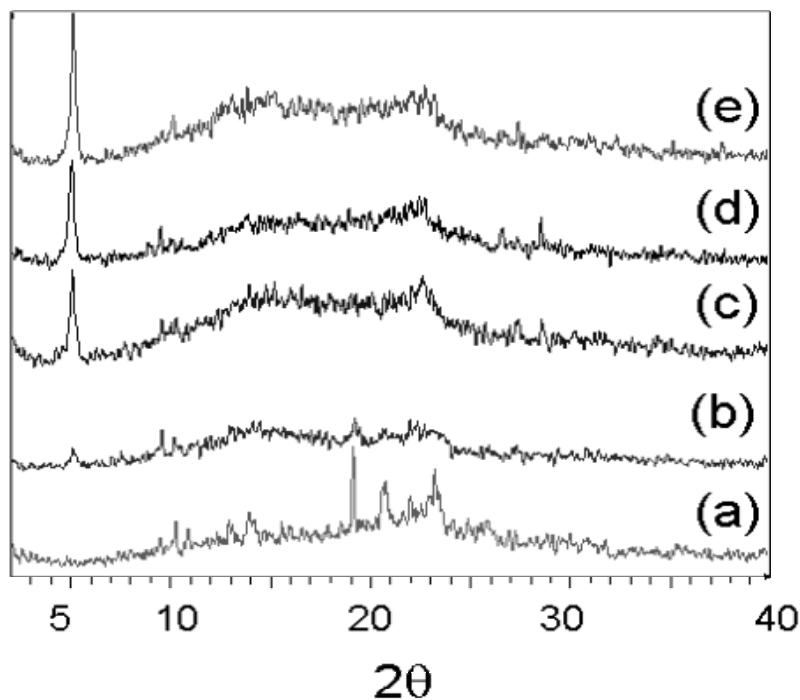


Figure 4.42 XRD patterns of P(EO)₈NaSCN/MMT, (a) P(EO)₈NaSCN, (b) P(EO)₈NaSCN/5%MMT, (c) P(EO)₈NaSCN/10%MMT, (d)P(EO)₈NaSCN/15%MMT and (e) P(EO)₈NaSCN/20%MMT

The percentage of crystallinity was evaluated from the following equation.

$$\% \text{ crystallinity} = \frac{\Delta H_m}{\Delta H_m^0} \times 100 \quad (4.25)$$

where ΔH_m is the enthalpy of melting of each sample and ΔH_m^0 is the enthalpy of melting of 100% crystalline PEO. The reported value of ΔH for 100% crystalline PEO is 45 cal g⁻¹ or 188.1 J g⁻¹ (Preechatiwong *et al.*, 1996).

4.2.3.1 PEO/Montmorillonite nanocomposite

The melting temperatures and percentage of crystallinities for each PEO-salt samples are summarized in Table 4.20. From DSC thermograms of pure PEO (in Figure 4.43), its melting temperature is 69°C and the percentage of

crystallinity is approximately 91%. The percentage of crystallinity of PEO decreases with increasing clay concentration. This finding suggests that there is more amorphous domain in the system. XRD results of PEO/MMT system in Section 4.2.2.1 also support this conjecture. DSC results are summarized in Table 4.20. It can be seen that T_m of PEO/MMT containing 5, 10, 15 and 20 wt% of MMT decreases slightly with increasing the clay mineral content. This result implies that small PEO crystallites are formed in the presence of the clay mineral. ΔH_m also decreases slightly with increasing the clay mineral content. This result means that the total crystallinity of PEO is influenced by the presence of the clay mineral. In other words, it is implied that PEO molecules are intercalated into the silicate layers to some extent. Similar curves have also been obtained for other electrolytes (Ogata *et al.*, 1997).

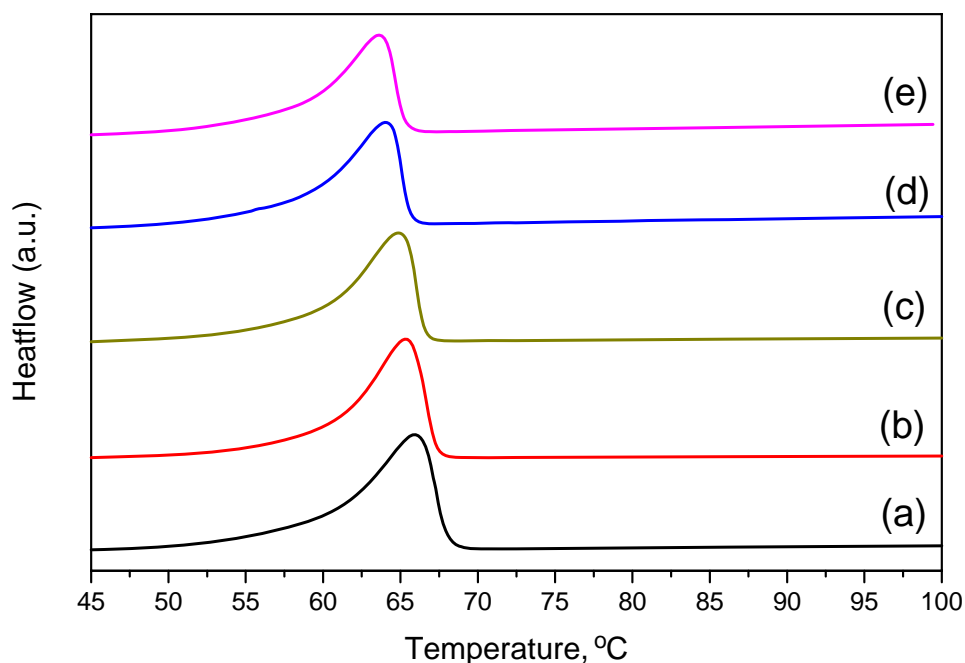


Figure 4.43 DSC thermogram for (a) pure MMT, (b) PEO/5%MMT, (c) PEO/10%MMT, (d) PEO/15%MMT and (e) PEO/20%MMT

Table 4.20 Melting temperatures (T_m), enthalpy of melting (ΔH_m) and percentage crystallinity ($\%X_c$) of PEO and PEO+clay at various clay concentration

Composition	T_m (°C)	ΔH_m (J g ⁻¹)	Crystallinity ($\%X_c$)
PEO	65.98	166.90	91.46
PEO/5%Clay	65.28	152.54	83.47
PEO/10%Clay	65.13	139.11	65.84
PEO/15%Clay	64.09	121.23	64.43
PEO/20%Clay	63.64	116.36	61.86
P(EO) ₈ NaSCN	62.58	135.33	52.10
P(EO) ₈ NaSCN/5%Clay	54.24	57.90	30.80
P(EO) ₈ NaSCN/10%Clay	63.95	66.14	34.45
P(EO) ₈ NaSCN/15%Clay	62.11	54.50	30.31
P(EO) ₈ NaSCN/20%Clay	61.78	46.78	23.88

The reported value of ΔH_m of 100% crystalline PEO is 45 cal g⁻¹ or 188.1 J g⁻¹.

(Preechatiwong *et al.*, 1996)

4.2.3.2. PEO/NaSCN/MMT nanocomposite

Figure 4.44 presents DSC curves for pure, undoped PEO and the P(EO)₈NaSCN /MMT electrolyte containing 5, 10, 15 and 20 wt% of MMT. In order to clarify the phenomenon of increasing PEO crystallinity with the presence of the small amount of clay, Figure 4.44 shows plots of the percent of crystallinity against clay content (wt%). The percent of crystallinity is calculated by using Eq. (4.25). It is found that $\%X_c$ of undoped PEO system shift towards lower values with increasing.

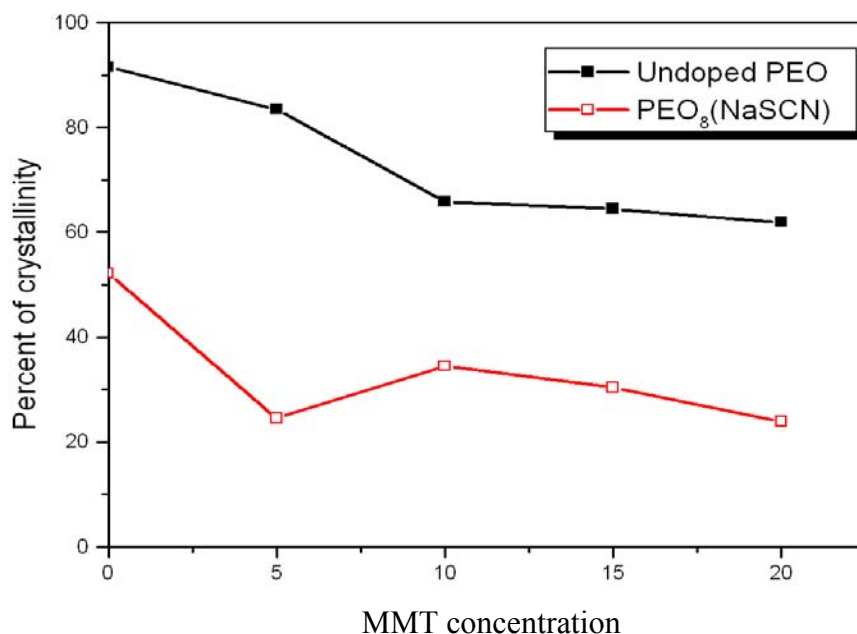


Figure 4.44 Percentage of crystallinity ($\%X_c$) versus MMT concentration (wt%) for PEO/MMT and P(EO)₈NaSCN/MMT nanocomposite

MMT content. For MMT concentration <10 wt%, the reduction of $\%X_c$ is almost 30%. With more adding MMT content >10 wt%, $\%X_c$ drop slightly within 10% range.

As can be seen, for of the undoped PEO system, $\%X_c$ decreases gradually with increasing MMT content, and this phenomenon can be attributed to a steric hindrance caused by huge surface area of the clay. This observed trend in PEO crystallinity can be interpreted as the Lewis acid–base type interactions among polyether matrix, clay filler, sodium cation and corresponding anion. (Chang *et al.*, 2002) The PEO crystallinity ($\%X_c$) in the P(EO)₈NaSCN /clay system is also altered with the addition of MMT. The PEO crystallinity initially decreases with increasing MMT content up to 5%. Then it increases and reaches a maximum value at 10%MMT. After that $\%X_c$ slightly decreases as the MMT content is further increased (less than 10%). Although,

we did not study the change in the glass transition temperature (T_g) in PEO/MMT and P(EO)₈NaSCN/MMT system, we expect that T_g will decline as the MMT content increases and reach a minimum when MMT concentration is about 5%. Subsequently, T_g should increase dramatically with a further increase of the MMT concentration. The decrease in T_g is caused by the weakening of the salting effect when the MMT is incorporated. In other words, adding MMT can reduce the interaction between ether group and sodium cations. A higher MMT content reduces the interaction between silicate layers and sodium salts because of the strong self-aggregation among these silicate layers. Meanwhile, the ether group has more chances to cluster the sodium cation leading to a higher PEO T_g . Self-aggregation not only reduces the probability of interaction between silicate layers and lithium cations but also creates a steric hindrance that retards the chain mobility. In this system, two adverse and competitive effects are present; one favors lower T_g (Lewis base-acid interaction), and the other favors higher T_g (steric effect of clay agglomeration). For the P(EO)₈NaSCN/MMT system; T_g increases slightly as the content of clay increases. This behavior is attributable to the strong agglomeration among the silicate layers and the fact that the unfavorable effect (steric hindrance) dominates the favorable effect (draw Na⁺ into the MMT region), even with a small quantity of the MMT. Therefore, T_g of PEO increases steadily with MMT content.

From the results of DSC described previously, three types of complexes can be proposed, which are depicted in Figure 4.45. Complex I are present in the pure PEO phase and complex III is located within the clay phase. Complex II located at the interphase plays the key role in stabilizing these two microstructure phases. Without containing clay, the P(EO)₈NaSCN system forms only the complex I. Portion of the

complex I tends to convert into complex II and complex III, due to strong interaction existing between Na^+ cations and silicate layers of the clay. Shifting from complex I into complex II and complex III, portion of the original sodium cations have been drawn into the clay region and induces higher PEO chain flexibility and also higher crystallinity. In this aspect, the presence of clay (<10 wt%) causes higher PEO crystallinity due to greater PEO chain flexibility. However, more clay content (>10 wt%) results in forming more complex II and complex III, which can act as crystallization retarders (especially complex II) due to the steric hindrance and leads to lower PEO crystallinity as shown in Figure 4.44. In this system, two adverse and competitive effects occur, one is favorable and other unfavorable for PEO crystallinity.

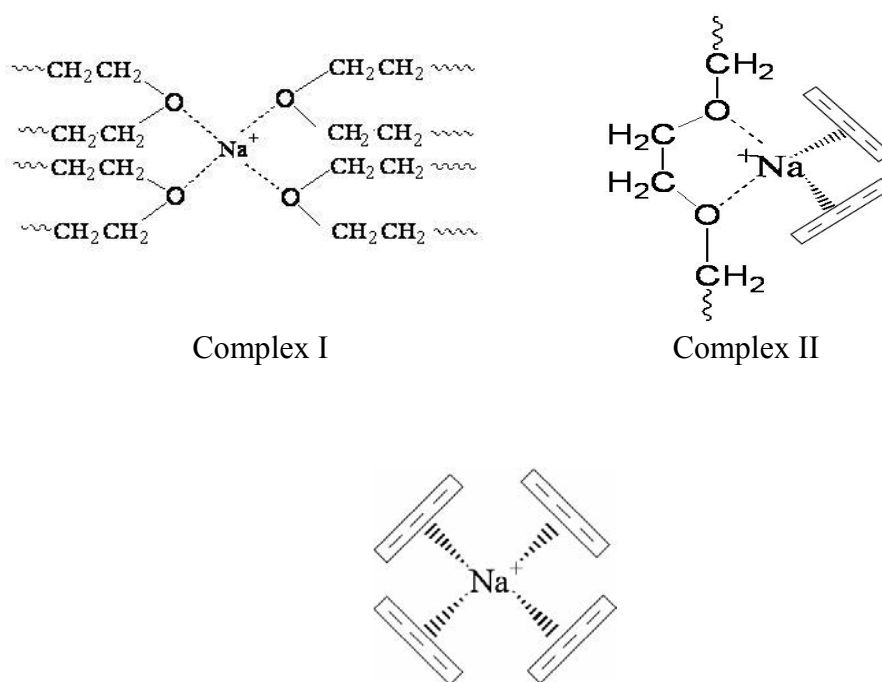


Figure 4.45 Schematic structure of Complex III coordinated by Na^+ cation with (a) polyether chains (complex I), (b) polyether and silicate layers (complex II), (c) silicate layers (complex III)

For the undoped salt (PEO/MMT) system, the $X_c\%$ decreases progressively with increasing MMT content (Figure 4.44, square line). The favorable effect is the steric hindrance caused by adding clay and thus retards PEO crystallinity. Therefore, PEO crystallinity decreases progressively with the increase in MMT content. In addition we also analyse the effect of salt and MMT on the crystallization kinetics of PEO/MMT and $P(\text{EO})_8\text{NaSCN/MMT}$ complexes using DSC. For the results and discussions of this part were presented separately in Section 4.2.1.

4.2.4 Fourier Transform Infrared Spectroscopy (FT-IR)

Although XRD results supply information on the gallery size from the increase of basal spacing, the structure of the polymer itself cannot be deduced due to a very low (if any) crystallinity of the polymer in the hybrid gallery. Spectroscopic techniques, such as IR, Raman and NMR are useful in order to establish the PEO structure inside the gallery, as well as the existence of interactions between the PEO chains and the cations in the gallery. A brief introduction to previous IR analyses on PEO, PEO–alkali metal salt complexes and PEO–clay nanocomposites is summarized prior to results being presented and discussed.

4.2.4.1 PEO/Montmorillonite nanocomposite

PEO has been studied extensively in last 40 years by IR or Raman spectroscopy. Vibrational studies have been carried out on the PEO in the crystalline state, in molten state, in aqueous solution and in chloroform solution (Wang *et al.*, 2003; Simon *et al.*, 2003). For the crystalline PEO, these conformational assignments have been supported by normal coordinate treatments of various skeletal models and by detailed X-ray analysis. PEO is found to have a helical structure in the crystalline state. The polymer chain has seven $\text{CH}_2\text{CH}_2\text{O}$ units in two turns of the

helix with a crystallographic repeat distance of 19.3 Å. The conformation along this chain are nearly *trans* (CC–OC), *trans* (CO–CC) and *gauche* (OC–CO). These preferred conformations for each bond are also consistent with prediction from an *ab initio* calculation and RIS model presented in Section 4.1.3, e.g. the *trans* fraction of CC-OC bond (f_t^{CO}) and fraction of OC-CO (f_t^{CC}) are 0.7 and 0.2, respectively. In this work, some characteristic vibrations of PEO were investigated. For example, the 1000-800 cm^{-1} spectral region is due to of C-O stretching and CH_2 rocking modes. The characteristic of crystalline PEO is represented by CH_2 wagging modes 1360-1340 cm^{-1} .

For polymer electrolyte system, the vibrational spectroscopy and structure of a number of PEO complexes of alkali metal salts have also been studied (Wang *et al.*, 2003, 2005). In particular, NaX and KX complexes of PEO are believed to be in the crystalline state and have a helical configuration for the polymer, some of the PEO chains possibly wound around the alkali cations. The conformation may be approximated as a compressed helix, as opposed to the more extended and open helix of pure crystalline PEO. In addition, the IR spectra of PEO/MMT nanocomposites have been recently studied. In general, the preparation method for those polymer samples was solution intercalation using water or acetonitrile as a solvent. However, the ratio of PEO/MMT was not determined in those studies, but excess PEO (to the amount necessary to saturate the gallery) was likely since characteristic PEO peaks in the corresponding X-ray diffractograms could be seen, and removed by washing with acetonitrile followed by methanol. A helical structure of PEO in the gallery of the hybrid was claimed, supported by ^{23}Na NMR results and by comparing IR results with those from PEO–alkali salt complexes.

As suggested by XRD results in Section 4.2.2, the interaction between PEO and MMT should be very weak compared to that of PEO and salt. It is therefore hardly to observe any change in FTIR spectra for PEO versus PEO/MMT. In this respect, alternative sample preparation is needed in order to obtain higher MMT:PEO ratio so that one can enhance IR signal and gain better peak resolution for PEO/MMT interaction. Besides the solution method using methanol as a solvent, we also employ melt intercalation and microwave irradiation technique were also employed to prepare samples with higher proportion of MMT:PEO (20-80 wt%). Polymer melt intercalation was accomplished by annealing the pressed pellets in an electrical resistance furnace at 80°C and the annealing time allowed for full intercalation to take place was about 8 h. For microwave irradiation technique, the same sample as melt intercalation was put into the microwave oven and heated at 472 watts for about 5 minutes to make sure that PEO was completely intercalated into MMT. From XRD, FTIR and DSC results, it was found that there was no significant difference between the samples prepared from melt intercalation and microwave technique. Therefore, only the results from the melt intercalation are presented in this section.

Figure 4.46 illustrates the FTIR spectra from 4000 to 400 cm^{-1} for PEO, dry MMT and PEO/MMT hybrids via melt intercalation, respectively. Here, we report only the results of 60%MMT/PEO system were reported to illustrate either similarity or difference compared to the pristine MMT and PEO. In order to facilitate this comparison, Figure 4.46 was divided into sub-regions of 3000-2600 cm^{-1} (Figure 4.47), 1400-1300 cm^{-1} (Figure 4.48) and 1000-800 cm^{-1} (Figure 4.49). Results and discussion are presented as following.

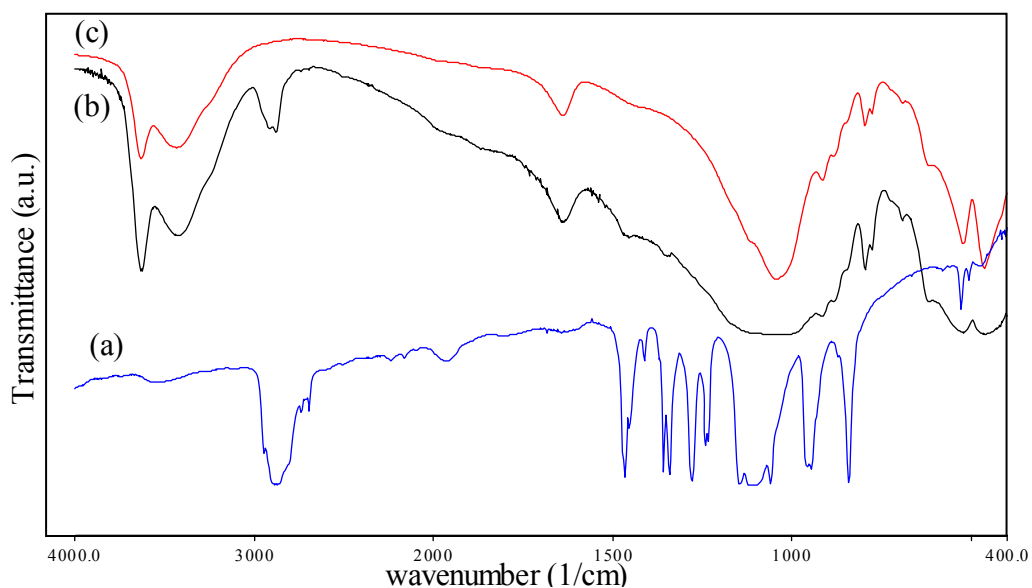


Figure 4.46 FTIR spectra for (a) PEO, (b) 60%MMT/PEO(prepared by melt intercalation) and (c) MMT in the 4000-400 cm^{-1} region

The most significant changes upon intercalation, illustrated in Figure 4.47, correspond to the stretching and deformation vibration of the methylene groups. Pure PEO exhibits a large, broad band of asymmetric CH_2 stretching between 2935 and 2850 cm^{-1} and two narrow bands of lower intensity at 2738 and 2693 cm^{-1} . In the intercalated hybrids, these bands are disappeared. In relation to the CH_2 stretching bands, which appear in the 1500-1200 cm^{-1} regions, the most notable changes occur to the band at 1342 cm^{-1} (CH_2 bending mode) and 1360 cm^{-1} (CH_2 wagging). In the intercalated hybrids, these two bands are also disappeared. Figure 4.48 shows the IR peaks at 1360 and 1342 cm^{-1} which are the characteristics of crystalline PEO. With an addition of MMT into PEO sample, the intensities of these peaks decrease drastically and completely disappear for 60%MMT/PEO mixture. This result suggest a disruption of PEO crystal caused by MMT. In a previous study (Simon *et al.*, 2002) this was interpreted in terms of ion-dipole interaction between the oxygen atoms of PEO units,

and the interlayer cations. It can, thus be inferred that PEO interacts with the interlayer cations in a similar manner to conventional PEO-salt complex as the same cation (Na^+) exist in both salt (NaSCN) and clay (Na-MMT).

Aranda and Ruiz-Hitzky (1992) claimed that the spectra at low clay content were indicative of the presence of *gauche* conformations of the $-\text{CH}_2-\text{CH}_2-$ groups, as required for a helical PEO conformation. The factors supporting this assignment were as follows: (i) the presence of two bands near 945 and 842 cm^{-1} assigned to CH_2 rocking vibrations of methylene groups in the *gauche* conformation, like in PEO-salt complexes and (ii) the absence of a characteristic IR band near 1320 cm^{-1} assigned to CH_2 stretching vibration of ethylene groups in the *trans* conformation.

In this study, the two bands at 945 and 842 cm^{-1} which are related to helical structures are only clearly observed in the pure PEO sample, and are not apparent in the intercalated hybrid (Figure 4.11). In Figure 4.10, the bands at 2238, 2163 and 1963 cm^{-1} in the spectrum of pure PEO sample, are also not observed for the hybrids. A new band appears at 798 and 916 cm^{-1} as shown in Figure 4.10(c) and (d) indicating a stretching mode of the Al-O-H band in MMT hybrid but not observed in pure PEO. Since the IR absorption bands of samples are compared to that of crystalline PEO with a helical conformation, it leads to the conclusion that the PEO helical conformation (945 and 842 cm^{-1}), is highly distorted, or at least rather stretched, if indeed it still exists. In addition, the molecular model to describe the PEO conformation in MMT hybrids has been proposed and presented previously in Section 4.2.1.

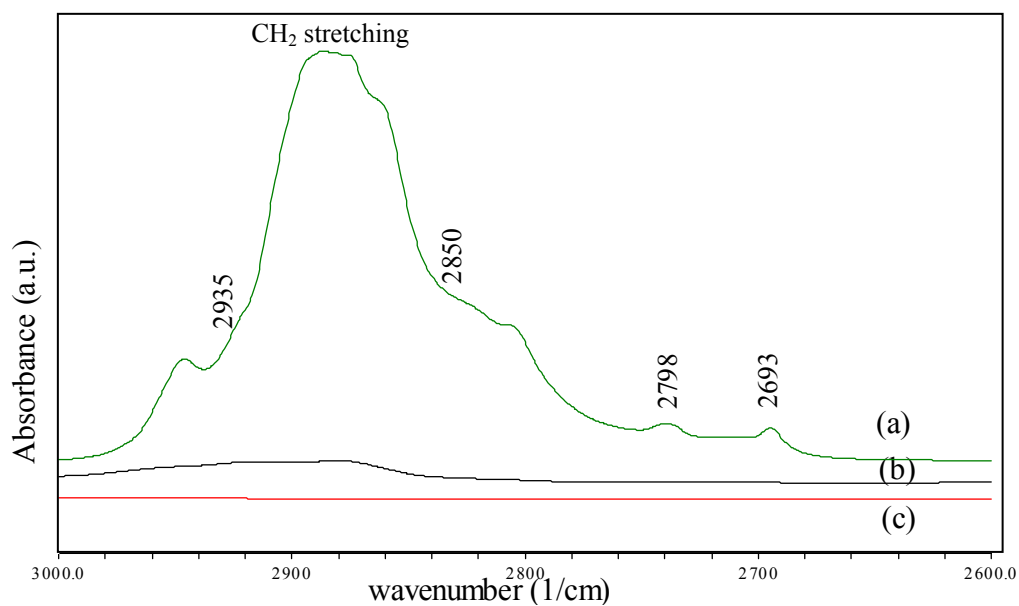


Figure 4.47 FTIR spectra for (a) PEO, (b) 60%MMT/PEO (prepared by melt intercalation) and (c) MMT in the 3100-2600 cm^{-1} region

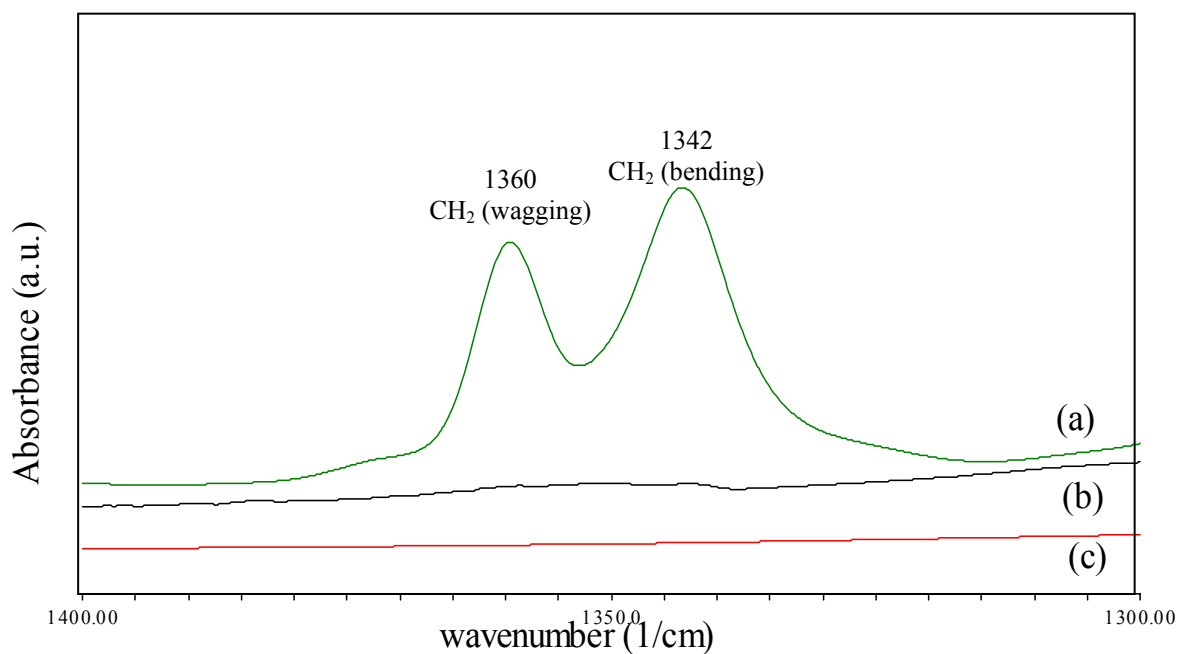


Figure 4.48 FTIR spectra for (a) PEO, (b) 60%MMT/PEO(prepared by melt intercalation) and (c) MMT in the 1400-1300 cm^{-1} region

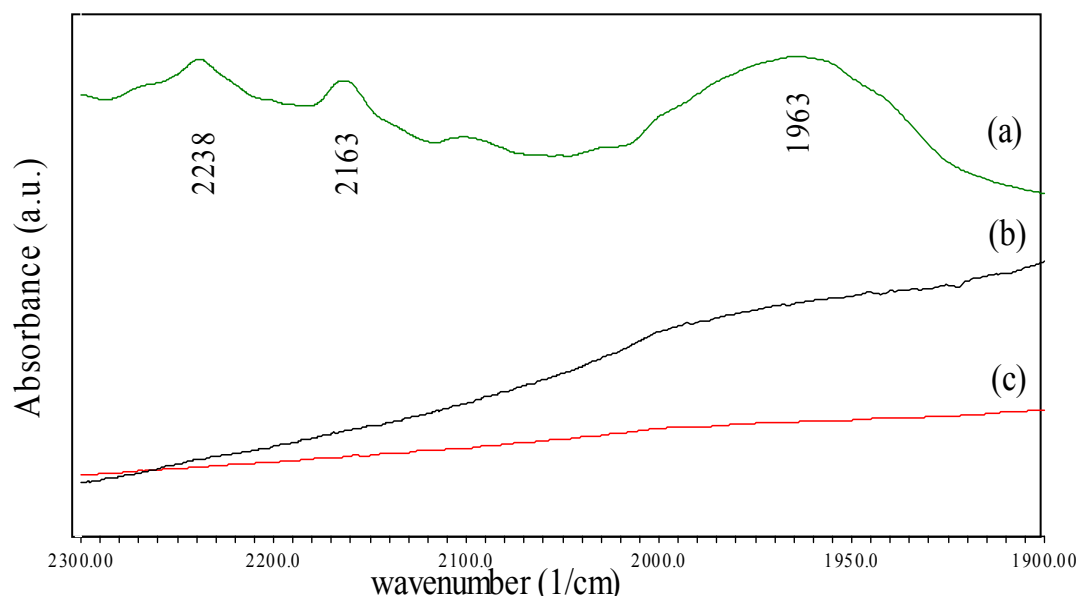


Figure 4.49 FTIR spectra for (a) PEO, (b) 60%MMT/PEO (prepared by melt intercalation) and (c) MMT in 2300-1900 cm^{-1} region

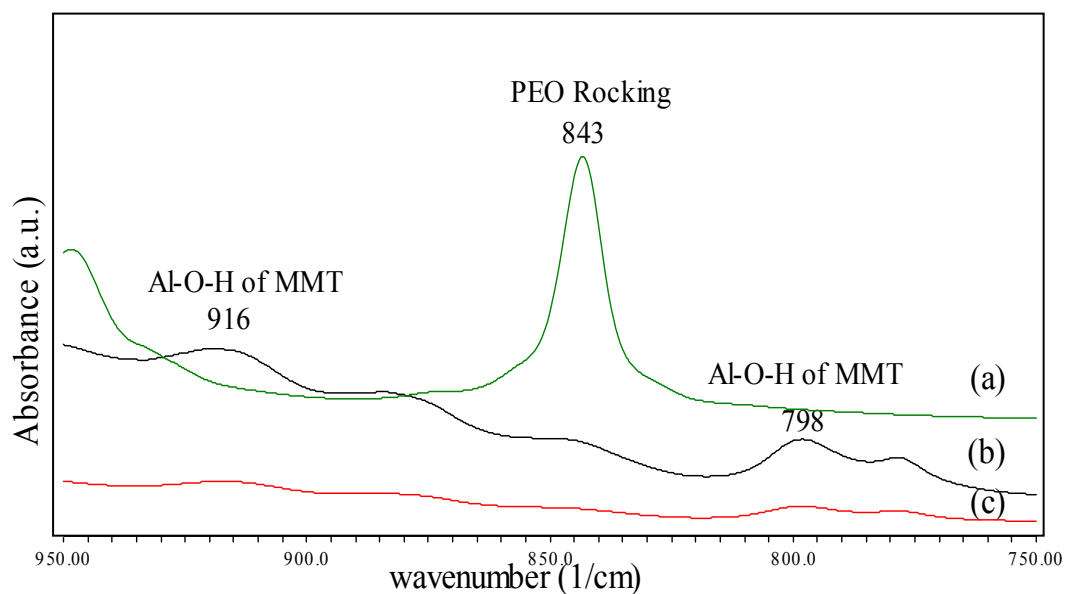


Figure 4.50 FTIR spectra for (a) PEO, (b) 60%MMT/PEO (prepared by melt intercalation) and (c) MMT in 950-750 cm^{-1} region

Table 4.21 IR absorption bands and their assignments of PEO, dry MMT and PEO/MMT hybrid (4000-400 cm^{-1}) (mode assignments: ν (stretching); δ (bending); w (wagging); t (twisting); r (rocking). The subscripts a and s denote the asymmetric and symmetric motions with respect to the twofold axis perpendicular to the helix axis and passing through the O atom or through the center of the C–C bond)

Frequency (cm^{-1})	Frequency in the reference* (cm^{-1}) (Simon <i>et al.</i> , 2002)	Assignment	Appearance in materials
2945-2890	2940-2840	$\nu(\text{CH}_2)_a$	PEO
2901-2859	2923,2910	$\nu(\text{CH}_2)_a$, $\nu(\text{CH}_2)_a$	Hybrid, Hybrid
2238	2240		PEO
2196	2170		PEO
1965	1970		PEO
1645	1640	$\nu(\text{C}-\text{O})_a$	PEO; Clay
1467	1462	$\delta(\text{CH}_2)_a$	PEO, hybrid
1413	1455	$\delta(\text{CH}_2)_a$	PEO, hybrid
1360	1362	$\omega(\text{CH}_2)_s$	PEO
1343	1342	$\delta(\text{CH}_2)_a$	PEO
1280	1282	$t(\text{CH}_2)_a$	PEO, hybrid
1242	1242	$t(\text{CH}_2)_a$	PEO, hybrid
962	962	$r(\text{CH}_2)_a$	PEO
798,916	800,916	$V(\text{Al}-\text{O}-\text{H})$	MMT, hybrid
843	840	$r(\text{CH}_2)_s$	PEO
530,465	525,470	$N(\text{Al}(\text{Mg})-\text{O}-\text{Si})$	Clay, hybrid

4.2.4.2. PEO/NaSCN electrolyte complex

Ionic Association

For PEO/NaSCN complexes, absorption intensity of the stretching mode of SCN^- anion is high and sensitive to its ionization states. In addition, the overlap of absorption of SCN^- with that of PEO is negligible. In this research, NaSCN was selected to investigate the ionic association in PEO-based SPEs by vibrational spectroscopy according to the following reasons: (Wang *et al.*, 2003, 2005)

- SCN^- is known to be a linear anion and may form complex with metal ions through the nitrogen or sulfur atom.
- SCN^- belongs to point group symmetry C_v and has three vibrational modes that are associated with the CN stretching, the CS stretching, and the doubly degenerate SCN^- bending modes, respectively.
- The CN stretching modes have high absorption intensity, high sensitivity to its ionization states, and little overlap with the FT-IR spectrum of PEO.
- The bonding of SCN^- with a given metal cation can be well explained by hard/soft acid/base theory. The alkali cations are hard acid and are expected to form ion pairs with SCN^- at N-end where the charge density distribution is more tightly bound
- The formation of N- or S-bonded complex gives rise to spectral changes since the vibrational frequencies of CN stretching mode in SCN^- are sensitive to such interactions.

Figure 4.51 is a representative plot of the infrared spectrum for CN stretching vibrational mode in PEO–NaSCN complex (at varied salt concentration). The peak at

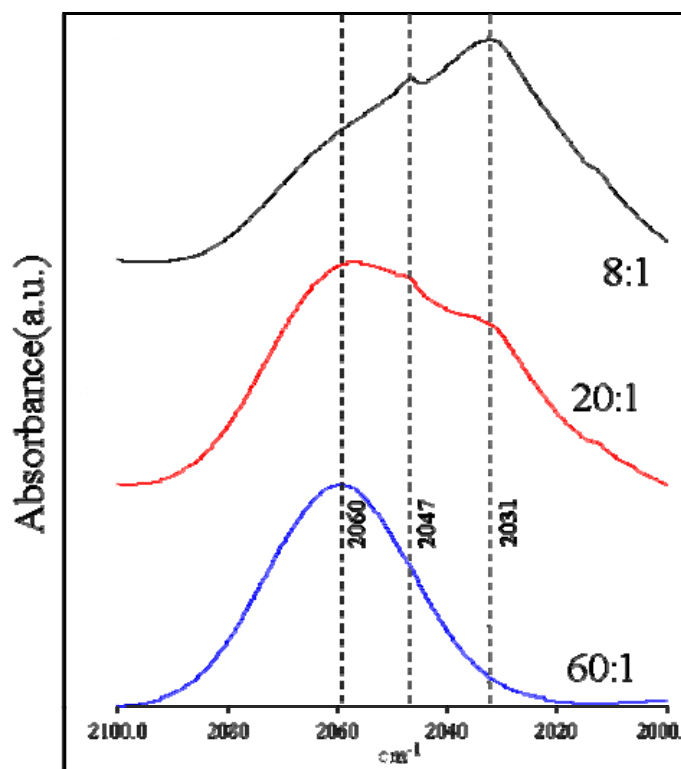


Figure 4.51 IR spectra of PEO–NaSCN system. The compositions of SPEs were indicated for each curve.

2047 cm^{-1} is assigned to spectroscopically free SCN^- and solvent-separated ion pair ($\text{Na}^+ \dots \text{SCN}^-$). The predominant peak at 2060 cm^{-1} is ascribed to the contact ion pairs ($\text{Na}^+ \text{SCN}^-$), and solvent-separated dimers ($\text{Na}^+ \text{SCN}^- \dots \text{Na}^+ \text{SCN}^-$). The peak at 2031 cm^{-1} is associated possibly with the stretching vibration of SCN^- in $\text{P}(\text{EO})_8\text{NaSCN}$ and indicative of the formation of crystalline complex $\text{P}(\text{EO})_8\text{NaSCN}$.

To determine the relative quantity of each ionic species, the spectra in the interested region (2000–2100 cm^{-1}) were adjusted to have a straight base line and deconvoluted by the product of Lorentzian functions. All of these operations were done using Origin version 4 software.

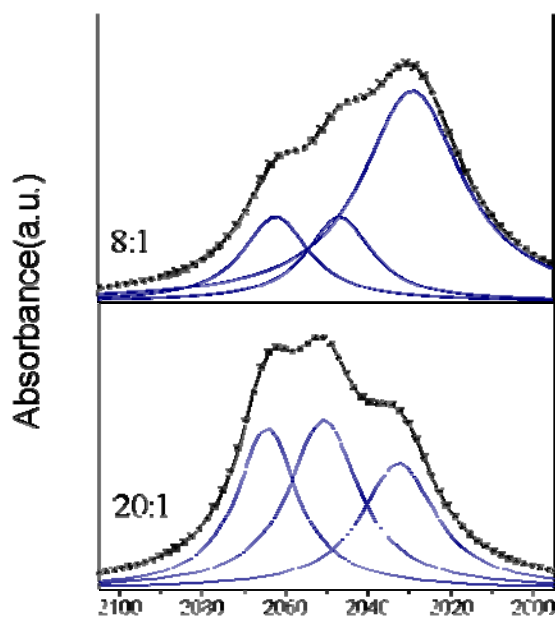


Figure 4.52 Deconvolution of the CN stretching mode for P(EO)₂₀NaSCN and P(EO)₈NaSCN electrolyte

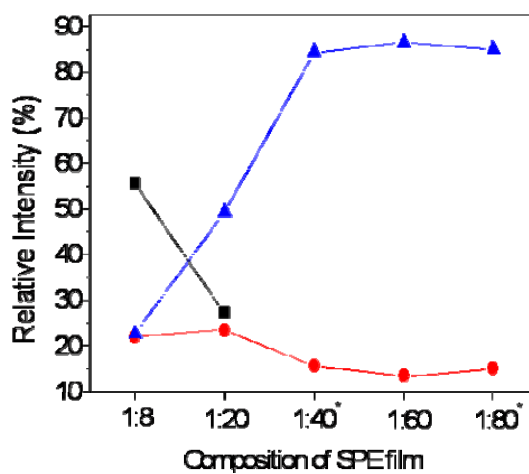


Figure 4.53 The results of curve-fitting data for deconvolution of P(EO)_nNaSCN electrolytes. ●: 2047 cm⁻¹, ▲: 2060 cm⁻¹, ■: 2031 cm⁻¹

The results of the curve fitting for P(EO)_nNaSCN electrolytes are shown in Figure 4.53 in which the relative intensities of three peaks are expressed as percents. Key observations can be pointed out as follows. In the range of high content of salt, it can be seen that the percent of free ions and contact ion pairs decreases with increasing concentration of salt. It is well known that the introduction of salt into the pure polymeric matrix can modify PEO morphology which is composed of crystalline and amorphous phases. Therefore, when SCN⁻ ions are added to PEO, the crystalline phase of PEO is progressively transformed into amorphous phase since the large-size anions from the salt can play a role of "plasticizer". The solvation ability of PEO to metal cations was then improved, leading to the decrease of the higher ion aggregations with increasing concentrations of free ion and ion pairs. This experimental result indicates that P(EO)₈NaSCN is formed at the expense of the "free" Na⁺ wrapped by the ether oxygen of the PEO backbone, and the contact ion pairs become predominant species under the condition of PEO amorphous phase.

PEO Backbone Conformation

The spectral region 1000-800 cm⁻¹ (Figure 4.54) consists of a mixture of CH₂ rocking and C-O stretching vibrational modes. Spectral changes in this region reflect changes occurring in the local structure of the polymer backbone. The mode responsible for the band at 844 cm⁻¹ is primarily due to the CH₂ rocking motion with a little C-O stretching motion mixed in, while the bands at 964 and 949 cm⁻¹ originate primarily in the C-O stretching motion with some contribution from the CH₂ rocking motion. This assignment is in agreement with the observation of an 844 cm⁻¹ IR-active CH₂ rocking mode in crystalline PEO which has all -O-C-C-O- torsional angles in *gauche* conformations. Thus, this bond is ideal for monitoring the changes in

the conformation of PEO upon addition of clay and NaSCN. From Figure 4.54, no significant changes are seen in the spectra of the dilute samples with O:M ratios of 60:1. However, the peaks split considerably in the 20:1 system, signifying that the local structure is considerably disordered. In the 20:1 system, new peaks appear at 920 and 825 cm^{-1} , which increase in their intensity with increasing salt concentration. When the O:M ratio = 8:1, the bands at 844 cm^{-1} are split and appear at 853, 834 cm^{-1} (Figure 4.54). The frequencies of these bands primarily due to CH_2 rocking motion are particularly sensitive to the local conformation of the polymer, specifically the O-C-C-O torsional angle. This local structural modification of the backbone is caused by the cations interacting with the oxygen atoms as the sodium ions are coordinated by the polymer.

Figure 4.55 shows IR spectra in the 1200-1100 cm^{-1} region which is the C-O-C stretching. This vibrational mode is also sensitive to interactions of the polyether oxygen atoms with the cation. The position of the C-O stretching mode of pure PEO at 1115 cm^{-1} is shifted to 1100 cm^{-1} for the mixture with salt. The single broad peak of PEO is replaced by two distinct peaks at 1100 and 1074 cm^{-1} , which grow in their intensity with increases salt concentration. These experimental data indicate the solvating ability of PEO to NaSCN. It is also appropriate to state that the peak at 2037 cm^{-1} resulting from the stretching vibration of SCN^{-1} in $\text{P}(\text{EO})_8\text{NaSCN}$ complex. Therefore the crystalline complex $\text{P}(\text{EO})_8\text{NaSCN}$ is formed at high salt content. Along with the occurrence of this 2037 cm^{-1} peak, some other peaks also appear at 825, 834, 853, 920, 1074, 1136, 1351 and 1368 cm^{-1} . They become visible at salt concentration higher than that in $\text{P}(\text{EO})_8\text{NaSCN}$ complex as shown in Figures 4.54-4.56.

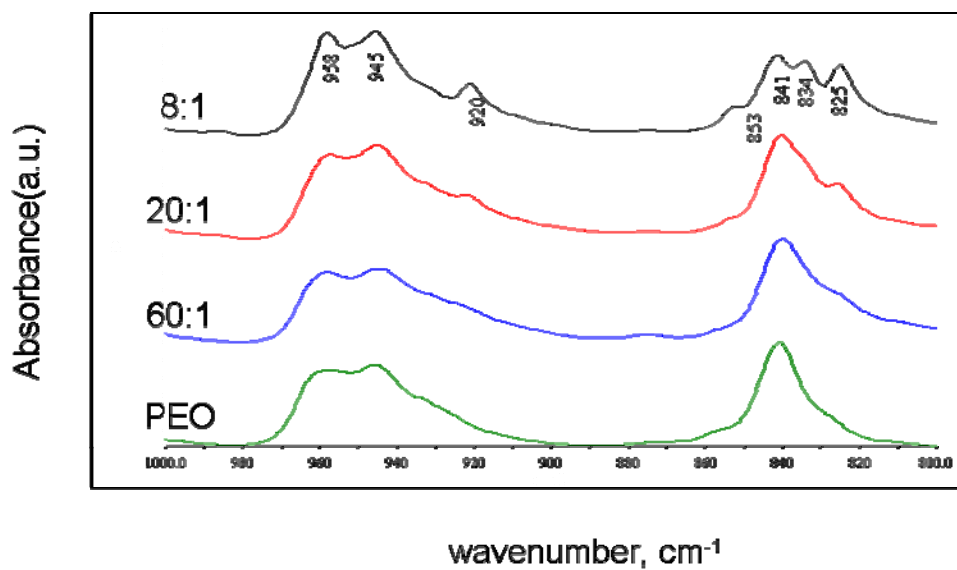


Figure 4.54 FTIR spectra of PEO in $P(\text{EO})_n\text{NaSCN}$ system in the $1000\text{-}800\text{ cm}^{-1}$ region. Content of each curve are given as concentration of NaSCN in PEO

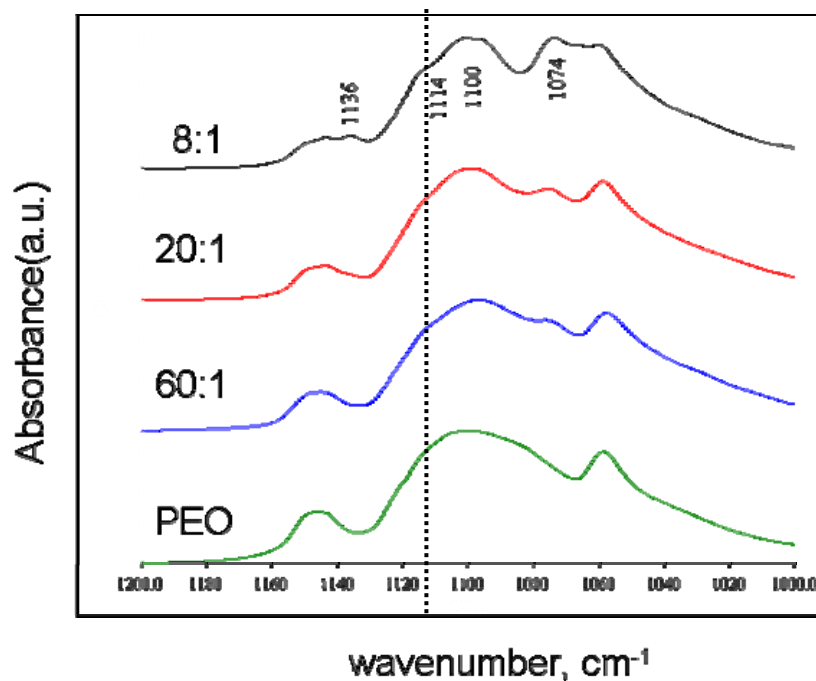


Figure 4.55 FTIR spectra of PEO in $P(\text{EO})_n\text{NaSCN}$ system in the $1200\text{-}1000\text{ cm}^{-1}$ region. Content of each curve are given as concentration of NaSCN in PEO.

Next, the 1300-1500 cm^{-1} spectral region of PEO is present in Figure 4.56. This band is a mixture of the vibrational modes of CH_2 wagging and twisting and is related to the crystalline phase of PEO. The peaks at 1360 and 1343 cm^{-1} are CH_2 wagging modes which are the characteristic of crystalline PEO. With an addition of NaSCN to PEO, the intensities of two peaks decrease drastically and are replaced by a sharp band at 1351 cm^{-1} . The sharp band at 1351 cm^{-1} is assigned to the amorphous content of PEO. All of these results support the formation of a crystalline complex with a well-defined stoichiometry, $\text{P}(\text{EO})_3\text{NaSCN}$, in addition to the crystalline and amorphous phase of PEO. In addition to these IR results, XRD and DSC data presented in Sections 4.2 and 4.3 also confirm this hypothesis.

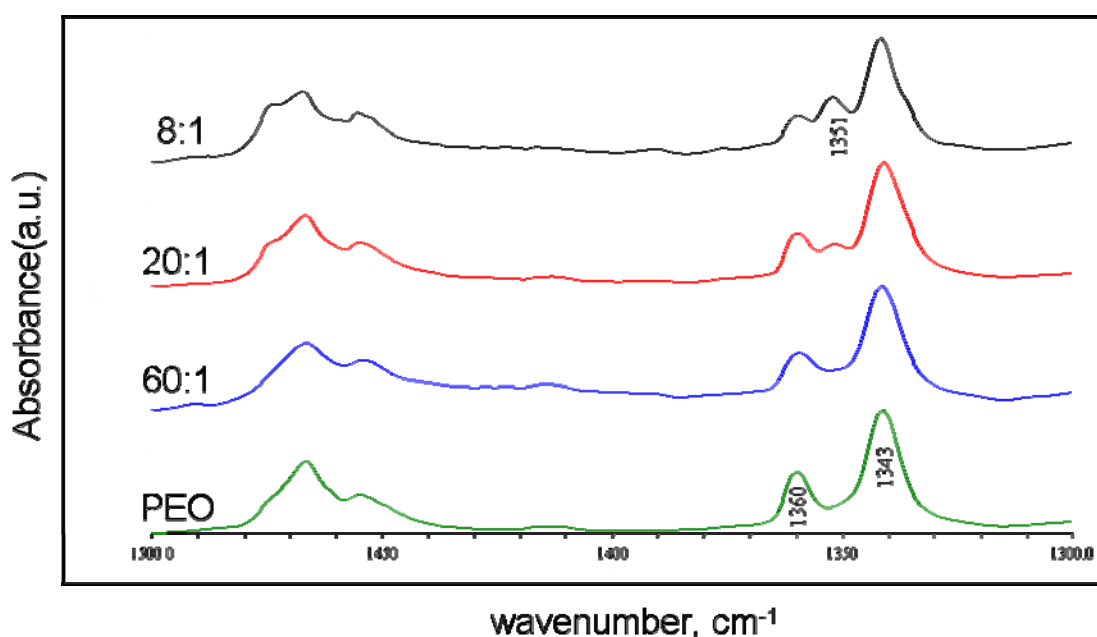


Figure 4.56 FTIR spectra of PEO in $\text{P}(\text{EO})_n\text{NaSCN}$ system in the 1500-1300 cm^{-1} region. Content of each curve is given as the concentration of NaSCN in PEO

4.2.4.3 PEO/NaSCN/MMT Electrolyte Nanocomposite

Ionic Association

The ambient property of SCN^- makes it possible to complex metal ions through its nitrogen or sulfur atoms and to form N- or S-bonded or bridge complexes, depending on the type of metals, the nature of the ligands, and the steric effects. Therefore, the interactions of Lewis acid-base type in PEO-NaSCN-MMT nanocomposite electrolytes involve the ether oxygen, the Lewis acid site on the MMT surface, Na^+ , nitrogen, and sulfur of SCN^- . Because Na^+ is a harder Lewis acid than MMT surface and has a tendency to bond with the hard base in SCN^- to form N-bonded complex, the contact ion-pairs and solvent-separated dimers formed by the interactions of Na^+ with N in SCN^- are the dominant forms of ion association in PEO-NaSCN electrolytes. For this reason, it can be believed that the effect of adding MMT on the ion association in PEO-NaSCN electrolytes depends mainly on the balance of interactions of MMT with ether oxygen and with sulfur of SCN^- .

Figure 4.57 shows the FT-IR spectra of $\text{P(EO)}_8\text{NaSCN}$ mixed with various MMT contents. For the undoped $\text{P(EO)}_8\text{NaSCN}$ electrolyte, the band at 2031 cm^{-1} is the dominant composition of the spectral envelope for CN stretching modes in the $2150\text{-}2000\text{ cm}^{-1}$ region. With the adding MMT content up to 15%, no significant changes are observed for the FT-IR spectrum of PEO vibration and the spectral envelope of SCN^- . The band at 2037 cm^{-1} is an indication of the formation of crystalline complex $\text{P(EO)}_8\text{NaSCN}$ and is associated with the CN stretching vibration in $\text{P(EO)}_8\text{NaSCN}$, discussed in details in Section 4.2.4.2.

On the other hand, the relative intensity of the band at $\sim 2060\text{ cm}^{-1}$ (stretching vibration of SCN^-) increases to 10 wt% clay concentration and then decreases at the

expense of the band at $\sim 2037\text{ cm}^{-1}$, indicating that the disintegration of crystalline PEO phase causes a decrease in the crystalline $\text{P(EO)}_8\text{NaSCN}$ complex. When the clay content in blend-based electrolytes is 5-10%, PEO has higher amorphous other clay concentration and the stretching vibration of SCN^{-1} exhibits a dominant band at 2060 cm^{-1} . For more MMT content ($>10\%$), FTIR spectra were similar to that of $\text{P(EO)}_8\text{NaSCN}$ (without adding MMT) because $\text{P(EO)}_8\text{NaSCN}$ was formed and free Na^+ cation was surrounded by ether oxygen of PEO backbone, thus the contact ion pairs (2031 cm^{-1}) became predominant species under the higher MMT ($>10\%$) content. In order to describe clearly the effect of clay on ion association in $\text{P(EO)}_8\text{NaSCN}$ electrolyte, the spectral envelope was reproduced by curve fit in the range of $2000\text{--}2100\text{ cm}^{-1}$. The results of curve-fitting for $\text{P(EO)}_8\text{NaSCN}$ /MMT complexes were expressed as the percentages of relative intensity for the bands present. Figure 4.19 shows the dependence of relative intensities of the bands at 2031 cm^{-1} (SCN^{-1} in $\text{P(EO)}_8\text{NaSCN}$), 2047 cm^{-1} (free SCN^{-1}) and 2060 cm^{-1} (contact ion pairs (Na^+SCN^-)) on MMT content. It can be seen that the relative intensity of the 2060 cm^{-1} band increases, while that of the band at 2047 cm^{-1} is almost unchanged with increasing MMT concentration. However, the relative intensity of the band at 2031 cm^{-1} decreases at the 0-10% MMT content and then increases again after 10% MMT.. When the MMT content in $\text{P(EO)}_8\text{NaSCN}$ electrolyte is higher than 5%, the relative intensity of the 2060 cm^{-1} band decreases whereas that of the reduction of the band at 2031 cm^{-1} increases. It is suggested that the superfluous MMT can cause the reduction of the solvating ability of PEO due to the dipolar interactions occurring among PEO, MMT and NaSCN. These facts substantiate that the band at 2060 cm^{-1} is related to PEO amorphous phase.

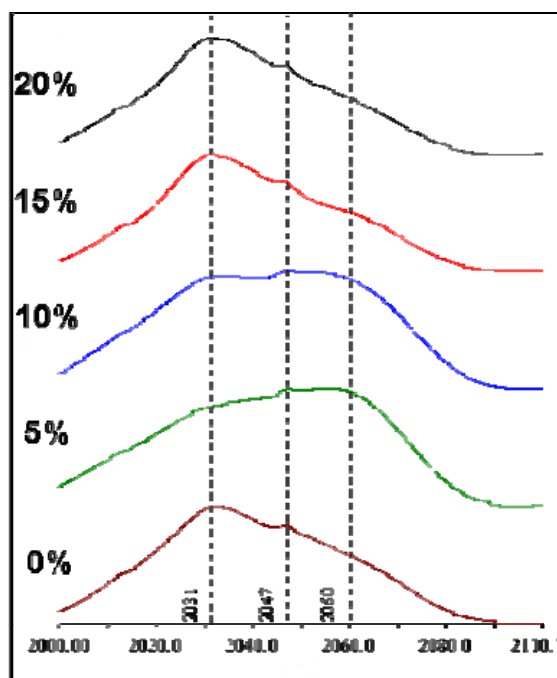


Figure 4.57 FT-IR spectra of SCN^- in blend-based (PEO/NaSCN/MMT) electrolytes in the region of $2000\text{-}2100\text{ cm}^{-1}$. The MMT contents for each curve are given as the weigh percentage of MMT in $\text{P}(\text{EO})_8\text{NaSCN}$ complexes

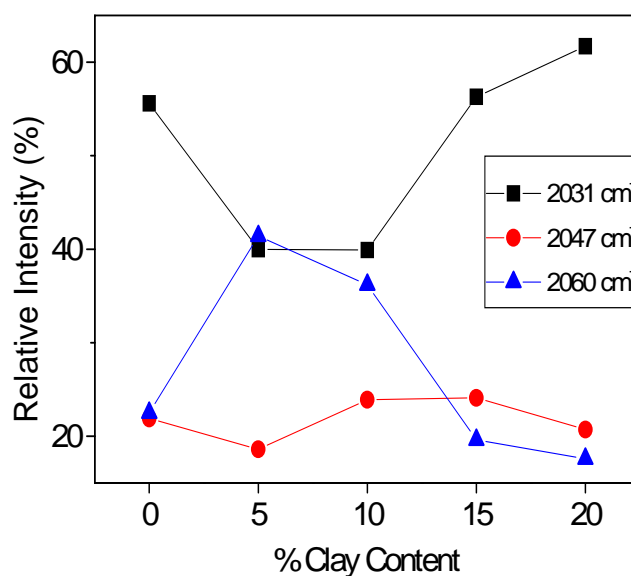


Figure 4.58 The relative intensities of three absorption peaks in $\text{P}(\text{EO})_8\text{NaSCN}$ electrolytes as a function of clay content

Therefore the effect of MMT on ion association in PEO–NaSCN electrolyte is caused by the transformation of PEO crystalline phase. These results suggest that the addition of clay to P(EO)₈NaSCN electrolyte in appropriate contents can effectively decrease the amount of crystalline complex.

In section 4.2.3.2, three types of complexes can be proposed to explain unusual characteristics of FTIR spectra for ionic association in PEO/NaSCN/MMT. The characteristic of MMT itself makes this polymer have more advantages for preparation of blend-based electrolytes. (i) MMT can keep its semi-crystalline nature even at low content, which provides the mechanical stability for PEO/MMT based electrolytes. (ii) The interactions of MMT with PEO in their polar domains result in their good compatibility, but do not depress the solvating ability of PEO if the MMT content is not too high ($\approx 5\%$). (iii) MMT can form intercalated nanocomposite structure with PEO, which decrease significantly the crystallization degree in the blend-based electrolytes and results in significant changes of ion association components. When MMT content in P(EO)₈NaSCN electrolyte is 0-10 wt%, PEO takes almost amorphous phase and the ion association of NaSCN in such blend host behaves like that in liquid PEO medium.

PEO Backbone Conformation

The spectral 1000-800 cm^{-1} region of PEO vibration is a mixture of C–O stretching and CH₂ rocking modes and is sensitive to the changes of macromolecular conformations as shown in Figure 4.59. When NaSCN was mixed salt in PEO, the peaks at 844, 945 and 958 cm^{-1} were broadened significantly. These peaks curve less seen for P(EO)₈NaSCN/10%MMT system compared to the corresponding peaks in PEO pristine and salt-doped PEO. Some peak also existed for P(EO)₈NaSCN which

were the characteristics of P(EO)₃NaSCN crystalline complexes at 825, 834, 853 cm⁻¹ (see Section 4.2.3.2). All of these peaks were almost disappeared when MMT was added to the structure. These findings indicate the formation of fully amorphous phase in P(EO)₈NaSCN/10%MMT system.

The 1200-1000 cm⁻¹ region is the position for C–O–C stretching which changes with the formation of cross-links due to the interactions of alkali metal cations with ether oxygen atoms in PEO as seen from Figure 4.60. The position of the C–O stretching mode was found to shift from 1114 cm⁻¹ to 1100 cm⁻¹ for P(EO)₈NaSCN and 10%MMT/P(EO)₈NaSCN system, respectively. These spectral changes were indicative of the formation for P(EO)₈NaSCN crystalline complex while MMT were added in P(EO)₈NaSCN system.

The spectral 1300-1500 cm⁻¹ region of PEO is a mixture of the vibrational modes of CH₂ wagging and twisting and is related to the crystalline phase of PEO as shown in Figure 4.23. With NaSCN was added into PEO the intensity of two peaks decreased drastically and there was a new sharp band at 1351 cm⁻¹ for P(EO)₈NaSCN. The sharp band at 1351 cm⁻¹ was assigned to amorphous content of PEO. This peak got higher intensity when 10%MMT was added, thus MMT caused PEO to transform its crystalline portion to an amorphous phase.

4.2.5 Impedance Analyzer

Ionic conductivity and impedance response were obtained using Solartron 2610 Impedance Analyzer. The composite film sample was sandwiched between two stainless steel blocking electrodes provided by Prof. Muhammad Careem (Department of Physics, University of Peradeniya, Sri Lanka). The specimen thickness varied from 0.03 to 0.08 mm. The impedance response was gauged at room temperature (30°C).

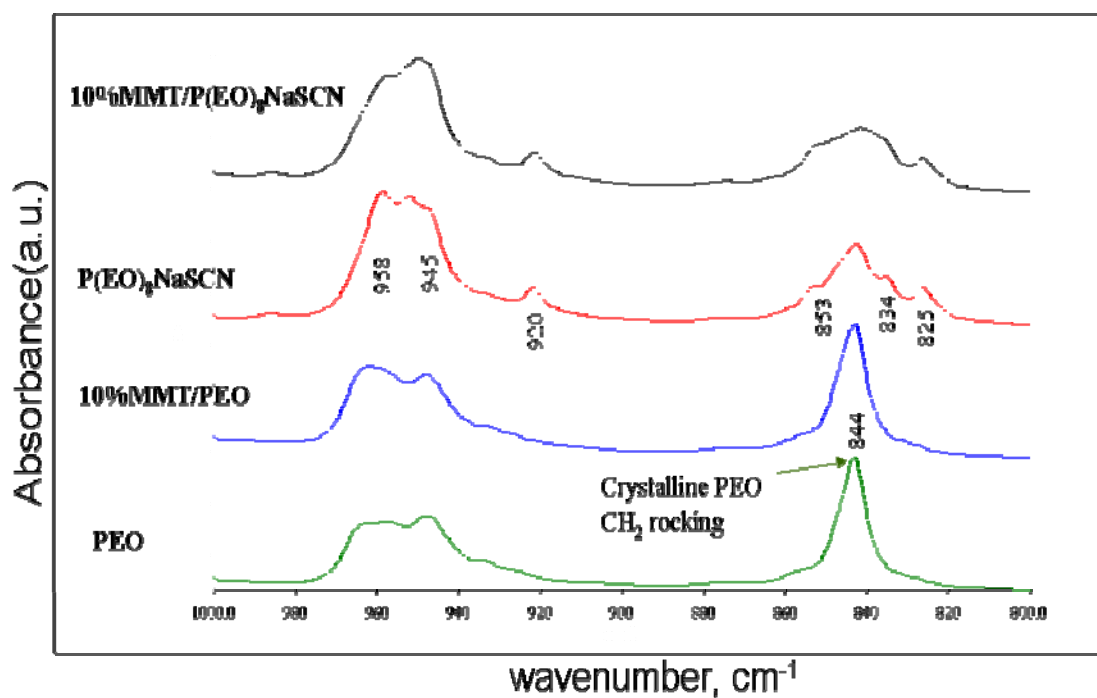


Figure 4.59 FTIR spectra of PEO, PEO/10%MMT, P(EO)₈NaSCN and P(EO)₈NaSCN/10%MMT system in the 1000-800 cm^{-1} region

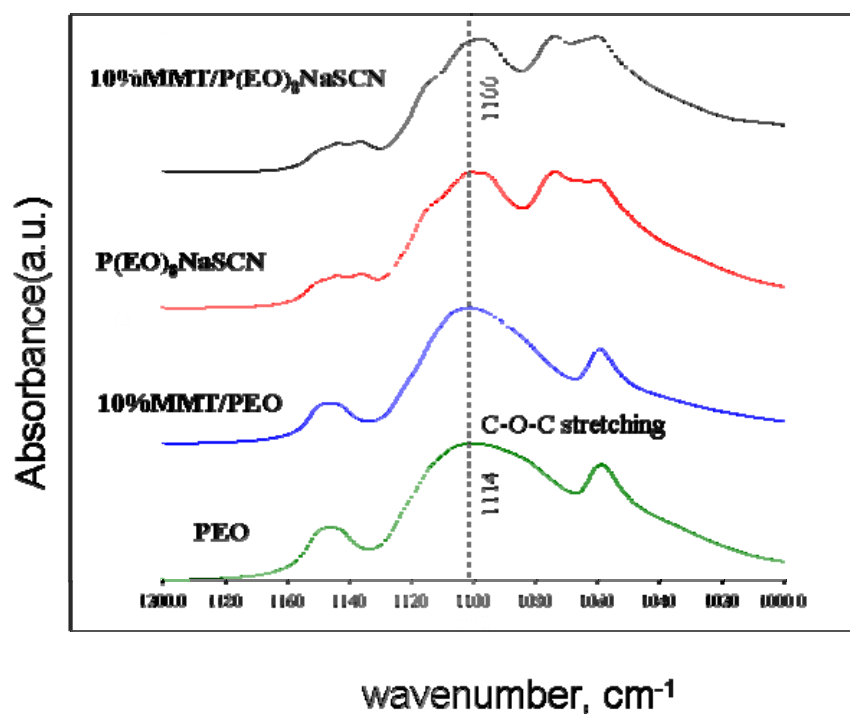


Figure 4.60 FTIR spectra of PEO, PEO/10%MMT, P(EO)₈NaSCN and P(EO)₈NaSCN/10%MMT system in the 1200-1000 cm^{-1} region

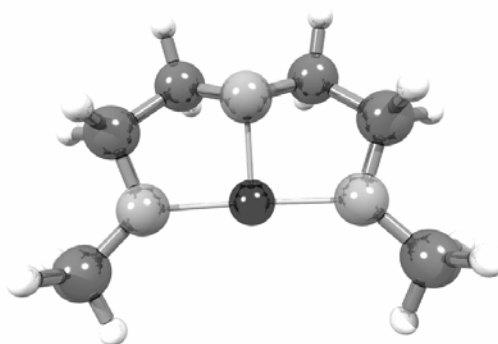


Figure 4.61 The model of C–O–C with the formation cross-link of alkali metal cations with ether oxygen atoms in PEO

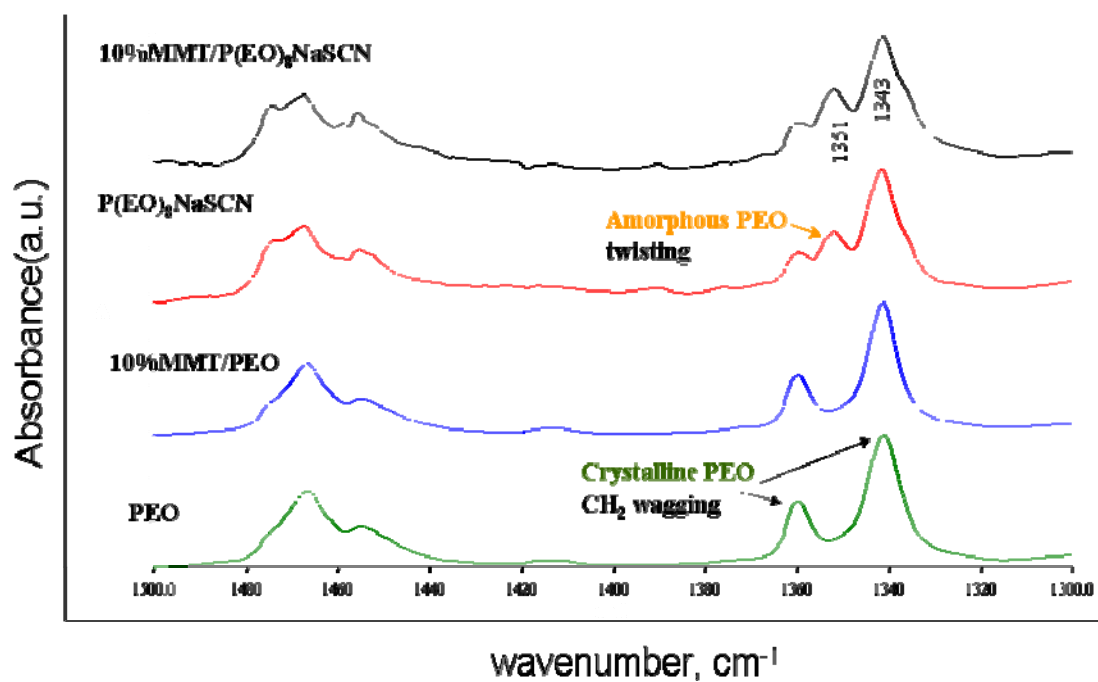


Figure 4.62 FTIR spectra of PEO, PEO/10%MMT, P(EO)₈NaSCN and P(EO)₈NaSCN/10%MMT system in the 1500–1300 cm⁻¹ region

These films were contacted with polished steel disc electrodes in an O-ring sealed sample holder, and the room temperature conductivity determined from A.C. impedance measurements in the frequency interval 10 MHz to 1 Hz. The experimental impedances were analyzed in terms of a model or equivalent circuit, using the computerized fitting software (Zview version 2.8d, Scribner Associates, Inc.)

It should be mentioned that Na⁺-montmorillonite samples in equilibrium with the atmospheric moisture have water molecules associated with the interlayer cations (Ruiz *et al.*, 1992) which show high degrees of dissociation, and consequently these materials present protonic conductivity. The magnitude of proton conductivity from MMT is very low so it affect very little of the overall conductivity in PEO/salt/MMT system. A typical Cole-Cole impedance diagram of these samples (Figure 4.63) consists of a semicircle at high frequencies followed by a "tail". That semicircle can be ascribed mainly to ionic conductivity of ions from NaSCN. The intercept point of the semicircle with the real axis (Z) at low frequency gives the ionic resistance (R_b) value and therefore the specific conductivity (10^{-5} - 10^{-7} S/cm at room temperature, depending on the water content and on the nature of the interlayer Na⁺ cation). PEO-NaSCN and PEO/MMT/NaSCN complexes show impedance diagrams as represented in Figure 4.63. As shown in Figure 4.63(a) and (b) when increase salt concentration, the depressed capacitive arcs are observed, probably due to the higher mobility ion is in system. In previous Sections, it is shown that PEO intercalated into silicate layer of MMT. Comparing Figure 4.63(b) and (c), the arcs are depressed, thus when adding 10%MMT into P(EO)₈NaSCN, the complex got higher ionic conductivity. These results indicate that the random state of polymer chains can weaken the interaction

between Na^+ ions and polymer chains, which is advantageous to Na^+ ions transport in polymer matrix.

Figure 4.64 shows a typical impedance diagram for a cell with blocking SS electrodes and a $\text{P(EO)}_{60}\text{NaSCN}$ electrolyte. The measured impedances can be modeled by the equivalent circuit shown in the insert on Figure 4.64, where C_b is referred to the capacitance arisen from dielectric polarization over the cell, C_{el} represents the capacitive coupling across the interface between electrolyte and the blocking electrodes, and R_b is the resistance to ionic conduction in the bulk electrolyte obtained from an x-intercept of Z' axis of the cole-cole plot. From R_b and the dimensions of the electrolyte pellet, the conductivity of the electrolyte can be calculated by $\sigma = l/R_b A$ (where l and A are film thickness and area respectively). Film thickness (l), bulk resistance (R_b) and ionic conductivity (σ) for each sample are presented in Table 4.22. The effect of adding MMT to ionic conductivity PEO/NaSCN was analyzed and discussed next.

Table 4.22 Film thickness, Bulk Resistance (R_b) and conductivity.

Sample	Thickness (mm)	R_b (ohm)	Conductivity(S/cm)
$\text{P(EO)}_8\text{NaSCN}$	0.090	66285	8.58E-06
$\text{P(EO)}_{20}\text{NaSCN}$	0.030	43422	5.19E-06
$\text{P(EO)}_{60}\text{NaSCN}$	0.045	100200	2.22E-06
$\text{P(EO)}_8\text{NaSCN}/5\%\text{MMTP}$	0.035	145890	1.80E-06
$\text{P(EO)}_8\text{NaSCN}/10\%\text{MMT}$	0.030	11251	2.00E-05
$\text{P(EO)}_8\text{NaSCN}/15\%\text{MMT}$	0.040	6238	4.82E-05
$\text{P(EO)}_8\text{NaSCN}/20\%\text{MMT}$	0.080	46720	1.29E-05

* Thickness for film samples were measured by micrometer.

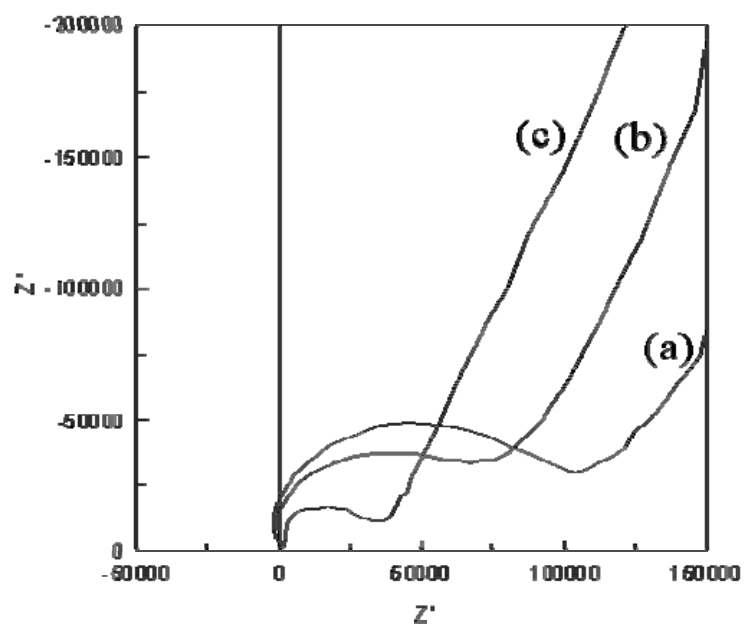


Figure 4.63 Typical impedance plots of the composite polymer electrolyte sample, (a) $P(\text{EO})_{60}\text{NaSCN}$, (b) $P(\text{EO})_8\text{NaSCN}$ and (c) $P(\text{EO})_8\text{NaSCN}/15\%\text{MMT}$ at room temperature (30°C)

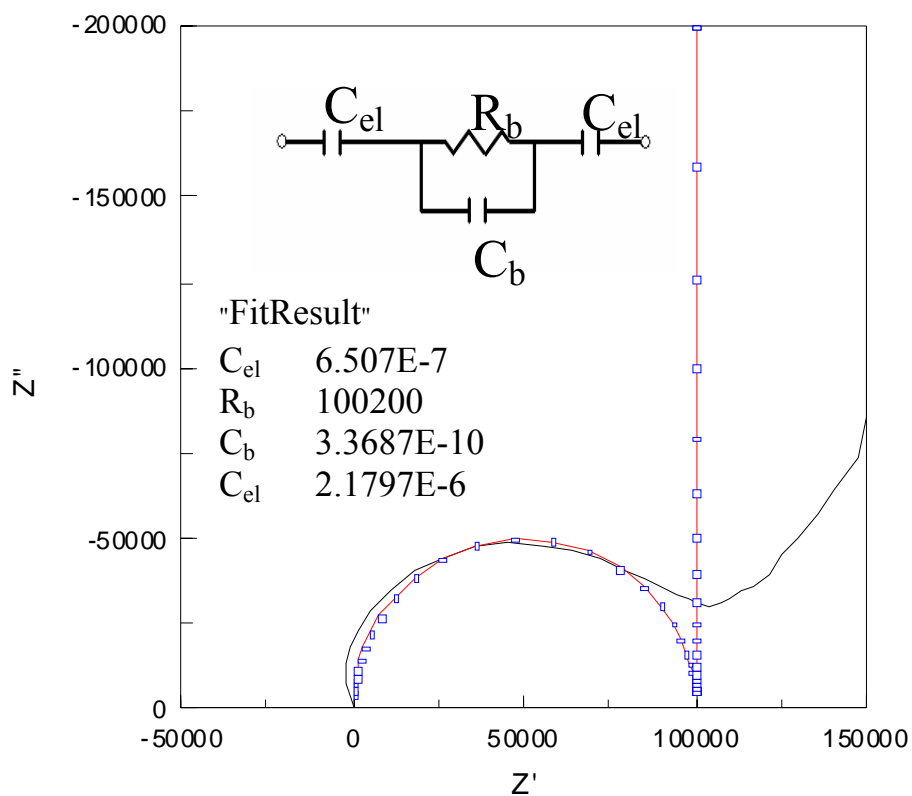


Figure 4.64 Impedance response and a fitting curve for $P(\text{EO})_{60}\text{NaSCN}$ complex

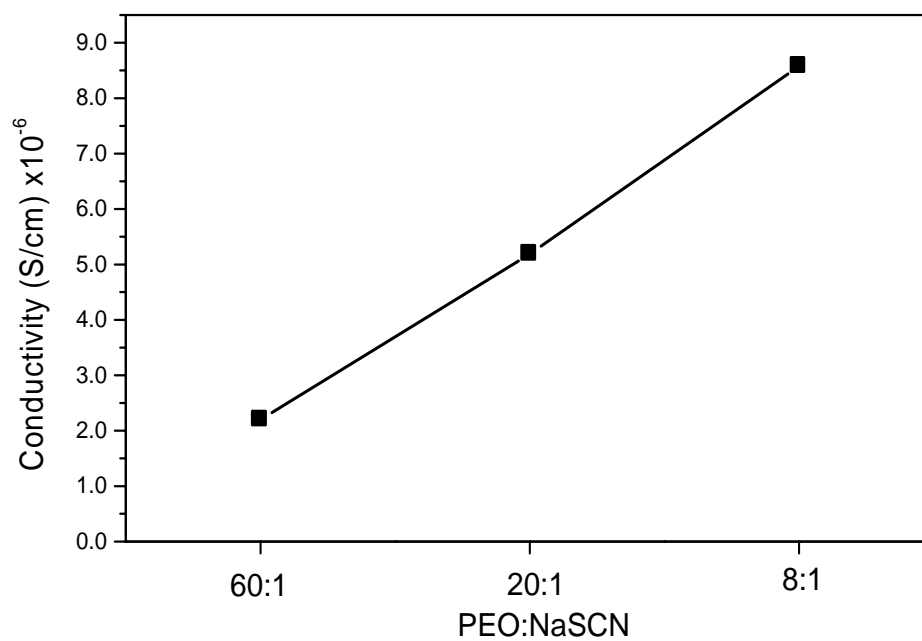


Figure 4.65 Ionic conductivity versus PEO:NaSCN at vary salt concentrations

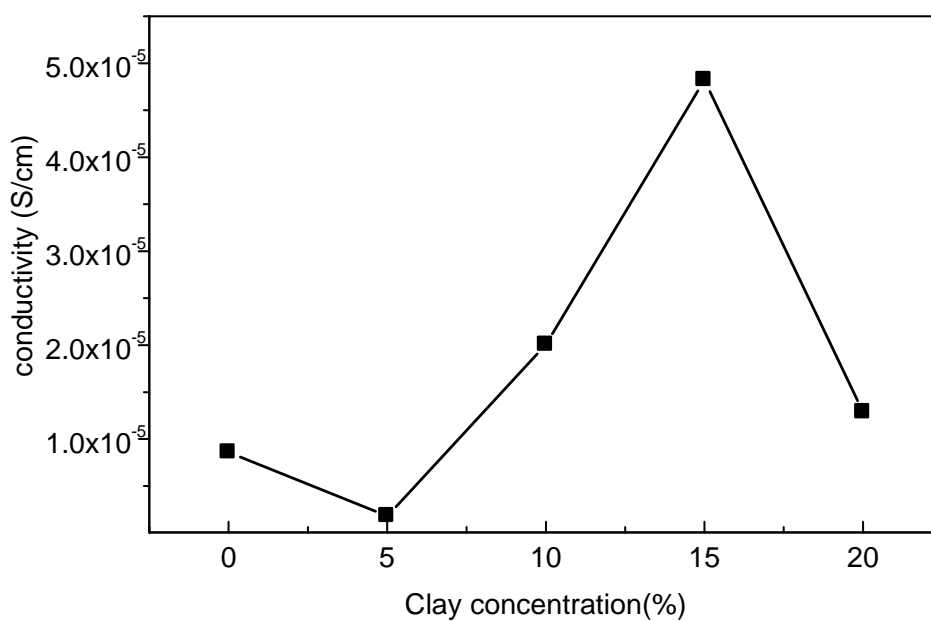


Figure 4.66 Ionic conductivity versus clay concentration (wt%) for P(EO)₈NaSCN:Clay nanocomposite at 30°C

Comparison of the ionic conductivity for $P(\text{EO})_n\text{NaSCN}$ at room temperature with various salt concentrations is illustrated in Table 4.22 and Figure 4.65. A trend is observed in which conductivity increases with increasing salt concentration to a maximum (8:1). An increase in ionic conductivity at the salt concentration regions is expected as a result of more numbers free carrier ions from salt dissociation. It, however, should be noted that the conductivity usually decrease after reaching a maxima. At the lower salt concentration, increasing the salt concentration increases conductivity because there is more number of free carrier ions at high salt concentrations. This is because conductivity decreases because the crystalline complex between PEO and salt is formed. Preechatiwong *et al.*, 1996 and Chaodamrongsakul *et al.*, 2003 found that the ionic conductivity increases when the salt concentration increase until the $\text{O}:\text{Na}^+ = 8:1$. After this point, the ionic conductivity decrease at high salt concentration. The highest ionic conductivity of $P(\text{EO})_n\text{NaSCN}$ was at 8:1. Thus in this we choose the $\text{O}:\text{Na}^+ = 8:1$ was selected to study the effect of adding MMT to the complex on its ionic conductivity.

Figure 4.66 shows a plot of ionic conductivity versus clay content at 30°C for the $P(\text{EO})_8\text{NaSCN}$ system. It was found that the conductivity increases with an increase of the clay content and approaches a maximum when the clay concentration is around 15 wt%. Subsequently, the conductivity decreases drastically with further increase in the clay content. A similar observation can also be found in other system such as the $(\text{PEO})_8\text{LiClO}_4:\text{MMT}$ electrolyte system^{ref}. Therefore, this characteristic should be general as it does depend on the MMT content but not on the salt types.

The effect of MMT on polymer and salt in the electrolyte complex can be described as follow. Because the negative charges in the silicate layers can interact

with sodium cations and disturb the attractive force between the cationic and anionic ions of the sodium salt, an excess of clay may increase the system's viscosity and thus restricts cationic ions mobility and results in lower ionic conductivity. According to Eq. (4.25) in Section 4.2.2.1, the ionic conductivity depends on the amount of charge carriers (n_i) in the system and the mobility (μ_i) of the various species. Addition of MMT can increase the fraction of 'free' anions (increase n_i), meanwhile, the ionic mobility may be reduced (decrease μ_i) owing to the higher viscosity of MMT concentration. These two adverse and competitive effects occur in this system, one is favorable and other is unfavorable for ionic conductivity. It can be concluded that the addition of optimum clay content to the complex provides the most suitable environment for the ionic transportation and achieves the highest conductivity.

In this work, it was found that the plain P(EO)₈NaSCN electrolyte system requires 15 wt% of clay content to attain the maximum conductivity. From Figure 4.66, it can be seen that the ionic conductivity can be increased by 5 times the undoped P(EO)₈NaSCN system. Although the magnitude of conductivity is not much increased, the use of MMT as a nanofiller still has an advantage in an increasing of the mechanical property of this electrolyte. From the FTIR results, deconvolution of FTIR spectra suggest that at 15 wt% MMT/PEO ratio, there is a highest amount of free ions but lowest content of ion pairs. Since ionic conductivity depends largely on the amount of free ion and fraction of ions that interact with backbone oxygen atom, we can conclude that these conductivity results are consistent with the findings in other experimental parts. The molecular model, as proposed in Section 4.2.3.3 to describe DSC results also can be used to explain this data in a similar manner.

4.2.6 PEO/NaSCN/PVP Electrolytes

4.2.6.1 X-Ray Diffraction (XRD)

The XRD patterns of PEO mixtures with different weight percent of PVP ranging from 0.2-0.6 are shown in Figure 4.67. Interestingly, the intensity of characteristic peaks of PEO around 19° and 22° still exist for mixture of PEO/NaSCN/PVP according to Figure 4.67 (d), (e) and (f). Moreover, these crystalline peaks become more intense as a function of PVP content. On the other hand, if either NaSCN or NaSCN/MMT was added into PEO, the intensities of these crystallinity peaks are almost diminish. This result suggests that NaSCN and MMT may interact with PEO better than PVP. Previously, it has been shown that PEO can be intercalated into the silicate layer of MMT to form the nanocomposite structure. In addition, PEO can also interact with NaSCN to form the solid electrolyte complex. Both of these structures cause a reduction of the PEO crystallinity. For the case of PEO/PVP/Salt mixture, a decrease in the crystalline portion of PEO may be arisen from a weaker interaction between PEO/salt compared with PVP/salt. We propose that PVP may attract salt from PEO/Salt complex and result in a larger amount of free PEO which has a helical conformation in the crystalline form. This assumption will be verified next using DSC and FTIR data.

4.2.6.2 Differential Scanning Calorimetry (DSC)

From DSC thermograms in Figure 4.68 the percentage of PEO crystallinity increases with increasing PVP content. This finding also confirms that there is more PEO crystalline content in the system as a function of PVP content which is in accord with the XRD results described in Section 4.2.5.1.

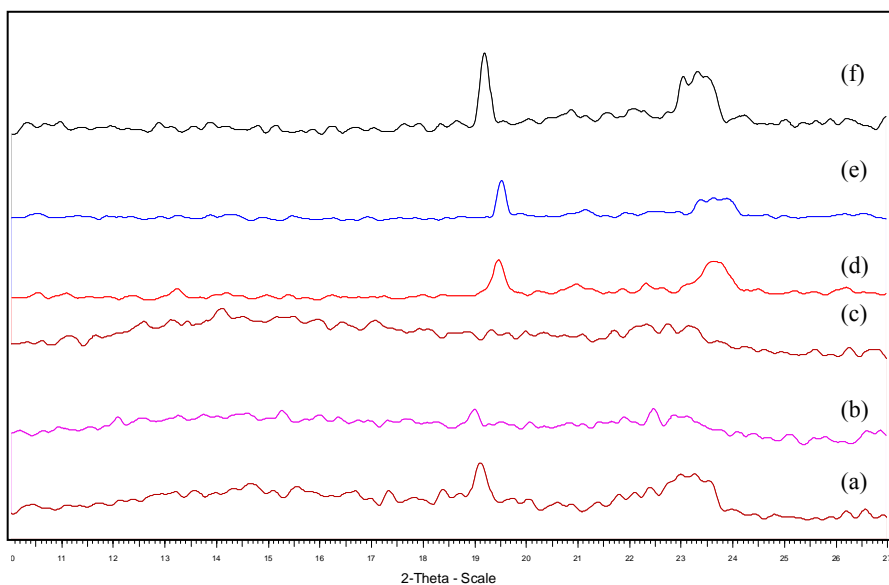


Figure 4.67 XRD patterns of: (a) PEO, (b) $\text{P}(\text{EO})_8\text{NaSCN}$, (c), $\text{P}(\text{EO})_8\text{NaSCN}/10\text{MMT}$, (d) $\text{P}(\text{EO})_8\text{NaSCN}/0.2\text{PVP}$, (e) $\text{P}(\text{EO})_8\text{NaSCN}/0.4\text{PVP}$ and (f) $\text{P}(\text{EO})_8\text{NaSCN}/0.6\text{PVP}$

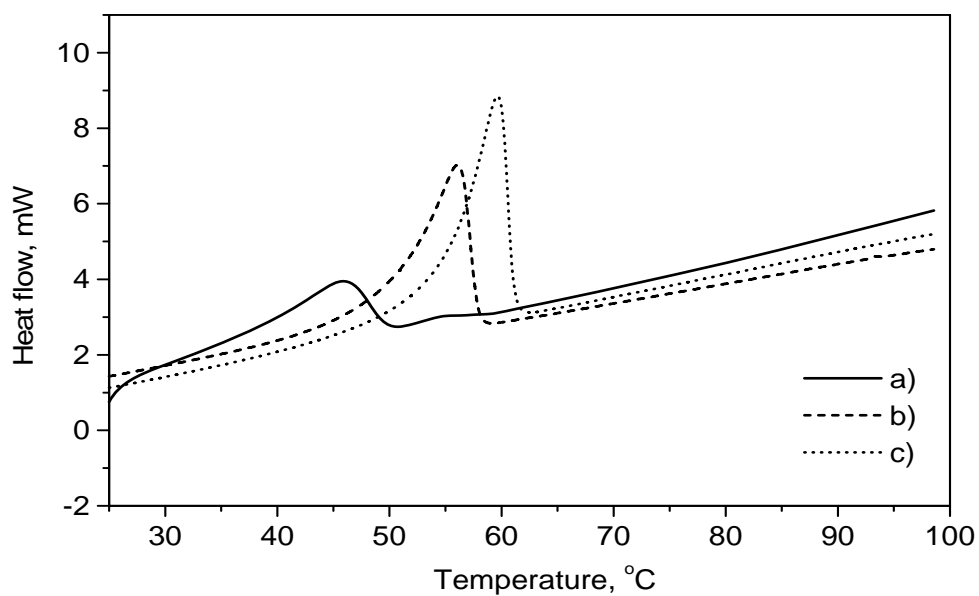


Figure 4.68 DSC thermogram for (a) $\text{P}(\text{EO})_8\text{NaSCN}/0.2\text{PVP}$, (b) $\text{P}(\text{EO})_8\text{NaSCN}/0.4\text{PVP}$ and (c) $\text{P}(\text{EO})_8\text{NaSCN}/0.6\text{PVP}$

In addition, T_m of PEO/NaSCN/PVP complexes are seen to increase with increasing PVP content, and the magnitude of T_m more closer to the value of pure PEO (at 60°C). This result also supports that PEO may crystallize separately from the polymer mixture. Since T_m peaks get larger for higher values of PVP content, these PEO/PVP mixtures are expected to be immiscible at high PVP content. For lower values of PVP, a small gap of miscibility might exist from a mutual interaction between polymers and salt i.e. PEO...salt...PVP. To confirm this assumption, FTIR technique is employed next to elucidate the functional/active group in PEO or PVP dealing with the intermolecular interaction that may induce a region of miscibility of this complex.

4.2.6.3 Fourier Transform Infrared (FTIR) Spectroscopy PEO backbone conformation

The spectral 880-800 cm^{-1} region of PEO which is the vibrational mode of CH_2 rocking and is related to the crystalline phase of PEO is shown in Figure 4.69. The frequencies of these bands are particularly sensitive to the local conformation of the polymer. This local structural modification of the backbone is caused by the cations interacting with the oxygen atoms as the sodium ions are coordinated by the polymer. The intensity of 844 cm^{-1} (crystalline of PEO) peak was found to increase as a function of PVP content. It means that less amount of cation can interact with the oxygen atom in polymer backbone upon addition of PVP. It seems, that PVP interact with Na^+ better than PEO. Thus, free PEO chains are increased and more crystalline domains are formed accordingly. XRD and DSC results of PEO/NaSCN/PVP system in Sections 4.2.6.1 and 4.2.6.2 also support this conjecture. To verify the origin of PVP/salt interaction, the change in the vibrational frequency of C=O group in PVP was investigated.

PVP backbone conformation

The degree of the complexed IR C=O stretching as function of blend composition is the most frequently employed method to quantify the relative fraction of free and complexed C=O sites within the PVP chain. As shown in Figure 4.70, the band of C=O stretching is broadened gradually with the decrease of PVP content. Those peaks are composed of one "free" C=O absorptions (centered at 1695 cm^{-1} and two complexed C=O absorptions (centered at 1658 cm^{-1}), respectively. The intensity of the free C=O group decreases with the increase of PVP content. On the other hand, the intensity of C=O complexes with Na^+ ion increase with the increase of the PVP content. This results suggests that not only PEO but also PVP can interact with cation to form the polymer–salt complex. In addition, the carbonyl group in $\text{C}=\text{O}\cdots\text{Na}^+$ in PVP/NaSCN seem to stronger than the $\text{O}\cdots\text{Na}^+$ interaction in PEO/NaSCN. Thus, the overall results is found to increases the crystalline portion of PEO/NaSCN/PVP complex as a function of PVP content. XRD, DSC and FTIR give consistent to verify this assumption.

4.2.6.4 Polarized Optical Microscope

Polarized optical microscope (POM) was used to compare the crystal morphology of $\text{P}(\text{EO})_8\text{NaSCN}/\text{PVP}$ complex with various proportions of PVP content. It is well known that the morphology of pure PEO is a spherulite shape (Manias *et al.*, 2003). It was observed that the boundaries of the PEO spherulite were moved far away from each other and phase separation was clearly seen as a function of PVP content according to Figure 4.71 (a), (b) and (c). Since there are grain boundaries among separated phases of PEO and PVP, the ion movement across the boundary should be more difficult.

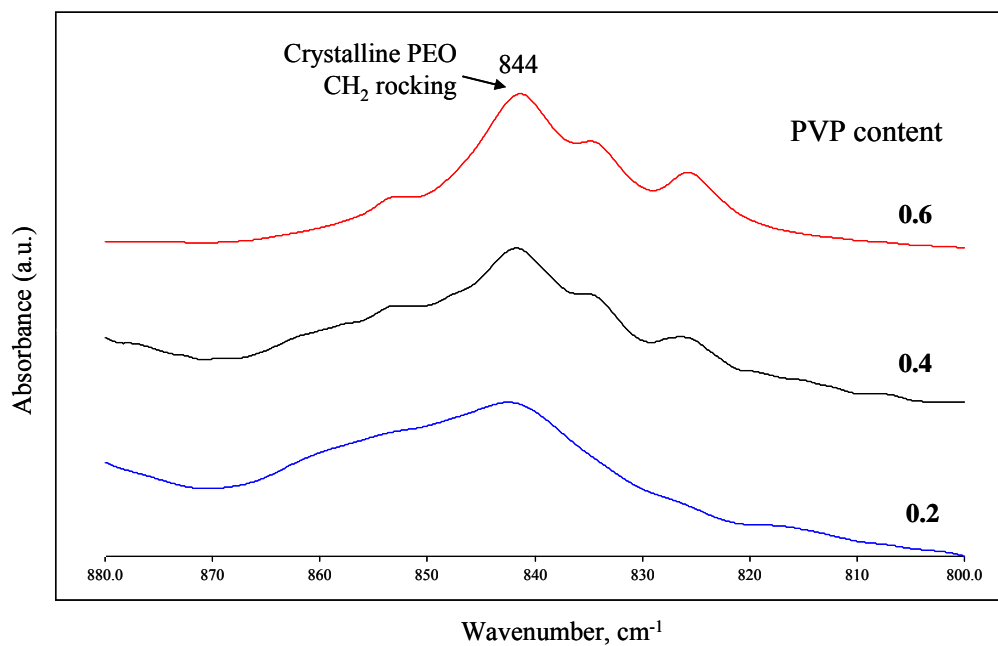


Figure 4.69 FTIR spectra of P(EO)₈NaSCN/0.2PVP, P(EO)₈NaSCN/0.4PVP and P(EO)₈NaSCN/0.6 PVP system in the 880-800 cm⁻¹ region.

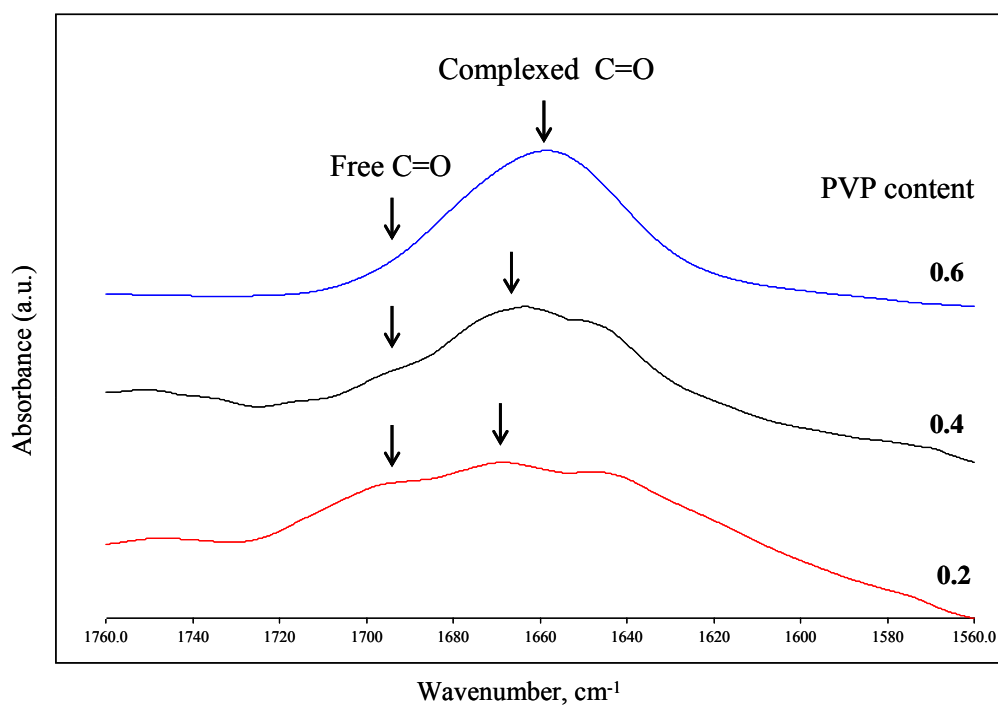


Figure 4.70 FTIR spectra of P(EO)₈NaSCN/0.2PVP, P(EO)₈NaSCN/0.4PVP and P(EO)₈NaSCN/0.6 PVP system in the 1760-1560 cm⁻¹ region

Therefore, the ionic conductivity of this complex is expected to be lower than the unmixed PEO.

4.2.6.5 Impedance Analyzer

The ionic conductivities of various PEO/NaSCN/PVP complexes at 30°C are shown in Figure 4.72. When adding PVP into P(EO)₈NaSCN complexes, the ionic conductivity decreases. Apparently the influence of high crystallinity of PEO as discussed in Sections 4.2.6.1 to 4.2.6.4 produces a complex with very low conductivity. There is no clear trend of ionic conductivity change as a function of PVP content. Nevertheless, the results shown in Figure 4.44 clearly indicate a large reduction of ionic conductivity upon addition PVP to the PEO/NaSCN complex for all proportion.

Comparing the ionic conductivity in PEO/NaSCN/MMT (Section 4.2.5) and PEO/NaSCN/PVP system, the ionic conductivity in PEO/NaSCN/MMT is higher than PEO/NaSCN/PVP about 2 order of magnitude. Thus, adding PVP into PEO/NaSCN complexes can not improve the ionic conductivity of PEO/NaSCN complex. In addition, the of PEO/NaSCN/PVP films become more brittle that inhibit further use of this polymer electrolyte blend.

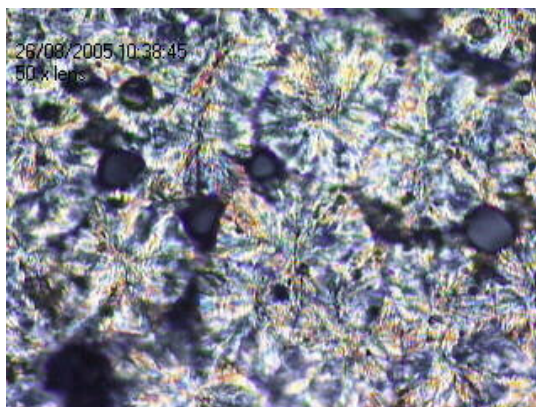
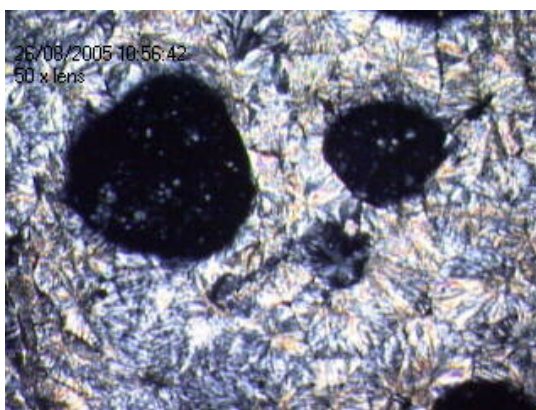
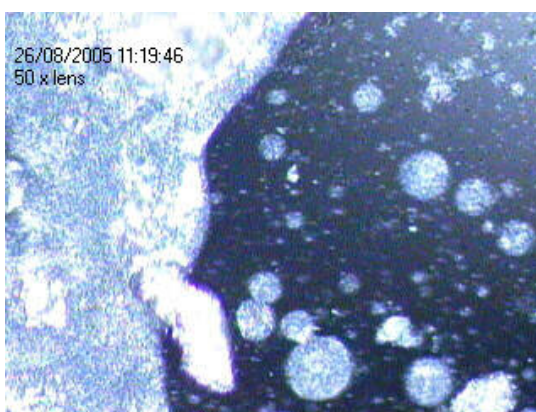
**(a)****(b)****(c)**

Figure 4.71 Polarized optical microscope of P(EO)₈NaSCN/0.2PVP, (b) P(EO)₈NaSCN/0.4PVP and (c) P(EO)₈NaSCN/0.6PVP system

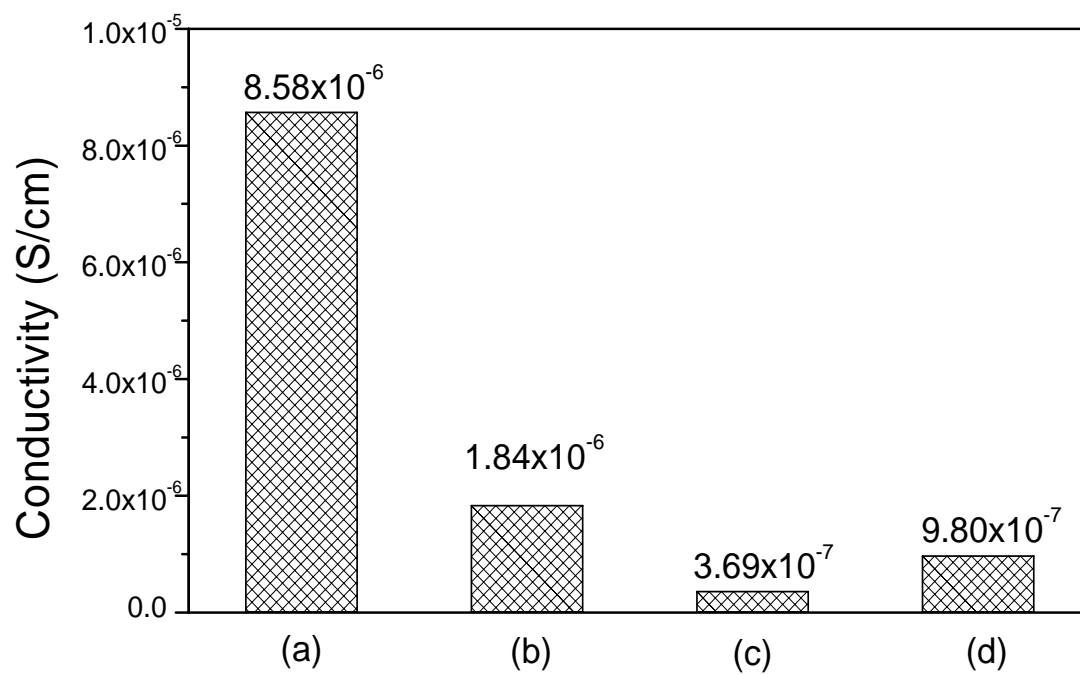


Figure 4.72 Ionic conductivity of (a) P(EO)₈NaSCN, (b) P(EO)₈NaSCN/0.2PVP, (c) P(EO)₈NaSCN/0.4PVP and (d) P(EO)₈NaSCN/0.6PVP system

CHAPTER V

CONCLUSION

In this thesis, the structure, interaction, thermal behavior and ionic conductivity of polymer nanocomposite and blend electrolytes were investigated via computational molecular modeling and instrumental analysis techniques. First, the conformational dependent properties of PEO and PVP was modeled successfully via the Rotation Isomeric State (RIS) model. The prediction of NMR coupling constant, the characteristic ratio, the dipole moment ratio and, and temperature coefficients are in good agreement with the experimental observations implying that the statistical weight matrices of these RIS models can reasonably be parameterized from the force field-based MM technique and *ab initio* quantum chemistry calculation for PVP and PEO, respectively. From DSC studies, the overall rate of an isothermal and nonisothermal crystallization kinetics of PEO increase with adding MMT while it become slower for the system of PEO/NaSCN. Using an equivalent circuit to model an impedance response, it was found that the ionic conductivity of PEO/NaSCN/MMT is first increased as a function of MMT content up to a maximum at 15%wt, then it is decreased. The best composition that gave the highest ionic conductivity for a electrolytes was PEO/NaSCN 8:1 with 15%wt MMT. The magnitude of ionic conductivity are ordered as: PEO/NaSCN/MMT > PEO/NaSCN > PEO/NaSCN/PVP. From XRD and DSC results, the crystalline portion of PEO/NaSCN/MMT complexes is smaller than the PEO/NaSCN system whereas it is

larger for PEO/NaSCN/PVP complexes. FTIR spectra had demonstrated that the addition of MMT can dissolve the NaSCN salt effectively and results in higher fraction of free ions and higher ionic conductivity. If PVP is added as a filler to PEO/NaSCN complexes, free ions in PEO phase become less. Finally, it can be concluded that an addition of optimum clay content to the complex provides the most suitable environment for the ionic transportation and achieves the highest conductivity.

REFERENCES

REFERENCES

- Abe, A., Furuya, H., Mitra, M. K. and Hiejima, T. (1998). The polyoxyethylene chain on the origin of its conformational flexibility. **Computational and Theoretical Polymer Science**. 8: 253.
- Alexandre, M., Dubois, P. (2000). Polymer-layer silicate nanocomposites: Preparation, Properties and Uses of A New Class Materials. **Materials Science and Engineering Reports**. 28: 1-63.
- Armand, M. B. (1979). **Fast Ion Transport in Solids**. Elsevier North-Holland.
Quoted in Puatrakul, T. (2000). **Studies of Ionic Conductivity of Uniaxially Stretched Polymer Electrolytes Films**. Ph.D. Thesis, University of Arkron, USA.
- Bernson, A., Lindgren, J. (1995). Coordination and conformation in PEO, PEGM and PEG systems containing lithium or lanthanum triflate. **Polymer**. 36: 4471-4478.
- Brown, G. (1961). **The X-Ray identification and crystal structures of clay mineral**. London, Mineralgical Society.
- Carrado, K.A. (2000). Synthetic Organo and Polymer-clays: Preparation, Characterization, and Materials Application. **Applied Clay Science**. 17: 1-23.

- Chandra, A., Chandra, S. (1994). Mixed-anion effect in polyethylene-oxide-based sodium-ion-conducting polymer electrolytes. **Journal of Physics D: Applied Physics**. 27: 2171.
- Chaodamrongsakul, J. (2003). **Structure and Properties of Solid Polymer Electrolyte : Poly(Ethylene Oxide)/Salt system**. M. Sc. Dissertation, Suranaree University of Technology, Thailand.
- Chintapalli, S. (1996). **Structural characterization of polymer – salt complexes and the role of plasticizers in ionic transport**. Ph. D. Dissertation, University of Oklahoma Graduate College, USA.
- Chen, H. W., Chiu, C. Y., Wu, H. D., Shen, I. W., Chang, F. C. (2002). Solid state electrolyte nanocomposites based on poly(ethylene oxide), poly(oxypropylene) diamine, mineral clay and lithium perchlorate. **Polymer**. 43: 5011.
- Chang, F.C., Wu, H. D. and Wu, I. D. (2001). The interaction behavior of polymer electrolytes composed of poly(vinyl pyrrolidone) and lithium perchlorate (LiClO₄). **Polymer**. 42: 555.
- Decha, P. (2002). **Effect of Adding Poly(propylene oxide) on Structure and properties of Solid Polymer Electrolyte: Poly(Ethylene oxide): Salt System**. M. Sc. Dissertation, Suranaree University of Technology, Thailand.
- Darsey, J. A. (1981). Self-Consistent Field Conformational Energy Calculations for n-Alkanes and Characterizations of Polymethylene. **Macromolecules**. 14: 1575-1581.

- Dias, B. F., Plomp, L., Veldhuis, J. B. J. (2000). Trends in polymer electrolytes for secondary lithium batteries. **Journal of Power Sources**. 88: 169.
- Doeff, M. M., Visco, S. J., Ma, Y., Peng, M., Ding, L. and De Jonghe, L. C. (1995). Thin film solid state sodium batteries for electric vehicles. **Electrochimica Acta**. 40: 2205.
- Flory, P. J. (1953). **Principles of Polymer Chemistry**. New York: Cornell University Press.
- Flory, P. J. and Mark, J. E. (1965). The configuration of the Polyoxyethylene Chain. **Journal of the Chemical Society**. 87: 1415-1422.
- Fontenella, J. J., Wintergill, M. C., Calame, J.P. and Andeen, C.G. (1983). Electrical relaxation in pure and alkali metal thiocyanate complexed with poly(ethylene oxide), **Solid State Ionics**. 8: 333.
- Giannelis, E. P., Krishnamoorti, R., Manias, E. (1999). Polymer-Silicate Nanocomposites: Model Systems for Confined Polymers and Polymer Brushes. **Advances in Polymer Science**. 138: 108-147.
- Gray, F. M. (1997). **Polymer Electrolytes**. London: The Royal Society of Chemistry.
- Hooper, A. and North, J. M. (1983). The fabrication and performance of all solid state polymer-based rechargeable lithium cells, **Solid State Ionics**. 9-10: 1161.
- Jaffe, R. L., Smith, G. D. and Yoon, d. Y. (1993). Conformations of 1,2 Dimethoxyethane from ad Initio Electronic Structure Calculations. **Journal of Physical Chemistry**. 97: 12745.
- Johansson, P. **Conformations and Vibrations in Polymer Electrolytes** [On-line]. Available: <http://fy.chalmers.se/~patrikj/thesis.htm>

- Kamigaito, M., Wan, D., Satoh, K., Okamoto, Y. (2005). Xanthate-Mediated Radical Polymerization of *N*-Vinylpyrrolidone in Fluoroalcohol for Simultaneous Control of Molecular Weight and Tacticity. **Macromolecules**. 38: 10397.
- Karayannidis, G. P., Papageoriou, G. Z., Achilias, D. S. and Bikiaris, D. N. (2005). Crystallization kinetic and nucleation activity of filler in polypropylene/surface-treated SiO₂ nanocomposites. **Thermochimica Acta**. 427: 117.
- Kim, S. H., Ahn, S. H. and Hirai T. (2003). Crystallization Kinetic and nucleation activity of silica nanoparticle-filled poly(ethylene 2,6-naphthalate). **Polymer**. 44: 5625.
- Lee, K., Mattice, L. W. (1991). Population of Rotational Isomers and the Unperturbed Dimensions of Poly(vinyl chloride) either and without Chloromethyl Branches, as Deduced from Molecular Dynamics Trajectories. **Computational and Theoretical Polymer Science**. 1: 213-224.
- Manias, E. and Strawhecker, K. E. (2003). Crystallization Behavior of Poly(ethylene oxide) in the presence of Na⁺ Montmorillonite Fillers. **Chemistry of Materials**. 15: 844.
- Mendolia, M. S., Farrington, G. C., (1995). High-Conductivity, Solid Polymeric Electrolytes. **Materials Chemistry: An Emerging Discipline** (108). American Chemical Society.
- Murata, K., Izuchi, S. and Yoshihisa Y., (2000). An overview of the research and development of solid polymer electrolyte batteries. **Electrochimica Acta**. 45: 1501.

- Ogata, N., Kawakage, S. and Ogihara T. (1997). Structure and thermal/mechanical properties of poly(ethylene oxide)-clay mineral blends. **Polymer**. 38: 5115.
- Quartarone, E., Mustarelli, P., Magistris, A. (1998). PEO – based composite polymer electrolytes. **Solid State Ionics**. 110: 1-14.
- Preechatiwong, W. and Schultz, J. M., (1996). Electrical conductivity of poly(ethylene oxide)- alkali metal salts systems and effects of mixed salts and mixed molecular weights. **Polymer**. 37: 5109 – 5116.
- Qui, X., Xi, J., Zheng, S. and Tang, X. (2005). Nanocomposite polymer electrolyte comprising PEO/LiClO₄ and solid super acid: effect of sulphate-zirconia on the crystallization kinetic of PEO. **Polymer**. 46: 5702.
- Ray, S.S., Okamoto, M. (2003). Polymer/layer Silicate Nanocomposites: A Review from Preparation to Processing. **Progress in Polymer Science**. 28: 1539.
- Rhodes, C. P., Frech, R. (2001). Vibrational Study of the Polymer Electrolyte Poly(ethylene oxide):LiAsF₆. **Macromolecules**. 34: 1365.
- Ruiz, E. and Aranda P. (1992). Poly(ethylene oxide)-Silicate Intercalation Materials. **Chemistry of Materials**. 4: 1395.
- Ruiz, E. and Aranda, P. (2000). Electroactive Polymers Intercalated in Clay and Related Solids. **Polymer-Clay nanocomposites**. John Wiley&Sons.
- Saiz, E., Tarazona, M. P., Gargallo, L. and Radic, D. (1993). Conformational characteristic of poly(vinylpyrrolidone) solvent-dependence of the chain dimensions. **Huthig & wepf Verlag, Basel**.
- Simon, G. P., Shen, Z. and Cheng, Y. B (2002). Comparison of solution intercalation and melt intercalation of polymer–clay nanocomposites. **Polymer**. 43: 4251.

- Simon, G. P., Shen, Z. and Cheng, Y. B. (2003). Saturation ratio of poly(ethylene oxide) to silicate in melt intercalated nanocomposites. **European Polymer Journal**. 39: 1924.
- Song, J. Y., Wang, Y. Y., Wan, C. C. (1999). Review of gel – type polymer – electrolytes for lithium – ion batteries. **Journal of Power Sources**. 77: 183 .
- Spindler, R. and Shriver, D. F. (1986). Physical and spectroscopic properties of ternary polymer electrolytes composed of poly(vinylpyrrolidone), polyethylene glycol, and lithium trifluoromethanesulfonate. **Macromolecules**. 19: 347.
- Stephan, A. M. (2006) Review on gel polymer electrolytes for lithium batteries. **European Polymer Journal**. 42: 21.
- Stuart, B. H. (2002). **Polymer Analysis**. West Sussex: John Wiley&Sons.
- Szaraz, I. and Forsling, W. (2000). A spectroscopy study of the solvation of 1-vinyl-2-pyrrolidone and poly(1-vinyl-2-pyrrolidone) in different solvents. **Polymer**. 41: 4831.
- Takahashi, Y. and Tadokoro, H. (1973). Structural Studies of Polyethers, $(-(\text{CH}_2)_m\text{O}-)_n$. X. Crystal Structure of Poly(ethylene oxide). **Macromolecules**. 6: 672.
- Tarazona, M. P., Saiz, E. (1993). Conformational Characteristics of Poly(vinylpyrrolidone) Solvent-dependence of the chain dimension. **Huthing&Wepf**. 697.
- Tonelli, A. E. (1982). Conformational characteristic of Poly(N-vinyl pyrrolidone). **Polymer**. 23: 676.

- Tsuzuki, S., Uchimaru, T., Tanabe, K. and Hirano, T. (1993). Conformational Analysis of 1,2-Dimethoxyrthane by ab Initio Molecular Orbital and Molecular Mechanic Calculation. **Journal of Physical Chemistry**. 97: 1946.
- Wang, J., Zhang, H., Xuan X. and Wang, H. (2003). FT-IR investigations of ion association in PEO-MSCN (M=Na,K) polymer electrolytes. **Solid State Ionics**. 164: 73.
- Wang, J., Zhang, H., Xuan, X. and Wang, H. (2005). Effect of poly(vinylidene fluoride) on solvation of NaSCN in PEO. **Spectrochimica Acta, Part A**. 61: 345.
- Wright, P. V., Br. (1975). **Polymer Journal**. 7:319. Quoted in Puatrakul, T. (2000). **Studies of Ionic Conductivity of Uniaxially Stretched Polymer Electrolytes Films**. Ph.D. Thesis, University of Arkron, USA.
- Xu, M., Eyring, E. M., Petrucci, S. (1996). Anion solvation effects in polymer-electrolytes: NaSCN and LiSCN in PEO-400 and in PEG-400. **Solid State Ionics**. 83: 293.
- Xu, W., Ge, M. and He, P. (2001). Nonisothermal Crystallization Kinetic of Polyoxymethylene/Montmoriilonite Nanocomposite. **Journal of Applied Polymer Science**. 82: 2281.

APPENDICES

APPENDIX A

THE INPUT FILE OF PVP AT 298 K

THE INPUT FILE OF PVP AT 298 K

Ud (CH₂-CHX-CH₃)

0.143 0.143 0.143

0.143 0.143 0.000

0.143 0.000 0.143

180.0 60.0 -60.0

112.0 112.0 112.0

1.53 0.00.0

Udd (CHX-CH₂-CHX)

0.005 0.006 0.370

0.370 0.010 0.224

0.006 0.000 0.010

180.0 60.0 -60.0

112.0 112.0 112.0

1.53 0.00.0

Udl (CHX-CH₂-CHX)

0.184 0.061 0.001

0.061 0.638 0.028

0.001 0.028 0.000

180.0 60.0 -60.0

112.0 112.0 112.0

1.53 0.0 0.0

APPENDIX B
PAPER PRESENTATION

Structure, Interaction and Thermal Behavior in Electrolytes of Polyethylene oxide/Sodium thiocyanate/Montmorillonite Nanocomposites

Sireerat Intarakamhang¹, Jittima Chaodamrongsakul², Visit Vao-soongnern^{1*}

¹Laboratory of Computational and Applied Polymer Science, School of Chemistry, Institute of Science, Suranaree University of Technology, Nakhon Ratchasima 30000

²Program of Chemistry, Nakhon Ratchasima Rajapat University, Nakhon Ratchasima

บทคัดย่อ ได้ศึกษาโครงสร้าง อันตรกิริยา และสมบัติเชิงความร้อนของพอลิเมอร์อิเล็กโทรไลต์แบบนาโนคอมโพสิตระบบ PEO/NaSCN/MMT โดย PEO, MMT และ NaSCN ทำหน้าที่เป็นพอลิเมอร์ตัวกลาง สารเติมแต่งอนินทรีย์และประจุไอออน ตามลำดับ ระบบที่ศึกษาคือ $(\text{PEO})_8\text{NaSCN}/y\text{MMT}$ และมีอัตราส่วนระหว่าง PEO:NaSCN คงที่เท่ากับ 1:8 โดย y มีค่าตั้งแต่ 0 ถึง 20 wt% เตรียมตัวอย่างโดยการเคลือบสารละลายเป็นฟิล์มบางบนแผ่นกระจก จากนั้นนำมาวิเคราะห์ด้วย XRD, FTIR และ DSC เพื่อศึกษาผลของการเติมเกลือและดินเหนียวต่อโครงสร้าง อันตรกิริยา และสมบัติเชิงความร้อน จากข้อมูลของ DSC และ XRD พบว่าร้อยละความเป็นผลึกของพอลิเมอร์มีค่าลดลงเมื่อเติมดินเหนียวและเกลือ การเกิดสารประกอบระหว่างพอลิเมอร์กับเกลือสามารถพิสูจน์ได้โดยการเกิดแถบการดูดกลืนของ FTIR ใหม่ที่ไม่พบใน PEO และทำให้แถบการสั่นของ C-O-C กว้างขึ้นเมื่อปริมาณเกลือเพิ่มขึ้น การเติม MMT มีส่วนทำให้เกลือแตกตัวได้ดีขึ้นและเพิ่มจำนวนไอออนในระบบ การจับกันระหว่าง PEO/NaSCN และ PEO/MMT สามารถเปรียบเทียบได้โดยดูจากข้อมูล FTIR

ABSTRACT The structure, interaction and thermal behavior of polymer electrolyte nanocomposites has been investigated. The system of interest is the mixture of PEO/NaSCN/MMT where PEO, MMT and NaSCN act as polymer host, inorganic filler and ionic charge, respectively. We present the results from the system $(\text{PEO})_8\text{NaSCN}/y\text{MMT}$, where the molar ratio of PEO:NaSCN is fixed at 1:8 and y varies from 0 to 20 wt%. All samples were prepared by solution casting on glass surface. XRD, FTIR and DSC were employed to investigate the effect of clay and salt addition on structure, interaction and thermal behavior of these materials. From DSC and XRD results, the percent of polymer crystallinity was decreased upon addition of clay and salt. Complexation of salt to polymer was substantiated by an appearance of new bands not present in pure PEO and also broaden the C-O-C vibrations as the salt content increased. Adding MMT seems to enhance salt dissociation and increase the carrier concentration. Competitive interaction between PEO/NaSCN and PEO/MMT can also be illustrated by FTIR data.

Introduction :

The rapid development of portable electronic devices and electric/hybrid vehicles has increased the demand for compact, lightweight, high capacity batteries. Polymers are widely studied due to their significant potential for an application as a medium in rechargeable batteries. One of the earliest example involved complexes of alkali salts with poly(ethylene oxide) (PEO) studied in details

by *Wright* [1, 2]. However, it was particularly *Armand* who pointed out and explored the usefulness of ion-conducting polymer electrolytes in high energy storage materials [3]. Since then, an application of this polymer-salt complex or Solid Polymer Electrolyte (SPEs) to solid state batteries has been much interest. Poly(ethylene oxide)/alkali metal salt-based solid electrolytes is the most interesting base material because of its high chemical and thermal stability. PEO is a semicrystalline polymer, possessing both an amorphous and a crystalline phase at room temperature. It can also solvate a wide variety of salts, even at very high salt concentrations. The solvation of salts occurs through the association of the metallic cations with the oxygen atoms in the backbone. Considerable efforts have been devoted to the development of solid polymer electrolytes (SPEs) with high ionic conductivity ($\sim 10^{-4}$ S/cm) and dimensional stability. The multi-phase nature of PEO is most often regarded as a major problem in real working systems, since the ionic conduction has been shown to take place mainly in the amorphous phase. Many investigations have been done to reduce the crystalline content, via various approaches such as using blends, copolymers, comb-branch polymers and cross-linked polymer networks [4, 7-9].

Our interest here is to overcome these problems by the incorporation of mineral clay which is an inorganic filler with intercalation property. Intercalating polymer in layered clay host can produce huge interfacial area to sustain the mechanical property of polymer electrolyte system and imparts salt-solvating power to dissolve the salts. In this work, we present a novel polymer electrolyte nanocomposite consisting of $(\text{PEO})_8\text{NaSCN/MMT}$ at various clay (Montmorillonite, MMT) content. The role of clay addition on structures and properties of SPEs will be investigated via differential scanning calorimetry (DSC), X-Ray diffraction (XRD), and Fourier transform infrared (FTIR) spectroscopy.

Methodology :

PEO (MW 1×10^5 g mol⁻¹, Aldrich) and Na-MMT (SWy-2, Clay Mineral Depository) were used as received. The salts, sodium thiocyanate (NaSCN, Fluka), were dried in the vacuum oven at ~ 140 °C for 48 hours. Stoichiometric amount of PEO, salt and clay were dissolved in methanol and stirred continuously for 24 hours at room temperature. After continuous stirring, the solution was allowed to stand at room temperature for 24 h to facilitate degassing. To obtain thin film of the sample, the gelatinous polymer solution was cast on the glass plate. The films were dried in vacuum oven at 50 °C for 24 hours to remove solvent. The interactions between salt and polymer and salt association in $(\text{PEO})_8\text{NaSCN/MMT}$ complexes were investigated by FTIR. The study was carried out with FT-IR spectrometer Perkin-Elmer model: spectrum GX. The numbers of scans were 4 at the resolution of 4 cm⁻¹. The range of measurement was between 4000 cm⁻¹ and 400 cm⁻¹. The diffraction patterns were recorded with a Bruker D5005 X-ray generator at room temperature between 2θ values 10 ° to 60 °. DSC data were collected with DSC (Perkin-Elmer Diamond) of 8 – 10 mg from 25 to 100 °C at heating rate of 10 °C min⁻¹ under N₂ atmosphere.

Results and Discussions:

X-Ray Diffraction (XRD)

The intercalation of polymer chains usually increases the interlayer spacing of clay, leading to a shift of the diffraction peak towards lower angle values which are related through the Bragg's relation: $\lambda = 2d \sin \theta$. Upon intercalation, the basal spacing was expanded from 1.24 to 2.07 nm indicating the incorporation of large PEO molecules. The magnitude of a shift was not constant but varied with the clay content. The diffractograms of the 8:1 PEO/NaSCN with 0-20 wt% MMT displayed the characteristic crystalline peaks centered around 15°, 19° and 23° and it was ascribed to crystalline PEO. Addition MMT to the sample also gave peaks at the same positions but with lower intensities. It should be emphasized that the crystalline phase of 8:1 PEO/NaSCN with different % weight of MMT still existed but at a lower content than that of 8:1 PEO/NaSCN.

Fourier Transform Infrared Spectroscopy (FT-IR)

For PEO/NaSCN and PEO/MMT system, the new bands were found at 2000-2100 cm^{-1} regions (stretching modes of SCN^- in PEO/NaSCN), indicating the formation of crystalline complex of $\text{P(EO)}_8\text{NaSCN}$ (the band at 2060 cm^{-1} was ascribed to the contact ion-pairs and solvent-separated dimers). Upon addition of MMT to PEO/NaSCN, the relative intensity of the band at 2060 cm^{-1} was increased at the expense of the band at 2031 cm^{-1} , indicating the disintegration of crystalline PEO phase and resulting in a decrease of crystalline $\text{P(EO)}_8\text{NaSCN}$ complex. Spectral changes in 1000-800 cm^{-1} region (the characteristics of C-O stretching and CH_2 rocking modes) were related to changes occurring in the local structure of polymer backbone. When NaSCN was added, the bands occurred at 860, 834 cm^{-1} which particularly were sensitive to the local conformation of the O-C-C-O torsional angle. The appearance of one mode at a higher frequency and the second mode at a lower frequency than that in pure PEO are originated from the interaction of sodium ion with ether oxygens. For the CH_2 wagging modes at 1360 and 1343 cm^{-1} (the characteristic of crystalline PEO), the intensity of these two peaks was decreased drastically and replaced by sharp band at 1350 cm^{-1} upon addition of NaSCN. These results indicated an amorphous content for $\text{P(EO)}_8\text{NaSCN}$. The character of 1280 cm^{-1} peak (CH_2 twisting mode in pure PEO) were also changed upon adding of salt as well as clay. Therefore both clay and NaSCN were able to reduce the crystalline phase of pure PEO.

Differential Scanning Calorimeter (DSC)

The effect of adding MMT on the changes of T_m and ΔH_m of PEO and PEO-NaSCN complexes were investigated using DSC technique. The melting temperature of PEO are changed from 69.0 °C to 66.8 °C with MMT addition. There was more amorphous domain in the complex due to the miscibility of MMT with PEO. ΔH_m and the percentages crystallinity of PEO+MMT were lower than that of PEO. In agreement with XRD data, these results suggested that MMT was compatible with PEO and caused a reduction of the crystallinity of the complex.

Conclusions

FTIR, XRD and DSC results showed that the MMT was able to decrease the crystalline content and enhanced salt dissociation of PEO-NaSCN systems. Complexation of salt to polymer was substantiated by an appearance of new bands not present in pure PEO and also broaden the C-O-C vibrations as the salt content increased. Competitive interaction between PEO/NaSCN and PEO/MMT were also illustrated by FTIR data.

References:

- [1] Fenton D. E., Parker J. M., Wright P. V. *Polymer*. 14, 1973. p589.
- [2] Wright P. V. *Br. Polym. J.* 7, 1975. p319.
- [3] Armand, M. B., Chabagno J. M., Duclot J. M. *Fast Ion Transport in Solids*. Elsevier. 1979. p131.
- [4] Mendolia M. S., Farrington G. C. *Materials Chemistry: An Emerging Discipline* 1995. p108.
- [5] Chintapalli, S. Ph. D. Dissertation, University of Oklahoma Graduate College, USA 1996.
- [6] Bruce, P. G. *Solid state electrochemistry*. United Kingdom: Cambridge University Press 1995.
- [7] Quartarone E., Mustarelli P., Magistris A. *Solid State Ionics* 110, 1998. p1. p14.
- [8] Song J. Y., Wang Y. Y., Wan, C. C. *J. Power Sources* 77, 1999. p183. p197.
- [9] Sukeshini A. M., Kulkarni A. R., Sharma, A. *Solid State Ionics*. 113-115, 1998. p179. p186.
- [10] Preechatiwong W., Schultz J. M. *Polymer*. 37, 1996. p5109. p5116.
- [11] Sekhon S. S., Singh G., Agnihotry S. A., Chandra S. *Solid State Ionics*. 80, 1995. p37. p44.

Keywords: Polymer electrolytes, Polymer nanocomposites

**Rotational Isomeric State Model of Poly(ethylene oxide) from
ab initio Electronic Structure Calculation**

Visit Vao-soongnern^{*1}, *Sireerat Intarakamhang*¹, *Nattida Rakgapao*¹
*Jittima Chaodamrongsakul*²

¹Laboratory of Computational and Applied Polymer Science
School of Chemistry, Suranaree University of Technology, Nakhon Ratchasima
²Program of Chemistry, Nakhon Ratchasima Rajapat University, Nakhon Ratchasima

ABSTRACT: The conformational properties and new RIS model have been derived for poly(ethylene oxide), PEO, based upon both semi-empirical (PM3) and *ab initio* (HF-SCF and MP2) electronic structure calculation of the three representative segments of PEO (semi-empirical) and 1,2-dimethoxyethane, DME (*ab initio*). In order to better understand the influence of oxygen *gauche* effects on the conformational energies and populations of PEO. It is demonstrated that the low energy of the of DME resulting from strong O...H attraction. The energy of *gauche* conformation of the O—C—C—O bond relative to the *trans* conformation depends strongly not only on the basis set size but also on electron correlation effects. The energy of *tgt* conformation relative to *ttt* conformation was determined for various basis sets at both HF-SCF and MP2 levels. The RIS model, with all the parameters derived from the conformational geometries and energies of DME, predicts the chain dimensions, the dipole moments, and their temperature coefficients for PEO in good agreement with experiments. At a more local scale, the RIS model reproduces the fraction of bond conformers in close agreement with the data from electron diffraction and NMR coupling constants

INTRODUCTION: Poly(ethylene oxide), PEO, is known to be one of the most flexible polymers characterized by a small value of the unperturbed dimension. The polymer is soluble in various organic solvents as well as in water. It has long been established that PEO chains have a large fraction of bonds in *gauche* conformations. This is a specific example of the *gauche* effect in which polar substituents cause the preferred conformation about a C—C bond to switch from *trans* to *gauche*. Several attempts have been made to describe PEO using rotational isomeric state (RIS) models parameterized on the basis of molecular mechanics predictions of the conformational energies and geometries of small model molecules. Prior *ab initio* electronic calculations indicate the energy of O—C—C—O *gauche* conformation in PEO is approximately 0.6 kcal/mol higher than the *trans* conformation. In an effort to account for discrepancies between RIS model, electron diffraction and *ab initio* results of PEO model compound (dimethyl ethane, DME), we have undertaken a detailed *ab initio* analysis of the conformational energies of DME in this work.

COMPUTATION: Geometries and conformational energies of model segments of PEO are determined at HF-SCF and MP2 level. The basis set used in this study, 6-311G and D95, are split valence (with three functions for the valence orbitals) and double-x, respectively. The basis sets can be further augmented by including a set of diffuse sp function [+ and ++] and polarization function [* and **]. Conformational

geometries are determined by fully optimizing the original molecule geometries. Vibrational frequencies are calculated to verify the stationary points. Semi-empirical calculation of 3 model units of PEO is also performed at the PM3 level to determine the overall shape of the conformational energy map. Parameters for RIS model are obtained via multiple linear least square regression. RIS calculation is performed using an in-house Fortran program. All calculation are performed with the quantum chemistry package GAUSSIAN 98w which is installed on Pentium 4 CPU 3.2 GHz with 1 GB RAM.

RESULTS, DISCUSSIONS AND CONCLUSION: We obtained the geometries and energies of the low-energy conformers of DME employing quantum chemistry methods. Specifically, we determined HF, MP2 and DFT various basis sets. The effect of basis set and electron correlation on the calculated relative conformational energies of *tgt* with *ttt* are presented in Table 1. The geometries and conformational energies of nine rotamers of DME were optimized at the HF/6-311+G* and D95** level. Calculated dihedral angles of the skeleton bonds and conformational energies of the nine rotamers are also summarized in Table 2. Then, we develop a simple three state second-order RIS model for PEO and have establishes all parameter values based upon the *ab initio* conformational energies of model compound. Our RIS model of PEO includes low-energy $g^{\pm}g^{\mp}$ C-O-C-C-O conformations and the energy of the O-C-C-O *gauche* conformation is considered to be slightly higher than that of the *trans* conformation. Standard matrix multiplication methods were utilized to determine mean-square chain dimensions and dipole moments from statistical weights and matrices estimated from conformational average of *ab initio* optimized conformational energies of DME. Calculated and experimental values of polymer properties are also given in Table 3. Results from our RIS model are relatively in close agreement with experiment.

On the basis of high-level quantum chemistry calculations (HF-SCF, MP2, DFT), we have shown that the conformer populations of PEO determined from *ab initio* electronic structure calculations of the low-energy conformation of model compounds using a large basis set and including electron correlation effects agree with those estimated from experimental electron diffraction data and reproduce NMR coupling constants, characteristic ratio and dipole moment reasonably well. These finding stimulate to have a further investigation of the conformational properties of other polymer chains by an RIS model of which the energy parameters derived from first principle *ab initio* quantum chemistry calculation.

Table 1 The difference in Energy between the *ttt* and *tgt* Conformer of DME

Basis set	Δ HF	Δ MP2	Δ B3LYP
6-31G*	1.40	0.60	0.52
6-31+G*	1.40	0.41	0.64
6-311+G*	1.26	0.28	0.71
6-311++G*	1.24	0.23	0.54
D95**	1.30	NA	NA
D95+(2df,p)	0.96	NA	NA

Table 2 DME Geometries and Energies (calculates at HF/6-311+G* and D95)**

Conformation (degeneracy)	ϕ_1^a	ϕ_2^a	ϕ_3^a	Δ		Δ	
				6-311+G*		D95**	
				HF	MP2	HF	MP2
TTT	179.94	-179.92	-179.99	0.00	0.00	0.00	0.00
TGT	-174.78	-174.75	73.42	1.26	0.29	1.30	0.75
TTG	-178.21	89.72	179.52	2.08	1.67	1.89	1.24
TGG	-178.34	79.96	65.95	3.34	1.96	3.13	1.77
TGG'	-177.86	-91.13	71.46	1.78	0.28	1.63	0.24
GTG	90.12	90.08	178.19	4.30	3.48	3.52	2.90
GTG'	88.95	-88.96	178.00	4.09	3.37	3.10	2.61
GGG'	85.24	-82.45	72.68	4.13	2.10	3.52	1.68
G'GG'	-90.16	-178.20	-90.07	4.31	3.48	3.84	2.53

a torsion angles for the C-O, C-C and O-C bonds, in deg, Using the 6-311+G Opt

Table3. Characteristic ratio and dipole moment ratio for PEO

	$\langle r \rangle^2/nl^2$	$\langle \mu \rangle^2/nm^2$	$\frac{[d \ln \langle r \rangle^2/dT]}{(10^{-3} K^{-1})}$	$\frac{[d \ln \langle \mu \rangle^2/dT]}{(10^{-3} K^{-1})}$
Observed	5.2	0.53	0.23	2.6
Calculated	5.2	0.35	0.74	3.0

Observed: D. R. Beech and C. Booth, *J. Polym. Sci., Part A-2*, 1969, 7, 575.

Calculate: A. Abe *Polym. J.*, 1982, 14, 427.

REFERENCES

1. W. L. Mattice and U. W. Suter, (1994), *Conformational Theory of Large Molecules. The Rotational Isomeric State Model in Macromolecular Systems*, John Wiley & Sons, New York
2. A. Abe, H. Furuya, K. Mitra T. Hiejima, (1998), The polyoxyethylene chain—on the origin of its conformational flexibility, *Computational and Theoretical Polymer Science*, **8**, 253-258.

**Computational Molecular Modeling of Polymer Solid Electrolytes I:
ab initio Calculation of Polyethylene oxide and its Alkali Salt Complexes**

Sireerat Intarakamhang^{1,2}, Jittima Chaodamrongsakul^{1,2}, Visit Vao-soongnern^{1,2}
Supagorn Rugmai^{3,4}, Wanata Klysubun⁴

*Laboratory of Computational and Applied Polymer Science*¹, *School of Chemistry*²,
*School of Physics*³, *Institute of Science, Suranaree University of Technology, National
Synchrotron Research Center*⁴, Nakhon Ratchasima, 30000

ABSTRACT

The *ab initio* calculation on the conformation of a single PEO chain and the structure of PEO/salt complexes were reported. First, the conformational properties and new Rotational Isomeric State (RIS) model have been derived, based upon both semi-empirical (PM3) and *ab initio* (HF-SCF and MP2) electronic structure calculation of the three representative segments of PEO (semi-empirical) and 1,2-dimethoxyethane, DME (*ab initio*). The RIS model, with all the parameters derived from the conformational geometries and energies of DME, predicts the chain dimensions, the dipole moments, and their temperature coefficients for PEO in good agreement with experiments. At a more local scale, the model reproduces the fraction of bond conformers in close agreement with the data from electron diffraction and NMR coupling constants. Next, several stable structures of the 1:1 complexes of an alkali ion with di-, tri-, tetra-, penta- and hexaglyme [CH₃O(CH₂CH₂O)_nCH₃, n=2–6] were obtained at HF level of theory employing the 3-21G* basis set. Various different stable complexes were found with coordination numbers ranging from two to six. The total energies and the binding energies were evaluated by using density functional theory (DFT) calculations (B3LYP/6-31G*//HF/3-21G*) and showed the total binding energy to increase with the chain length. The average binding energy per bond for a specific coordination number for alkali cation shows only minor changes when extending the oligomer.

INTRODUCTION: Polymer solid electrolytes (PSE) based on polyethylene oxide (PEO), (CH₂CH₂O)_n, polymers and/or oligomers and an alkali salt are of great interest in the context of developing modern and environmentally friendly large secondary batteries and of fundamental scientific interest. These types of PSE to a large extent still rely on the ability of the repeated ethylene oxide unit to coordinate cations. PEO is known to be one of the most flexible polymers characterized by a small value of the unperturbed dimension. The polymer is soluble in various organic solvents as well as in water. It has long been established that PEO chains have a large fraction of bonds in *gauche* conformations. This is a specific example of the *gauche* effect in which polar substituents cause the preferred conformation about a C—C bond to switch from *trans* to *gauche*. Several attempts have been made to describe PEO using rotational isomeric state (RIS) models parameterized on the basis of molecular mechanics predictions of the conformational energies and geometries of small model molecules. In an effort to account for discrepancies between RIS model, electron diffraction and *ab initio* results of PEO model compound (dimethyl ethane, DME), we have undertaken a detailed *ab initio* analysis of the conformational energies of DME. As we

plan to study PEO/Salt complexes using both experimental (Extended X-Ray Absorption Spectroscopy, EXAFS) and computational (*ab initio* calculation) approaches, some preliminary results concerning structures and energetics of PEO/Li⁺ were investigated based on a first principle calculation. It is expected that the outcome of this work will lead to a more understanding about the relationship between their atomistic nanostructures and material properties

COMPUTATION: RIS Model: Geometries and conformational energies of model segments of PEO are determined at HF-SCF and MP2 level. The basis set used in this study, 6-311G and D95, are split valence (with three functions for the valence orbitals) and double-x, respectively. The basis sets can be further augmented by including a set of diffuse sp function [+ and ++] and polarization function [* and **]. Conformational geometries are determined by fully optimizing the original molecule geometries. Vibrational frequencies are calculated to verify the stationary points. Semi-empirical calculation of 3 model units of PEO is also performed at the PM3 level to determine the overall shape of the conformational energy map. Parameters for RIS model are obtained via multiple linear least square regression. RIS calculation is performed using an in-house Fortran program. **PEO/Li⁺ Complexes:** Initial calculations on the starting geometries were made with the semi-empirical PM3 method. The subsequent final geometry optimizations at HF level used the standard 3-21G* basis set. Vibrational frequency calculations were performed at this level of theory to confirm that the structures obtained were true minima. Because of the size of the systems, the energies were finally evaluated using DFT methods at the B3LYP/6-31G* level of theory (B3LYP/6-31G*//HF/321G*). The bonding energies are defined as $E_{\text{bond}} = \{E(\text{Li}^+ \text{-glyme complex}) - [E(\text{glyme (in the complex geometry)}) + E(\text{Li}^+)]\}$. Suitable starting geometries were selected on the basis of two different stable complexes/structures with the conformations **aG⁻a aG⁺a** and **aG⁺a g⁺G⁺a**, referred to as structure **1** and **2**. Next, a sequence of three ether oxygen atoms is suitably arranged for coordination to a metal ion. All calculation are performed with the quantum chemistry package GAUSSIAN 98w which is installed on Pentium 4 CPU 3.2 GHz with 1 GB RAM.

RESULTS AND DISCUSSIONS:

Conformational Characteristics of PEO: The geometries and energies of the low-energy conformers of DME employing quantum chemistry methods (HF, MP2 and DFT) at various basis sets were obtained. The energy of *gauche* conformation of the O—C—C—O bond relative to the *trans* conformation depends strongly not only on the basis set size but also on electron correlation effects. The effect of basis set and electron correlation on the energy of the *tgt* conformer of DME relative to the *ttt* conformer were investigated as followed. First, molecular geometry of the *tgt* and *ttt* conformers of DME were optimized at the MP2 level using D95** basis set. Then, these optimized geometry was used in single-point energy calculation at both SCF and MP2 levels for various basis sets. These data are given in Table 1. Electron correlation effects were found to be quite important. The MP2 energy differences are all at least 0.5 kcal/mol lower than SCF values for the same basis set. The electron correlation effects increase as the size of basis set increases. Geometries and conformational energies of nine rotamers of DME were optimized at the HF/6-311+G* and D95** level. Calculated dihedral angles of the skeleton bonds and

conformational energies of the nine rotamers are also summarized in Table 2. Next, we develop a simple three state second-order RIS model for PEO and have established all parameter values based upon the *ab initio* conformational energies of model compound. The RIS model for poly(A-A-B) chains, in which all bonds are subject to a symmetric 3-fold torsion potential with the nearest neighbor interdependence, is given by the following three statistical weight matrices for three successive bonds of type A-A, A-B, and B-A.

$$U_{AA} = \begin{bmatrix} 1 & \sigma_{BB} & \sigma_{BB} \\ 1 & \sigma_{BB} & \sigma_{BB}\omega_{AB} \\ 1 & \sigma_{BB}\omega_{AB} & \sigma_{BB} \end{bmatrix} \quad U_{AB} = \begin{bmatrix} 1 & \sigma_{AA} & \sigma_{AA} \\ 1 & \sigma_{AA} & \sigma_{AA}\omega_{AB} \\ 1 & \sigma_{AA}\omega_{AB} & \sigma_{AA} \end{bmatrix} \quad U_{BA} = \begin{bmatrix} 1 & \sigma_{AA} & \sigma_{AA} \\ 1 & \sigma_{AA} & \sigma_{AA}\omega_{AA} \\ 1 & \sigma_{AA}\omega_{AA} & \sigma_{AA} \end{bmatrix}$$

In the matrices, the rows and columns define the states of bonds $i - 1$ and i , respectively. The three accessible rotational isomeric states for each bond are t , g^+ , and g^- , used in this order in the matrices. The σ_{AA} and σ_{AB} are the statistical weights for the A-A and A-B type first-order interactions, and ω_{AA} and ω_{AB} represent the second-order interactions. They are calculated as Boltzmann factors using the energies calculated from an *ab initio* QM calculation. The short-range interactions determine the local chain conformation for an unperturbed chain. Our RIS model of PEO includes low-energy g^+g^- C-O-C-C-O conformations and the energy of the O-C-C-O *gauche* conformation is considered to be slightly higher than that of the *trans* conformation. Some sets of the *ab initio* and representative RIS conformational energies are summarized in Table 3. All statistical weight parameters were calculated from these results. Next, standard matrix multiplication methods were utilized to determine mean-square chain dimensions and dipole moments from statistical weights and matrices estimated from conformational average of *ab initio* optimized conformational energies of DME. Calculated and experimental values of polymer properties are also given in Table 4. The local bond property i.e. NMR vicinal coupling constant was also found in close agreement with experiment.

Structures and Energetics of PEO/Alkali Salt Complexes: Several stable structures of the 1:1 complexes of a lithium ion with tetra-, penta- and hexaglyme [$\text{CH}_3\text{O}(\text{CH}_2\text{CH}_2\text{O})_n\text{CH}_3$, $n=4-6$] have been obtained with *ab initio* calculations at the Hartree-Fock level of theory employing the 3-21G* basis set. Twenty-three different stable complexes were found with coordination numbers of lithium ranging from four to six. The total energies and the binding energies were evaluated by using density functional theory (DFT) calculations (B3LYP/6-31G**/HF/3-21G*) and showed the total binding energy to increase with the glyme length. The average binding energy for the different glymes reaches a maximum of 620 kJ mol^{-1} for the hexaglyme complexes, with an absolute maximum of 631 kJ mol^{-1} obtained for a hexacoordinated Li^+ -hexaglyme complex. The average binding energy per bond for a specific coordination number for lithium shows only minor changes when extending the oligomer ($<5 \text{ kJ mol}^{-1} \text{ bond}^{-1}$). The large number of complexes obtained with clearly different geometry within a small energy range — six different complexes within 15 kJ mol^{-1} for lithium-tetraglyme — clearly reflects the flexibility of the oligomer chains. To compare all the Li^+ -oxygen distance qualitatively for all complexes obtained, a histogram is shown in Figure 1(b) from which an estimate give us a peak at 2.03 Å. This value will be later compared with the RDF obtained the

EXAFS experimental results. The large number of complexes obtained with clearly different geometry within a small energy range clearly reflects the flexibility of the oligomer chains.

CONCLUSION: On the basis of high-level quantum chemistry calculations (HF-SCF, MP2, DFT), we have shown that the conformer populations of PEO determined from *ab initio* electronic structure calculations of the low-energy conformation of model compounds using a large basis set and including electron correlation effects agree with those estimated from experimental electron diffraction data and reproduce NMR coupling constants, characteristic ratio and dipole moment reasonably well. The structures and energetics of PEO/Li⁺ complexes showed the total binding energy to increase with the chain length. Distribution of Li-O distance are found in the range of 1.9 to 2.4 Å with the highest peak at 2.0 Å.

Acknowledgement: This work is supported by NSRC (Grant number 2-2548/PS02). We also thank Dr. Patrik Johansson (Chalmers, Sweden) for a helpful discussion.

References

1. P.G. Bruce, (Ed), *Solid State Electrochemistry*, Cambridge University Press, Cambridge, (1995).
2. K. Murata, S. Izuchi, Y. Yoshihisa, *Electrochimica Acta*, *45*, 1501, (2000).
3. E. Quartaron, P. Mustarelli, A. Magistris, *Solid State Ionics*, *110*, 1, (1998).
4. J. Chaodamrungsakul, *Physical Chemistry Study on Structures and Properties of PEG and PEO/PEG/Salts Complexes*, Master Thesis, School of Chemistry, SUT, (2003).
5. S. Chintapalli, R. Frech, B. Grady, *Polymer*, *38*, 6189, (1997).
6. B. Grady, C.P. Rhodes, S. York, R.E. Frech, *Macromolecules*, *34*, 8523, (2001).
7. P. Johansson, J. Tegenfeldt, J. Lindgren, *Polymer*, *40*, 4399, (1999).
8. V. Vao-soongnern, R. Ozisik, W.L. Mattice, *Macromol. Theory Simul*, *10*, 553 (2001).
9. O. Borodin, G.D. Smith, R. Douglas, *J. Phys. Chem. B*, *107*, 6824, (2003).

Table 1 The difference in Energy between the *ttt* and *tgt* Conformer of DME

Basis set	Δ HF	Δ MP2	Δ B3LYP
6-31G*	1.40	0.60	0.52
6-31+G*	1.40	0.41	0.64
6-311+G*	1.26	0.28	0.71
6-311++G*	1.24	0.23	0.54
D95**	1.30	NA	NA
D95+(2df,p)	0.96	NA	NA

Table 2 DME Geometries and Energies (calculates at HF/6-311+G* and D95**)

Conformation (degeneracy)	Φ_1	Φ_2	Φ_3	Δ 6-311+G*		Δ D95**	
				HF	MP2	HF	MP2
				TTT	179.94	-179.92	-179.99
TGT	-174.78	-174.75	73.42	1.26	0.29	1.30	0.83
TTG	-178.21	89.72	179.52	2.08	1.67	3.85	1.40
GTG	90.12	90.08	178.19	4.30	3.48	3.52	3.01
GTG'	88.95	-88.96	178.00	4.09	3.37	3.10	2.69
TGG	-178.34	79.96	65.95	3.34	1.96	1.65	1.90
TGG'	-177.86	-91.13	71.46	1.78	0.28	3.96	0.44
GGG	63.83	63.84	48.22	4.26	1.68	3.85	1.69
GGG'	85.24	-82.45	72.68	1.26	2.10	3.52	1.77

Table 3 RIS model of PEO from *ab initio* calculation of DME model compound

Conformer	RIS	MP2	MP2	RIS	RIS
	Representation	6-311+G*	D95**	Energy ^a	Energy ^b
ttt	0	0.00	0.00	0.00	0.00
tgt	E_σ	0.29	0.75	-0.20	0.23
ttg	E_ρ	1.67	1.24	1.40	1.75
tgg	$E_\sigma + E_\rho$	1.96	1.77	1.20	1.98
tgg'	$E_\sigma + E_r + E_\omega$	0.28	0.24	0.38	0.30
gtg	$2E_\rho$	3.48	2.90	2.80	3.50
gtg'	$2E_\rho$	3.37	2.61	2.80	3.50
ggg'	$E_\sigma + 2E_\rho + E_\omega$	2.10	1.68	1.78	2.05
g'gg'	$E_\sigma + 2E_\rho + 2E_\omega$	3.48	2.53	0.95	0.37
ggg	$E_\sigma + 2E_\rho$	1.68	1.69	2.60	3.73

^aParameter set 3 $E_\sigma = -200$, $E_r = 1400$ and $E_\omega = -825$ cal/mol. ^bParameter set 4 $E_\sigma = 230$, $E_\rho = 1750$ and $E_\omega = -1680$ cal/mol. Disagreement for g'g'g and ggg conformational energy is due to third order interaction effect (not included in the present work)

Table 4 Characteristic ratio and dipole moment ratio for PEO

	$\langle r \rangle_0^2/nl^2$ (273 K)	$\langle \mu \rangle_0^2/nm^2$ (273 K)	$[d \ln \langle r \rangle_0^2/dT]$ ($10^{-3}K^{-1}$)	$[d \ln \langle \mu \rangle_0^2/dT]$ ($10^{-3}K^{-1}$)
Observed*	5.2	0.53	0.23	2.6
PM3	2.08	0.54	0.17	0.27
Ab initio				
Parameter sets 3	5.2	0.24	0.26	1.98
Parameter sets 4	3.75	0.15	0.95	3.34

Observed: D. R. Beech and C. Booth, *J. Polym. Sci., Part A-2*, 1969, 7, 575.

Calculate: A. Abe *Polym. J.*, 1982, 14, 427.

Table 5 Bond conformations and NMR vicinal coupling constants of PEO

Case	f_t^{CC}	f_t^{CO}	298 K		
			J_{HH} (Hz)	J_{HH}^1 (Hz)	J_{CH}^1 (Hz)
PM3	0.19	0.63	6.17	4.51	4.41
Ab initio					
Parameter sets 3	0.22	0.81	6.03	4.72	3.03
Parameter sets 4	0.27	0.74	5.79	5.07	3.61
Electron diffraction ^a	0.21	0.64	-	-	-
RISa	0.21	0.79	-	-	-
Exptla,b	-	-	5.85 5.81	4.69 4.78	4.09 4.23

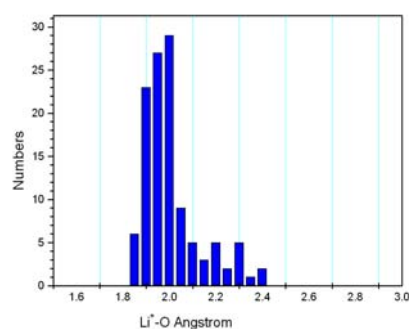
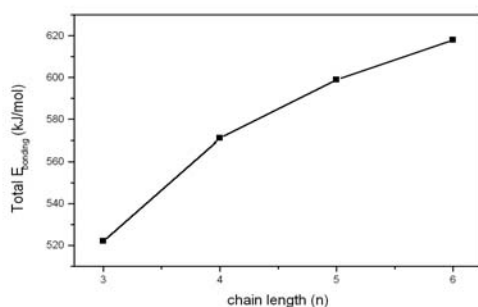
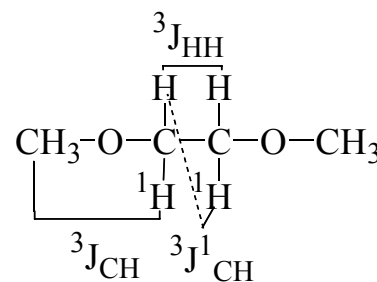


Figure 1 (a) Total bonding energy as a function of chain length (b) histograms of Li^+ -oxygen distance.

CURRICULUM VITAE

SIREERAT INTARAKAMHANG

Born: July 27, 1981, Nakhon Ratchasima

Citizenship: Thailand

Education

1999 – 2002 B.Sc. Chemistry

Khonkaen University, Khonkaen, Thailand

Experience

2001 Training in Laboratory, Rayong, Apex Petrochemical Company Limited, Thailand.

2004-2005 Teaching Assistance, School of Chemistry, Institute of Science, Suranaree University of Technology, Nakhon Ratchasima.

Presentation

1. Poster presentation at 31st Congress on Science and Technology of Thailand, 18-20 October 2005, Suranaree University of Technology.

2. Oral presentation at 31st Congress on Science and Technology of Thailand, 18-20 October 2005, Suranaree University of Technology.

3. Oral presentation at 10th Annual National Symposium on Computational and Engineering, 22-24 March 2006, Chiang Mai University

4. Poster presentation at 7th International Symposium of Polymer Physics, 1-5 June 2006, Suzhou, China.